

Cyclone Forcing of Coupled Dynamic and Thermodynamic Processes
In Arctic Sea Ice, and Across the Ocean-Sea Ice-Atmosphere Interface

by

Matthew Grant Asplin

A thesis submitted to the Faculty of Graduate Students of
The University of Manitoba
in partial fulfillment of the requirements for the degree of

DOCTOR OF PHILOSOPHY

Department of Environment and Geography
University of Manitoba
Winnipeg

Copyright © 2013 Matthew Grant Asplin

ABSTRACT

The declining summer Arctic sea ice is impacting cyclone-forcing of dynamic and thermodynamic processes in Arctic sea at different spatial and temporal scales throughout the annual cycle. A catalogue of daily synoptic weather types is generated for the southern Beaufort Sea, covering the period 1979 to 2011 using NCEP/NCAR reanalysis mean sea level pressure data, principle components and k-means cluster analyses. Synoptic type statistics are used to assess changes in atmospheric circulation characteristics, sea ice vorticity, and lead formation. Significant ($p < 0.05$) seasonal synoptic type frequency anomalies are revealed between 1979 – 1998 and 1999 – 2011, and indicate a stronger Beaufort high, and increased easterly wind forcing in autumn and winter. High rates of young ice production in November and December 2007 were linked to strong easterly wind forcing. A case study of the atmospheric boundary layer during a lead formation event (03 – 18 February 2008) revealed sensible heat fluxes between 0 – 80.14 W · m² (13 February 2008).

First-ever observations of a physical forcing mechanism between Arctic cyclones, the Arctic Ocean, and Arctic sea ice within the southern Beaufort Sea were observed on 06 September 2009. Large swells intruded into the multi-year pack ice, causing instantaneous widespread fracturing, and reduced the large (>1 km) parent ice floes to small (100 – 150 m diameter) floes. This process increased the ice floe perimeter exposed to the ocean by a factor of 4.5. Analysis of Radarsat-2 imagery showed that open water fractional area in the multi-year ice cover initially decreased from 3.7% to 2.7%, then increased to ~20% due to wind-forced divergence. 11.54 MJ · m⁻² of additional energy

was estimated for lateral melting as a result of the fracture event using radiation budgets prior to and following the event. Earlier occurrences of flexural fracture could hypothetically provide up to three times more additional energy for lateral melt. Furthermore, this process may increase the likelihood of storm-driven upwelling of ocean heat, thereby enhancing bottom melt in the ice cover. This process is therefore presented as a potentially powerful positive feedback process that may accelerate the loss of Arctic sea ice.

ACKNOWLEDGEMENTS

First and foremost, I would like to acknowledge the mentorship and support, both academic and financial, from my supervisor, Dr. David Barber. I would also like to thank Drs. John Hanesiak, Tim Papakyriakou, and Paul Bullock for their support and feedback as my PhD committee over the past five years. I would also like thank Dr. James Overland for fulfilling the role of external examiner for my dissertation.

I would like to extend a general thanks to all the graduate students, staff, research associates, post-doctoral fellows, technical, and administrative staff at the Centre for Earth Observation Science for helping make this work possible. In particular I would like to thank Lauren Candlish, Jennifer Lukovich, Brent Else, Ryan Galley, Randall Scharien, Richard Raddatz, and Simon Prinsenberg for their collaborations and insightful commentary on my four manuscripts. Furthermore, I would like to thank Daniel Leitch for all of his hard work coordinating the 2007-2008 International Polar Year Circumpolar Flaw Lead System Study (IPY-CFL).

I would like to thank the University of Manitoba for a Graduate Fellowship, the Garfield W. Weston Foundation for a Doctoral Scholarship, the Northern Scientific Training Program for support on two of my field seasons, and the V.E. Barber Memorial Fellowships for Arctic Research. I would also like to extend thanks to ArcticNet and the Industrial Partnership program with BP and Imperial Ltd. Their financial support helped make the 2009 and 2010 field seasons possible.

I would also like to thank my wife Laura Asplin for all of her support and for kindly helping to improve my manuscripts despite her own commitments to her professional training as a family physician.

DEDICATION

I dedicate this dissertation in loving memory of my father, Robert Grant Asplin, whose career developing sonar technology took him to the Arctic on several occasions, including a search for the lost Franklin expedition ships in 2000. His passion for boats and the ocean inspired my interest in weather and climate, and led me to my career as an Arctic research scientist.

1942 – 2006



TABLE OF CONTENTS

ABSTRACT	II
ACKNOWLEDGEMENTS	IV
DEDICATION	V
TABLE OF CONTENTS	VI
LIST OF TABLES	IX
LIST OF FIGURES	X
CHAPTER ONE: INTRODUCTION	15
1.0 Rationale and Context	15
1.1 Science Objectives	18
1.2 Dissertation Structure	19
1.3 References	22
CHAPTER TWO: BACKGROUND AND LITERATURE REVIEW	25
2.1 The Nature of Arctic Cyclones	25
2.1.1 The Global Energy Balance	25
2.1.2 Atmospheric and Ocean Dynamics	29
2.1.3 Cyclogenesis	33
2.1.4 Fronts and Frontogenesis	35
2.1.5 Arctic Cyclone Climatology	37
2.1.6 Teleconnections and Arctic Cyclones	42
2.2 Cyclone Forcing of Sea Ice Dynamic Processes	46
2.2.1 Large-Scale Atmospheric Forcing of Sea Ice	46
2.2.2 Momentum and Sea Ice Motion	51
2.2.3 Sea Ice Thickness and Morphology	55
2.2.4 Waves and Flexural Failure	56
2.2.5 Sea Ice Floe Size and Lateral Melting	59
2.3 Cyclone Forcing of Sea Ice Thermodynamics	61
2.3.1 Sea Ice Formation	61
2.3.2 Snow Cover Influences on Sea Ice Thermodynamics	62
2.3.3 Radiative Processes	66
2.3.4 Turbulent Fluxes	68
2.3.5 Polynyas and Sea Ice Leads	71
2.3.6 Leads, Polynyas, and Cyclone-Coupling	74
2.3.7 Ocean Heat Flux	78
2.4 Sea Ice Coupled Processes and Climate Change	79
2.4.1 Atmospheric Response to Climate Change	80
2.4.2 Sea Ice Response to Climate Change	82
2.4.3 Coupled Ocean-Sea-Ice Atmospheric Processes	83

2.5 Conclusions.....	91
2.6 References.....	92
CHAPTER THREE: ATMOSPHERIC FORCING OF THE BEAUFORT SEA ICE GYRE: PART 1: SURFACE PRESSURE CLIMATOLOGY AND SEA ICE MOTION	
.....	104
3.1 Introduction.....	104
3.2 Methods.....	109
3.3 Results.....	116
3.3.1 Synoptic Climatology	116
3.3.2 Temporal Variability of Synoptic Patterns	119
3.3.3 Synoptic types and the AO	126
3.3.4 Synoptic Types and BG Reversals.....	128
3.3.5 Within-type Variability of BG Vorticity.....	133
3.4 Conclusions.....	136
3.5 References.....	138
CHAPTER FOUR: SYNOPTIC ATMOSPHERIC CIRCULATION CHANGES AND SEA ICE LEAD FORMATION IN THE SOUTHERN BEAUFORT SEA	
.....	140
4.1 Introduction.....	140
4.2 Data and Methods	144
4.2.1 Regional Synoptic Climatology.....	146
4.2.2 Regional Sea Ice Data.....	149
4.2.3 Ship-based Meteorology	150
4.3 Results and Discussion	154
4.3.1 Synoptic Climatology and Declining Sea Ice Extent.....	154
4.3.2 ABL Profiles for 2007 - 2008	158
4.3.3 Sea Ice in the southern Beaufort Sea	161
4.3.4 Cyclone Wind Forcing and Lead Formation in 2007-08.....	167
4.3.5 Lead Formation Case Study: 03 – 18 February 2008.....	169
4.4 Conclusions.....	177
4.5 References.....	181
CHAPTER FIVE: FRACTURE OF SUMMER PERENNIAL SEA ICE BY OCEAN SWELL AS A RESULT OF ARCTIC STORMS.	
.....	187
5.1 Introduction.....	187
5.2 Data and Methods	191
5.3 Results.....	197
5.4 Discussion.....	208
5.5 Conclusions.....	213
5.6 References.....	215
CHAPTER SIX: IMPLICATIONS OF FRACTURED ARCTIC PERENNIAL ICE COVER ON THERMODYNAMIC AND DYNAMIC SEA ICE PROCESSES.	
.....	219
6.1 Introduction.....	219
6.2 Data and Methods	226

6.3 Results.....	238
6.4 Discussion.....	247
6.5 Conclusions.....	253
6.6 References.....	256
CHAPTER SEVEN: CONCLUSIONS AND RECOMMENDATIONS.....	262
7.1 Summary of contributions.....	262
7.2 Conclusions.....	264
7.3 Future Work.....	269
APPENDIX A: CONTRIBUTIONS OF COLLABORATING AUTHORS.....	271
APPENDIX B: ADDITIONAL CONTRIBUTIONS TO THE PEER-REVIEWED LITERATURE.....	273

List of Tables

Table 3.1. Cluster/circulation type characteristics for 1979 – 2006.	120
Table 3.2. Cluster/circulation type characteristics for 1979 – 2006, MJJASO and NDJFMA seasons.	120
Table 3.3. Kolmogorov D and P-values from a Kolmogorov-Smirnov test for seasonal variability in Δ vorticity distributions between positive and negative BG vorticity regimes for all types. Boldface is significant at the 95% level.	133
Table 4.1. Synoptic type climatology for 1979 – 1998 and for 1999 – 2011. Significant associations at the 90% and 95% levels are indicated by * ($p < 0.1$) or + ($p < 0.05$).	155
Table 4.2. Seasonal percent synoptic type frequencies. 1979 – 1998, 1999 – 2011, and (1999-2011) – (1979 – 1998). Significant associations at the 90% and 95% levels are indicated by * ($p < 0.1$) or + ($p < 0.05$).	157
Table 6.1. Cumulative radiative energy to lateral melting in sea ice leads versus timing of the flexural failure event.	244

List of Figures

Figure 2.1. The global energy balance showing an energy deficit (surplus) in the polar (equatorial) regions.	27
Figure 2.2. The geostrophic balance between the pressure-gradient force, and the Coriolis force.	31
Figure 2.3. Conceptual model of general circulation in the atmosphere (from: Pidwirny, 2006).	32
Figure 2.4. Back-tilted structure of upper-level flow in a cyclone (Arhens, 2007).	34
Figure 2.5. Horizontal cross section showing a cold front (left) and a warm front (right).	36
Figure 2.6. Winter (a), spring (b), summer (c) and autumn (d) cyclone tracks for cyclones traveling into the Arctic, accounting for at least 5% of the total activity for that season. (modified from: Sorteberg and Walsh 2008).	39
Figure 2.7. Relative intensities of cyclones by region of origin (from: Zhang et al., 2004).	41
Figure 2.8. Typical Arctic Ocean circulation pattern, showing an anticyclonic Beaufort Gyre, and the Transpolar Drift (from: AMAP, 1998).	47
Figure 2.9. Influence of passing cyclones on sea ice drifting beacon speeds (from: Brümmer et al., 2003).	54
Figure 2.10. Modeled decay of ocean waves ($t = 13 - 35$ s) as they propagate through 1670km of irregular ice terrain (from: Squire et al., 2009).	58
Figure 2.11. Typical conditions over a sea ice lead in the winter (from Barry, 2007).	70
Figure 2.12. Modeled thermal plume created by an Arctic lead. Contour surface is 0.2 m s^{-1} vertical motion. Color shade indicates height, sliced at 4-m increments. The x-axis is angled at 15° to orient the geostrophic wind parallel to the vertical figure frame (from: Glendening, 1995).	73
Figure 2.13. Atmospheric profile over a seasonally ice-free Arctic: Vertical structures of the geopotential heights (m; contours) and temperature ($^\circ\text{C}$; color) responses along 90°E in (left) November-December and (right) January-February (from: Deser et al., 2010).	84
Figure 2.14. Observed 2005 – 2008 minimum sea ice extents and 1979 – 2000 median ice extent (purple line).	90

Figure 3.1. Synoptic typing boundaries (solid line) and sea ice vorticity study area (red).	110
Figure 3.2. a) Cumulative variance explained by each PC, and b) average cluster distance, which represents average homogeneity within the clusters.....	112
Figure 3.3. MSLP (mb) composites for the 12 synoptic types.	117
Figure 3.4a. Cumulative probability distributions of the 12 synoptic types.....	121
Figure 3.4b. Synoptic type percent occurrences for within MJJASO, NDJFMA, and the annual cycle.	122
Figure 3.5. Dominant weekly synoptic types from 1979 to 2006 show weekly types from week 25 to week 24 of the following year. Cyclonic (anticyclonic) types are shown in warm (cool) colors. Weeks with no dominant synoptic type are white.....	124
Figure 3.6. Residuals of the Chi-square test of annual synoptic type frequencies in relation to the AO with Arctic cyclone types identified by circles.....	127
Figure 3.7. BG sea ice average weekly vorticity. Cyclonic (Anticyclonic) sea ice motion is indicated in shades of red (blue). Data missing in 2004, weeks 46 - 52: (After Lukovich and Barber, 2006).	129
Figure 3.8. Lag correlations between twelve-week running mean synoptic type frequencies and spatially-averaged BG sea ice vorticity data that are significant at the 95% level ($p < 0.05$).....	131
Figure 4.1. Top: Distributed open-water sample sites sampled in the autumn of 2007 and the summer of 2008. Bottom: Drift stations and fast ice stations sampled in the winter and spring of 2007 – 2008.	145
Figure 4.2. Mean sea level pressure (mb) composites for the 12 synoptic types for the analysis period 1979 – 2008. Prevailing circulation and time of year most prevalent (Yr = all-year, Sp = spring, Su = summer, A = autumn, W = winter) are described in parenthesis. Modified following Asplin et al., [2009].	148
Figure 4.3. Daily synoptic type classifications for 01 September 2007 – 31 August 2008 presented weekly by day-of-year. Synoptic types are color-coded by the prevailing synoptic-scale circulation over the study region: green: easterly, blue: northerly, orange: southerly, cyan, westerly.....	149
Figure 4.4. Top) Daily mean sea level pressure from 22 November (J326) to 04 August 2008 (J217), Middle) Daily mean air temperature at surface (~18m) and 1500m from the microwave profiling radiometer, Bottom) 0 – 10 km daily mean atmospheric temperature profile from the microwave profiling radiometer.	159

Figure 4.5. 0 – 2000 m microwave profiling radiometer temperature profile (top) and absolute humidity profile (bottom) for JFM (A) and AMJ (B).	160
Figure 4.6. 1983 – 2008 areal average week-year sea ice concentration (in tenths) for total sea ice (top left), old sea ice (top right), first-year sea ice (bottom left), and young sea ice types (bottom right).....	163
Figure 4.7. Flaw lead areas in Amundsen Gulf during 2007 - 2008 and component areas of young ice types. Total flaw lead area is the cumulative areas of component young ice types including thin first-year (FYtn, 30 – 70 cm), young (Yng, 10 – 30 cm), and new ice (New, < 10 cm).....	165
Figure 4.8. Top: photo taken near Nelson Head, Banks Island, N.W.T. Canada on 19 November 2007 showing young and new ice that persisted in this region into early December 2007 due to strong easterly winds associated with synoptic types 10 and 11. Bottom: rapidly refreezing winter lead observed 14 February 2008.	166
Figure 4.9. Top: Advanced Very High Resolution Radiometer (AVHRR) image for 11 February 2008 20:55:55 UTC showing consolidated sea ice in Amundsen Gulf, and a lead forming southeast of the ship’s position (denoted in red). Bottom: AVHRR image for 16 February 2008 19:31:41 UTC showing 85% of Amundsen Gulf sea ice cover as fractured, containing numerous sea ice leads. Vector winds for 03 – 18 February 2008 show wind forcing during this period. AVHRR imagery acquired from the NOAA/ AVHRR satellite via the receiving station at the Meteorological Service of Canada’s Prairie and Arctic Storm Prediction Centre.	170
Figure 4.10. Mean sea level pressure composites for 03 – 07 February 2008 (top), 08 – 12 February 2008 (middle), and 13 – 18 February 2008 (bottom) (Images provided by the NOAA/ESRL Physical Sciences Division, Boulder Colorado from their Web site at http://www.cdc.noaa.gov/).	172
Figure 4.11. Microwave profiling radiometer temperature (top) and water vapor (middle) profiles for 0 – 2000m, and SLP and surface air temperature (bottom) for 03 – 18 February 2008 (DOY 34 – 49). A thermal internal boundary layer (T-IBL) is present from 08 – 12 February 2008 (DOY 39 – 42) and from 15 – 16 February (DOY 46 – 47), and is identified as periods of near-surface atmospheric warming caused by sensible heat fluxes to the atmosphere. Warm air advection reaching the surface on 17 February (DOY 48) removes the contrast between the area-average surface temperature and the air temperature, thereby eliminating sensible heat fluxes to the atmosphere and preventing the formation of a T-IBL.	174
Figure 4.12. Clear-sky upward surface sensible heat fluxes calculated for 03 – 18 February 2008 (DOY 34 – 49).....	176

Figure 5.1. a, National Snow and Ice Data centre (NSIDC) sea ice aerial extent, b, Canadian Ice Service ice chart for 07 September 2009 showing sea ice concentration and stage of development. Ship-based sampling sites and EMI survey FEM09397, flown on 09 September 2009, are shown.....	193
Figure 5.2. Summary of 06 September 2009 afternoon helicopter EMI survey (FEM09381) flown over multi-year ice floes at station MYI. The image shows a thick (~5 m) second-year ice floe after flexural fracture as observed from the wheelhouse of the ship. The histogram shows a distribution of ice thicknesses with a mean of 2.0 m.....	198
Figure 5.3. a, Laser altimeter data from the EMI system at 13:30LST. b, Example of 100 Hz ship heave while at station MYI (06 September 2009, 18:00 to 18:05 UTC) and at station L3 (07 September 2009, 13:40 to 13:45 UTC). c, 17:02 UTC from 06 September 2009 at station MYI, video width = 140. No cracks in old, 2m thick ice floe are visible. d, 19:00 UTC 06 September 2009. Thick ice (2m thick in level ice sections) at station MYI now has cracks aligned perpendicular to swell direction running from NW to SE. Crack spacing is approximately the width of the video (110 m).....	200
Figure 5.4. Summary of 09 September 2009 afternoon long-line (FEM09397) helicopter EMI survey flown over fractured first and second-year ice floes from 72.52°N 136.75°W to 72.52°N 133.40°W. Image shows rounded first-year ice floes ranging in diameter from 20 – 50 m as observed from the helicopter survey. The histogram describes the ice thickness distribution with a bi-modal distribution with peaks at 0.8 m and 2.5 m.....	201
Figure 5.5. a, Daily MSLP composites for 01 – 06 September 2009. b, Daily mean vector wind (m/s) composites for 01 – 06 September 2009. (Images provided by the NOAA/ESRL Physical Sciences Division, Boulder Colorado from their Web site at http://www.cdc.noaa.gov/).....	203
Figure 5.6. a, Atmospheric relative humidity and b, temperature profiles for 06 September 2009. c, Ice salinity d, and temperature profiles for old ice and heavily decayed first-year ice taken at stations MYI and L2 respectively. e, 0 – 50m ocean salinity and f, temperature profiles taken at station L2.....	205
Figure 5.7. Incoming shortwave (K_{\downarrow}) and longwave (L_{\downarrow}) radiation time series measured from the CCGS Amundsen from 01 – 09 September 2009.	207
Figure 6.1. Top: National Snow and Ice Data centre (NSIDC) sea ice aerial extent with study area boundary, Bottom: Canadian Ice Service ice chart for 04 September 2009 showing sea ice concentration and stage of development. Ship-based sampling sites and cruise plan are shown.	227

Figure 6.2. Southern Beaufort Sea study region. CCGS Amundsen Cruise average hourly positions are shown for 01 August – 30 September 2009.	229
Figure 6.3. Radarsat-2 image for 1513 UTC 03 September 2009, three days prior to the 06 September 2009 flexural failure event.	233
Figure 6.4. Radarsat-2 image for 1538 UTC 06 September 2009, immediately following the 06 September 2009 flexural failure event.	234
Figure 6.5. ROI: 25 by 25km square centred on 74°N 26.266' 133°W 23.141' full scene prior to the flexural fracture event 03 September 2009 1525 UTC (top left), and following the flexural fracture event 06 September 2009 1538UTC (top right). ROI Subset RGB: r =hh; g=hv; b=hv. Before (middle left) and after (middle right) flexural failure event. Open water classification: (class: 0 = open water; 1 = ice). Open water 3.7% before (bottom left), and 2.7% after (bottom right) flexural failure event.	239
Figure 6.6. Left: 17:02 UTC from 06 September 2009 at station MYI, video width = 140. No cracks in old, 2m thick ice floe are visible. Right: 19:00 UTC 06 September 2009. Thick ice (2m thick in level ice sections) at station MYI now has cracks aligned perpendicular to swell direction running from NW to SE. Fractured ice floes have a diameter approximately the width of the video (110m). Surface is characterized by old and new meltponds ranging from 10 – 30% coverage. Open water coverage between floes is <5%, but total floe perimeter exposed to ocean has increased by a factor of 4.	240
Figure 6.7. Image taken during 09 September 2009 afternoon long-line (FEM09397) helicopter EMI survey flown over fractured first and second-year ice floes 20 – 50m in diameter from 72.52°N 136.75°W to 72.52°N 133.40°W. Fractured ice floes have diverged to 80% sea ice coverage and yield a heterogenous surface in conjunction with meltponds.	241
Figure 6.8. Hourly average values of in situ K_{\downarrow} for 01 August to 30 September 2009...	242
Figure 6.9. Hourly average values of in situ L_{\downarrow} for 01 August to 30 September 2009. ..	243
Figure 6.10. Estimated cumulative radiative energy ($L^* + K^*$) going into lateral melting via sea ice leads versus timing of a regional swell-driven flexural fracture event.	245
Figure 6.11. Drifting ice beacon data from beacons deployed on 08 September (282070, 284060), 520590 (06 September 2009; deployed during flexural failure event at station MYI). Data is classified by month (red = September, green = October, blue = November, Black = December) and shows considerable divergence of the beacons over time.	246

CHAPTER ONE: INTRODUCTION

1.0 Rationale and Context

Global climate change is impacting the Arctic Ocean, sea ice and atmosphere. The most tangible evidence of change in the sea ice cover is the decline of summer minimum Arctic sea ice extents (defined as areas with >15% sea ice cover) at a rate of approximately $-81,310 \text{ km}^2$ per year (-12.4% per decade for September for 1979 - 2010)[*Stroeve et al.*, 2011]. Other studies document declines in sea ice thickness [*Rothrock et al.*, 1999; *Hilmer and Lemke*, 2000], age of sea ice [*Nghiem et al.*, 2007; *Maslanik et al.*, 2011], and sea ice volume [*Kwok et al.*, 2009; *Laxon et al.*, 2013]. Furthermore, an increasing melt season length has been observed in the Northern hemisphere [*Markus et al.*, 2009]. These trends have recently been highlighted by a new record minimum sea ice extent of $3.41 \times 10^6 \text{ km}^2$ observed on 16 September 2012 [*Parkinson and Comiso*, 2013], which surpassed the 18 September 2007 extent ($4.2 \times 10^6 \text{ km}^2$) on 26 August 2012 by $790,000 \text{ km}^2$. The rate of areal sea ice decline in 2012 was impressive as it represents the greatest summer ice extent loss ($11.83 \times 10^6 \text{ km}^2$) relative to the winter maximum extent ($15.24 \times 10^6 \text{ km}^2$, 18 March 2012) in the satellite record.

Arctic cyclones can ‘pre-condition’ the Arctic sea ice cover for large declines in seasonal sea ice cover [*Screen et al.*, 2011; *Parkinson and Comiso*, 2012]. Many of the physical atmospheric and oceanic forcings that influence year-to-year Arctic sea ice variability are, in fact, linked to changes in cyclone activity. The September minimum sea ice extent appears to be strongly influenced by changes in seasonal mean sea level pressure (MSLP), [*Deser and Teng*, 2008], wind [*Ogi et al.*, 2010; *Ogi and Wallace*, 2012; *Overland et al.*, 2012], cloud [*Kay and Gettelman*, 2009], and regional air

temperatures [*Stroeve et al.*, 2007; *Overland*, 2009], all of which are directly linked to cyclone activity. Furthermore, interactions between cyclones, the sea ice and the ocean may influence observed increases in summer ocean mixed-layer depth [*Stroeve et al.*, 2011], increased ocean heat fluxes [*Shimada et al.*, 2006; *Woodgate et al.*, 2006; *Steele et al.*, 2008], increased solar heating [*Perovich et al.*, 2008], and increased ice motion and deformation [*Rampal et al.*, 2009; *Rampal et al.*, 2011; *Kwok et al.*, 2013].

We expect the future Arctic Ocean to resemble that of a marginal ice zone (MIZ), which is known to contain important zones of biological productivity [*Wassman et al.*, 2006; *Pabi et al.*, 2008], and are also important contributors of moisture and energy to local climate systems in the Arctic [*Maykut*, 1978]. Sea ice can be dynamically forced by strong winds arising from cyclones, revealing openings in the sea ice called leads or polynyas [*Barry and Maslanik*, 1989]. These openings expose the relatively warm surface of the ocean to the cold atmosphere above. The exchange of energy and moisture is a dominant process in the winter surface climate of MIZs [*Maykut*, 1978], and will become increasingly important to the winter climate system with an increase in first-year ice formation, and sea ice lead formation.

Temperature advection, precipitation, and winds associated with cyclones represent significant sources of cyclone forcing upon energy, mass and momentum transfers in the Arctic [*Barry and Carleton*, 2001; *Sorteberg and Walsh*, 2008]. The role of cyclones in moderating momentum, mass and energy fluxes across the OSA interface in MIZs is presently not well understood, and therefore represents an important area of research. However, given the nonlinearity in surface winds and ocean heat fluxes, their evaluation requires knowledge of conditions on all spatial-temporal scales. A broad perspective is

first provided by examining changes in the synoptic climatology of cyclones, and investigating observations of emerging interactions between cyclones and the changing Arctic Ocean and icescape, which is defined as the complex surface of the Arctic sea ice cover including ridges, melt ponds, snow cover, sea ice leads, and different ice types [Barber *et al.*, 1995]. This is followed by investigation of *in situ* observations of cyclone forcing of the ocean-sea ice-atmosphere interface through analysis of field data collected from the ocean, sea ice and atmosphere from 2007 – 2011, a period in which the Arctic is characterized by rapidly declining summer sea ice cover.

1.1 Science Objectives

Recognizing that storms influence the Arctic sea ice at different temporal and spatial scales, the overall goal of this research is to investigate dynamic and thermodynamic processes between Arctic sea ice and Arctic cyclones at different scales of study. In order to achieve this goal, this thesis is sub-divided into four research sections that investigate the following objectives:

- 1) What is the synoptic climatology of surface atmospheric circulation patterns in the Southern Beaufort Sea?
- 2) What role do Arctic cyclones have on forcing sea ice motion, particularly in the case of summer reversals of the Beaufort Sea ice gyre?
- 3) Is the recent acceleration in the declining summer sea ice extent linked to changes in atmospheric circulation patterns, and how do these changes impact first-year ice formation during autumn and winter?
- 4) Investigate the process of ocean swell fracturing of perennial sea ice by swells generated within the Arctic Ocean. Will this mechanical forcing mechanism, emerging as a result of large open water anomalies in the Arctic Ocean, act as a positive feedback in the loss of summer sea ice?
- 5) What are the dynamic and thermodynamic implications of reduced mean floe sizes resulting due to 4) on Arctic sea ice cover?

1.2 Dissertation Structure

This thesis is comprised of seven chapters. Chapter one places the topic of this thesis into broad scientific context. Chapter two comprises a comprehensive literature review, which investigates the nature of Arctic cyclones, dynamic and thermodynamic processes in the growth and decay of sea ice, and the impacts of Arctic cyclones on these processes. It also describes how climate change may impact Arctic cyclones, and how declining sea ice cover may introduce new forms of ocean-atmosphere coupling that may modify cyclone forcing of the sea ice cover. Chapter three investigates the surface pressure climatology of the Southern Beaufort Sea, and atmospheric forcing of the Beaufort Sea ice gyre. This is achieved by first developing a synoptic climatology of the Southern Beaufort Sea for 1979 – 2006 using Principal Components Analysis, and subsequent k-means clustering. The resulting synoptic catalogue, consisting of twelve synoptic types, is then linked to sea ice vorticity using lag correlation analysis. The material in chapter three appears in this thesis as it has been published in the peer-reviewed literature in the journal *Geophysical Research – Oceans*.

Asplin, M. G., J. V. Lukovich, and D. G. Barber (2009), Atmospheric forcing of the Beaufort Sea ice gyre: Surface pressure climatology and sea ice motion, *J. Geophys. Res.*, *114*, C00A06, doi:10.1029/2008JC005127.

Chapter four investigates the relationship between declining summer Arctic sea ice extent and atmospheric circulation patterns in all seasons. I accomplish this by extending the synoptic climatology of chapter three to cover 1979 – 2011, and investigating changes in synoptic type frequency between the period 1979 – 1998 (slow decline in sea ice extent), and 1999 – 2011 (rapid decline in sea ice extent). The combined impacts of declining sea ice cover and changing atmospheric circulation

patterns are then linked to winter lead formation in the southern Beaufort Sea, using young ice type areal extent. A case study of a large lead formation event and resulting surface sensible heat fluxes as a result of a winter Arctic cyclone are presented. The material in chapter four appears in this thesis as it has been submitted and currently in review for publication in the peer-reviewed literature in the *Journal Geophysical Research – Atmospheres*.

Asplin, M.G., Candlish, L.M., Else, B.G.T. Raddatz, R.L., Galley, R.G., Papakyriakou, T., Barber, D.G., (2013), Synoptic atmospheric circulation changes and sea ice lead formation in the southern Beaufort Sea, *Jour. Geophys. Res. (In Review)*.

Chapter five investigates wind forcing from Arctic Cyclones on emerging large expanses of open water within the Arctic basin. We present first-ever observations of long period swell propagation into a region containing thick, multi-year ice floes that are simultaneously fractured through flexural failure. The origins of the long period swells are linked to winds from a series of migratory Arctic cyclones originating in Siberia interacting with fetch in the Chukchi and Laptev Seas. Ice floe distributions are calculated prior to and following the event. This process increases the amount of ice floe perimeter surface area by a factor of approximately four. The material in chapter five appears in this thesis as it has been published in the peer-reviewed literature in the *Journal Geophysical Research – Oceans*.

Asplin, M.G., Galley, R.J., Barber, D.G., Prinsenber, S., (2012), Fracture of summer perennial sea ice by ocean swell as a result of Arctic storms, *J. Geophys. Res. 117*, C06025, doi: 10.1029/2011JC007221.

Chapter six investigates the dynamic and thermodynamic implications of the process described in chapter five on the Arctic sea ice cover. The area impacted by the swell propagation event, estimated at 40,000 km², is analyzed for fractional ice and water

cover before and after the event. The change in regional surface albedo and ice floe size distributions is then used to evaluate the impact on lateral melting. The timing of large expanses of open water capable of producing long period swell in a future climate scenario is identified as key to determining the significance of this process in further reducing sea ice cover. This process is also discussed in context of the great Arctic cyclone of August 2012. The material in chapter six appears in this thesis as it has been submitted and currently in review for publication in the *Journal Geophysical Research – Oceans*.

Asplin, M.G., Scharien, R., Else, B.G.T., Barber, D.G., Papakriakou, T., Howell, S., and Prinsenberg, S., (2013), Implications of Fractured Arctic Perennial Ice Cover on Thermodynamic and Dynamic Sea Ice Processes, *Jour. Geophys. Res.*

Chapter seven summarizes the results of chapters three through six, and presents concluding remarks and recommendations for future work.

Appendix A describes the contributions of collaborating authors to the work presented in chapters three to six.

Appendix B lists contributions made as co-author to other sections within and outside the research group at the Centre for Earth Observation Science, during my time as a Ph.D. student at the University of Manitoba.

1.3 References

- Barber, D.G., S.P. Reddan, and E.F. Ledrew, (1995), Statistical characterization of the geophysical and electric properties of snow on land-fast first-year sea ice, *J. Geophys. Res.*, 100(CS): 2673 – 2686.
- Barry, R.G., J. Maslanik (1989), Arctic sea ice characteristics and associated atmosphere – ice interactions in summer inferred from SMMR data and drifting buoys: 1979 – 1984
- Barry, R.G., and A.M. Carleton (2001), *Synoptic and Dynamic Climatology*, Routledge, London, pp 620.
- Deser, C., and H. Teng (2008), Evolution of Arctic sea ice concentration trends and the role of atmospheric circulation forcing, 1979 – 2007. *Geophys. Res. Lett.*, 35, doi:10.1029/2007GL032023.
- Hilmer, M., and P. Lemke (2000), On the decrease of Arctic sea ice volume, *Geophys. Res. Lett.*, 27(2), 3751 – 3754.
- Kay, J.E., and A. Gettelman (2009). Cloud influence on and response to seasonal Arctic sea ice loss, *J. Geophys. Res.*, 114, D18204, doi:10.1029/2009JD011773.
- Kwok, R., G. F. Cunningham, M. Wensnahan, I. Rigor, H.J. Zwally, and D. Yi (2009), Thinning and volume loss of the Arctic Ocean sea ice cover: 2003 – 2008, *J. Geophys. Res.*, 114, C07005, doi:10.1029/2009JC005312.
- Kwok, R., G. Spreen, and S. Pang (2013), Arctic sea ice circulation and drift speed: decadal trends and ocean currents, *Jour. Geophys. Res. (in press)*, doi: 10.1002/jgrc.20191.
- Laxon S. W., K. A. Giles, A. L. Ridout, D. J. Wingham, R. Willatt, R. Cullen, R. Kwok, A. Schweiger, J. Zhang, C. Haas, S. Hendricks, R. Krishfield, N. Kurtz, S. Farrell and M. Davidson (2013), CryoSat-2 estimates of Arctic sea ice thickness and volume, *Geophys Res Lett.*, 40, doi:10.1002/grl.50193.
- Markus, T., J.C. Stroeve, and J. Miller (2009), Recent changes in Arctic sea ice melt onset, freeze-up and melt season length, *J. Geophys. Res.* 114, C12024, doi: 10.1029/2009/JC005436.
- Maslanik, J., J. Stroeve, C. Fowler, and W. Emery (2011), Distribution and trends in Arctic sea ice age through spring 2011, *Geophys. Res. Lett.*, 38, L13502, doi: 10.1029/2011GL047735.
- Maykut, G.A. 1978, Energy exchange over young sea ice in the Central Arctic. *J. Geophys. Res.* 83 (C7): 3646 – 3658.

Nghiem, S. V., I. G. Rigor, D.K. Perovich, P. Clemente-Colon, J.W. Weatherly, and G. Neumann, (2007), Rapid reduction of Arctic perennial sea ice, *Geophys. Res. Lett.*, 34, L19504, doi: 10.1029/2007GL031138.

Ogi, M., K. Yamazaki, and J. Wallace (2010), Influence of winter and summer surface wind anomalies on summer Arctic sea ice extent, *Geophys. Res. Lett.*, 37, L07701, doi: 10.1029/2009GL042356.

Ogi, M., and J. M. Wallace (2012), The role of summer surface wind anomalies in the summer Arctic sea ice extent in 2010 and 2011, *Geophys. Res. Lett.*, 39, L09704, doi:10.1029/2012GL051330.

Overland, J.E. (2009), Meteorology of the Beaufort Sea. *J. Geophys. Res.*, 114, C00A07, doi: 10.1029/2008JC004861.

Overland, J.E., J.A. Francis, E. Hanna, and M. Wang (2012), The recent shift in early summer Arctic atmospheric circulation, *Geophys. Res. Lett.*, 39, L19804. doi:10.29/2012GL053268.

Pabi, S., G. L. van Dijken, and K. R. Arrigo (2008), Primary production in the Arctic Ocean, 1998–2006, *J. Geophys. Res.*, 113, C08005, doi: 10.1029/2007JC004578.

Parkinson, C. L., and J. C. Comiso (2013), On the 2012 record low Arctic sea ice cover: Combined impact of preconditioning and an August storm, *Geophys. Res. Lett.*, 40, doi:10.1002/grl.50349.

Perovich, D.K., J.A. Richter-Menge, K.F. Jones, and B. Light (2008), Sunlight, water, and ice: Extreme Arctic sea ice melt during the summer of 2007, *Geophys. Res. Lett.* 35, L11501, doi:10.1029/2008GL034007.

Rampal, P., J. Weiss, and D. Marsan (2009), Positive trend in the mean speed and deformation rate of Arctic sea ice, 1979–2007, *J. Geophys. Res.*, 114, C05013, doi:10.1029/2008JC005066.

Rampal, P., J. Weiss, C. Dubois, and J.M. Campin, (2011), IPCC climate models do not capture Arctic sea ice drift acceleration: consequences in terms of projected sea ice thinning and decline, *J. Geophys. Res.*, 116, C00D07, doi:10.1029/2011JC007110, 2011.

Rothrock, D.A., Y. Yu., G.A. Maykut, (1999), Thinning of the Arctic sea-ice cover. *Geophys. Res. Lett.*, 23: 3469 – 3472.

Screen J.A., I. Simmonds, and K. Keay (2011). Dramatic inter-annual changes of perennial Arctic sea ice linked to abnormal summer storm activity, *J. Geophys. Res.*, 116, D15105, doi:10.1029/JD015847.

Sorteberg A., and J.E. Walsh, (2008), Seasonal cyclone variability at 70°N and its impact on moisture transport into the Arctic, *Tellus* 60A, 570 – 586.

Steele, M., W. Ermold, and J. Zhang, (2008), Arctic Ocean surface warming trends over the past 100 years, *Geophys. Res. Lett.*, 35, L02614, doi: 10.1029/2007GL031651.

Shimada, K., T. Kamoshida, M. Itoh, S. Nishino, E. Carmack, F. McLaughlin, S. Zimmermann and A. Proshutinsky (2006): Pacific Ocean inflow: Influence on catastrophic reduction of sea ice cover in the Arctic Ocean. *Geophys. Res. Lett.*, 33, L08605, doi: 10.1029/2005GL025624.

Stroeve, J., M. M. Holland, W. Meier, T. Scambos, and M. Serreze, (2007), Arctic sea ice decline: Faster than forecast, *Geophys. Res. Lett.*, 34, L09501 doi:10.1029/2007GL029703.

Stroeve, J.C., M.C. Serreze, M.M. Holland, J.E. Kay, J. Maslanik, and A.P. Barrett (2011), The Arctic's rapidly shrinking sea ice cover: a research synthesis, *Clim. Ch.* doi: 10.1007/s10584-011-0101-1.

Wassman, P., M. Reigstad, T. Haug, B. Rudels, M.L Carroll, et al., (2006) Food webs and carbon flux in the Barents Sea, *Prog. Oceano.* 71 (2006) 232 – 287.

Woodgate, R. A., K. Aagaard, and T. J. Weingartner, (2006), Interannual changes in the Bering Strait fluxes of volume, heat and freshwater between 1991 and 2004, *Geophysical Research Letters*, 33, L15609, doi: 10.1029/2006GL026931.

CHAPTER TWO: BACKGROUND AND LITERATURE REVIEW

2.1 The Nature of Arctic Cyclones

This chapter describes the physical formation mechanisms of cyclones, and their role in nature in the geophysical context of the Arctic basin. This chapter is also my candidacy exam essay, which responds to my PhD Candidacy exam question:

“Explain the nature of Arctic cyclones, evaluate the role they play in forcing sea ice dynamic and thermodynamic processes, and evaluate whether climate change may affect these coupled processes.”

2.1.1 The Global Energy Balance

Solar irradiance is the principle energy source that drives ocean and atmosphere dynamic and thermodynamic processes. The sun emits energy as electromagnetic radiation, following the Stefan-Boltzman law, which dictates that all bodies with a temperature greater than absolute zero emit radiation:

$$E = \varepsilon\sigma T^4 \tag{2.1}$$

Where E is the quantity of energy emitted, ε is the emissivity of the material ($\varepsilon < 1$ for most surfaces, with $\varepsilon = 1$ being a perfect emitter, or a “blackbody.”), σ is the Stefan-Boltzmann constant ($5.67 \times 10^{-8} \text{ W}\cdot\text{m}^{-2}\cdot\text{K}^{-4}$), and T is the temperature (K) of the body’s surface. Energy density is typically quantified as a quantity per unit area ($\text{W}\cdot\text{m}^{-2}$), and

follows a fourth-power relationship with temperature. The sun ($T_{\text{SUN}} \approx 5780\text{K}$) thus emits a considerably higher energy density than the earth ($T_{\text{AVG}} \approx 288\text{K}$).

The peak wavelength of emission for body of a given temperature is described by Wiens law, which states that there is an inverse relationship between the wavelength of the peak emissivity of a black body, and its temperature when expressed as a function of wave length:

$$\lambda_{\text{MAX}} = \frac{b}{T} \quad (2.2)$$

where λ_{MAX} is the peak wavelength, T is the absolute temperature ($^{\circ}\text{K}$) of the blackbody, and b is a constant called ‘Wiens displacement constant’ that is $\sim 2.898 \times 10^{-3} \text{ m}\cdot\text{K}$. Radiative energy from the sun has peak intensity at wavelength $0.5 \mu\text{m}$, whereas energy emitted from relatively cooler bodies on earth peaks at $\sim 12 \mu\text{m}$; hence, we term these two regimes shortwave (K) and longwave (L), respectively. The amount of shortwave radiation received at the top of the earth’s atmosphere is $\sim 1366 \text{ W}\cdot\text{m}^{-2}$. This value is widely referred to as the solar constant I , and is known to vary on a decadal scale by $\sim 1.0 \text{ W}\cdot\text{m}^{-2}$.

The generalized radiation budget of the Earth is as follows:

$$Q^* = K\downarrow - K\uparrow + L\downarrow - L\uparrow \quad (2.3)$$

or

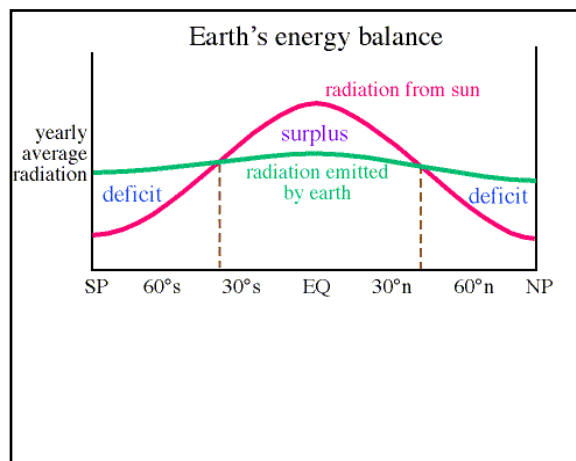
$$Q^* = (1 - \alpha) K\uparrow + L\downarrow - L\uparrow \quad (2.4)$$

where Q^* is the net radiation received, K_{\downarrow} is the downwelling shortwave (solar) radiation, L_{\downarrow} is downwelling longwave radiation, K_{\uparrow} is reflected shortwave radiation, and L_{\uparrow} is longwave radiation emitted and/or reflected to space, and α is albedo, defined as a fraction representing the radiative reflectivity of a surface. Albedo varies with the physical properties of different surfaces (including colour, roughness, etc), and is given for a particular wavelength of incoming radiation as:

$$\alpha(\lambda) = \frac{K_{\uparrow}}{K_{\downarrow}} \quad (2.5)$$

All surfaces on earth have unique reflective properties, and absorb / reflect radiative accordingly. Albedo values vary from 0.5 – 0.7 for MY sea ice and freshly fallen, dry snow, to ~0.1 for open water (Hertzman, 1997). Open water therefore absorbs a great deal more solar energy per unit area than sea ice, and is principal to the ice-albedo feedback, where global albedo decreases along with sea ice cover, resulting in increased absorption of solar energy in the Arctic Ocean.

Figure 2.1. The global energy balance showing an energy deficit (surplus) in the polar (equatorial) regions.



The greatest (least) amount of solar energy reaches the Earth's surface in the equatorial regions (Polar Regions), where the solar zenith angle (defined as the angle between the local zenith and the sun) is small (large). Radiative shortwave heating (longwave cooling) dominates the energy budget at the equator (poles), and results in a global imbalance in the global energy budget (Figure 2.1). This imbalance drives the general atmospheric circulation of the Earth. This imbalance is further forced by the seasonal effects of Earth's orbital obliquity, or Earth's axial tilt, which is $\sim 23.5^\circ$. As the earth revolves around the sun, the axial tilt results in seasonal variations of solar zenith angle, increasing in magnitude with latitude. This effect is most prominent in the Polar Regions north of 66° latitude where daily solar insolation can decrease to zero for one or more days in the winter season. This results in a seasonal strengthening of the polar energy deficit in one hemisphere, and weakening in the other.

The energy surplus-deficit contrast between the equator and Polar Regions results in a strong north-south temperature gradient. Energy is transferred from the equator to the Polar Regions meridionally by atmospheric and oceanic circulation. Ocean currents that distribute this energy are considerably slower than atmospheric circulation; hence the dominance of atmospheric circulation in redistributing global energy. The atmosphere is responsible for about 80% of the heat transfer, and the ocean is responsible for about 20% (Djuric, 2004).

Three principal processes drive energy transfer across the Earth's surface: sensible heat flux (Q_H), latent heat flux (Q_E), and surface heat flux (Q_S). These terms make up the general energy budget of the Earth:

$$Q^* = Q_E + Q_H + Q_S \quad (2.6)$$

Sensible heat flux is the process where heat energy is transferred from the Earth's surface to the atmosphere by conduction and convection. Latent heat flux is energy that is used to convert solid or liquid water into vapor. Water vapor is typically moved by atmospheric circulation vertically (convection), and horizontally (advection) where it is condensed into precipitation, and releases the heat energy stored within it. Surface heat flux refers to ocean heat transferred by ocean currents. The high specific heat capacity of water ($\sim 3996 \text{ J} \cdot \text{kg} \cdot \text{K}^{-1}$ for salt water) permits the Earth's oceans to absorb large quantities of solar energy. Radiative energy enters the ocean at the surface, and is then transferred downward into the water column by convection and conduction within the water column.

2.1.2 Atmospheric and Ocean Dynamics

Dynamic processes in the ocean and atmosphere are governed by fluid mechanics, and the ocean and atmosphere can be described as baroclinic or barotropic fluids. A baroclinic fluid is one for which the fluid's density depends on temperature and pressure, whereas density within a barotropic fluid depends only on pressure. The largest barotropic zones in the Earth's atmosphere are found in the tropics, and baroclinic zones are found in the mid-latitude regions (Djuric, 1994).

Three main forces affect atmospheric and oceanic circulation: the pressure-gradient force, the Coriolis force, and friction. The pressure-gradient force naturally drives circulation in a fluid from areas of high pressure to low pressure; circulation is

perpendicular to the pressure gradient. Earth's rotational momentum is transferred to all mass on the surface, and is known as the Coriolis force, and is defined as:

$$f_c = 2\Omega \sin(\Phi) \quad (2.7)$$

where Ω is the angular rotational velocity of the earth ($2\Omega = 1.458 \times 10^{-4} \cdot \text{s}^{-1}$), and Φ is latitude. The Coriolis force is strongest (zero) at the poles (equator) and is proportional to mass. The Coriolis force deflects ocean and atmospheric circulation from an area of high to low pressure to the right (left) in the northern (southern) hemisphere. This can result in fluidic rotational motion, termed "vorticity."

Vorticity is defined by fluid mechanics as "the tendency for a fluid to spin" (Stull, 2000). "Planetary vorticity" is generated by the rotation of the earth, and the magnitude depends on latitude. "Relative vorticity" is a measure of shear and curvature in a fluid, and can be generated by ageostrophic motions in geostrophic flow, wind shear in the atmosphere, and planetary vorticity. The total vorticity in a body is defined as "absolute vorticity." Relative vorticity is most commonly used to describe rotation in the ocean and atmosphere, and can be calculated as the vertical component of curl stress in a geostrophic fluid:

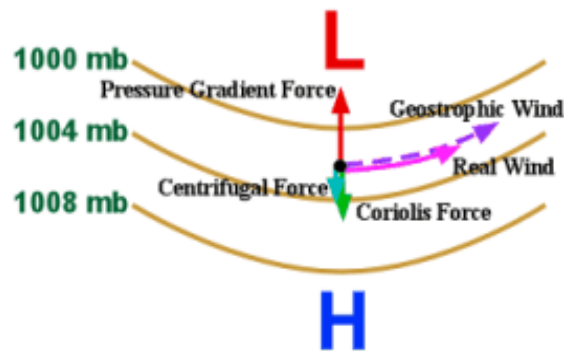
$$\zeta = \frac{\partial v}{\partial x} - \frac{\partial u}{\partial y} \quad (2.8)$$

where $\partial v/\partial x$ and $\partial u/\partial y$ represent the change in magnitude of motion vectors v and u along the x and y plains respectively. Vorticity can be positive (cyclonic) or negative (anti-cyclonic).

A theoretical balance, known as geostrophic balance, between the pressure-gradient force and the Coriolis force, yields a circulation known as the geostrophic wind

(Figure 2.2). Geostrophic circulation is defined as “circulation flowing parallel to isobars (line of constant pressure) or isohypse (line of constant geopotential height, which typically represent theoretical surfaces of equal pressure (hPa) in the atmosphere).” (Stull, 2000). True geostrophic flow does not typically occur in nature as frictional effects from a surface, or internal friction within the fluid introduces ageostrophy in the flow. Ageostrophic flow can be horizontal or vertical in nature, is most (least) noticeable at the surface (in the upper troposphere), and is key in describing divergence and convergence in a fluid.

Figure 2.2. The geostrophic balance between the pressure-gradient force, and the Coriolis force.

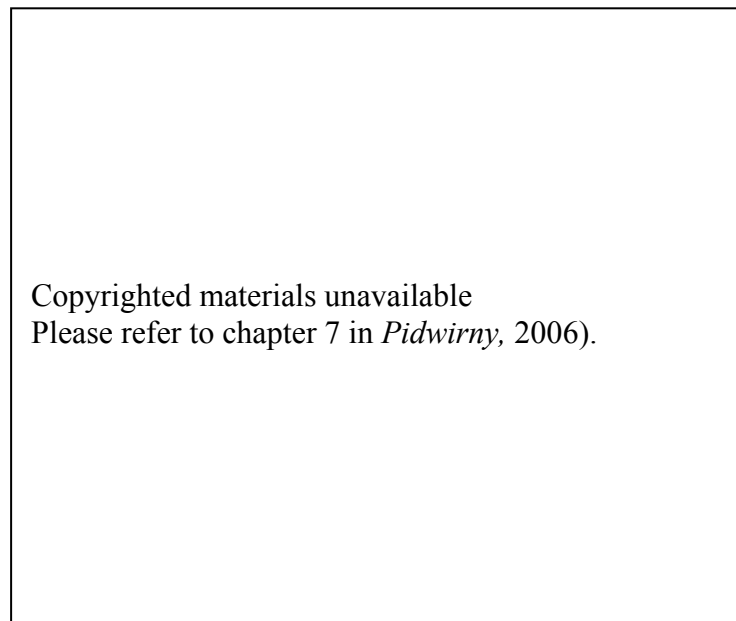


Atmospheric circulation can be further conceptualized into sub-global circulation patterns (Figure 2.3). Surface heating and convection at the equator causes upward vertical transport of sensible and latent heat, resulting in low pressure at the surface. Advection aloft moves this air poleward, where it cools, and eventually descends to the surface at $\sim 30^\circ$ latitude, creating sub-tropical areas of high pressure. Surface winds flowing towards the low-pressure zone at the equator are deflected by the Coriolis force, and are known as the “easterly tradewinds.” This circulation feature is referred to as the Hadley cell. Similar circulation cells exist between $30^\circ - 60^\circ$, and $60^\circ - 90^\circ$ latitude respectively, and are known as the Ferrel and Polar cells respectively. The Coriolis force

deflects surface flow into the surface low at 60°, created by the Polar and Ferrell cells, and results in a band of winds known as the “westerlies.” Large baroclinic pressure gradients aloft that exist between these cells produce strong winds, a feature known as the polar jet stream. The strongest winds in the jet stream occur between air masses have the largest temperature differences over the deepest layer of the troposphere.

Atmospheric circulation at the poles forms the polar vortex, a large upper-level permanent low-pressure feature. Atmospheric subsidence drives high pressure at the surface, forming cold, dry polar air masses. These polar airmasses interact with warm, moist airmasses at lower latitudes, and create a baroclinic environment, which subsequently leads to the formation of synoptic-scale cyclones, (or “frontal systems”, “low-pressure systems”). Upper-level atmospheric steering forces can cause these storms to migrate northward into the Arctic basin, where they may succumb to cyclolysis, or re-intensity through cyclogenesis in localized baroclinic environments in the Arctic.

Figure 2.3. Conceptual model of general circulation in the atmosphere (from: Pidwirny, 2006).



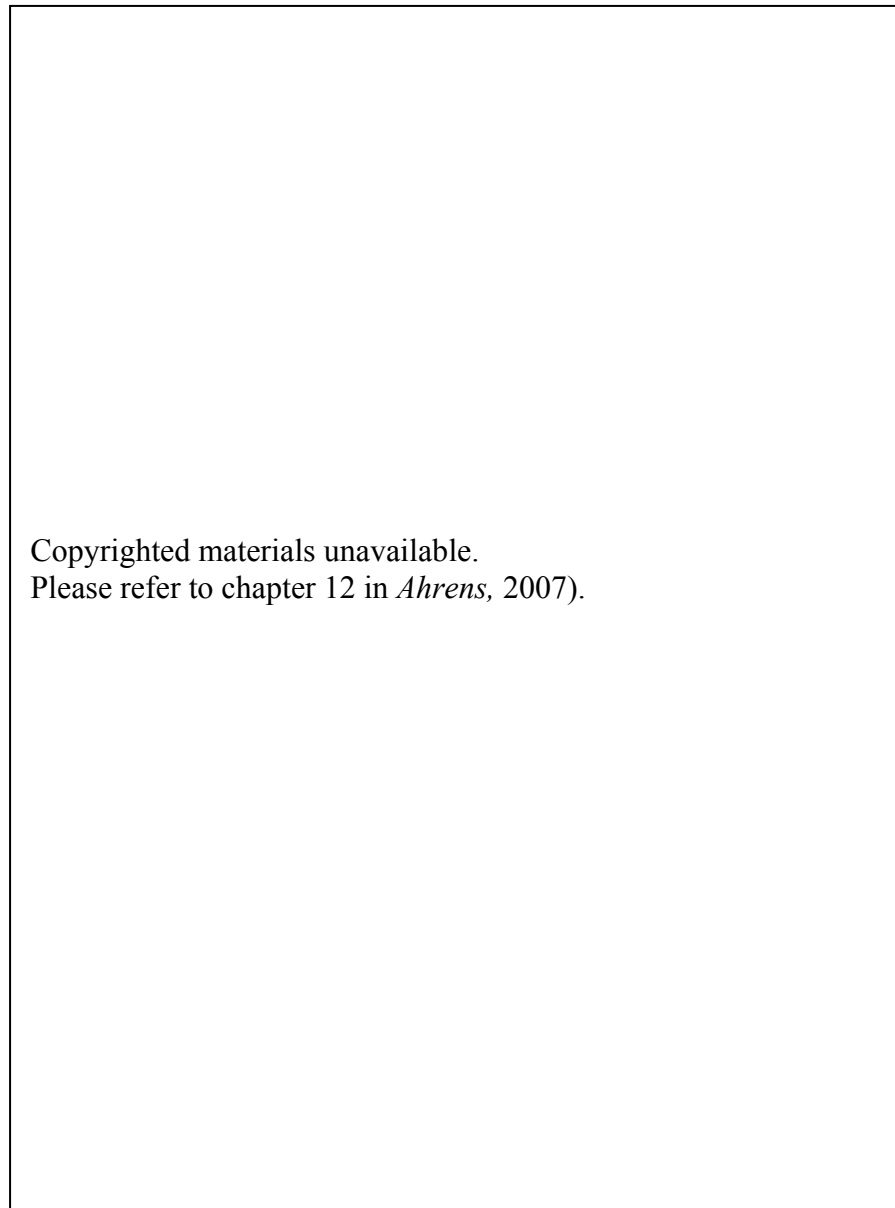
2.1.3 Cyclogenesis

Cyclones are expressions of the potential energy of the global temperature gradient (north – south or pole – equator) converted to kinetic energy. Cyclones grow from flow instabilities on the jet stream, in the presence of baroclinicity, and are essentially “baroclinic instabilities.” Cyclonic circulation strengthening format formation is known as cyclogenesis. Cyclogenesis typically occurs in association with several conditions in the atmosphere: positive-vorticity advection in the middle and upper levels, divergence or diffluence aloft at 500 - 250 hPa, differential temperature advection either occurring or possible, pre-existing vorticity and circulation, weak atmospheric stability that is not conducive to upright convection, and upstream back-tilt with height of the troughs and ridges (Djuric, 1994). Not all of these factors listed above are required simultaneously; however, more intense cyclogenesis occurs when all of them take place. Geographical features that produce low-level convergence can also aid in cyclogenesis and frontogenesis, and may be a coast, mountain range, or an ice edge (Barry and Carleton, 2001).

Vertical atmospheric structure is important to large-scale cyclone formation and maintenance, but not in all cases. Atmospheric divergence at upper-levels must lead the corresponding centre of low pressure at lower levels (Figure 2.4), (a structure referred to as “back-tilt”) so that upward motion occurs, and positive vorticity is generated. Warm air advection within the cyclone builds ridges of high pressure aloft, which can be above the surface low-pressure of the cyclone. Cold air advection deepens troughs aloft which trail the surface-low. Cyclones weaken rapidly when their structure becomes vertical due to the absence of forcings that cause upward vertical motion. This can happen when the

surface low is slowed by interaction with topography. A back-tilted vertical atmospheric structure is not required in the case of “dynamic lows,” which are generated via vorticity advection and potential vorticity. These types of lows, such as ‘heat lows’ in deserts and convective storms, are initiated by solar heating.

Figure 2.4. Back-tilted structure of upper-level flow in a cyclone (Ahrens, 2007).



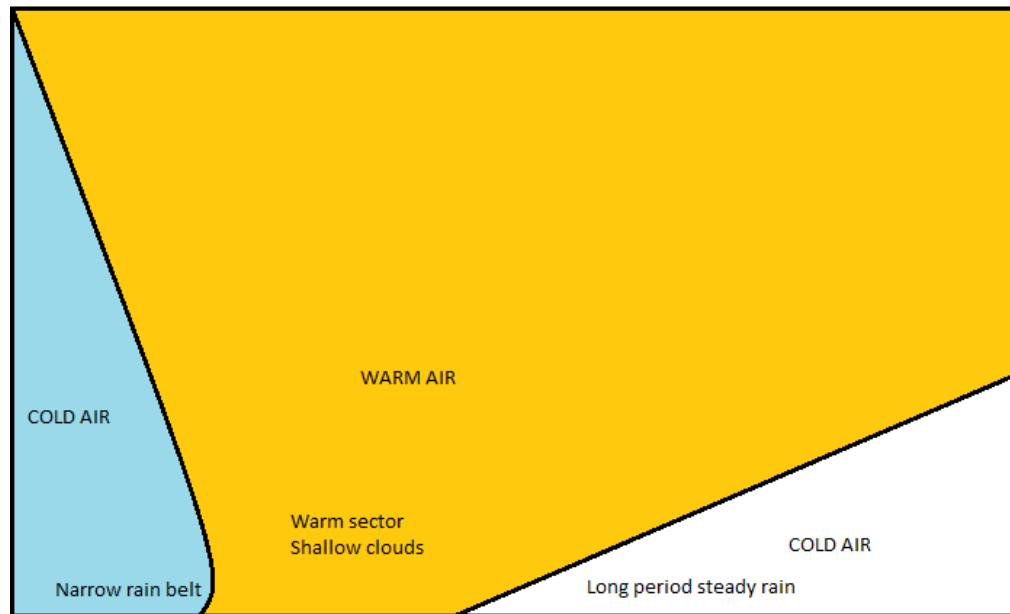
2.1.4 Fronts and Frontogenesis

Fronts are three-dimensional features that separate air masses that are accompanied by a temperature inversion at some level in the atmosphere. The surface expression of a front separates air with similar air and dewpoint temperatures on one side, and rapidly changing temperature and dewpoint behind the front. Fronts can also be characterized, in some cases, by wind direction changes, turbulence, and vertical motion, the latter of which is important to precipitation formation. Fronts typically occur in strongly baroclinic zones of the atmosphere where strong ageostrophic motions exist, where horizontal gradients of temperature are large, and where rapid vertical changes occur in the speed and direction of the geostrophic flow (Djuric, 1994). The prominence of ageostrophic motions along a front is characterized by the isobars bending outward from the low at the point, where they intersect the surface front (seen in Figure 2.4). Fronts can be found near the surface, solely aloft, or a combination of both. They can be synoptic-scale in their long dimension (1000 km) and mesoscale in their short dimension (across the front, ~100 km). A front's cross-frontal structure may change hourly, while the long dimensional frontal structure may remain similar, or change very slowly.

There are several different types of fronts that are associated with cyclones: warm fronts, cold fronts, occluded fronts, and stationary fronts. Warm fronts are wide fronts where warm sector air rises up over cool air ahead of the cyclone, and are typically characterized by warm air advection at 850 hPa (Figure 2.5). There typically is precipitation ahead of the surface front. Precipitation in some cases can be organized by slantwise convection into mesoscale bands parallel to the long dimension of the front. Cold fronts are sharp boundaries with a narrow surface expression indicating that cold

air, acting as a density current, is undercutting the warm sector of the cyclone (Figure 2.5). Warm air lifted by forced convection can often reach its level of free convection, resulting in higher rates of precipitation. Precipitation bands are typically organized parallel to the long dimension of the front, ahead and behind the front. The cold front often advances faster than the warm front, and forces the formation of an occluded front. Finally, stationary fronts are a boundary between two airmasses, of distinct temperature and humidity regimes, that are moving relative to the front, but the front itself does not move.

Figure 2.5. Horizontal cross section showing a cold front (left) and a warm front (right).



Frontogenesis is defined as the process in which a frontal boundary forms or intensifies in the atmosphere. Frontogenesis is driven by an increase in the cross-frontal gradient of potential temperature over time, and is described by:

$$\frac{\partial}{\partial t} \left(\frac{\partial \theta}{\partial y} \right) = -\frac{\partial v}{\partial y} \left(\frac{\partial \theta}{\partial y} \right) + \frac{-\partial \omega}{\partial y} \left(\frac{\partial \theta}{\partial p} \right) + \frac{\partial}{\partial y} \left(\frac{\partial \theta}{\partial t} \right) \quad (2.10)$$

Eqn. 10 is simplified for discussion:

$$\mathbf{A} = \mathbf{B} + \mathbf{C} + \mathbf{D} \quad (2.11)$$

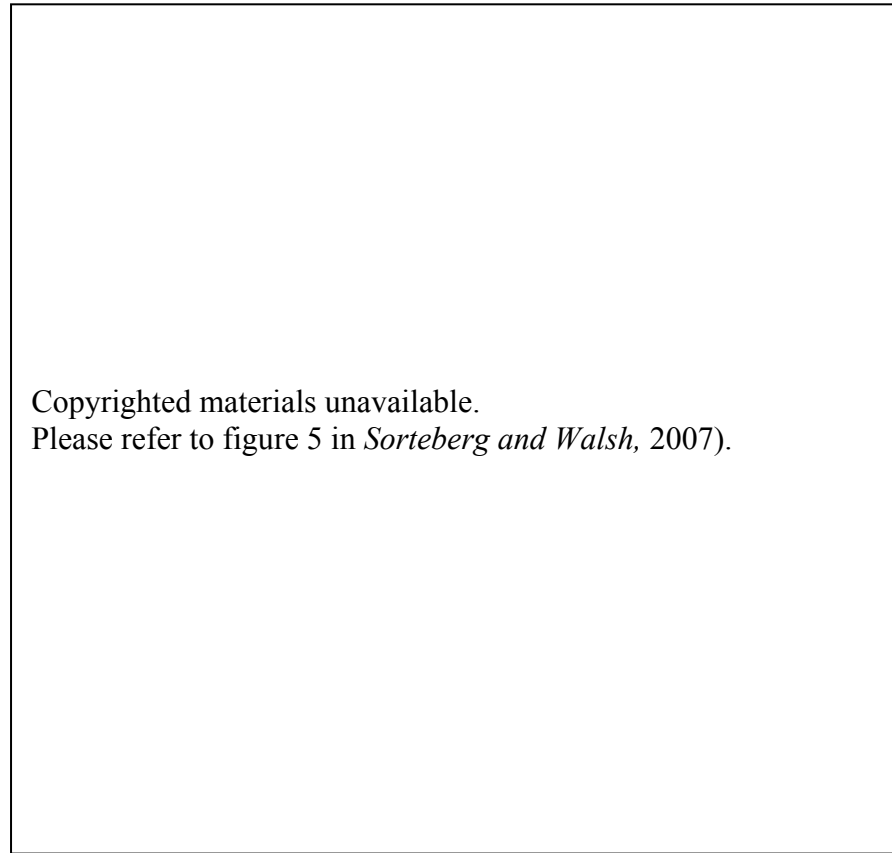
Where **A** is the increase in the cross-frontal gradient of potential temperature (θ) over time, **B** is the confluence of the horizontal flow where flow in the direction across the front drags isotherms towards the frontal location, **C** represents changes in the vertical motion across the front, and tilt of stable layers from the vertical partially into the horizontal, and **D** represents differences in the atmospheric boundary layer (ABL) or cloud heating on either side of the front increase the temperature difference. **A** is predominantly a horizontal process, **B** is horizontal and vertical, and **C** represents heating from latent and sensible turbulent fluxes (Stull, 2000).

2.1.5 Arctic Cyclone Climatology

The Arctic Ocean is widely viewed as a region of cyclolysis, where storms emigrate from mid-latitude regions and decay (Serreze, 1995). Sorteberg and Walsh (2008) provide the most recent seasonal storm track summary (Figure 2.6). Arctic cyclones most frequently enter the Arctic from the Barents and Norwegian Seas (Serreze *et al.*, 1993; Zhang *et al.*, 2004; Sorteberg and Walsh, 2008). They can form within the Arctic basin, particularly within zones of summer cyclogenesis over the Eurasian continent. The receding ice edge in the summer provides a baroclinic pathway for cyclones, and therefore summer storms are longer in duration (Zhang *et al.*, 2004), and travel further into the Arctic basin. Cyclones can also enter the Arctic basin from the

Pacific Ocean during all seasons; however, friction induced by interaction with land destroys their back-tilt, causing the surface low to fill rapidly. Keegan, (1958) noted that cyclones passing over Alaska were much less intense when they reached the Arctic basin. Remnant cyclones that reach the Arctic may reform in a zone of lee cyclogenesis found north of the Alaska Range (Pickart *et al.*, 2009) or the Yukon Mountains (Serreze and Barry, 2005).

Figure 2.6. Winter (a), spring (b), summer (c) and autumn (d) cyclone tracks for cyclones traveling into the Arctic, accounting for at least 5% of the total activity for that season. (modified from: Sorteberg and Walsh 2008).

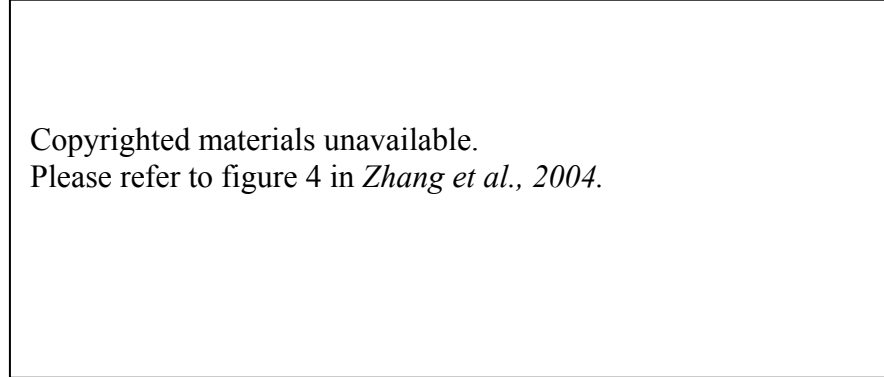


Arctic cyclone frequency (North of 65° latitude) peaks during summer and is at a minimum during winter (Serreze *et al.*, 1993). Seasonal cyclone frequencies can vary by region as cyclone frequencies depend on storm paths, and the seasonal variability in sea ice cover. Hudak and Young (2002) present storm climatology for the Southern Beaufort Sea for the period 1970 – 1995. The highest (lowest) monthly storm frequency occurs during October (July). 58% of storms are identified as of Arctic origin, including storms that had moved over the Arctic basin from the North Atlantic Ocean. 27% are identified with origins in the Pacific Ocean, and 15% are irregular (formed over eastern Siberia, etc). Prominent zones of winter cyclogenesis are found in the Barents Sea, northern

Baffin Bay, in the lee of the Canadian Rocky Mountains, and the North Pacific (Serreze *et al.*, 1993; Zhang *et al.*, 2004). Summer cyclogenesis can occur in similar locations, as well as over Eurasia.

A cyclone's central barometric sea level pressure reflects its intensity. Cyclone intensity is considered a key property of cyclone strength, and the intensity of cyclogenesis can be characterized by the change in a cyclone's intensity over a period of time. Summer cyclones are found to exhibit little regional variability in mean central pressure and are typically 5 – 10 hPa weaker than their winter counterparts (Serreze *et al.*, 1993). Zhang *et al.*, (2004) classified relative seasonal cyclone intensities by regional origin (Figure 2.7). Cyclones entering the Arctic that are of Atlantic origin are typically 3 – 5 hPa more intense than cyclones of Pacific origin. Cyclones generated within Eurasia are of similar intensity to those from the North Pacific, with the exception of during spring when Eurasian cyclones are 3 – 4 hPa more intense. Cyclones generated over North America are of comparable intensity from May to October, and corresponds with increased continental temperatures. Cyclones generated within the Arctic basin are generally of least intensity.

Figure 2.7. Relative intensities of cyclones by region of origin (from: Zhang *et al.*, 2004).



Many studies have investigated trends in cyclones frequencies (Serreze *et al.*, 1993; Serreze *et al.*, 2000; McCabe *et al.*, 2001), intensities (Zhang *et al.*, 2004; Simmonds and Keay, 2009), deepening rates (Serreze, 1997; Walsh *et al.*, 1996), and rates of increased poleward heat and moisture transport (Serreze *et al.*, 2000; Sorteberg and Walsh, 2008). Serreze *et al.*, (1993) investigated long-term trends in cyclone activity over the Arctic basin, and found a positive trend for cyclone counts during winter, spring and summer. They also identified an increase in anticyclonic activity during spring, summer and autumn. Regional analysis showed increased summer cyclone activity over Siberia, the Canadian Arctic Archipelago, and the Central Arctic. These increases were attributed to increased cyclogenesis over northern parts of Eurasia and North America. Serreze (1995) identifies that for 1973 – 1992, mean maximum cyclone deepening rates over continental regions and the Arctic Ocean are slightly greater during winter, and notably lower over the Greenland Sea and North Atlantic (Serreze, 1995). Walsh *et al.*, (1996) linked trends in cyclone deepening rates to a corresponding MSLP anomaly identified for 1979 – 1994. Cyclone intensities and deepening rates are linked to increased poleward heat (Serreze *et al.*, 2000) water vapor transport (Sorteberg and Walsh, 2008), and corresponds with increased precipitation (Higgins and Cassano, 2009).

Several studies attempt to model the effects of climate change and sea ice reduction on cyclone frequencies, intensities, persistence, and their effect on temperature and moisture advection. Lambert (1995) presents results from a 2 x CO₂ run of the second generation Canadian Climate Centre general circulation model (GCM), and suggested that global warming may result in a reduction in cyclone frequencies in both hemispheres, and an increase in cyclone intensity in the Northern hemisphere. Stormtrack positions are relatively insensitive to the enhanced greenhouse effect. GCM models do not handle mesoscale changes in baroclinicity, and likely do not account for changes in baroclinicity arising from variability in the Arctic pack ice. More recent studies (Simmonds and Keay, 2009; Higgins and Cassano, 2009) take into account the recent dramatic reduction of Arctic sea ice cover. Increased cyclone intensities and deepening rates are attributed to baroclinicity arising from reduced sea ice cover. Higgins and Cassano (2009) identified an increase in the frequency of low-pressure synoptic patterns over North America and the Arctic basin.

2.1.6 Teleconnections and Arctic Cyclones

Teleconnections are coupled ocean-atmosphere oscillations in climate regimes. The influences of teleconnections within mid-latitude and polar atmospheric circulation regimes are well documented (Walker, 1923; Trenberth, 1990; Mantua *et al.*, 1997; Thompson and Wallace, 1998). Walker (1923) first noted a tendency toward simultaneous strengthening or weakening of the Icelandic Low and the Azores High, which he termed the North Atlantic Oscillation (NAO). The positive (negative) mode of the NAO occurs when the Icelandic Low and Azores High are simultaneously strong

(weak). The state of the NAO is characterized by the difference in normalized sea level pressure in winter between Lisbon, Portugal, and Stykkisholmur, Iceland, and is described by the NAO index.

The NAO signal has also been detected in the Arctic, leading Thompson and Wallace, (1998) to identify the Arctic Oscillation (AO). The AO is defined as the leading empirical orthogonal function of winter MSLP anomalies, above 20°N. The AO manifests as strong inter-annual fluctuations at the 50 hPa level, thereby affecting the polar vortex. Positive (negative) AO is characterized by a strengthened (weakened) polar vortex, and low (high) MSLP anomalies in the Arctic. The AO can also be interpreted as the surface signature of modulations in the strength of the polar vortex aloft (Thompson and Wallace, 1998). The AO is sometimes referred to as the “Northern annular mode” (NAM), as the AO actually describes the meridional distribution of atmospheric mass in the Northern hemisphere, where negative (positive) values indicate more (less) atmospheric mass near the poles.

The frequencies and intensities of Arctic Cyclones are known to exhibit a response to the state of the NAO/AO (Serreze *et al.*, 1993; Serreze *et al.*, 1997; Serreze *et al.*, 2000; McCabe *et al.*, 2001; Simmonds *et al.*, 2008). Teleconnection influences on cyclone frequencies and intensities vary regionally, and are typically found during the cold season (AO is a cold-season phenomenon). Negative AO conditions are attributed to negative MSLP anomalies (increased cyclonic atmospheric circulation) over the Arctic basin (Serreze *et al.*, 1993). This implies increased cyclone activity within the Arctic basin; however, negative AO conditions are also linked to decreased intensities and frequencies of migratory cyclones from the North Atlantic. A two-fold decrease in cold

season cyclonic events within the Icelandic Low is linked to extreme negative phases of the NAO (Serreze *et al.*, 1997; McCabe *et al.*, 2001). These cyclones tend to be less intense and exhibit little change in origin or cyclonic deepening rates. More recently, Simmonds *et al.*, (2008) linked strong cyclones to positive AO conditions.

The frequency of Pacific cyclones is linked to El Niño events in the Pacific Ocean, which are described as the warm mode of the El Niño Southern Oscillation (ENSO). The ENSO is described by anomalous pooling of warm or cool surface water in the Pacific tropical region, and is caused when a reversal in the easterly tradewinds disrupts deep-ocean cold-water convection. This affects the locations of significant atmospheric convection, and alters atmospheric circulation throughout the Pacific basin. The most striking effects of an El Niño on atmospheric circulation over North America are deepened, and east-displaced Aleutian Low, and a split jet stream with a northerly branch flowing northeast over Southern Alaska and the Yukon. Pacific cyclones can track into the Arctic basin more frequently along the northern branch of the split jet stream. Frequencies of Pacific storms penetrating into the Arctic region, most notably within the Southern Beaufort Sea, are purported to increase during an El Niño (Hudak and Young, 2002). ENSO oscillates on an annual to bi-annual time scale; thus, synoptic circulation patterns can differ greatly between consecutive years (Barry and Carleton, 2001).

The Pacific Decadal Oscillation (PDO) is a large-scale, atmosphere-ocean teleconnection that is characterized by an inter-decadal oscillation between warm and cold sea surface temperature (SST) anomalies in the northern and eastern tropical regions of the Pacific Ocean (Mantua *et al.*, 1997). The PDO is characterized by a striking

pattern of widespread atmospheric circulation and climate variability that is detectable in many different regions of the Pacific basin. Frequencies and intensities of cyclones originating in the northern Pacific Ocean are linked to the PDO (Graham and Diaz, 2001), and thus may affect Arctic cyclone climatology.

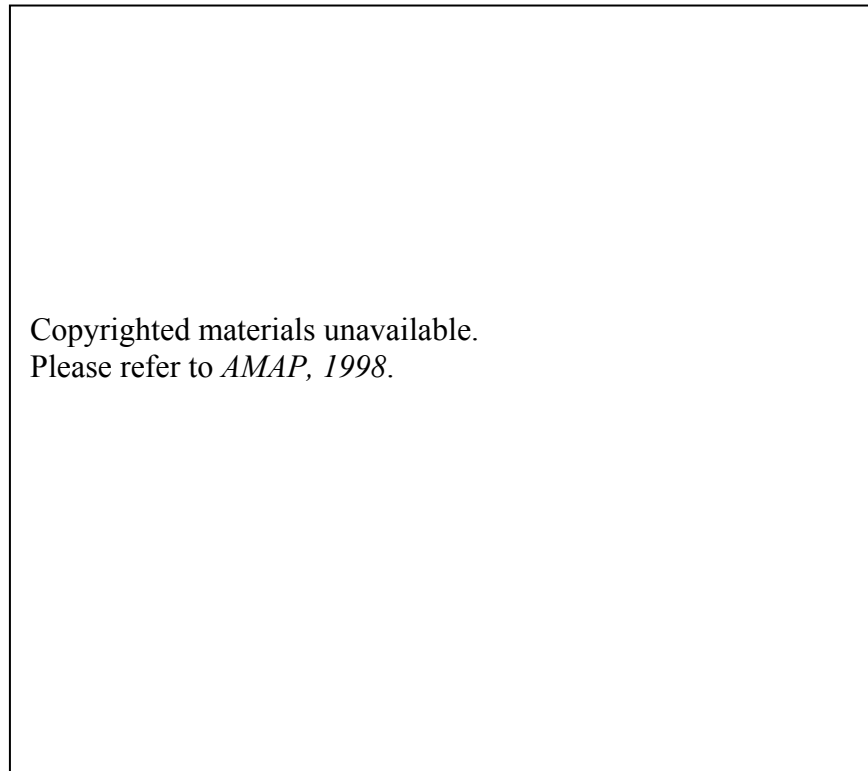
2.2 Cyclone Forcing of Sea Ice Dynamic Processes

This section is constructed from the point of view that dynamic processes initiate cyclone forcing of coupled dynamic and thermodynamic OSA system. A discussion of cyclone forcing on the coupled OSA system is therefore best commenced with a comprehensive discussion of sea ice dynamic processes.

2.2.1 Large-Scale Atmospheric Forcing of Sea Ice

Dynamic forcing of Arctic sea ice is largely driven by synoptic-scale MSLP circulation patterns. Surface winds transfer momentum to the sea ice-covered ocean, forcing ice drift which can locally increase sea ice concentrations, or remove ice from the Arctic via sea ice export. There is predominantly anticyclonic atmospheric circulation over the Arctic Ocean throughout most of the year, with a mean center of high pressure over the Canada basin (Keegan, 1958). Summer circulation is characterized with cyclonic atmospheric circulation (Serreze and Barry, 1988; Serreze *et al.*, 1993; Barry and Carleton, 2001). The dominance of anticyclonic atmospheric activity during winter and spring forces wind-driven anticyclonic circulation in the sea ice, creating two large and important features termed the Beaufort Gyre (BG)(Fig. 2.8), and the Transpolar Drift (Figure 2.8) The BG circulates sea ice around the Arctic basin, where it may undergo several annual cycles of growth and ablation, and be modified by other dynamic processes. The Transpolar Drift exports sea ice into the North Atlantic via Fram Strait along the east side of Greenland (Hertzman, 1997).

Figure 2.8. Typical Arctic Ocean circulation pattern, showing an anticyclonic Beaufort Gyre, and the Transpolar Drift (from: AMAP, 1998).



Wind-driven ice motion in the central Arctic alternates between anticyclonic and cyclonic circulation regimes, each persisting between five to seven years (Proshutinsky and Johnson, 1997). The two ice circulation regimes are coupled to the atmosphere, affecting the locations and intensities of the Icelandic Low and Siberian highs. These two ice circulation regimes may also help explain basin-scale changes in the Arctic's temperature, salinity, and the variability of sea ice conditions in the Arctic Ocean (Proshutinsky and Johnson, 1997). The cyclonic circulation regime is characterized by increased lead formation in the Arctic pack ice, and increased precipitation over the ocean (Polyakov, *et al.*, 1999).

The BG and Transpolar Drift control ice motion, and thicknesses within the Arctic Basin. Ice motion within the BG is generally the weakest (greatest) during April (August

and September) when Arctic ice cover is well developed (decayed), and when ice extent and concentrations are at their annual maximum (minimum). The BG rotates clockwise during the anticyclonic regime, and builds ice concentrations in the southern Beaufort and Chukchi Seas.

This process tends to transport sea ice up against the Canadian Archipelago and Greenland, building the thickest, oldest ice in the Arctic basin. The BG also drives the formation of the circumpolar flaw lead system throughout the annual cycle, which is defined as the regions where the mobile pack ice moves away from the coast or land attached (fast) ice, forming areas of open water. The thinnest ice is typically found in flaw lead regions along the Laptev Sea coast, and Southern Beaufort Sea. Barber and Hanesiak (2004) describe flaw leads, caused by the rotational motion of the BG, as a key formation characteristic of the Cape Bathurst Polynya, which is located in the Southern Beaufort Sea. Polynyas and flaw leads, and their interactions with cyclones are discussed in detail in section 2.4.

Cyclonic atmospheric circulation during the summer can slow down the circulation of the BG, and even reverse its circulation to cyclonic circulation (McLaren *et al.*, 1987; LeDrew *et al.*, 1991; Johnsen *et al.* 1999; Lukovich and Barber, 2006). Summer reversals of the BG occur primarily during the August / September period when negative atmospheric pressure anomalies prevail, and cyclones are most frequent. The strength and duration of the reversals can vary between years (Barry and Maslanik, 1989), and may be occurring more frequently throughout the annual cycle (Lukovich and Barber, 2006). Walsh *et al.*, (1996) identifies a tendency towards increased cyclonic wind forcing over the Arctic Ocean, and suggests that the concomitant increase in BG reversals will

reduce the fractional concentration of MY ice and increase divergence in the Arctic ice pack. Summer reversals of the BG transport sea ice from the Chukchi and southern Beaufort Seas northward, subsequently increasing ice volume export through Fram strait via the Transpolar Drift (Yu *et al.*, 2004), and reducing ice extent and thickness (McPhee *et al.*, 1998). A cyclonic BG can also promote oceanic and sea ice divergence via Ekman drift, a process identified as an important control regulating the annual Arctic sea ice minimum extent (Ogi *et al.*, 2008).

Reversals of the BG have been linked to stratospheric forcing on the polar vortex, that subsequently manipulates the troposphere. Bleck (1973) linked the creation or advection of potential vorticity in the lower stratosphere broadly to cyclogenesis during the cold season. Large amounts of very stable stratospheric air moving closer to the surface during the hemispheric change from warm to cold-season regimes is known as a stratospheric cooling event, and can provide vorticity for a large, long-lasting low-pressure system. This process was attributed to the formation of a persistent cold barotropic upper-level low-pressure system (lasting for 26 days), and coupled with low-level baroclinicity, which led to a reversal of the BG in the summer of 1980 (LeDrew *et al.*, 1991). Lukovich and Barber (2006) investigate the coupled response of BG vorticity to stratospheric circulation, and identify a time-lagged response of 2 – 6 weeks in sea ice motion and concentration to stratosphere relative vorticity fields.

Sea ice thickness, volume, and motion are strongly linked to teleconnections. Ice thickness profiles collected during SCICEX submarine cruises found that thicker (thinner), more ridged (smoother), ice corresponded with positive (negative) NAO conditions (Rothrock, *et al.*, 1999). Zhang *et al.*, (2003) attribute positive AO conditions

to a net volumetric gain of sea ice in the Beaufort Sea of approximately $462.9 \text{ km}^3 \cdot \text{yr}^{-1}$, but a net loss of sea ice in the Chukchi Sea, $\sim -910.8 \text{ km}^3 \cdot \text{yr}^{-1}$, and represents an 87% drop in sea ice transport, compared with the negative phase of the AO (Zhang *et al.*, 2003). Yu *et al.*, (2004) reveals that stronger BG circulation during the Negative NAO phase resulted in less direct advection of ice from the East Siberian and Laptev Seas to the Transpolar Drift stream, and caused ice to circulate longer within the Arctic basin. Conversely, positive NAO values are correlated with a doubled rate of ice divergence in the eastern Arctic, a 13% increase in ice divergence throughout the entire Arctic basin. The NAO is also linked to increased ice export through Fram Strait. Yu *et al.* (2004) note a gradual increase of about $9900 \text{ km}^2 \cdot \text{yr}^{-1}$ in the area flux through Fram Strait from 1978 – 1995, and attribute the increase to strong northerly winds associated with the strengthened Icelandic Low, characteristic of positive NAO conditions.

Large-scale coupling between atmospheric and oceanic changes appears to be leading to a reduction in ice thickness. Rothrock *et al.*, (1999) identifies an average 1.3 m reductions in ice draft in most of the deep waters of the Arctic Ocean from between the periods 1958-1976 to the 1990s, and proposes several mechanisms that could account for the reduction: Increased poleward atmosphere heat transport of approximate $13 \text{ W}\cdot\text{m}^{-2}$ from a nominal value of $100 \text{ W}\cdot\text{m}^{-2}$, stronger warm-air advection, or a combination, a $4 \text{ W}\cdot\text{m}^{-2}$ increase in ocean heat flux from a nominal value of $2 - 4 \text{ W}\cdot\text{m}^{-2}$, or a $23 \text{ W}\cdot\text{m}^{-2}$ increase in downwelling shortwave radiation from a nominal value of $\sim 200 \text{ W}\cdot\text{m}^{-2}$ for about half the year. It is likely that a combination of two or more of these mechanisms is forcing sea ice decline.

2.2.2 Momentum and Sea Ice Motion

The transfer of momentum from the ocean and atmosphere drives sea ice dynamic processes. The momentum budget for sea ice consists of five terms: air stress (winds), water stress (underlying ocean circulation), the Coriolis force (rotation of earth), stress attributed to the tilt of the ocean surface (Uneven surface due to tides, low atmospheric pressure, etc.), and internal stress within and between sea ice floes. Air (wind) stress drives momentum transfer from the atmosphere to sea ice, affecting the sea ice morphology, ocean currents and turbulence, and sea surface tilt (Guest *et al.*, 1995). Cyclones further complicate the momentum balance of sea ice, with rapidly changing barometric pressure, and as winds change direction and velocity during their passage (*e.g.* Brümmer *et al.*, 2003).

The degree of air stress (τ_a) on an area of sea ice is expressed by the air-ice drag coefficient (C_a), and is dependent on the degree of sea ice surface roughness (smooth ice surface, versus heavily ridged).

$$\tau_a = \rho_a C_a |U_a - U_i| (U_a - U_i) \quad (2.12)$$

where ρ_a is the air density, C_a is the air-ice drag coefficient, U_a is the wind velocity at a the height of wind measurement (typically 2 m) and U_i is the ice velocity. C_a ranges between 0.0014 and 0.0021 for sea ice (Wadhams, 2000), and typically increases with sea surface roughness resulting in greater momentum transfer to the sea ice (Andreas *et al.*, 1993; Wadhams, 2000). Wind stress on the ice-ocean mixing layer can also induce inertial oscillations within sea ice (Hibler *et al.*, 2006), and within the ocean (*e.g.* Rainville and Woodgate, 2009).

Water stress (τ_w) is the force on the ice bottom relative to the motion of the ocean beneath it, and is calculated in the same way as air stress, via a drag coefficient (C_w). Ice morphology becomes very important with respect to water drag as large keels typically protrude underneath pressure ridges in sea ice (Wadhams, 2000). Typical values of C_w are ~ 0.0055 (Hibler, 1979; Wadhams, 2000).

Sea surface tilt is a phenomenon analogous to geopotential heights in the atmosphere. A variety of natural forces can cause the ocean sea surface height to vary slightly from mean sea level. The ocean responds to restore balance to sea surface height by moving water from areas of high to low pressure. Sea surface tilt is attributed to tidal forces, uneven heating (thermal expansion of the water column), local changes in water volume (evaporation, precipitation), or responses to changes in atmospheric pressure. The latter is referred to as a “storm surges.” The degree of tilt caused by a storm surge is proportional to the central pressure of the cyclone.

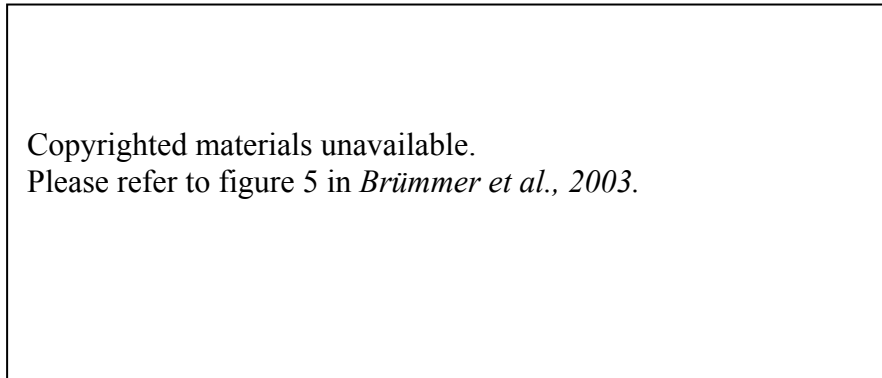
The Coriolis force generates vorticity momentum in the sea ice cover, in much the same manner that it is generated in the atmosphere. This deflects sea ice motion to the right (left) in the northern (southern) hemisphere. The interaction of wind stress with vorticity results in non-linear ice motion. As wind forces the ice, it may turn so that its motion contains a vector component that is against the mean flow of the wind. This reduces the relative ice vorticity, and results in the floe following a path known as an inertial loop (Wadhams, 2000).

Internal ice stress accounts for the force acting on an area of ice within an ice sheet due to stress transmitted through the ice from the surrounding sea ice. Internal stress forces are constantly changing and depend on ice rheology, strength and the areal

mass balance (Hibler, 1979). Internal ice stress is a key parameter in determining whether an ice floe will fracture when subjected to strain, flexure, or divergent forces (e.g. Asplin *et al.*, 2012).

Cyclones force the momentum balance by introducing wind stress, and sea surface tilt to the sea ice cover. Strong winds associated with the approach of a cyclone typically introduce a vertical or horizontal component of air-stress that is contrary to the pre-existing motion of drift. This can introduce internal sheering stress within the sea ice, which may cause it to fracture and diverge. Abrupt changes in wind velocity and direction associated with frontal passage rapidly change the direction of the air-stress vector, which then must rebalance against the other momentum-driving forces. Brümmer, *et al.*, (2003) present a case study of cyclone forcing upon ice drift in Fram Strait (Figure 2.9). A cyclone tracking from south to north (with an easterly vector), and northerly winds behind the storm are observed to enhance southward ice drift through Fram Strait, and induced dilation within the sea ice cover, reducing fractional concentrations by ~11%. The influence of cyclones on sea ice momentum is further complicated by the cyclone's relative motion. This can introduce divergence and dilatation in the sea ice cover along the path of the storm.

Figure 2.9. Influence of passing cyclones on sea ice drifting beacon speeds (from: Brümmer et al., 2003).



Dilatation and divergence of sea ice arising from cyclone-induced air stress couples dynamic and thermodynamic sea ice processes through the formation of sea ice leads (Barry and Maslanik, 1989; Brümmer *et al.*, 2003). Cyclone forcing of sea ice motion is noted to change the direction of heat fluxes, where fluxes are driven from the ocean to the atmosphere after cyclone passage (Dierer *et al.*, 2005). The nature of this coupling can also be affected by the roughness of the sea ice surface. The interaction of winds with a rough sea ice surface can introduce substantial variability in the ABL profile (Guest *et al.*, 1995). This may serve to enhance coupling between cyclones and dynamic-thermodynamic processes in regions of sea ice with large roughness lengths, which can modify surface exchanges of turbulent fluxes.

Sea ice in momentum can exert a significant control on the circulation of the ocean below it. The roughness of the sea ice surface, in contact with the water “drags” water in the surface layer, creating a layer of vertical shear in the ocean. The Coriolis force deflects the vertical profile of ocean shear currents to the right, the angle of deflection increasing, further down in the water column. The velocity of resultant currents in the spiral decreases with depth. The depth to which an Ekman spiral can

penetrate into the water column is determined by the magnitude of surface forcing; therefore, maximum spiral depth can be related to sea ice velocity.

2.2.3 Sea Ice Thickness and Morphology

Both dynamic and thermodynamic processes control sea ice thickness. Thermodynamic sea ice formation (freezing) creates ice cover that is relatively smooth and equal in thickness, whereas dynamic processes deform the sea ice, locally thickening it. Sea ice deforms under convergent and shear motion, inducing rafting and ridging (pressure ridges), and sea ice lead formation. Pressure ridge height depends on the thickness of the parent ice floes. They can be up to several meters in height (increasing the surface roughness of the sea ice surface). They have a keel extending underneath the ice that can be three to seven times as thick as the pressure ridge. Ridges are known to contain large volumes of ice; (Melling and Riedel, 1995) noted that pressure ridges in the Beaufort Sea contained upwards of two thirds of the total sea ice volume. Refreezing sea ice leads are characterized by ice thicknesses, thinner relative to surrounding ice floes.

Pressure ridges, leads, uniform ice floes, and open water in a given region comprise a sea ice thickness distribution. Thorndike *et al.* (1975) defined the sea ice thickness distribution ($g(h)$, m^{-1}) for a region as:

$$g(h)dh = \frac{dA(h, h + dh)}{R} \quad (2.13)$$

where $dA(h, h+dh)$ represents the area of region R , covered by sea ice with thicknesses ranging between h and $h+dh$. The ice thickness distribution for a location evolves over time, and is expressed as:

$$\frac{\partial g}{\partial t} = \text{div}(vg) - \frac{\partial(fg)}{h + \varphi(h)} \quad (2.14)$$

where $\partial g / \partial t$, is the thermodynamic growth rate, v is the horizontal component of ice velocity, and ψ is a function that redistributes sea ice from one thickness class to another (Wadhams, 1973). $\text{Div}(vg)$ accounts for sea ice divergence, reducing area covered by ice. The second term accounts for thermodynamic processes and the redistribution function (ψ) accounts for lead and ridge formation by convergence.

2.2.4 Waves and Flexural Failure

Wave energy regulates ice morphology, and dynamics near the ice margin (Wadhams, 1973; Squire and Moore, 1980). Waves are formed by friction between moving air and the ocean surface. Wave formation begins as small ripples on the ocean surface, at a minimum wind speed of $0.23 \text{ m} \cdot \text{s}^{-1}$ moving at $\sim 75^\circ$ angles to the prevailing wind. These ripples increase the roughness, (and drag coefficient of the water), and grow to wavelets, and start to follow in the direction of the wind. At wind speeds of $2 - 3 \text{ m} \cdot \text{s}^{-1}$, the wavelets become high enough to interact with the wind, and the surface begins to roughen. The wind becomes increasing turbulent above the roughening surface, and transfers energy to the waves at a greater rate. Depending on wind duration, and distance over water (fetch), the waves expand into large swells, with increasing period and wavelength. Wavelength and period are related by the equation:

$$\lambda = \frac{gt^2}{2\pi} \quad (2.17)$$

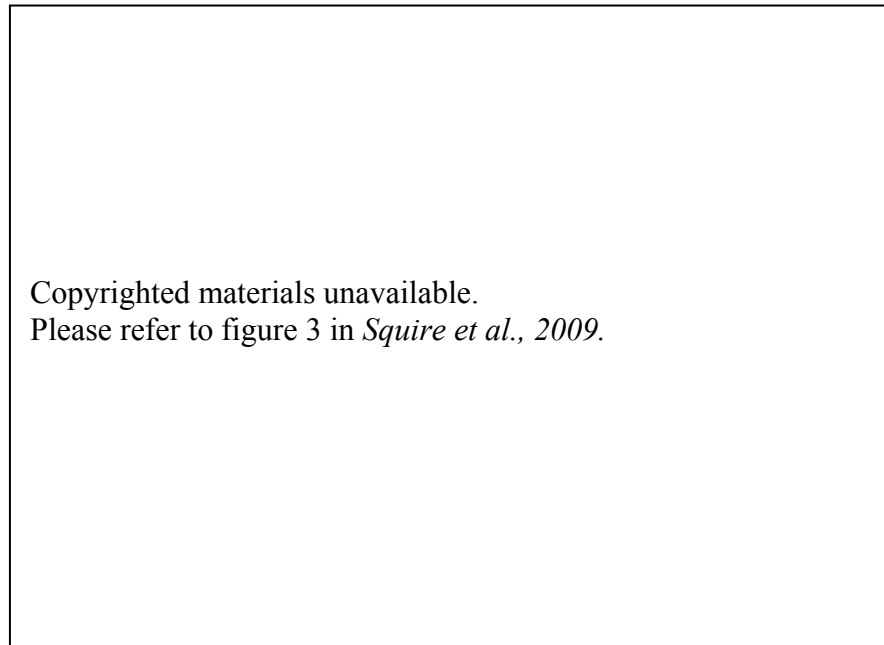
where λ is wavelength (m), t is wave period (sec), and g is gravitational acceleration ($9.81 \text{ m} \cdot \text{s}^{-2}$). Wave speed c ($\text{m} \cdot \text{s}^{-1}$) is given by:

$$c = \frac{\lambda}{t} \quad (2.18)$$

Waves develop irregularly, forming two or more wave trains of different periods, amplitudes, and wavelengths. Wave trains travel at half the average speed of the actual waves within the train, and therefore the energy associated with these waves travels at the speed of the wave train. Wave trains consisting of the longest wavelengths typically travel the fastest. Distant storms can send out long waves in groups (wave trains) over great distances.

Long-distance wave train propagation from distant storms into sea ice cover has been observed by several studies (Hunkins, 1962; Liu and Mollo-Christensen, 1988; Lammert *et al.*, 2009; Wadhams and Doble, 2009). Large amplitude wave propagation events linked to distant storms in the North Pacific have been felt deep in the Arctic Pack Ice (*e.g.* Liu and Mollo-Christensen, 1988). This corresponds with measurements conducted on different ice floes and ice islands that show regular oscillations in Arctic sea ice at $t = 15 - 60$ s (Wadhams and Doble, 2009). Squire *et al.*, (2009) investigated ocean wave train evolution, and propagation in a 1670 km-long profile of irregular Arctic sea ice, obtained from a submarine transect using upward-pointing sonar (Figure 2.10). Analysis shows that an ocean wave with $t = 22$ s advances completely through a 1670 km path of irregular Arctic sea ice. It is attenuated by scattering interactions between leads and pressure ridges, and its amplitude is reduced exponentially by a factor of 3. The attenuation coefficient depends on the period t . Bennetts *et al.*, (2007) conducted similar studies on wave propagation in sea ice, modeling the ice sheet as a spatially variable, thin flexible plate with an ancillary viscosity term.

Figure 2.10. Modeled decay of ocean waves ($t = 13 - 35$ s) as they propagate through 1670km of irregular ice terrain (from: Squire et al., 2009).



The nature of flexural swell in sea ice depends on ice floe size, and is most prominent within large, contiguous ice floes (Rothrock and Thorndike, 1984), and may not affect smaller floes at all. The minimum size of a resultant ice floe also depends on the ice thickness of the parent floe. Mellor (1986) estimates the minimum floe sizes after breakup at 14, 24, and 33 m for 1, 2 and 3 m parent ice floe thickness respectively. Ocean and flexural swells affect ice floe size distributions. Steer *et al.*, (2008) attributed a significant increase in the number of small floes (< 100m) over a 23-day period in the western Weddell Sea during the ISPOL program to wave-forced divergence in the pack ice, coupled with lateral ice melting.

Large ocean swells propagating under Antarctic sea ice have been observed to cause flexural fracture in the sea ice cover (Wadhams *et al.*, 1988). This process increases the number of small floes, which are susceptible to lateral melting (Toyota *et al.*, 2006; Steer *et al.*, 2008). More recently, this phenomenon was observed in September 2009 in

the Southern Beaufort Sea. Asplin *et al.*, (2012) describes *In situ* observations indicated that flexural failure in thick MY ice floes was due to deteriorated ice strength, attributed to summer warming (Eicken *et al.*, 1995), and a heavily decayed ice edge margin, consisting of rotten ice, described in detail in Barber *et al.*, (2009).

Flexural failure within sea ice depends highly on the ice floe physical properties, floe size distribution, sea ice concentration, and the properties of the wave train that is affecting the ice. Fracturing of sea ice due to air stress (wind) or ocean stress (waves), or other forms of stress depends highly on sea ice strength. The physical strength of a sea ice floe depends on its internal temperature (Timco and Johnston, 2002; Tison *et al.*, 2008), with decreasing compressive strength with increasing temperature of the ice slab. Ice floe properties and ice floe distributions in a given region are dependant on the mechanical and thermal properties of the surrounding sea ice (Tison *et al.*, 2008).

2.2.5 Sea Ice Floe Size and Lateral Melting

Rothrock and Thorndike (1984) propose that the distribution of ice floe sizes typically follows a single power-law distribution that can vary from year to year:

$$f(x)_i = ax_i^k + o(x_i^k) \quad (2.15)$$

where $f(x)$ is the distribution for floe size regime i , k is the scaling exponent, a is a constant, and $o(x^k)$ is an asymptotically small function of x^k . Recent studies (Toyota *et al.*, 2006; Steer *et al.*, 2008) identify distinct floe size regimes with their own distinct power law distributions. Toyota *et al.*, (2006) identifies two distinct ice floe size distributions: 0 – 40 m diameter, and > 40m. Steer *et al.*, (2008) described floe size distributions during the Ice Station Polarstern program (ISPOL), and identified three

distinct distributions are identified for ice flow size: 2 – 20 m, 20 – 50 m, and > 50 m. Each distribution follows a power law distribution with its own unique exponent k .

Ice floes < 40 m in diameter are difficult to break mechanically and distributions of floes this size are therefore driven by thermodynamics, (Mellor, 1986). Toyota *et al.*, (2006) investigates the influence that an increasing distribution of smaller floe sizes has on lateral melting. They calculate the total perimeter of all the ice floes within their two defined floe regimes, and compare it with that for the case for only one ice distribution regime ($k = 1.87$). They accomplish this by calculating a fixed sea ice concentration ($A=0.8$) for each regime calculated as follows:

$$A = \int_{d_1}^{d_2} n_a(x)s(x)dx + \int_{d_2}^{d_3} n_b(x)s(x)dx \quad (2.16)$$

where $n(x)s(x)dx$ is the cumulative number distribution for regime a and b with floe sizes ranging from $d_2 - d_1$ and $d_3 - d_2$ respectively.

Evaluating the integral gives us:

$$= -\frac{\pi\beta_1 k_1}{4(k_1 - 2)} (d_2^{k_1+2} - d_1^{k_1+2}) - \frac{\pi\beta_2 \alpha_2}{4(k_2 - 2)} (d_3^{k_2+2} - d_2^{k_2+2}) \quad (2.17)$$

where $d_1 = 1\text{m}$, $d_2 = 40\text{m}$, $d_3 = 1500\text{ m}$ are floe diameters (the upper and lower sizes within each regime), $k_1 = 1.15$ and $k_2 = 1.87$, and area of a floe ($\pi d^2/4$). This exercise revealed a total ice floe perimeter for two floe size regimes that was ~ 4.8 times less than that for only one regime. This indicates that the size distribution of ice floes smaller than 40 m has a strong effect on the lateral melting.

2.3 Cyclone Forcing of Sea Ice Thermodynamics

Sea ice thermodynamics are controlled by energy exchange between the ocean and atmosphere. This section examines key thermodynamic processes in sea ice, and evaluates how they are forced by Arctic cyclones. Dynamic-thermodynamic coupling is also described.

2.3.1 Sea Ice Formation

Sea ice is a layered composite of ice and brine, and is formed by freezing of salt water. The freezing point of salt water depends on its salinity, (-1.93°C for 35 PSU). Convection in the top of the ocean surface-mixed layer is driven by densification of salt water (maximum point of density occurs at the freezing point for salt water), and is enhanced by surface winds. Ice crystals float to the surface, and then grow laterally into small discs known as frazil ice (Weeks and Ackley, 1986). Under calm conditions, frazil ice will coalesce and form a surface layer of thin, slushy ice, known as ‘grease ice.’ As it thickens, ice transitions to become nilas ice. Nilas, thinner (thicker) than 5 cm, is referred to as dark (white) nilas (WMO, 1970). Sea Ice formation is very different in turbulent oceans. Strong winds from cyclones can cause compression and accumulation of frazil ice crystals, leading to the formation of small pans of ice termed “pancake ice.” (WMO, 1970). Continued ocean turbulence can cause these pancakes to collide and coalesce with one another, into a rarely observed ice type, “consolidated pancake ice.”

Ice sheets grow thicker thermodynamically through a process known as congelation. Continuous sheets of ice grow thicker through the conduction of latent heat

upward through the ice sheet from the sea ice-seawater interface to the atmosphere. At this point the growth rate of the bottom of the ice sheet is determined by the temperature gradient and its effective conductivity (Weeks and Ackley, 1986). The ice will continue to grow thicker throughout the winter until it reaches its seasonal maximum thickness (Typically 2.0 m for FY ice). Ice that survives the melt season (MY ice) can also grow thicker through the process of ice congelation.

As sea ice grows downward into the water column, salts are removed through brine expulsion (Weeks and Ackley, 1986). This process forms a layer of salty, dense water at the sea ice-seawater interface, which then sinks into the deep ocean, and drives thermohaline circulation (Aagaard *et al.*, 1981). Brine discharge can also occur at the surface of nilas ice. With the presence of very cold air ($>-20^{\circ}\text{C}$), surface brine ejection may form expulsion features known as “frost flowers. Frost flowers are high-salinity features that are of great importance to studies involving sea ice electrical properties, OSA chemistry, and remote sensing. Frost flower production is particularly notable in polynyas and sea ice leads throughout the winter. Therefore, frost flower production is undoubtedly coupled to cyclone forcing of lead and polynya formation.

2.3.2 Snow Cover Influences on Sea Ice Thermodynamics

Snow is formed in the atmosphere when water vapor is lifted by positive vorticity advection and frontal ascent associated with cyclones, or adiabatically (ABL instability forcing convection of an air parcel to saturation). As the air ascends, it cools adiabatically and condenses out water vapor around aerosols, which are referred to condensation nuclei. Condensation nuclei may be small particles of dust, salt, or ice crystals that form

from deposition of super-cooled water droplets ($> -40^{\circ}\text{C}$). Snow crystals grow into snowflakes as they are suspended within the saturated frontal airmass, through aggregation in which ice crystals collide, or through riming in which super-cooled water is added to the existing snow crystal. Snowflake morphology may change as the snowflake falls through different air layers containing different air temperatures and vapor pressures. Snow grains within the snow layer on sea ice may undergo additional metamorphisms, including grain growth, and rounding (Langlois *et al.*, 2007; Langlois *et al.*, 2008).

Measurement of precipitation and snow cover is a challenging prospect in the Polar Regions. The depth of snow cover can be measured using basic physical sampling equipment, but multiple measurements are required to characterize the distribution of snow cover in a region. Measuring rates of precipitation is far more difficult. Extreme winds and blowing snow contaminate physical attempts to measure rates of snowfall. This challenge can be augmented with the use of weather radar, or passive microwave radiometric measurements of column water vapor. Total column integrated precipitable water content W can be made using the equation:

$$W = \int_{z=0}^{z_{top}} \rho_v dz \quad (2.18)$$

Precipitable water is the vertically integrated mass of water vapor per unit area in the water column (kg/m^2), and is calculated from the density of water vapor ρ_v , and the change in height in the atmosphere, denoted as dz . (Stull, 2000). Precipitable water and water vapor density are typical parameterizations within studies concerning atmospheric

water content (*e.g.* Sorteberg and Walsh, 2008) and represent a maximum potential for precipitation, although actual precipitation amounts are usually less than the precipitable water values.

Maximum rates of snow accumulation on sea ice correspond with autumn cyclone frequencies. Snowfall decreases considerably when FY sea ice becomes established; however winds from cyclones may open leads in FY ice, and force water vapor fluxes to form precipitation streamers from open leads that may enhance snow accumulation locally. Little snowfall occurs during winter when high atmospheric pressure and clear skies dominate the region. Snow depths are influenced by strong winds creating blowing snow events, and forming significant snow drifts. May snow depths are ~21 – 24 cm over FY ice, and ~30cm on MY sea ice (Warren *et al.*, 1999).

Snow deposition and distribution exerts a strong control on sea ice thermodynamic processes. Snow cover regulates the growth and decay of sea ice by impeding ice growth by reflecting shortwave radiation, and reducing conductive heat fluxes from the ocean to the atmosphere. Snow is a highly reflective surface ($\alpha \sim 0.6 - 0.9$), and exerts a strong control on downwelling solar radiation. The thermal conductivity of dry snow ranges from (0.1 to 0.4 $\text{W}\cdot\text{m}^{-1}\cdot\text{K}^{-1}$), and depends highly on its porosity. Porosity is usually assessed as a function of snow layer density, which can range in value from 100 – 450 kg/m^3 (Barber *et al.*, 1995; Langlois *et al.*, 2007). Air has a low thermal conductivity of only 0.025 $\text{W}\cdot\text{m}^{-1}\cdot\text{K}^{-1}$, and therefore the ability of dry snow to insulate a surface increases with its porosity. Water content also influences snow thermal properties. Colbeck (1982) differentiates wet snow into two regimes known as the pendular and funicular regimes. The pendular regime is characterized by unsaturated

snow where porous space contains mainly air and less than 7% liquid water by volume. In contrast, the funicular regime contains greater than 7% liquid water volume. The thermal conductivity of water ($0.58 \text{ W}\cdot\text{m}^{-1}\cdot\text{K}^{-1}$) is greater than that of air; snow with high (low) liquid water content therefore conducts fluxes more (less) efficiently.

Frontal passage affects the surface energy balance and snow thermophysical properties, which subsequently affect the growth and decay of sea ice (Maykut, 1978).

Warm frontal boundaries are of particular interest, as they signify northward advection of temperature and moisture, along with increased cloudiness. Northward advection of temperature and moisture typifies the advancement of a warm front, along with increased cloudiness, temperatures and wind speeds. Moisture and warm air advection associated with an approaching warm front can affect snow metamorphism. Growth of snow grains is driven by the large temperature gradient induced by rising temperatures and deposition of water vapor on existing snow grains. Langlois *et al.*, (2008) identified snow grain growth rates of 1.28 and $2.3 \text{ mm}^2 \text{ d}^{-1}$ within thin and thick snow sites respectively,

Wind forcing from cyclones can affect brine volume migration, and the electrical properties of snow cover (Barber *et al.*, 1995). Wind-driven forced convection, termed “Wind-pumping” occurs when winds create variations in surface atmospheric pressure above a surface (Clarke and Waddington, 1991; Clarke *et al.*, 1987). The pressure gradient drives brine from the saline basal layer. The thermal conductivity of brine is similar to that for ice, the values of which are 1.6 and $2.2 \text{ W}^{-1}\text{K}^{-1}$ respectively. The distribution of brine upward into the snowpack thus increases the thermal conductivity of the snow layer (Langlois *et al.*, 2008). This process effectively reduces the insulating

effects of snow cover, and may become significant to radiative transfer processes if a volume of snow is subjected to repeated cyclone events.

2.3.3 Radiative Processes

The radiation budget of snow-covered sea ice can be described in an analogous manner to that described for the global budget in section 2:

$$Q^* = K\downarrow - K\uparrow + L\downarrow - L\uparrow \quad (2.19)$$

Where the terms are as described in section 2. Longwave radiation ($L\downarrow$) dominates Arctic radiative heat exchange during much of the year, having the net effect of removing heat from sea ice because the radiative temperature of sea ice is almost always higher than that of the atmosphere (Maykut, 1986). Incoming longwave radiation is lowest in Winter (DJF), ($\sim 150 \text{ W}\cdot\text{m}^{-2}$), and increases to $\sim 300 \text{ W}\cdot\text{m}^{-2}$ in Summer (JJA) (Maykut, 1982; Maykut, 1986; Lindsay, 1998). Persson *et al.*, (2002) identifies winter net longwave flux values ranging between -50 and $-30 \text{ W}\cdot\text{m}^{-2}$ in cloudy conditions during winter, and net annual longwave radiative flux near $0 \text{ W}\cdot\text{m}^{-2}$. The strongly negative winter net longwave flux represents intense radiative longwave cooling that forms a deep inversion in the ABL.

The influence of clouds on radiative fluxes is dependent on the cloud properties, namely cloud fraction, height, depth, and amount of condensed water (Curry and Ebert, 1992). These properties vary substantially within the frontal system of a cyclone. The initial advance of high, cirrus clouds, followed by 100% coverage of mid-level stratus,

and finally low-level stratus, or nimbostratus, typifies warm fronts. Inversions associated with warm fronts may additionally trap cold near the surface where fog may form. Forced convection associated with cold fronts can result in considerable vertical development in clouds, particularly during the summer.

Low-level clouds exert a strong control on surface radiative processes. Extensive low clouds and substantial atmospheric water vapor present near the surface in summer and early autumn minimize net longwave losses by maintaining a nearly isothermal air temperature profile at and near the surface. Prevailing winter clouds have higher cloud base, and decreased fractional cover, and permit increased longwave radiative loss to space. Clouds emit longwave radiative energy at wavelengths ranging between $0.7\mu\text{m}$ and $1.4\mu\text{m}$; and absorbing almost all energy with wavelength greater than $1.4\mu\text{m}$ (Grenfell and Perovich, 1984). The total transmission of energy through clouds depends on the atmospheric vapor density (Maykut 1986). Cloud cover generally warms the sea ice surface throughout the year (Curry and Ebert, 1992). Cloud albedos are higher than that of water, and therefore may have a net cooling effect during summer in large areas of open water (Serreze and Bradley, 1987; Wang and Key., 2003).

Wang and Key (2003) indicate that the Arctic has been warmer and cloudier in spring and summer; in contrast, the Arctic has been cooler and less cloudy in winter. In spring the increase in cloud cover suggests a strong increase in longwave cloud forcing (or cloud radiative effect), which is defined as the difference between net all-sky radiative flux and clear-sky radiative flux, and in warming, and a decrease in shortwave cloud forcing (reflection of incoming radiation) and cooling. The net effect is nearly balanced; as net spring warming is contrasted by net cooling in summer, autumn, and winter. A

follow-up study investigated trends in net radiative flux (Wang and Key, 2005), and found no trends in net radiative flux, downwelling minus upwelling fluxes, at the surface with more than 90% confidence in any season after surface temperature, albedo, and cloud cover change. However, there is a decrease in longwave radiative flux and net radiative flux in winter with 98% confidence.

The coupled dynamic-thermodynamic response between the passage of a cyclone and the ABL may exert a control on cloud radiative forcing. Cyclone-forced sea ice leads emit heat and vapor fluxes to the atmosphere (*e.g.* Dierer *et al.*, 2005) enabling localized low cloud and fog formation, particularly in late summer when air temperatures are near freezing, and saturated air is capped by an ABL inversion. During the spring and summer, it is possible that increased cloud radiative flux will be absorbed into the ocean-sea ice system via dynamically forced sea ice leads. Leads that refreeze slowly (or not at all) will maintain a heterogeneous surface albedo, thereby prolonging increased net surface cloud forcing. This process is apt to be significant when cloud heights are low (low stratus, fog), and the cloud-forcing component of the radiation budget is maximized (Kay and Gettelman, 2009).

2.3.4 Turbulent Fluxes

Turbulent transfers of heat and moisture are typically referred as sensible and latent heat fluxes (Q_H and Q_E), and are measured in units of $W\ m^{-2}$. Thick sea ice ($> 1m$) constrains the turbulent exchange of heat, and fluxes can be variable for thin ice types (Lupkes and Birnbaum, 2005). The rate of heat transfer within turbulent fluxes is dependent on surface roughness, wind speed, ABL stability, and the strength of

temperature and water vapor gradients (Maykut, 1986). Direct measurement of turbulent fluxes is extremely difficult, but two methods exist from which they may be calculated: the eddy covariance technique (Ruffieux *et al.*, 1995), and bulk aerodynamics (Lindsay, 1998). For brevity, the eddy covariance technique is presented.

The fluxes of Q_H , and Q_E can be computed using the eddy covariance technique (Ruffieux *et al.*, 1995), which calculates fluxes by correlating the turbulent fluctuations of the vertical component of the wind with fluctuations in temperature, water vapor, and wind. The equations used for this are derived from Monin-Obukhov similarity theory and are described in greater detail in Andreas and Murphy, (1986). The eddy-covariance equations for fluxes of Q_H and Q_E are as follows:

$$Q_H = \rho c_p (\overline{w'T'}) \quad (2.20)$$

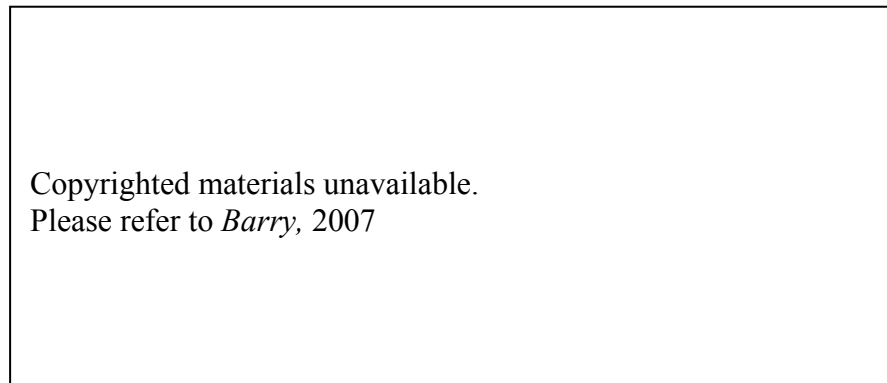
$$Q_E = \rho L_v (\overline{w'X'_q}) \quad (2.21)$$

where ρ is the density of air, L_v is the latent heat of vaporization and c_p is the specific heat capacity of air, X_q is the mixing ratio of water vapor, w and u are wind velocities in the vertical and horizontal directions, and T is air temperature.

Turbulent fluxes are key parameters to studies involving air-sea coupling. Air-sea coupling causes modifications in energy and mass content in the air and sea, and influence local and regional meteorological conditions, which in turn, feedback upon the initial air-sea interaction. An unsaturated parcel of air moving over the ocean will typically move towards saturation. In cold Polar Regions, air crossing open water should be warmer and contain more water vapor than air arriving from snow-covered land or ice

surfaces (Crane 1978). Furthermore, if the surface of the ocean is warmer (colder) than the air parcel, then a transfer of heat will occur from the ocean to the atmosphere to the ocean (atmosphere to the ocean)(Figure 2.11). The transfers of turbulent fluxes of sensible and latent heat from the ocean to the atmosphere are paramount to the coupled dynamic – thermodynamic systems of sea ice leads and polynyas.

Figure 2.11. Typical conditions over a sea ice lead in the winter (from Barry, 2007).



There is a limited history of sensible and latent flux measurement in the Arctic. Andreas *et al.*, (1979) and Andreas and Paulson (1979) describe the first measurements of fluxes over flaw leads, undertaken as part of the AIDJEX experiment. The difference in upwind and downwind atmospheric heat content was calculated for a number of leads. Momentum fluxes were measured using hot-film anemometers. Smith *et al.*, (1983) details the first use of a sonic anemometer in measuring heat and momentum fluxes in the Canadian Arctic. In 1992, the LEADDEX experiment attempted to build upon these earlier studies; however, the final volume of flux measurements over leads and polynyas was limited by technical difficulties during the field campaign. Nonetheless, the limited data revealed a marked change in the direction and magnitude of sensible heat fluxes with the onset of intense winds (Ruffieux *et al.*, 1995). Ship-based studies of this nature have also been conducted (*e.g.* Andreas, 1980).

2.3.5 Polynyas and Sea Ice Leads

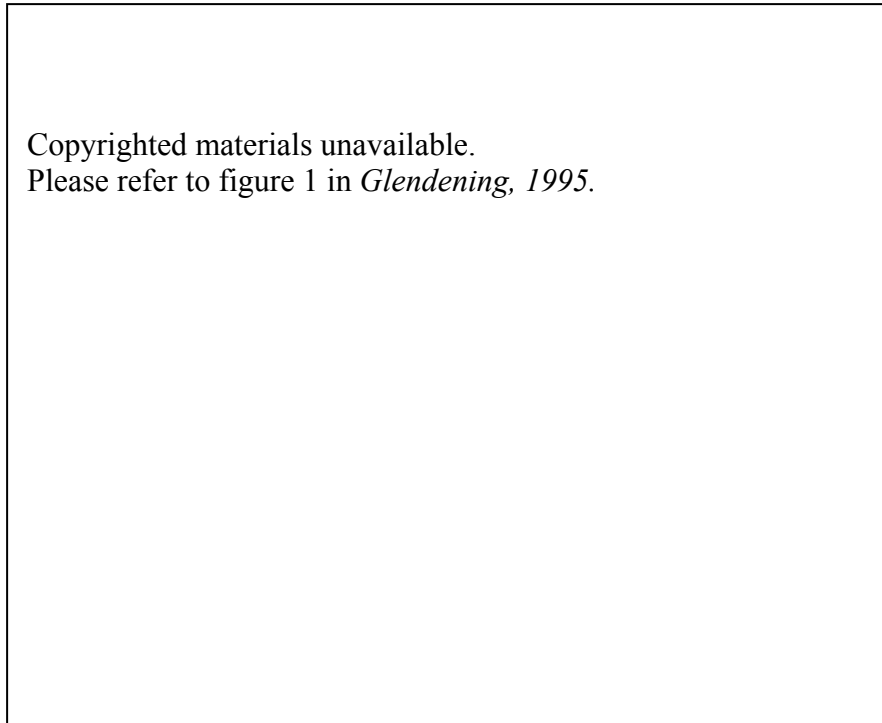
Polynyas are areas of open water that are generally surrounded by sea ice, or a combination of snow-covered land and sea-ice, and remain open for a long period of time. Polynyas are formed in winter sea ice and retained via atmospheric forcing (momentum transfer from winds), oceanic forcing (regions of upwelling warm, water), or a combination of both. There are two types of polynyas: latent heat polynyas, and sensible heat polynyas. A latent heat polynya results in a region where wind or ocean currents remove (or diverge) sea ice continuously. Ice production within a latent heat polynya releases latent heat to the atmosphere, and expels brine to the ocean surface layer. Regions where strong ocean upwelling exists may form sensible heat polynyas. Ocean heat fluxes maintain sensible heat polynyas by retarding sea ice growth (Smith *et al.*, 1990). A sea ice lead is a relatively thin, linear feature in sea that occurs mainly as a result of sea ice divergence, and typically remains open for a much shorter duration than a polynya.

Turbulent heat fluxes from polynyas and leads are important at local and regional scales. Maykut (1978) estimates that heat exchange from a lead or polynya is two orders of magnitude greater than that for snow-covered sea ice. Lupkes *et al.*, (2008) found that during the Arctic winter, leads regionally influence the flux of sensible heat where the leads constituted less than 5% of the total surface area. Large polynyas and sea ice leads can contribute significant turbulent fluxes of heat and water vapor to the ABL through high rates of sea ice production. Agnew *et al.*, (1999) estimated that over a 10-day period, ice production associated with the Cape Bathurst flaw lead, located in the Southern

Beaufort Sea, was approximately 7.36 km^3 , which equates to 22.7×10^{11} MJ of heat fluxes to the atmosphere. On a basin scale, Cavalieri and Martin (1994) estimate that the circumpolar flaw lead system produces upwards of 800 km^3 of new sea ice volume during winter, which equates to 2.467×10^{14} MJ of heat fluxes to the atmosphere.

The forcing of leads in sea ice on ocean-atmosphere fluxes can have varying influences on the atmosphere from near surface (Maykut, 1978; Glendening, 1995; Overland *et al.*, 2000) up to heights of approximately 800 hPa ($\sim 2000\text{m}$) during the winter (Rinke *et al.*, 2006). A newly formed lead or polynya will introduce significant variability in surface climate conditions. The rapid change from a cold surface ($\sim -25^\circ\text{C}$) to that of open water (-1.5°C) represents a strong temperature gradient. Local convective cells will form over the lead, transporting heat and moisture into the atmosphere, thus modifying the lower part of the ABL. During the winter, these leads usually freeze over rapidly, but they are capable of putting locally significant amounts of energy and moisture into the air. Pinto *et al.*, (2003) show that a freezing lead can continue to heat and moisten the atmospheric boundary layer with the area of influence being negatively correlated with time. Significant energy fluxes were measured 70 m and 2.4 km away from a lead for 2 days and 12 hours respectively. Glendening (1995) modelled convective thermal plumes from an Arctic leads, and showed that the largest heat transfers are significantly shallower than the depth of the plume, and depended upon the size of the lead (figure 2.12).

Figure 2.12. Modeled thermal plume created by an Arctic lead. Contour surface is 0.2 m s^{-1} vertical motion. Color shade indicates height, sliced at 4-m increments. The x-axis is angled at 15° to orient the geostrophic wind parallel to the vertical figure frame (from: Glendening, 1995).



Coupling between the ocean and atmosphere can help sustain a polynya. Turbulent heat fluxes to the lower atmosphere above a polynya or lead combined with the absence of any wind may warm the air directly above the polynya to a point where the sensible heat flux between the ocean and atmosphere is reduced. This process retards frazil ice production, and leads to wider polynyas that remain open longer. (Walkington and Willmott, 2006). Another mechanism of ice formation retardation may be a shift in radiation balance caused by the presence of clouds arising from moisture from the polynya (Smith *et al.*, 1990). Steffen and Ohmura (1985) suggest that 20% of oceanic heat flux is due to the release of latent heat (freezing the sea) and 80% is sensible heat from upwelling seawater.

2.3.6 Leads, Polynyas, and Cyclone-Coupling

Winds and atmospheric surface divergence arising from cyclones can promote sea ice lead formation by inducing motion, dilatation and divergence in the ice cover (Barry and Maslanik, 1989; Brümmer *et al.*, 2003; Dierer *et al.*, 2005). The newly formed leads can precondition a region for latent heat polynya development (Comiso and Gordon, 1996), or sensible heat polynya formation (Bailey *et al.*, 2004). Bailey *et al.*, (2004) modelled sensible polynya formation in Antarctica using specified oceanic heat flux. Polynya formation was attributed to surface wind and sea ice divergence arising from the interaction of synoptic-scale winds with the katabatic wind flow regime, characteristic of the continental glacier. Atmospheric divergence forced the ice to diverge within the region of enhanced heat flux, which subsequently melted the sea ice and formed a polynya, (Bailey *et al.*, 2004).

Turbulent heat fluxes over open large areas of open water can introduce instability to the atmosphere, and drive local and mesoscale wind patterns that may not otherwise be captured by existing climate models. Development of self-organized convective structures (convective vortices) over wide Arctic leads and polynyas may introduce a positive feedback between the horizontal entrainment of cold air in breeze and the turbulent heat exchange, thus amplifying heat and moisture fluxes (Esau, 2007). Optimal conditions for vortex development over a polynya include light surface and upper-level wind velocities, cloud cover, and partial ice coverage of the polynya, or a polynya with an extension oriented in the direction of the winds (Hebbinghaus, *et al.*, 2007). Higher wind velocities enhance heat fluxes, however decreases the time an air parcel remains over the polynya. Downward long-wave fluxes from low-level clouds confined to the

Polynya increase the existing temperature gradients between ice and open water, thus increasing buoyancy. Serreze et al., (1992) also shows that the influence of heat fluxes upon the atmosphere depend upon the amount of wind fetch available.

Heat fluxes from large polynyas during winter represent a zero-order discontinuity in the atmosphere, promoting a baroclinic atmospheric environment in which mesoscale cyclonic vortexes can develop (Hebbinghaus et al., 2007). Theoretically, there should not be any zeroth order discontinuities in the atmosphere (i.e. places where one or more meteorological variables changes its value so rapidly that at the scale of measurement, the values are discontinuous); however such discontinuities have been observed to exist in the atmosphere in mid-latitude cyclones (*e.g.* during ERICA; Paldor *et al.*, 1994). We therefore can surmise that an open lead or polynya in arctic sea ice during winter represents a step-like change in surface air temperature and humidity, and creates a zone of surface-based instability and baroclinicity where turbulent fluxes of heat and vapor drive vertical motions in the ABL, cloud formation, and precipitation enhancement. Polar lows can be sustained through sea surface energy supply being drawn upon by a large vortex-ocean interaction (Businger and Baik, 1991).

(Dierer *et al.*, 2005) investigated cyclone-OSA coupling on a regional scale in Fram Strait. Heat fluxes were found to influence cyclone development by affecting baroclinicity and convection, but the effect strongly depended on the stage of the cyclone, geographical location, and the degree of atmospheric preconditioning. Dierer *et al.* (2005) speculated that heat fluxes to the atmosphere from cyclone-OSA coupling could be significant if a cyclone tracks in the vicinity of the ice edge and the ice-covered region, drawing on the temperature gradient between the ice cover and ocean.

Furthermore, the impact of OSA coupling may be most pronounced during initial cyclogenesis rather than enhancing an existing storm.

Wind direction is a key factor in forcing heat and moisture fluxes from Arctic leads (Crane, 1978; Andreas, 1985; Barber *et al.*, 2001). Wind that originates from a cold, dry air mass, advecting over a lead can result in large heat fluxes of up to 100 w/m^2 (Andreas, 1985). Air crossing a large polynya should therefore be warmer than air advecting from snow-covered land surfaces (Crane 1978), and increased atmospheric water content should accompany an increase in saturation vapor pressure that accompanies warmer air temperature. This process adds energy and moisture to passing cyclones, and may subsequently enhance the cyclone's propensity to produce precipitation (Hebbinghaus, *et al.*, 2007), or precipitation efficiency of the storm (Szeto *et al.*, 1997). Regions having near – surface relative humidity values with respect to ice $> 80\%$ are found to have storms with high precipitation efficiencies. During the fall, and with the presence of open leads, the availability of moisture and an undeveloped arctic surface inversion layer should promote storms with high precipitation efficiencies (acting to dry out the atmosphere). Conversely, low precipitation efficiency storms should dominate during the winter, when humidity values are lower ($<80\%$) and stronger arctic inversion has developed (Szeto *et al.*, 1997). A modeling exercise by Higgins and Cassano (2009) showed that 98.5% of any apparent increase in a cyclone's proclivity to produce precipitation is attributable to thermodynamic warming, and a concomitant increase in saturation vapor pressure.

Evidence exists that frontal inversions associated with cyclones may limit the potential for transfer of turbulent fluxes of heat and vapor vertically through the ABL.

Burk and Thompson (1995) investigated the effect of the passage of a shallow front upon the boundary layer during the LEADDEX experiment of March-April 1992. A pre-existing well-mixed boundary layer over a small polynya to a height of 1.5km was modified. Initially, the mixing of the strong ABL with the leading edge of the front retarded the advance of the front, but the strength of the inversion of the advancing front became too strong and “broke through.” In turn, the front’s horizontal temperature gradient and inversion strength is weakened, but the vertical extent of the mixed layer in the ABL was limited to a depth of only a few hundred meters by the frontal inversion.

Our ability to predict how reductions in season sea ice extent, and sea ice leads affect the strength, deepening rate, and spatial distribution of Arctic clones and Polar lows depends upon developing a better understanding of how turbulent heat fluxes from leads and polynyas force atmospheric stability and diabatic in cold air masses (Businger and Reed, 1989). Businger and Baik (1991) emphasize the importance of baroclinicity and baroclinic instability in the case of rapid development of a very strong polar low (they deemed an “Arctic Hurricane). Roebber (1989) identified a need to improve our understanding of processes that influence the magnitudes and three-dimensional distribution of diabatic heating in cyclones, namely how surface fluxes modify large-scale static stability. Furthermore, a better understanding of the relationships between the air-sea thermal waves, storm pressure, and moistening and destabilization of the boundary layer will lead to a better understanding of the amplification of atmospheric baroclinicity due to the ice edge effect, and how it affects cyclone forcing of the OSA interface.

2.3.7 Ocean Heat Flux

Much of the energy in ocean heat fluxes originates from absorption of shortwave radiation into the ocean mixed surface layer (Maykut, 1982; Perovich *et al.*, 2008). Maykut (1982) suggests that a nominal ocean heat flux of $2 \text{ W}\cdot\text{m}^{-2}$ is sufficient to maintain an ice thickness of 3m during winter, however, observation values of ocean heat flux show that much spatial and temporal variability can exist in the magnitude of ocean heat fluxes. Wettlaufer, (1991) reports ocean heat fluxes can range from near zero to $\sim 70 \text{ W}\cdot\text{m}^{-2}$. Perovich and Elder (2002) report values range seasonally from $4 - 16 \text{ W}\cdot\text{m}^{-2}$ under MY sea ice in the Beaufort Sea.

Cyclones are well documented to induce large rates of ocean heat fluxes through wind-induced upwelling (Wettlaufer, 1991; Perovich and Elder, 2002; Pickart *et al.*, 2009) and mixing via vertical inertial currents (Rainville and Woodgate, 2009). Wettlaufer (1991) links high values of ocean heat fluxes to the passage of an intense cyclone, in which wind speeds were in excess of $30 \text{ m}\cdot\text{s}^{-1}$, and ocean currents in the surface layer reached $30 \text{ cm}\cdot\text{s}^{-1}$. A similar situation was observed by Perovich and Elder (2002) in March 1998, where strong winds and fast sea ice motion brought relatively warm water to the sea ice bottom, causing ice melt. Pickart *et al.*, (2002) revealed that cyclone – forced upwelling mixes warm salty Atlantic water to shallow depths and also that cyclones in the North Pacific Ocean can cause ocean upwelling along the continental slope of the Beaufort Sea. Upwelling events occurred frequently when intense northward-moving storms were located in a region near the eastern end of the Aleutian Island Arc. Lee cyclogenesis on the northern side of the Alaskan range enhances the meridional influence of North Pacific storms. Yu, *et al.*, (2004) suggest that increased mixing of

relatively warm fresh water into the ocean-surface mixed layer may partially account for long-term reductions in sea ice thickness and volume.

Intruding Pacific and Atlantic water into the Arctic basin influences ocean heat fluxes in the Arctic. Woodgate *et al.* (2006) characterized heat fluxes through the Bering Strait ($1 - 3 \times 10^{20} \text{ J}\cdot\text{yr}^{-1}$) one fifth the size of those found in Fram Strait ($5 - 13 \times 10^{20} \text{ J}\cdot\text{yr}^{-1}$) (Schauer *et al.*, 2004). An increase of total heat flux into the Arctic through the Bering Strait between 2001 and 2004 is capable of melting 640,000 km² of 1-m-thick ice, which matches the reduction in sea ice extent in September ($\sim 700,000 \text{ km}^2$) that is identified by Stroeve *et al.* (2005) for the same period. Intruding warm water from the Atlantic is showing signs of warming (Quadfasel *et al.*, 1991; Polyakov *et al.*, 2005), and may influence the nature of Arctic Ocean heat fluxes. Quadfasel *et al.* (1991) provide the first evidence of warming in the Atlantic Water. Two temperature measurements in Nansen Basin in 1990 exhibited maximum values of 2.8 °C. Positive Atlantic water temperature anomalies in the Arctic Ocean were found by Carmack *et al.* (1995), Swift *et al.* (1997), Steele and Boyd (1998) and Morison *et al.* (1998).

2.4 Sea Ice Coupled Processes and Climate Change

Dramatic reductions in sea ice extent and volume, changing seasonal atmospheric circulation patterns, and increasing areas of open water characterize the changing climate of the Arctic. A seasonally-free Arctic ocean, combined with later freeze-up and longer melt seasons is bound to affect the climate throughout the Arctic, alter atmospheric circulation in the Northern hemisphere, and may even modify the rate of the ocean

thermohaline circulation, thus affecting global circulation of heat in the oceans. This section presents a discussion on Arctic climate change, and discusses how cyclone forcing of coupled dynamic and thermodynamic sea ice processes may be affected by climate change.

Cyclones represent a key component of the atmospheric poleward transfer of heat and moisture to the Arctic. They can force coupled responses between sea ice dynamic (motion, morphology, fracture) and thermodynamic (temperature advection, snow-cover, radiative) processes, which may subsequently introduce coupling between the ocean and atmosphere.

2.4.1 Atmospheric Response to Climate Change

The high sensitivity of the Polar Regions to climate change is best described by a process referred to as “Polar amplification.” Polar amplification is characterized as positive temperature anomalies, increasing in magnitude poleward (*e.g.* Johannessen *et al.*, 2004; Serreze and Francis, 2006). Polar amplification may elucidate differentiation between anthropogenic warming and teleconnection-induced climate variability. Thompson and Wallace (1998) describe a systematic bias of several °K in surface temperature over Eurasia, cooling in the core of the lower stratospheric polar vortex by several °K, and a general decrease in MSLP of ~ 4 hPa over much of the Arctic basin. The AO index was characterized by a transition from negative to positive during this time period, which explains most of the temperature variability and sea ice loss (Rigor *et al.*, 2002). However, more recently, the AO index has not yielded a strongly negative or positive phase, despite observations of ongoing warming, and accelerating sea ice loss. It

is therefore possible that the reduction in sea ice loss is affecting atmospheric circulation to an extent that it is modifying existing modes of natural climate variability. Deser *et al.*, (2010) showed that the atmospheric response to greenhouse forcing resembles a characteristic negative NAO pattern only in February.

Arctic surface temperature anomalies are characterized by spatial and seasonal variability, (Rigor *et al.*, 2000; Comiso, 2003) and correspond with the changing Arctic sea ice cover (Parkinson *et al.* 1999; Overland, 2009). Rigor *et al.*, (2000) identified a spring warming trend over the eastern Arctic Ocean at the 99% significance level, and nearly zero areal-averaged trend in summer and a winter cooling trend over the western Arctic. Comiso (2003) extracted temperature trends from Infrared data from the Advanced Very High Resolution Radiometer (AVHRR). Highly positive temperature anomalies were identified in the Canadian Archipelago, Alaska, and the Beaufort Sea while negative values were located in Greenland, the eastern Bering Sea and parts of Russia. Temperature trends are mainly positive in summer, spring, autumn, but are negative in winter. The spatial distribution of surface atmosphere temperature trends is consistent with the change of sea ice cover in Arctic region (north of 60° N) (Parkinson *et al.* 1999).

Areas that show the greatest loss in summer sea ice cover are linked to the strongest surface temperature anomalies. Overland (2009) linked sea ice loss to strongly positive temperature anomalies ($>+^{\circ}6\text{C}$) in the Beaufort Sea region during the autumn, and concluded that it would be very difficult to quickly return to pre-1990 climate conditions in the Beaufort sea region due to the loss of MY sea ice. Field observations

during the International Polar Year Circumpolar Flaw Lead System Study (IPY-CFL) were similar for the Amundsen Gulf region in autumn 2007 (Barber *et al.*, 2010).

2.4.2 Sea Ice Response to Climate Change

Arctic sea ice is in an accelerating state of decline, and may transition to a seasonally ice-free regime in the Arctic Ocean for the first time in nearly one million years. Satellite observations of sea ice concentration underline a rapidly accelerating decline in summer sea ice extent in recent years (Parkinson and Cavalieri, 2008; Kwok *et al.* 2009). Parkinson and Cavalieri (2008) estimate the Annual Arctic sea ice minimum cover (determined for September), to be declining at a rate of $45,000\text{km}^2 / \text{year}$ ($\pm 4600\text{ km}^2$). Most notably, in September 2007, the summer sea ice extent reached the lowest level in satellite measurements beginning in 1979, reaching a record low area of $4.28 \times 10^6\text{ km}^2$, and broke the previous record for the month, set in 2005, by 23 percent. A perfect storm of abnormal atmospheric conditions coupled with negative trends in sea ice concentration and thickness were suggested as the main causes of the record minimum cover in 2007 (Stroeve *et al.*, 2007; Ogi *et al.*, 2008).

The recent declines in summer sea ice extent have also resulted in increased sea ice mobility, which renders the pack ice more susceptible to cyclone-forced reversals of the BG. This follows earlier speculation by Barry and Maslanik, (1989) who suggested that BG reversals could last for several months in the future. Walsh *et al.*, (1996) identified a clear tendency towards increased cyclonic wind forcing over the Arctic Ocean, which supported the idea of reduced fractional concentration of MY ice, and increased divergence in the Arctic ice pack. McPhee *et al.*, (1998) suggested that

continued weakening of the BG may lead to an eventual reversal of the mean state of the wind-driven BG, further increasing rates of ice divergence and fracture. A recent study by Lukovich and Barber (2007) shows that summer reversals of the BG have been increasing in frequency, and that reversals have recently been occurring at all times of the season. Reversals of the BG to cyclonic circulation may be influencing coupled dynamic and thermodynamic sea ice processes, leading to ice volume loss.

2.4.3 Coupled Ocean-Sea-Ice Atmospheric Processes

Predictions of a seasonally ice-free Arctic ocean have recently been revised to reflect the expected acceleration of sea ice decline (Drobot *et al.*, 2008), and the near absence of MY ice that is five years or older (Maslanik *et al.*, 2007). Drobot *et al.*, (2008) suggested that the Arctic basin is on a trajectory towards a seasonally ice-free state between 2020 and 2030. The loss of the perennial ice cover will significantly reduce the average summer albedo of the Arctic. This introduces a positive feedback loop, known as the ice-albedo feedback, which states that as we lose Arctic sea ice, the resultant areas of open water will absorb more energy. This process results in energy accumulation in the ocean surface mixed layers where sea ice is removed completely. The accumulated energy in the mixed surface layer of the ocean will then be forced to dissipate as latent heat into the atmosphere to form sea ice during the autumn and winter. This could significantly impact atmospheric circulation over the Arctic basin, thus leading to significant changes in coupled cyclone forcing of sea ice motion, and ocean currents.

A recent study by Deser *et al.* (2010) showed that a shift to a seasonally ice-free Arctic basin will considerably alter the seasonal, spatial and vertical structure of the atmosphere, and surface climate parameters. A particularly notable large-scale atmospheric circulation response was identified during winter, with a baroclinic (equivalent barotropic) vertical structure over the Arctic in November-December (January-March) (Figure 2.13). Of further note was the near absence of a deep low-level inversion over much of the Arctic basin. Temperature and precipitation responses are modeled to be greatest during winter, over terrestrial and marine Arctic environments, and notably increase snow depths over Siberia and northern Canada. The response of the net surface energy budget over the Arctic Ocean is largest in winter, despite the largest reductions in sea ice cover occurring in summer and autumn. A possible explanation for this may be an increase in regional turbulent heat fluxes due to enlarged areal coverage of sea ice leads and polynyas, known to exert a strong control on energy budgets (Lupkes and Birnbaum, 2005; Lupkes *et al.*, 2008).

Figure 2.13. Atmospheric profile over a seasonally ice-free Arctic: Vertical structures of the geopotential heights (m; contours) and temperature (°C; color) responses along 90°E in (left) November-December and (right) January-February (from: Deser et al., 2010).

Copyrighted materials unavailable.
Please refer to figure 13 in *Deser et al., 2010*.

A seasonal ice regime will increase energy available for cyclonic systems, particularly during the autumn freeze-up. The emergence of a baroclinic atmospheric environment dominating the region, coupled with increased turbulent fluxes in November and December represent conditions favorable for cyclogenesis, and maintenance of storms that may migrate in from other regions (Simmonds and Keay, 2009; Deser *et al.*, 2010). Simmonds and Keay (2009) identify changing cyclone intensity as being more important than cyclone frequency with respect to how climate change affects cyclone forcing of coupled sea ice dynamic and thermodynamic processes. Higgins and Cassano (2009) identified a modeled increase in strong Arctic lows, and a decrease in frequency of Eurasian and transitional lows.

Observed changes in the timing of autumn freeze-up in the Arctic (Stroeve *et al.*, 2006; Markus *et al.*, 2009) are apt to increase baroclinicity, and subsequently impact cyclone paths and rates of intensification. Autumn baroclinicity will increase due to the interaction of relatively warm and moist airmasses that will persist longer due to delayed freeze-up, with cold airmasses that form via radiative cooling in the Canadian Archipelago, Siberia, and any remaining MY sea ice. The delayed onset of complete freeze-up in Amundsen Gulf is also identified as a major source of heat fluxes. Strong easterly winds associated with a strong synoptic-scale pressure-gradient were noted over the region, and contributed to maintaining large areas of open water by advecting young ice out of the region (Barber *et al.*, 2010). This observation follows a trend towards the dominance of thick FY ice in the Cape Bathurst flaw lead system (Galley *et al.*, 2008).

The declining MY sea ice cover, increased ice mobility, coupled with a delayed onset of freeze-up may be enhancing cyclone-forcing of the circumpolar flaw lead

system, particularly during November-December. Increased rates of dynamically driven (cyclone forced) lead formation may be accompanied by simultaneous increases in pressure ridge formation. This will subsequently increase ice thickness and ice volume, and act as a positive forcing on sea ice cover. Coupled thermodynamic responses between increased sea ice lead formation and the atmosphere may introduce a negative forcing on sea ice growth rates. Turbulent fluxes of heat and vapor may locally increase air temperatures and saturation vapor pressure, thereby increasing rates of precipitation (Higgins and Cassano, 2009), and may result in faster rates of snow accumulation on the sea ice. An increase in early-season snow cover may insulate young sea ice, and slow thermodynamic sea ice growth.

The melt season is beginning earlier, and becoming longer in duration (Stroeve *et al.*, 2006; Markus *et al.*, 2009). The melt season was observed to increase in length by <2 weeks \cdot decade⁻¹ in the Eastern Arctic since the 1980's (Stroeve *et al.*, 2006). Melt-season length trends of over 10 d \cdot decade⁻¹ have been observed in Hudson Bay, the East Greenland Sea, and the Laptev / East Siberian Seas, and the Chukchi/Beaufort seas (Markus *et al.*, 2009). This follows a similar spatial pattern of changes in melt season length as identified by Stroeve *et al.* (2006). Thermodynamic rates of sea ice decay can be forced by warm airmasses associated with the warm frontal boundaries of cyclones. An increase in cyclone activity may result in increased warm air advection; however, late-season snow arriving from these systems may negatively affect rates of sea ice thermodynamic decay. Increased snow-cover can maintain high albedo values, reducing the amount of solar insolation absorbed by the snow-sea volume, and insulate the ice beneath during the melt-season, reducing the rate of snow loss. The ability of snow to

act as an insulator may be diminished by cyclone-forced wind pumping of brine into the snow layer, which is noted to increase the thermal conductivity of snow (Langlois *et al.*, 2008).

Changing cloud cover may accompany a coupled OSA response to climate change. Francis and Hunter (2006) demonstrated large inter-annual and regional variability in sea ice retreat anomalies. In particular in the Chukchi and Beaufort Seas the trend of maximum ice retreat anomalies were 168 and 113 kilometers per decade, respectively, with > 99% confident significance. Francis and Hunter (2006) calculate time series of anomalies for the likely drivers: downward longwave flux, downward shortwave flux, zonal and meridional winds, and temperature advection. Correlation between maximum ice retreat anomalies and downward shortwave flux anomalies were consistently negative in all six regions. In contrast, downward longwave flux anomalies were not only consistently positive, but also the primary factor of variability in maximum ice retreat anomalies among the four drivers considered. Downward longwave flux anomalies are linked to increase cloud cover and water vapor, which are contrasted with increased absorption of insolation in the ice – albedo feedback of Serreze and Francis (2006). Less than half of total maximum ice retreat anomalies are explicated by the four drivers, suggesting that ocean currents, snow depth, river discharge, amongst other factors, could be important to sea ice edge position.

The impact of climate change on Arctic cloud cover is hard to assess, and disagreement exists over whether cloud forcing actually is a positive or negative feedback in forcing Arctic sea ice decline. Cloud forcing is an important component of the “perfect storm” of abnormal atmospheric conditions attributed to the 2007 record sea ice

extent minimum (Schweiger *et al.*, 2008a, Schweiger *et al.*, 2008b, Kay and Gettelman, 2009). Schweiger *et al.*, (2008a) identified a decrease in low-level cloud during autumn and a simultaneous increase in mid-level clouds. The net radiative effect of this change in cloud cover is small, and therefore suggests that changes in cloud cover do not contribute to sea ice anomalies in autumn (Wang and Key, 2005; Schweiger *et al.*, 2008a). This is consistent with the study presented in Schweiger *et al.*, (2008b), which shows that unusually clear skies during summer 2007 did not contribute substantially to the record sea ice extent minimum.

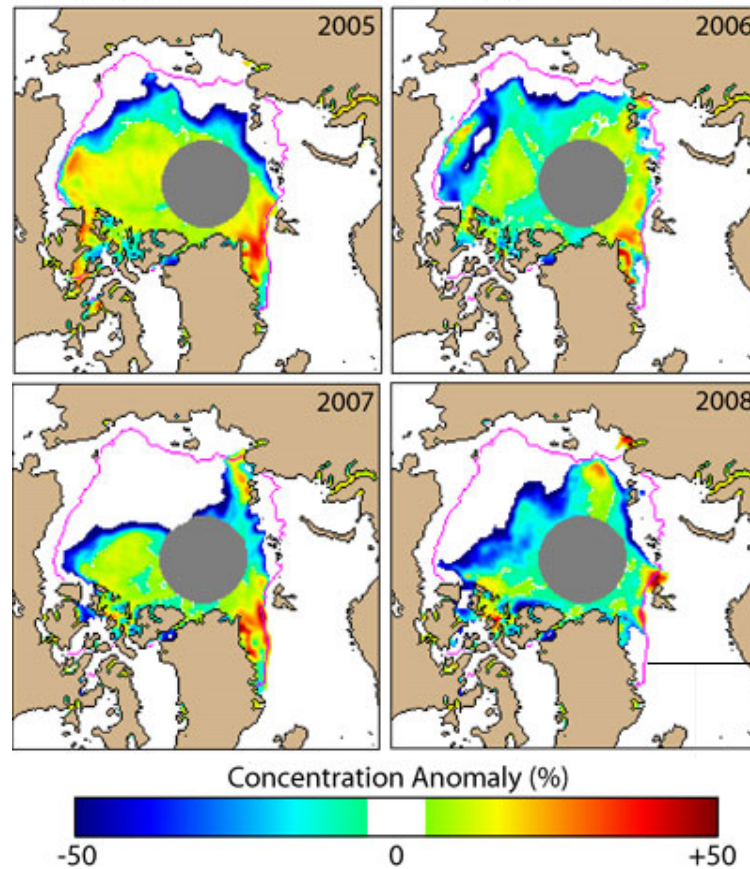
Increasingly larger areas of open water are forming seasonally due to sea ice cover reduction. These areas are susceptible to wind-forcing that may subsequently induce upwelling of ocean heat fluxes (Pickart *et al.*, 2009; Woodgate *et al.*, 2006; Perovich *et al.*, 2008), sea ice dynamic processes (*e.g.* swells; Steer *et al.*, 2008), and coupling between the OSA interface (*e.g.* wind-driven upwelling, Pickart *et al.*, 2009; Rainville and Woodgate, 2009). The presence or absence of sea ice is a key factor to whether a cyclone generates a significant upwelling in the ocean. Cyclone-forced ocean upwelling has been observed to occur in areas where MY ice has been lost (Rainville and Woodgate *et al.*, 2009). During ice-free seasons, local storms drive strong inertial currents (>20 cm/s) that propagate throughout the water column and significantly deepen the surface mixed layer. Perovich *et al.*, (2008) show a 500% increase in shortwave radiation absorption and entrainment in the ocean surface layer. This energy may be entrained deeper into the water column by cyclone-induced vertical currents in the ocean.

The large vertical shear associated with summer inertial motions suggests a dominant role for localized and seasonal vertical mixing in Arctic Ocean dynamics.

Rainville and Woodgate *et al.*, (2009) suggest that recent extensive summer sea-ice retreat will lead to significantly increased internal wave generation especially over the shelves and also possibly over deep waters. This internal wave activity will likely dramatically increase upper-ocean mixing in large areas of the Arctic, with important ramifications for ecosystems and ocean dynamics. Results from the Beaufort Sea storm modeling study indicate that cyclone-induced ocean upwelling events may cause large re-suspensions of organic and inorganic material along the Beaufort Sea coastline (Mucci *et al.*, 2008).

Recent dramatic reductions of the sea ice cover are introducing a new wind-fetch distance regime in the Arctic Basin. Large areas of open water are a recent phenomenon, with the past 5 years showing the most notable patterns (Figure 2.14). Waves and swells develop from the interaction of winds from slow-moving, intense cyclones interacting with large wave-fetch distances in these areas. These swells can propagate to coastal regions, eroding coastline through increased wave energy dispersion. The most significant dissipation of wave energy is expected to occur along the Tuktoyaktuk Peninsula, particularly along its northeast tip, and in MacKenzie Bay (Mucci *et al.*, 2008).

Figure 2.14. Observed 2005 – 2008 minimum sea ice extents and 1979 – 2000 median ice extent (purple line).



Large, fast-moving ocean swells can also propagate under sea ice, and induce flexural failure in large sea ice floes (Wadhams, 1973). This process significantly increases the numbers of small ice floes (*e.g.* Steer *et al.*, 2008) that are susceptible to lateral melting (Toyota *et al.*, 2006; Steer *et al.*, 2008). More recently, this phenomenon was observed in September 2009 in the Southern Beaufort Sea. Asplin *et al.*, (2012) describes *In situ* observations which indicated that flexural failure in thick MY ice floes was due to deteriorated ice strength, attributed to summer warming (Eicken *et al.*, 1995), and a heavily decayed ice edge margin, consisting of warm, weak, rotted ice, as described in detail in Barber *et al.*, (2009).

2.5 Conclusions

This work comprises a detailed review of the nature of Arctic cyclones, the role that they play in forcing sea ice dynamic and thermodynamic processes, and how these coupled processes may be affected by climate change. It is clear that a great deal is known about cyclones and cyclogenesis, and their synoptic-scale influence on the Arctic climate system. Furthermore, there is considerable knowledge about sea ice thermodynamic and dynamic coupled processes, despite the lack of a dense observation network in the Arctic. As the Arctic basin continues to lose sea ice volume, and sea ice extent, we can expect the Arctic climate system to continue to progress toward a seasonally ice-free state sometime between 2020 and 2030 (Drobot *et al.*, 2008), or possibly earlier.

Climate change appears to be introducing new seasonal forms of cyclone-OSA coupling (dynamic; open water and large wave generation), and intensifying existing ones (thermodynamic; increased lead formation in winter). In the autumn and winter, increasingly larger areas of FY ice will drive increased heat and moisture fluxes to the atmosphere through the thermodynamic formation of sea ice. Increased lead formation may result in higher rates of brine expulsion to the ocean, and may have implications for the thermohaline circulation that drives poleward oceanic heat transport, a key global energy circulation mechanism. It is therefore paramount that the scientific community continues to monitor climate change in the Arctic, investigates OSA coupled physical processes within the system as they evolve with the climate system.

2.6 References

- Aagaard, K., Coachman, L.K., Carmack, E., 1981, On the halocline of the Arctic Ocean. *Deep Sea Res.*, A, 28(6): 529 – 545.
- ACIA, 2005. Future Climate Change: Modeling and Scenarios for the Arctic. Chapter 4 in Arctic Climate Impact Assessment, URL: www.acia.uaf.edu.
- Agnew, T.A., Le, H., Shokr, M. 1999, Characteristics of large winter leads over the Arctic basin from 85.5GHz DMSP SSM/I and NOAA AVHRR imagery. *Can J. Remote Sens.* 25(1): 12 – 20.
- Ahrens, D.C., 2007, *Meteorology Today: An Introduction to Weather, Climate and the Environment*, (8th ed.), Thomson/Brooks/Cole, Belmont, California, pp 616.
- AMAP 1998. AMAP Assessment Report: Arctic Pollution Issues. Arctic Monitoring and Assessment Programme (AMAP), Oslo, Norway. 859pp.
- Andreas, E.L., and Paulson, C., 1979, Velocity spectra and cospectra and integral statistics over Arctic leads. *Quarterly Journal of the Royal Meteorological Society*, 105: 1053 – 1070
- Andreas, E.L., 1980: Estimation of heat and mass fluxes over Arctic leads. *Mon. Wea. Rev.*, 108, 2057 – 2063.
- Andreas, E.L. 1985, Heat and moisture advection over Antarctic sea ice, *Mon. Wea. Rev.*, 113, 736 – 746.
- Andreas, E.L., Murphy, B., 1986, Bulk transfer coefficients for heat and momentum over leads and polynyas, *J. Phys. Oceano.* 16, 1875 – 1883.
- Andreas, E.L., Lange, M.A., Ackley, S.F. and Wadhams, P., 1993, Roughness of Weddell sea ice and estimates of the air-ice drag coefficient, *J. Geophys. Res.*, 98 (C7): 12439 – 12452.
- Asplin, M. G., R. Galley, D. G. Barber, and S. Prinsenber (2012), Fracture of summer perennial sea ice by ocean swell as a result of Arctic storms, *J. Geophys. Res.* 117, C06025, doi:10.1029/2011JC007221.
- Bailey, D.A., Lynch, A.H., Arbetter, T.E., 2004: Relationship between synoptic forcing and polynya formation in the Cosmonaut Sea: 2. Regional climate model simulations, *J. Geophysical Res.* 109, C04023, doi: 10.1029/2003JC001838, 2004
- Barber, D.G., Reddan, S.P., Ledrew, E.F., 1995. Statistical characterization of the geophysical and electric properties of snow on land-fast first-year sea ice, *J. Geophys. Res.*, 100(CS): 2673 – 2686.

- Barber, D.G., Hanesiak, J.M., Chan., W., Piwowar, J., 2001. Sea-ice and meteorological conditions in northern Baffin Bay and the North Water Polynya between 1979 and 1996, *atmosphere-ocean* 39(3): 343 – 359
- Barber, D.G., and Hanesiak, J.M. 2004: Meteorological forcing of sea ice concentrations in the southern Beaufort Sea over the period 1979 to 2000, *J. Geophys. Res.* 109 (C06014), doi: 10.1029/2003JC002027, 2004
- Barber, D.G. Galley, R. Asplin, M.G. De Abreu, R. Warner, K.A., Pućko, M. Gupta, M., Prinsenberg, S., and Julien, S. 2009, Perennial pack ice in the southern Beaufort Sea was not as it appeared in the summer of 2009. *Geophys. Res. Lett.*, 36, 24, doi:10.1029/2009GL041434, 2009
- Barber, D. G., M. Asplin, Y. Gratton, J. Lukovich, R. Galley, R. Raddatz, and D. Leitch 2010. The International Polar Year (IPY) Circumpolar Flaw Lead (CFL) System Study: Overview and the Physical System. *Atmosphere-Ocean. In review* (Mar, 2010).
- Barry, R.G., Maslanik, J. 1989: Arctic sea ice characteristics and associated atmosphere – ice interactions in summer inferred from SMMR data and drifting buoys: 1979 – 1984
- Barry, R.G., Carleton, A.M. 2001. *Synoptic and Dynamic Climatology*, Routledge, London, pp 620.
- Barry, R.G. 2007, Arctic Ocean Ice-Atmosphere Interactions, unpublished notes, Cryospheric and Polar Research Division, CIRES, University of Colorado, Boulder.
- Bennetts, L. G., N. R. T. Biggs, and D. Porter (2007), A multi-mode approximation to wave scattering by ice sheets of varying thickness, *J. Fluid Mech.*, 579, 413– 443.
- Bleck, R. 1973: Numerical forecasting experiments based on the conservation of potential vorticity on isentropic surfaces, *J. Appl. Meteorol.*, 12, 737 – 752.
- Brümmer, B., Müller, G., Hoerber, H. 2003: A Fram Strait cyclone: properties and impact on ice drift as measured by aircraft and buoys. *J. Geophysical Res* 108, No. D7, 4217, doi:10.1029/2002JD002638, 2003.
- Businger, S., Baik, J. 1991, An Arctic Hurricane over the Bering Sea, *Monthly Weather Review*, 119, 2293 – 2322
- Businger, S., Reed, R.J. 1989, Cyclogenesis in cold air masses, *Weather and forecasting*, 4, 133 – 156
- Burk, S. D., W. T. Thompson, 1995, Passage of a shallow front across a Beaufort Sea polynya, *J. Geophys. Res.*, 100(C3), 4461–4472.

- Carmack, E. C., R. W. Macdonald, R. G. Perkin, F. A. McLaughlin, and R. J. Pearson (1995), Evidence for warming of Atlantic water in the southern Canadian Basin of the Arctic Ocean: Results from the Larsen-93 expedition, *Geophys. Res. Lett.*, 22, 1061–1064.
- Cavalieri, D.J., and Martin, S., 1994. The contribution of Alaskan, Siberian, and Canadian coastal polynyas to the cold halocline layer of the Arctic Ocean, *J. Geophys. Res.* 99(C9): 18343 – 18362.
- Clarke, G.K.C., Fisher, D.A., and Waddington, E.D., 1987, Wind pumping: A potentially significant heat source in ice sheets, *IAHS Publi.*, 180, 169 – 180.
- Colbeck, S.C. 1982, An overview of seasonal snow metamorphism, *Rev. Geophys. Space Phys.*, 20(1): 45 – 61.
- Comiso, J.C. 2003: Warming trends in the Arctic from clear sky satellite observations, *J. Clim.* 16: 3498 – 3510
- Comiso, J.C., and Gordon, A.L. 1996. Cosmonaut polynya in the Southern Ocean: Structure and Variability, *J. Geophys. Res.*, 101(C8), 18,297 – 18,313.
- Crane, R.G. 1978: Seasonal variations of sea ice extent in the Davis Strait-Labrador Sea area and relationships with synoptic-scale atmospheric circulation *Arctic* 31(4): 434 – 447.
- Curry, J.A., and Ebert, E.E., 1992, Annual cycle of radiation fluxes over the Arctic Ocean: Sensitivity to cloud optical properties. *J. Clim.*, 5: 1267 – 1280.
- Deser, C., Tomas, R., Alexander, M., Lawrence, D. 2010. The seasonal atmospheric response to projected Arctic sea ice loss in the late twenty-first century. *J. Clim.* 23(2): 333 – 351.
- Dierer, S., Schlünzen, K.H., Birnbaum, G., Brümmer, B., Müller, G. 2005: Atmosphere-sea ice interactions during a cyclone passage investigated by using model simulations and measurements. *Monthly Weather Review* 133: 3678 – 3692
- Djuric, D., *Weather Analysis*, 1994, Prentice Hall, Upper Saddle River, N.J. 304pp. ISBN 0-13-501149-3.
- Drobot, S., Gearheard, S., Stroeve, J., Scambos, T., Serreze, M., Maslanik, J, Meier, W., Holland, M. (2008): Arctic sea ice extent plummets in 2007, *EOS Trans. AGU*, 89, 2, doi:10.1029/2008EO020001

- Eicken, H., Lensu, M., Lepparanta, M., Tucker III, W.B., Gow, A.J. and Salmela, O., 1995. Thickness, structure and properties of level summer multiyear ice in the Eurasian sector of the Arctic Ocean, *J. Geophys. Res.* 100 (C11), 22,697 – 22,710.
- Esau, I.N., 2007, Amplification of turbulent exchange over wide Arctic leads: Large-eddy simulation study *J. Geophys. Res.* 112, D08109, doi:10.1029/2006JD007225
- Francis, J. A. and E. Hunter: 2006, New insight into the Disappearing Arctic Sea Ice, *EOS Trans.*, AGU, 87(46), 509.
- Galley, R.J., E. Key, D.G. Barber, B.J. Hwang, and J.K. Ehn (2008), Spatial and temporal variability of sea ice in the southern Beaufort Sea and Amundsen Gulf: 1980 – 2004, *J. Geophys. Res.*, 113, C05S95, doi: 10.1029/2007JC004553, 2008.
- Glendening, 1995, Horizontally integrated atmospheric heat flux from an Arctic lead, *J. Geophys. Res.* 100 (C3): 4613 – 4620
- Graham, N.E., Diaz, H.F. 2001: Evidence for intensification of North Pacific winter cyclones since 1948. *Bull Amer. Met. Soc.* (?): 1869 – 1893
- Grenfell, T.C., and Perovich, D.C, 1984, Spectral albedos of sea ice and incident solar irradiance in the southern Beaufort Sea. *J. Geophys. Res.* 89(C3): 3573 – 3580.
- Guest, P.S., Glendening, J.W., and Davidson, K.L., 1995, An observation and numerical study of wind stress variations within marginal ice zones. *J. Geophys. Res.* 100(C6): 10887 – 10904.
- Hebbinghaus, H., Schlünzen, H., Dierer, S. 2007: Sensitivity studies on vortex development over a polynya, *Theor. Appl. Climatol.* 88: 1 – 16
- Heinemann, G., 1996. Satellite climatological aspects of cold air mesocyclones in the Arctic and Antarctic, *The Global Atmos. And Ocean Sys.* 4(2): 89 – 123.
- Hertzman, O. 1997: Oceans and the Coastal Zone. In Bailey, W.G., Oke, T.R., and Rouse, W.R. (Eds), *The Surface Climates of Canada*, pp. 107-123, McGill-Queens University Press, Montreal.
- Hibler, W.D., 1979. A dynamic thermodynamic sea ice model. *J. Phys. Ocean.*, 9: 815 – 846.
- Hibler, W.D., Roberts, A., Heil, P., Proshutinsky, Y., Simmons, H.L., and Lovick, J. 2006. Modelling M@ tidal variability in Arctic sea-ice drift and deformation, *Ann. Glaciol.*, 44: 418 – 428.
- Higgins, M.E., and Cassano, J.J. 2009. Impacts of reduced sea ice on winter Arctic atmospheric circulation, precipitation, and temperature, *J. Geophys. Res.*, 114, D16107, doi:10.1029/2009JD011884.

- Hudak, D.R., Young, J.M.C., 2002, Storm climatology of the Southern Beaufort Sea, *Atmosphere-Ocean*, 40 (2), 145 – 158.
- Hunkins, K. (1962), Waves on the Arctic Ocean, *J. Geophys. Res.*, 67, 2477– 2489.
- Johannessen, O. M., L. Bengtsson, M. W. Miles, S. I. Kuzmina, V. A. Semenov, G. V. Aledseev, A. P. Nagumyi, V. F. Zakharov, L. P. Bobylev, L. H. Pettersson, K. Hasselmann, and H. P. Cattle, 2004: Arctic climate change: observed and modelled temperature and sea-ice variability, *Tellus*, 56A, 328–341.
- Johnson, M.A., Proshutinsky, A.Y., Polyakov, I.V. 1999: Atmospheric patterns forcing two regimes of Arctic circulation: A return to anticyclonic conditions? *Geophys. Res. Lett.*, 26 (23): 1621 – 1624
- Kay, J.E., and Gettelman, A., 2009. Cloud influence on and response to seasonal Arctic sea ice loss, *J. Geophys. Res.*, 114, D18204, doi:10.1029/2009JD011773.
- Keegan, T.J. 1958: Arctic synoptic activity in winter. *J. Meteor.* 15: 513 – 521
- Kwok, R., G. F. Cunningham, M. Wensnahan, I. Rigor, H.J. Zwally, and D, Yi (2009), Thinning and volume loss of the Arctic Ocean sea ice cover: 2003 – 2008, *J. Geophys. Res.*, 114, C07005, doi:10.1029/2009JC005312.
- Lammert, A., Brümmer, B., Kaleschke, L., 2009. Observation of cyclone-induced inertial sea-ice oscillation in Fram Strait, *Geophys. Res. Lett.*, 36, L10503, doi:10.1029/2009GL03719.
- Langlois, A., Mundy, C.J., Barber, D.G., 2007. On the evolution of snow thermophysical properties over land-fast first-year sea ice, *Hydrol. Process.*, 21: 705 – 716.
- Langlois, A., Fisico, T., Barber, D.G., Papakyriakou, T.N. 2008. Response of snow thermophysical processes to the passage of a polar low-pressure system and its impact on in situ passive microwave radiometry: A case study, *J. Geophys. Res.*, 113, C03S04, doi:10.1029/2007JC004197.
- LeDrew, E.L., Johnson, D., Maslanik, J.A. 1991. An examination of atmospheric mechanisms that may be responsible for the annual reversal of the Beaufort Sea ice field. *Int. J. of Clim.* 11: 841 – 859.
- Lindsay, R.W., (1998), Temporal variability of the energy balance of thick Arctic pack ice. *J. Clim.*, 11:313 – 333.
- Liu, A. K., and E. Mollo-Christensen (1988), Wave propagation in a solid ice pack, *J. Phys. Oceanogr.*, 18, 1702–1712.

- Lukovich, J.V., Barber, D.G. 2006: Atmospheric controls on sea ice motion in the southern Beaufort Sea. *J. Geophys. Res.* 111: D18103, doi:10.1029/2005/JD006408, 2006.
- Lukovich, J.V., Barber, D.G. 2007: On the spatiotemporal behavior of sea ice concentration anomalies in the Northern Hemisphere. *J. Geophys. Res.* 112: D13117, doi:10.1029/2006/JD007836, 2007.
- Lupkes, C., and Birnbaum, G. 2005, Surface drag in the Arctic marginal sea-ice zone: a comparison of different parameterization concepts. *Boundary-Layer meteorology*, 117: 179 – 211.
- Lupkes, C., Vihma, T., Birnbaum, G, and Wacker, U. 2008, Influence of leads in sea ice on the temperature of the atmospheric boundary layer during polar night. *Geophys. Res. Lett.* 35, L03805.
- Mantua N.J., Hare, S.R., Zhang Y., Wallace, J.M., Francis, R.C. 1997. A Pacific interdecadal climate oscillation with impacts on salmon production. *Bulletin of the American Meteorological Society*, 78(6): 1069 – 1079.
- Maykut, G.A. 1978, Energy exchange over young sea ice in the Central Arctic. *J. Geophys. Res.* 83 (C7): 3646 – 3658.
- Maykut, G.A. (1982). Large-scale heat exchange and ice production in the central Arctic. *J. Geophys. Res.*, 87:7971 – 7984.
- Maykut, G.A. (1986), The surface heat and mass balance, in N. Untersteiner (Ed.), *The Geophysics of Sea Ice*, Plenum, New York, 395 – 464.
- Markus, T., Stroeve, J.C., and Miller, J. 2009, Recent changes in Arctic sea ice melt onset, freeze-up and melt season length, *J. Geophys. Res.* 114, C12024, doi: 10.1029/2009/JC005436.
- McCabe, G.J., Clark, M.P., Serreze, M.C. 2001: Trends in northern hemisphere surface cyclone frequency and intensity. *J. Clim.* 14: 2763 – 2768.
- McPhee, M. G., T. P. Stanton, J. H. Morison and D. G. Martinson, 1998: Freshening of the upper ocean in the Arctic: Is perennial sea ice disappearing? *Geophysical Research Letters*, 25(10): 1729-1732.
- McLaren, A.S., Serreze, M.C. and Barry, R.G. 1987. Seasonal variations of sea ice motion in the Canada Basin and their implications. *Geophys. Res. Lett.*, 14, 1123 – 1126.
- Melling, H., and Riedel, D.A. 1995, The underside topography of sea ice over the continental shelf of the Beaufort Sea in the winter of 1990; *J. Geophys. Res.*, 100, 13,641 – 13,653.

- Mellor, M., 1986, Mechanical behaviour of sea ice, in Untersteiner, N (ed.), *The geophysics of Sea ice*, Plenum, New York, 165 – 281.
- Morison, J., M. Steele, and R. Andersen (1998), Hydrography of the upper Arctic Ocean measured from the nuclear submarine U.S.S. Pargo, *Deep Sea Res.*, Part I, 45, 15– 38.
- Mucci, A., Forest, A., Fortier, L., Fukuchi, M., Grant, J., Hattori, H., Hill, P., Lintern, G., Makabe, R., Magen, C., Miller, L., Sampei, M., Sasaki, H., Sundby, B., Walker, T., Wassmann, P., 2008, Organic and Inorganic Fluxes In: Fortier, L., Barber, D., Michaud, J. (eds.) *On Thin Ice: A synthesis of the Canadian Arctic Shelf Exchange Study (CASES)*, pp 215. *Aboriginal Issues Press, Winnipeg ISBN 978-0-9738342-6-0*
- Oke, T.R., (1987). *Boundary layer climates. 2nd edition*, Routledge, London, 435pp.
- Ogi, M., Rigor, I.G., McPhee, M.G., Wallace, J.M. 2008, Summer retreat of Arctic sea ice: Role of summer winds, *Geophys. Res. Lett.* 35, L24701, doi: 10.1029/2008GL035672.
- Overland, J.E. (2009), Meteorology of the Beaufort Sea, *J. Geophys. Res.*, 114, C00A07, doi:10.1029/2008JC004861.
- Overland, J.E., McNutt S.L., Groves, J., Salo, S., Andreas, E.L., Persson, P.O.G., 2000, Regional sensible and radiative heat flux estimates for the winter Arctic during the Surface Heat Budget of the Arctic Ocean (SHEBA) experiment, *J. Geophysical Res.* 105: C6, 14,093 – 14,102.
- Parkinson, C. L., D. J. Cavalieri, P. Gloersen, H. J. Zwally, and J. C. Comiso, 1999: Arctic Sea ice extends, areas, and trends, 1978–1996. *J. Geophys. Res.*, 104 (C9), 20 837–20 856.
- Parkinson and Cavalieri, 2008. Arctic sea ice variability and trends, 1979-2006, *Journal of Geophysical Research - Oceans*, 113, C07003, doi:10.1029/2007JC004558
- Perovich, D.K., and Elder, B. (2002). Estimates of ocean heat flux at SHEBA. *Geophys. Res. Lett.*, 29(9), doi:10.1029/2001GL014171.
- Perovich, D.K., Richter-Menge, J.A., Jones, K.F., and Light, B. (2008). Sunlight, water, and ice: Extreme Arctic sea ice melt during the summer of 2007, *Geophys. Res. Lett.* 35, L11501, doi:10.1029/2008GL034007.
- Persson, P.O.G., Fairall, C.W., Andreas, E.L., Guest, P.S., Perovich, D.K., (2002), Measurements near the atmospheric surface flux group tower at SHEBA: Near-surface conditions and surface energy budget, *J. Geophys. Res.*, 107 (C10), doi:10.1029/2000JC000705.

- Pickart, R. S., Moore, G. W. K., Torres, D.J., Fratantoni, P.S., Goldsmith, R.A., and Yang, J. 2009, Upwelling on the continental slope of the Alaskan Beaufort Sea: Storms, ice, and oceanographic response, *J. Geophys. Res.*, 114, C00A13, doi:10.1029/2008JC005009.
- Pidwirny, M. 2006. Chapter 7: Introduction to the atmosphere - Global Heat Balance: Introduction to Heat Fluxes. *Fundamentals of Physical Geography, 2nd Edition*.
- Pinto, J.O., Alam, A., Maslanik, J.A., Curry, J.A., 2003. Surface characteristics and atmospheric footprint of springtime Arctic leads at SHEBA, *J. Geophysical Res.* 108: C4, 8051, doi:10.1029/2000JC000473, 2003.
- Polyakov, I.V., Proshutinsky, A.Y., Johnson, M.A., 1999, Seasonal cycles in two regimes of Arctic Climate, *J. Geophys. Res.* 104: C11: 25,76- 25,788.
- Polyakov, I., A. Beszczynska, E. Carmack, I. Dmitrenko, E. Fahrbach, I. Frolov, R. Gerdes, E. Hansen, J. Holfort, V. Ivanov, M. Johnson, M. Karcher, F. Kauker, J. Morison, K. Orvik, U. Schauer, H. Simmons, Ø. Skagseth, V. Sokolov, M. Steell, L. Timokhov, D. Walsh, and J. Walsh, (2005), One more step toward a warmer Arctic, *Geophys. Res. Lett.*, 32, L17605, doi: 10.1029/2005GL023740.
- Proshutinsky, A.Y. and Johnson, M.A. 1997: Two circulation regimes of the wind-driven Arctic Ocean, *J. Geophys. Res.* 102 (C6): 12,493 – 12,514
- Quadfasel, D. A., A. Sy, D. Wells, and A. Tunik, Warming in the Arctic, *Nature*, 350, 385, 1991.
- Rainville, L., and Woodgate, R.A. (2009). Observations of internal wave generation in the seasonally ice free Arctic. *Geophys. Res. Lett.*, 36, L23604, doi:10.1029/2009GL041291.
- Rigor, I. G., R. L. Colony, and S. Martin, 2000: Variations in surface air observations in the Arctic, 1979–1997, *J. Climate*, 13, 896–914.
- Rigor, I.G., Wallace, J.M., Colony, R.L., 2002. On the response of sea ice to the Arctic Oscillation, *J. Clim.* 15:2648 – 2663.
- Rinke, A., Maslowski, W., Dethloff, K., Clement, J. 2006: Influence of sea ice on the atmosphere: A study with an Arctic atmospheric regional climate model. *J. Geophysical Res.* 111, D16103, doi: 10.1029/2005JD006957, 2006
- Roebber, P.J. 1989: The role of surface heat and moisture fluxes associated with large-scale ocean current meanders in maritime cyclogenesis, *Monthly Weather Review* 117: 1676 – 1694
- Rothrock, D.A. and Thorndike, A.S. 1984. Measuring the sea ice floe distribution, *J. Geophys. Res.* 89 (C4): 6477 – 6486.

- Rothrock, D.A., Yu., Y. Maykut, G.A. 1999. Thinning of the Arctic sea-ice cover. *Geophys. Res. Lett.*, 23: 3469 – 3472
- Ruffieux, D., Persson, P.O.G., Farall, C., and Wolfe, D.E. 1995, Ice pack and lead surface energy budgets during LEADDEX 1992, *J. Geophys. Res.*, 100(C3): 4593 – 4612.
- Schauer, U., E. Fahrbach, S. Osterhus, and G. Rohardt (2004), Arctic warming through the Fram Strait: Oceanic heat transport from 3 years of measurements, *J. Geophys. Res.*, 109, C06026, doi: 10.1029/2003JC001823.
- Schweiger, A.J., Lindsay, R.W., Vavrus, S., and Francis, J.A. (2008a). Relationships between Arctic sea ice and clouds during autumn, *J. Clim.* 21, 4799 – 4810, doi:10.1175/2008JCLI2156.1.
- Schweiger, A.J., Zhang, J., Lindsay, R.W., and Steele, M. (2008b). Did unusually sunny skies help drive the record sea ice minimum of 2007? *Geophys. Res. Lett.* 35, L10503, doi:10.1029/2008GL033463.
- Serreze, M.C., and Bradley, M.C. 1987, Radiation and cloud observations on a high plateau ice camp. *J. Glaciology*, 33(11): 162 – 168.
- Serreze, M.C., Walsh, J.E., Chapin III, F.S., Osterkamp, T., Dyurgerov, M., Romanovsky, V., Oechel, W.C., Morison, J., Zhang, T., Barry, R.G. 2000: Observational evidence of recent change in the northern high-latitude environment. *Climatic Change* 46: 159 – 207.
- Serreze, M.C., Carse, F. Barry, R.G., Rogers, J.C., 1997: Icelandic Low cyclonic activity: Climatological features, linkages with the NAO, and relationships with recent changes in the Northern Hemisphere Circulation. *Bull. Amer. Meteor. Soc.* 10: 453 – 464.
- Serreze, M.C., 1995, Climatological Aspects of Cyclone Development and Decay in the Arctic. *Atmos. Ocean.* 33 (1): 1 – 23.
- Serreze, M.C., Box, J.E., Barry, R.G., Walsh, J.E., 1993: Characteristics of Arctic synoptic activity, 1952 – 1989. *Meteorol. Atmos. Phys.*, 51: 147 – 164.
- Serreze, M.C., Barry, R.G. 1988: Synoptic activity in the Arctic basin. 1979-85, *J. Clim.* 1: 1276 – 1295.
- Serreze, M.C., Barry, R.G. 2005, *The Arctic Climate System*, Cambridge University Press, Cambridge, pp 385.
- Serreze, M.C. Maslanik, J.A., Rehder, M.C., and Schnell, R.C. 1992, Theoretical heights of buoyant convection above open leads in the winter Arctic pack ice cover. *J. Geophys. Res.*, 97(C6): 9411 – 9422.

- Simmonds, I., Burke, C., and Keay, K., 2008, Arctic climate change manifest as cyclone behavior, *J. Clim.* 21:5777 – 5796.
- Simmonds, I., and Keay, K. (2009), extraordinary September Arctic sea ice reductions and their relationships with storm behavior over 1979 – 2008, *Geophys. Res. Lett.*, 36, L19715, doi:10.1029/2009GL039810.
- Smith, S.D., Anderson, R.J., Hartog, G.D., Topham, D.R., Perkin, R.G., 1983, An investigation of a polynya in the Canadian Archipelago 2, Structure of turbulence and sensible heat flux, *J. Geophys. Res.* 88 C5 2900 – 2910.
- Smith, S.D., Muench, R.D., Pease, C.H., 1990, Polynyas and leads: An overview of physical processes and environment, *J. Geophysical Res.* 95, C6, 9461 – 9479
- Sorteberg A., and Walsh, J.E. 2008. Seasonal cyclone variability at 70°N and its impact on moisture transport into the Arctic. *Tellus* 60A, 570 – 586.
- Squire, V.A., Vaughan, G.L., Bennetts, L.G. 2009. Ocean surface wave evolution in the Arctic basin. *Geophys. Res. Lett.*, 36, L22502, doi:10.1029/2009GL040676.
- Steele, M., and T. Boyd (1998), Retreat of the cold halocline layer in the Arctic Ocean, *J. Geophys. Res.*, 103, 10,419– 10,435.
- Steer, A., Worby, A., Heil, P. 2008. Observed changes in sea-ice floe distribution during early summer in the Western Weddell Sea. *Deep-Sea Research II* (2008), 933 – 942.
- Steffen, K., and Ohmura, A., 1985, Heat exchange and surface conditions in North Water, Northern Baffin Bay, *Annals of Glaciology*, 6, 178 – 181.
- Stroeve, J. C., M. C. Serreze, F. Fetterer, T. Arbetter, W. Meier, J. Maslanik, and K. Knowles, 2005. Tracking the Arctic's shrinking ice cover: Another extreme September minimum in 2004, *Geophys. Res. Lett.*, 32, L04501, doi: 10.1029/2004GL021810.
- Stroeve, J., Markus, T., W. N. Meier, W.N., and Miller, J. 2006. Recent changes in the Arctic melt season. *Annals of Glaciology* 44(1): 367 – 374.
- Stroeve, J., M. M. Holland, W. Meier, T. Scambos, and M. Serreze, 2007: Arctic sea ice decline: Faster than forecast, *Geophys. Res. Lett.*, 34, L09501, doi:10.1029/2007GL029703.
- Stull, R. 2000. *Meteorology for Scientists and Engineers* 2nd edition, Brooks-Cole Thomson Learning.

- Swift, J. H., E. P. Jones, K. Aagaard, E. C. Carmack, M. Hingston, R. W. MacDonald, F. A. McLaughlin, and R. G. Perkin (1997), Waters of the Makarov and Canada basins, *Deep Sea Res.*, Part II, 44, 1503– 1529.
- Szeto, K.K., Stewart, R.E. Hanesiak, J.H. 1997. High-latitude cold season frontal cloud systems and their precipitation efficiency, *Tellus*, 49A, 439 – 454
- Thompson, D.W., and Wallace, J.M. 1998: The Arctic Oscillation signature in the wintertime and geopotential height and temperature fields. *Geophys. Res. Lett.*, 25: 1297 – 1300
- Thorndike, A.S., Rothrock, D.A., Maykut, G.A., and Colony, R., 1975, The thickness distribution of sea ice. *J. Geophys. Res.*, 80(33): 4501 – 4513.
- Timco, G.W. and M.E. Johnston, 2002. Sea ice strength during the melt season. *Ice in the environment: Proceedings of the 16th LAHR International symposium on ice*, Dunedin, New Zealand, 2-6 December.
- Tison, J.L., Worby, A.P., Delille, B., Brabant, F., Papadimitriou, S., Thomas, D., de Jong, J., Lannuzel, D., Haas, C., 2008, Temporal evolution of decaying summer first-year sea ice in the western Weddell Sea, Antarctica, *Deep-Sea Research II* (55), doi:10.1016/j.jdsr.2007.12.021).
- Toyota, T., S. Takatsuji, and M. Nakayama (2006), Characteristics of sea ice floe size distribution in the seasonal ice zone, *Geophys. Res. Lett.*, 33, L02616, doi:10.1029/2005GL024556.
- Trenberth, K.E. 1990: Recent observed interdecadal climate changes in the Northern Hemisphere, *Bull. Amer. Meteor. Soc.*, 71, 988 – 993.
- Wadhams, P., 1973. Attenuation of Swell by Sea Ice, *J. Geophys. Res.* 78 (18): 3552 – 3563.
- Wadhams, P., A. E. Gill, and P. F. Linden (1979), Transects by submarine of the East Greenland Polar Front, *Deep Sea Res.*, Ser. A, 26, 1311 –1327.
- Wadhams, P., V. A. Squire, D. J. Goodman, A. M. Cowan, and S. C. Moore (1988), The attenuation of ocean waves in the marginal ice zone, *J. Geophys. Res.*, 93, 6799– 6818.
- Wadhams, P. 2000, *Ice in the ocean*. Gordon and Breach Science Publishers, London.
- Wadhams, P., and M. J. Doble, 2009, Sea ice thickness measurement using episodic infragravity waves from distant storms, *Cold Reg. Sci. Technol.*, 56, 98– 101.
- Walker G.T., 1923: Correlation in seasonal variations of weather VIII: A preliminary study of world weather. *Mem. Ind. Meteor. Soc.*, 103: 29 – 64

- Walkington, I.A., Willmott, A.J. 2006, A coupled polynya-atmospheric boundary layer model, *Jour. Phys. Oceano.* 36, 897 – 913.
- Walsh, J.E., Chapman, W.L., Shy, T.L. 1996: Recent decrease of sea level pressure in the central Arctic. *J. Clim.*9: 480 – 486
- Wang, X. J. and J. R. Key, 2003: Recent trends in Arctic surface, cloud, and radiation properties from space. *Science*, 299, 1725–1728.
- Wang, X. J. and J. R. Key, 2005: Arctic surface, cloud, and radiation properties based on the AVHRR Polar Pathfinder dataset. Part II: Recent Trend. *J. Climate*, 18, 2558– 2574.
- Warren S.G., Rigor, I.G., Untersteiner, N., Radionov, V.F., Bryazgin, N.N., Aleksandrov, Y.I., R. Colony (1999), Snow depth on Arctic sea ice. *J. Clim.*, 12 1814 – 1829.
- Weeks, W.F., and Ackley, S.F. 1986, The growth, structure, and properties of sea ice in N. Understeiner, (ed.), *The Geophysics of Sea Ice*, Plenum, New York, 9 –64.
- Wettlaufer, J.S. (1991). Heat flux at the ice-ocean surface. *J. Geophys. Res.*, 96(C4):7215 – 7236.
- Woodgate, R. A., K. Aagaard, and T. J. Weingartner, 2006: Interannual changes in the Bering Strait fluxes of volume, heat and freshwater between 1991 and 2004, *Geophysical Research Letters*, 33, L15609, doi: 10.1029/2006GL026931.
- World Meteorological Organization (WMO), 1970, Part 1 Ice terms arranged by subject, In *WMO Sea ice nomenclature*, WMO rep. #259, T.P.145, 6pp, Geneva.
- Yu, Y., Maykut, G.A., Rothrock, D.A. 2004: Changes in the thickness distribution of Arctic sea ice between 1958-1970 and 1993-1997, *J. Geophysical Res.* 109, C08004, doi:10.1029/2003JC001982, 2004.
- Zhang, X. Ikeda, M., Walsh, J.E. 2003: Coordinated changes of sea ice over the Beaufort and Chukchi Seas: regional and seasonal perspectives. *Polar Res.* 22(1): 83 – 90.
- Zhang, X. Walsh, J.E. Zhang, J., Bhatt, U.S., Ikeda, M., 2004: Climatology and interannual variability of Arctic cyclone activity. *J. Clim.* 17, 2300 – 2317, doi: 10.1175/1520-0442(2004).

CHAPTER THREE: ATMOSPHERIC FORCING OF THE BEAUFORT SEA ICE GYRE: PART 1: SURFACE PRESSURE CLIMATOLOGY AND SEA ICE MOTION

Asplin, M. G., J. V. Lukovich, and D. G. Barber (2009), Atmospheric forcing of the Beaufort Sea ice gyre: Surface pressure climatology and sea ice motion, *J. Geophys. Res.*, *114*, C00A06, doi:10.1029/2008JC005127.

3.1 Introduction

The Beaufort gyre (BG) is a large ocean circulation feature that plays a significant role in regulating variability in the climate of the Arctic [McLaren *et al.*, 1987; Serreze *et al.*, 1989; LeDrew *et al.*, 1991; Proshutinsky *et al.*, 2002]. The circulation of the BG is strongly driven by synoptic-scale atmospheric circulation variability, arising from cyclones and anticyclones, and generally follows an anticyclonic (clockwise) rotational regime that promotes sea ice convergence and higher ice concentrations (increased ice ridging) via Ekman convergence [Proshutinsky *et al.*, 2002]. During the summer, the BG can occasionally reverse to a cyclonic (counterclockwise) circulation pattern. Reversals of the BG are attributed to lower SLP throughout the Arctic basin, and persistent low-pressure systems occurring over the southern Beaufort Sea [McLaren *et al.*, 1987; Serreze *et al.*, 1989, LeDrew *et al.*, 1991]. Lukovich and Barber [2006] also identify a time-lagged response between stratospheric and upper-level tropospheric relative vorticity and reversals of the BG.

The nature of the control that the BG has upon sea ice motion and sea ice concentration depends upon the sea ice extent, the circulation regime of the gyre, and the magnitude of the vorticity within the gyre itself [Barry and Maslanik, 1989; Lukovich and Barber, 2006]. Sea ice velocity and vorticity values within the gyre are generally the weakest during April, when Arctic sea ice is at its maximum extent and highest

concentrations, and the greatest during the summer (August and September) when ice extent and concentrations are at their annual minimum. A predominantly anti-cyclonic BG tends to transport sea ice into the Canadian Archipelago, and westward into the Chukchi Sea [*Kwok et al.*, 2006; *Lukovich and Barber*, 2006]. The amount of sea ice being exported through Fram Strait has also been linked to the rotational regime of the BG. During the cyclonic rotation of the BG, northerly transport of sea ice from the Chukchi and southern Beaufort Seas increases sea ice concentrations within the transpolar drift, hence increasing the volume of ice that is exported through Fram Strait [*Yu et al.*, 2004; *Lukovich and Barber*, 2006].

Changing circulation characteristics within the BG may be enhancing anthropogenic forcing of sea ice thermodynamics [*Zhang et al.*, 2000; *Stroeve, et al.*, 2007]. The work of *Yu et al.*, [2004] reveals that buoy motions during the 1990s show a smaller, weaker BG and somewhat greater transport of ice toward the Canadian Archipelago, but they did not find evidence of an ice build-up to account for the loss of ice volume observed in the central basin.

Sea ice dynamics in the Arctic can also be impacted by cyclones. An area of reduced ice concentration in the Canada basin in August 1981 was linked to westerly winds associated with a persistent cyclone situated to the NE [*Barry and Maslanik*, 1989]. Furthermore, a cyclone can fracture the underlying sea ice and create conditions favorable for local-scale ice divergence during and immediately following the passage of the cyclone [*Brummer et al.*, 2003]. This may introduce coupling between the ocean-sea ice-atmosphere system where increased upward energy and moisture fluxes from the ocean may lead to the intensification of cyclones. This process would be most prevalent

during the autumn and early winter seasons when there is a rapidly increasing temperature difference between the ocean and atmosphere, and when thin first-year ice can easily be fractured by strong winds associated with cyclones. Flux-driven intensification of cyclones may increase if sea ice concentration and extent continues to decline.

Cyclone activity in the Arctic (north of 65°N) peaks during the summer and is at a minimum during the winter and spring when anticyclonic conditions dominate [Serreze and Barry, 1988; Serreze *et al.*, 1993; McCabe *et al.*, 2001]. Cyclonic activity in the Arctic is twice that of anticyclonic activity during the summer months [Keegan, 1958; Serreze, 1995; Zhang *et al.*, 2004]. Summer cyclones and anticyclones exhibit little regional variability in mean central pressure and are typically 5-10mb weaker than their winter counterparts [Serreze *et al.*, 1993]. Increases in the frequency and intensity of cyclones during the winter, spring and autumn in the Arctic, since the 1960's, are commonly linked to a shift in the average SLP pattern over the Arctic basin, which is attributed to the Arctic Oscillation (AO) [Thompson and Wallace, 1998] and Northern Atlantic Oscillation (NAO) [Serreze, 1995; Serreze *et al.*, 2000; Zhang *et al.*, 2004]. The negative phase of the AO is characterized by a relatively high SLP over the Arctic basin and low SLP at midlatitudes, whereas the positive phase is characterized by a SLP low over the Arctic basin, and SLP high at midlatitudes. McCabe *et al.*, [2001] also suggests that cyclone frequencies oscillate with the state of the AO, but cannot objectively determine whether changes in summer cyclone intensity are due to greenhouse gas influences or other long-term climate trends.

There is considerable interannual variability in cyclone tracks, especially over the Canada basin [Serreze and Barry, 1988]. Mean cyclone tracks from 1979-1989 show that winter cyclones most frequently enter the Arctic from the Barents and Norwegian Seas [Serreze et al., 1993]. Cyclones can also enter from the Pacific Ocean, however, they fill rapidly over Alaska, and those that do reach the Arctic Ocean are much less intense [Keegan, 1958]. Summer Arctic cyclones can form within the Arctic basin, primarily over Siberia and the Canadian Archipelago. A summer cyclone maximum over the Arctic basin represents a significant area of cyclosis resulting from the movement and subsequent decay of cyclones into the region [Serreze, 1995]. Recent studies of cyclone variability in the Arctic from 1949 - 2002 (Sorteberg and Walsh [2008]) have shown that cyclones generated along the coast of Alaska travel into the East Siberian Sea via the Beaufort Sea during winter; during summer a convergence of cyclones is observed in keeping with earlier studies by Serreze and Barry [1988] demonstrating the establishment of a minimum in SLP and accompanying BG reversal during summer.

In this study, we examine the relationship between atmospheric circulation and the surface environment in the southern Beaufort Sea region (SBSR) by constructing a synoptic climatology consisting of a finite number of atmospheric circulation types [Yarnal, 1993; Barry and Parry, 2001]. In particular, we propose to develop an understanding of the nature of synoptic weather patterns that precede reversals of the BG by developing a synoptic climatology specific to the SBSR. The value of this approach lies in its ability to provide an interpretation of spatial variability in SLP (and in the Beaufort High in particular), based on a set of spatially-distinct circulation patterns, which may account for variability in the Beaufort Gyre. This study will focus upon the

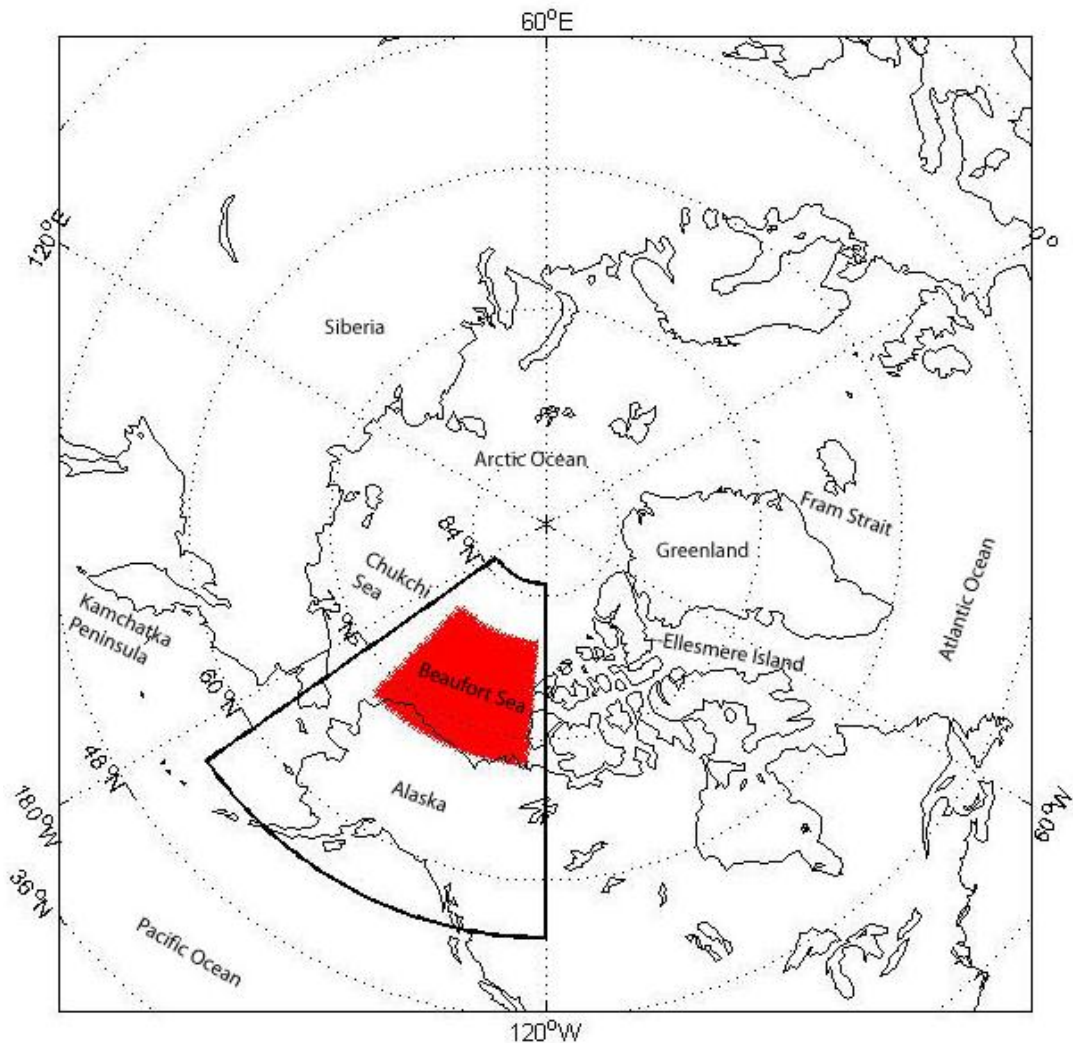
circulation characteristics of the synoptic weather patterns, and investigate how late spring and summer synoptic weather patterns are linked to BG reversal events. More specifically we address the following interrelated research questions:

- 1) What are the statistically separable types of synoptic-scale sea level pressure patterns over the period 1979 - 2006 in the SBSR? (Synoptic climatology)
- 2) How do these synoptic types vary temporally? (Synoptic type variability)
- 3) Is there a statistical relationship between the synoptic climatology of the SBSR and the Arctic Oscillation? (Synoptic types and the AO)
- 4) Is there a statistically significant relationship between synoptic types and reversals of the BG? (Synoptic types and BG reversals)
- 5) Is there statistically significant seasonal variability in how BG vorticity responds to the synoptic types? (Within-type variability of BG vorticity)

3.2 Methods

Data encompassing the period 1979-2006 are exploited in this study. Daily gridded mean sea-level pressure data (MSLP) were retrieved from archives maintained by the NOAA-CIRES Climate Diagnostics Centre (CDC) which originate from the National Center for Environmental Prediction (NCEP) Reanalysis I Project [Kalnay *et al.*, 1996]. The spatial resolution of these data is a $2.5^\circ \times 2.5^\circ$ (latitude and longitude) grid, encompassing the Beaufort and Chukchi Sea regions. The boundaries for the synoptic typing exercise (Figure 3.1) were 55°N , 175°W to 85°N , 120°W , and were selected to capture the Aleutian low and synoptic scale meteorological features originating over Eurasia, and the North Pacific as these may influence circulation of the BG. This area also includes the Canadian-led Canadian Arctic Shelf Exchange Study (CASES), ArcticNet, and most recent IPY Canadian-led Circumpolar Flaw Lead (CFL) study regions. Monthly AO climate index data were retrieved from the Department of Atmospheric Science, Colorado State University [Thompson and Wallace, 2000].

Figure 3.1. Synoptic typing boundaries (solid line) and sea ice vorticity study area (red).



Sea ice motion data were obtained from the National Snow and Ice Data Center (NSIDC) (There are missing data in 2004, weeks 46 – 52). Weekly averages were calculated from a combination of data from the Special Sensor Microwave/Imager (SSM/I), Scanning Multi-channel Microwave Radiometer (SMMR) Advanced Very High Resolution Radiometer (AVHRR), and the International Arctic Buoy Program (IABP) buoy data following *Fowler* [2003]. Weekly averages were calculated and then used to compute average weekly vorticity values using finite differencing (see *Lukovich and*

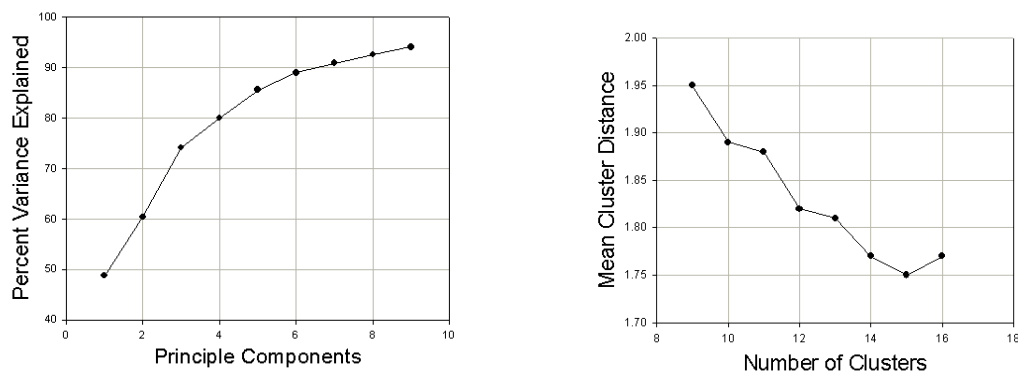
Barber [2006]). The vorticity values were then spatially averaged to provide an average measure of rotation within the BG. The spatial extent of the sea ice vorticity calculation is from 125°W to 165°W longitude and 70°N to 80°N latitude (Figure 3.1) to include the Beaufort Gyre and in keeping with previous studies of temporal BG variability [*Lukovich and Barber, 2006*], and is situated within the limits of the synoptic weather typing exercise. This area is smaller than that used for the synoptic typing exercise so that atmospheric circulation characteristics immediately surrounding the ice vorticity area are considered.

Synoptic-scale atmospheric circulation patterns, hereafter termed ‘synoptic types’, are classified from daily MSLP data, and then related to sea ice vorticity within the SBSR. The synoptic types are derived using Synoptic Typer 2.2, an application developed by the Australian Bureau of Meteorology [*Dahni and Ebert, 1998; Dahni, 2003*]. Synoptic Typer 2.2 applies a commonly used pattern recognition scheme comprised of principal components analysis (PCA) and a subsequent k-means cluster analysis. The user interface of the program allows the researcher to specify temporal and geographical parameters, and more importantly, permits the researcher to easily compare output from schemes using different principal component score and cluster counts.

Daily grids of MSLP data from 1979 to 2006 (9862 days) were processed using Synoptic Typer 2.2. The grids were not standardized (the seasonal effects are retained) because one purpose of the study, among others, is to contrast circulation type characteristics by season. The typing algorithm determines the eigenvalues for the daily MSLP grids from the correlation matrix with no rotation applied. The first six eigenvectors explain 89% of the variability and were retained (Figure 3.2a). K-means

cluster analyses were then performed on the component scores of the retained eigenvectors for 9 to 16 clusters. Cluster distance is the dimensionless difference between a sample (daily calculated component scores) and a cluster centroid. The sample is then assigned to the cluster for which the shortest distance to the cluster centroid is calculated. The mean of the cluster distances within each type represents the cluster homogeneity. Possible cluster-count selections of 10, 12 and 15 are determined by the presence of inflection points in the cluster distance curve (Figure 3.2b). The cluster distance decreases (increases) as greater (smaller) cluster counts are employed and provides a measure of how closely the actual circulation for each day matches its assigned synoptic type (Table 3.1). For our study, a 12-cluster solution was chosen as the optimal number based on the inflection point for average cluster homogeneity and the representation of the major synoptic circulation situations in the region.

Figure 3.2. a) Cumulative variance explained by each PC, and b) average cluster distance, which represents average homogeneity within the clusters.



The output from the clustering algorithm identifies a specific synoptic type for each day of the study period (Figure 3.3). The representative mean circulation pattern can be visualized with MSLP composites that are created by averaging the gridded MSLP

data of all days within each synoptic type. Mean frequency, duration and transition statistics were calculated for the synoptic types, and provide insight into the composition of the synoptic weather patterns of the SBSR (Table 3.2). Mean monthly occurrence frequencies were then used to show the cumulative frequencies of the types as they occur throughout the annual cycle (Figure 3.4a).

Given that our interest lies in the summer cyclone season, due to a predominance of cyclone activity in the Arctic during summer months, we investigated the nature of summer atmospheric circulation patterns upon the circulation within the BG. In addition, we extended the summer into late spring by including the month of May for a ‘spring-summer’ season comprised of May, June, July, August, September and October (MJJASO). By including May, our analysis included any preconditioning within the Beaufort Sea ice gyre that may have arisen from late spring atmospheric circulation patterns. September and October were included to capture the minimum annual sea ice extent and the associated increase in sea ice mobility.

The average annual synoptic type percent occurrence frequencies are contrasted against those calculated within the MJJASO and NDJFMA seasons (Figure 3.4b). Decadal large-scale atmospheric circulation variability arising from the AO may affect synoptic type frequencies, was investigated using Chi-square analysis. The synoptic type frequencies were grouped by the corresponding value of the AO index, and then tested against the mean frequency for each synoptic type for the entire study period. The mean synoptic type frequencies were computed for the positive and negative modes of the AO, and are contrasted against the mean synoptic type frequencies for the study period to create relative frequency anomalies (figure 3.6).

An algorithm that combines synoptic type frequency and duration was derived to upscale daily synoptic types to weekly so that we may approximate how each synoptic type influences the circulation of the BG (figure 3.5). The data were divided into seven-day periods, effectively creating a weekly interval to which we linked atmospheric influences on sea ice motion. If a particular synoptic type occurred or persisted for a set threshold within each period, then that synoptic type was assigned to that week to represent the dominant atmospheric circulation influence on sea ice motion. In cases where no particular synoptic type dominates, that week was assigned a null classification. We selected a weekly frequency threshold of three days, and successfully classified 1185 weeks out of 1456 (81.4%) in the study period. Since 52 weeks comprises of 364 days, December 31st is dropped from each regular year, and December 30th / 31st were dropped during leap years.

Changes in sea ice motion are known to lag changes in atmospheric forcing at various temporal scales [Lukovich and Barber, 2006], and it is therefore prudent to investigate the relationship between the synoptic climatology of the SBSR and BG vorticity at several different temporal scales. We calculated spatially averaged BG vorticity values for running average periods of two, four, six, eight, ten, and twelve weeks. The frequencies of the synoptic types within each of the running average time periods were then correlated to the resulting average BG vorticity. Lag correlations were calculated with BG vorticity lagging the synoptic type frequencies by up to 24-weeks, where zero lag indicates a simultaneous relationship in BG vorticity to a particular synoptic type.

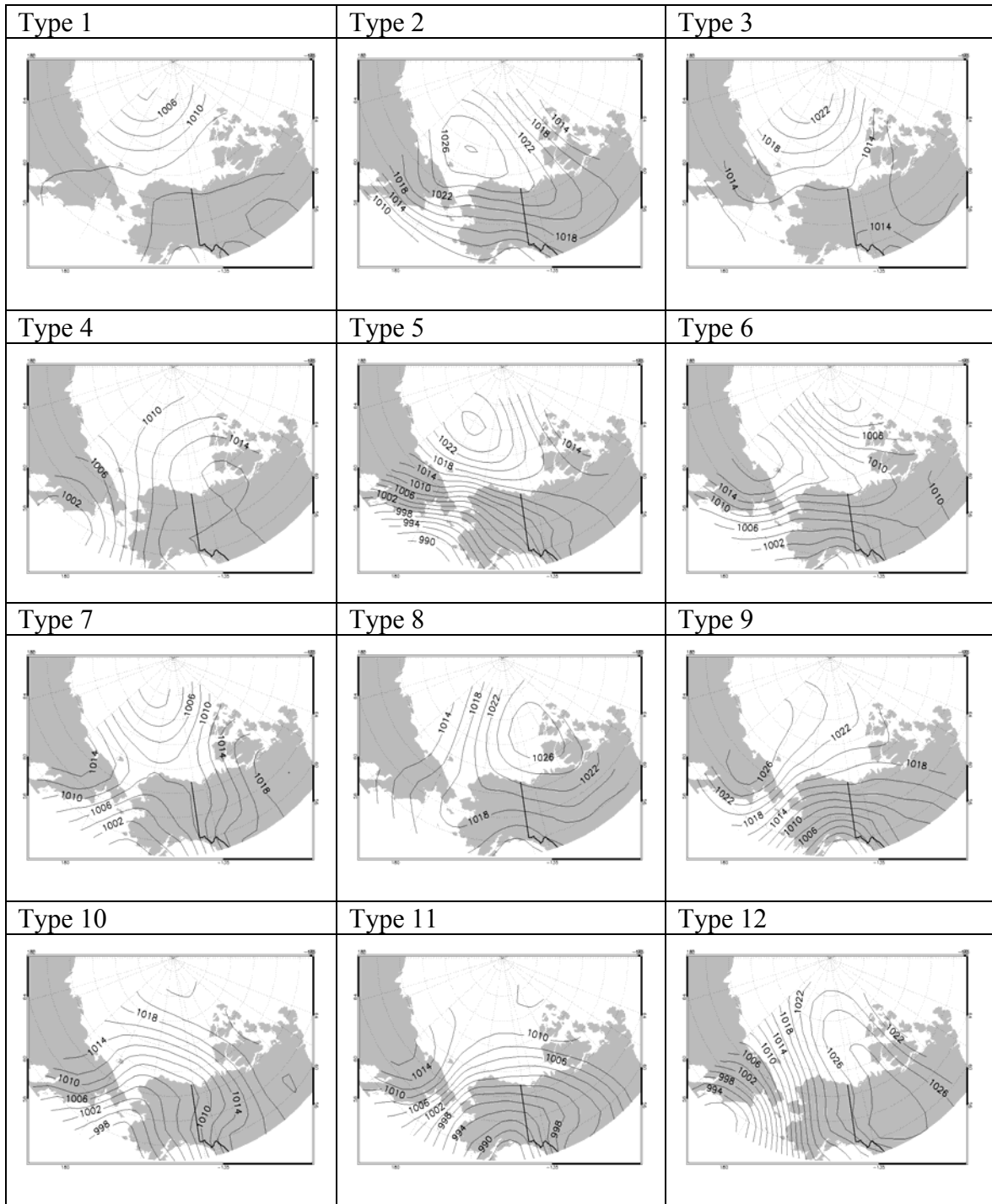
Seasonal within-type variability of BG vorticity was assessed for positive and negative BG vorticity regimes using a Kolmogorov-Smirnov (K-S) test. The K-S test is a non-parametric, distribution-free statistical test that is useful for time series data that may contain serial correlation. The positive (negative) vorticity regimes were first defined as weeks where the average weekly sea ice vorticity was greater than (less than) the threshold of $8.23 \times 10^{-6} \text{ s}^{-2}$. The threshold chosen reflects the first standard deviation of the average annual sea ice vorticity values, and values failing to meet the threshold were dropped. Vorticity generation is defined as a positive or negative change in weekly average sea ice vorticity, from one week to the next, and is hereafter referred to as ‘ Δ vorticity.’ We interpolated daily sea ice vorticity generation values and then linked them to the daily synoptic types. We then applied the K-S test to compare the distributions of vorticity generation data between the positive and negative vorticity regimes for within the NDJFMA and MJJASO seasons.

3.3 Results

3.3.1 Synoptic Climatology

The synoptic classification yielded 12 synoptic types for the SBSR. The synoptic types are visualized using MSLP composites (Figure 3.3). The Beaufort high, a prominent semi-permanent ridge of high pressure that is situated over the SBSR for much of year, is represented within seven of the twelve synoptic types (Types 2, 3, 5, 8, 9, 10 and 12), which exhibit a range of anticyclonic atmospheric circulation patterns. The key difference between these seven synoptic types is the intensity and direction of the geostrophic wind over the SBSR, which is discernable by the varying isobar patterns. The mean centre of the Beaufort high varies between synoptic types, appearing over the SBSR in types 2 and 5, Northern Canada in types 8 and 12, over the Canada basin in type 3, and over eastern Siberia in types 6 and 9. In addition, a smaller mean high pressure system also exists over eastern Siberia in types 6, 7 and 11. Types 2 and 5 both represent a well-developed Beaufort high centered over the SBSR (Figure 3.3), and therefore portray the anticyclone atmospheric circulation regime that persists throughout the cold season. The strong northerly and northwesterly flows of types 2 and 5 over the SBSR likely contribute to the normal anti-cyclonic rotation of the BG; however type 5 shows a well-developed Aleutian low over the North Pacific which may also impact the circulation of the BG.

Figure 3.3. MSLP (mb) composites for the 12 synoptic types.



Types 10 and 11 show easterly and southeasterly flow patterns over the SBSR, and likely contribute to normal anticyclonic rotation within the BG, and westward ice transport from the SBSR respectively. Type 12 also depicts a deep Aleutian low, but with a southerly flow persisting over the SBSR. This provides strong wind-driven support for anticyclonic rotation in the BG by enhancing the western half of the BG, and thus may increase strain and stress in the sea ice throughout the rest of the SBSR. Prolonged occurrences of type 12 may account for significant moisture and temperature advection into the Arctic basin that may influence sea ice thermodynamics directly through temperature advection, or indirectly through additional precipitation. The weak pressure gradients of the Beaufort high in type 3 show a weakened northeasterly synoptic flow over the SBSR (Figure 3.3). Type 4 shows a center of mean low-pressure situated to the east of the Kamchatka Peninsula, and may represent Pacific storms that track into the Arctic basin. Type 4 also shows a large, weak area of high pressure centered over northern Canada.

The well-developed mean low-pressure features depicted in the synoptic types 1, 6 and 7 represent Arctic cyclones and polar lows. The mean centers of the lows for types 1 and 7 are located over the northern Chukchi Sea, and approximately 200km west of Ellesmere Island for type 6. The mean pressure gradient of type 1 is weaker than that found in types 6 and 7, which corresponds to weaker cyclones in the summer than during the winter [Zhang *et al.*, 2004]. Types 1 and 7 produce southerly and southwesterly flows, and type 6 yields a northwesterly flow. The origin of cyclones represented by these types is not clearly identifiable from the MSLP composites; however, the location of the mean low pressure in type 6 suggests that it represents cyclones that have tracked

into the Arctic basin from the North Atlantic Ocean. Types 1 and 7 may better represent storms tracking in from the North Pacific, or from Eurasia.

There is likely a considerable amount of spatial variability within the synoptic weather classifications, as the illustrations of each synoptic type presented in figure 3.3 are merely averages of the gridded daily MSLP within each synoptic type. The spatial variability is lost in the classification and cannot readily be quantified; however, variability in the temporal characteristics of the synoptic types is of great interest.

3.3.2 Temporal Variability of Synoptic Patterns

The synoptic climatology of the SBSR is represented by the pattern in which the synoptic types occur throughout the seasons, and interannual variability is depicted by the frequencies of the synoptic types. The mean frequency, persistence and duration values are presented in table 3.1 for the entire annual cycle and in table 3.2 for NDJFMA and MJJASO for each of the synoptic types. The frequencies of some of the synoptic types are highly dependent on season. Some have summer or winter maximum occurrences, and others are year-round types. The seasonal nature of the frequencies of each synoptic type was assessed by calculating occurrence frequency statistics (Figures 3.4a and 3.4b).

Table 3.1. Cluster/circulation type characteristics for 1979 – 2006.

Synoptic Type	Cluster homogeneity (distance)	Frequency (% occurrence of type)	Persistence[% of time same type follows]	Duration [days]	
		Annual	Annual	Annual	
				Mean	Max
Type 1	0.61	15.2	56.4	2.3	17
Type 2	1.80	12.4	49.2	2.0	15
Type 3	1.78	11.4	50.1	2.0	11
Type 4	1.74	9.9	48.2	1.9	10
Type 5	1.94	8.8	52.8	2.1	15
Type 6	1.95	7.5	46.0	1.9	9
Type 7	1.91	7.1	38.5	1.6	5
Type 8	1.78	6.4	52.9	2.1	12
Type 9	1.85	6.3	53.2	2.1	10
Type 10	1.89	6.2	41.9	1.7	7
Type 11	1.86	4.8	43.2	1.8	12
Type 12	2.04	4.2	43.2	1.8	12

Table 3.2. Cluster/circulation type characteristics for 1979 – 2006, MJJASO and NDJFMA seasons.

Synoptic Type	Frequency [% occurrence of type]		Persistence [% of time same type follows]		Duration [days]			
	NDJFMA	MJJASO	NDJFMA	MJJASO	NDJFMA		MJJASO	
					Mean	Max	Mean	Max
Type 1	5.5	24.6	39.6	60.1	1.7	8	2.5	17
Type 2	15.0	9.9	51.5	45.7	2.1	15	1.8	7
Type 3	7.8	15.0	40.9	55.0	1.7	6	2.2	11
Type 4	5.2	14.3	34.1	53.3	1.5	6	2.1	10
Type 5	14.0	3.8	56.0	41.1	2.3	15	1.7	8
Type 6	9.3	5.7	50.8	38.1	2.0	9	1.6	5
Type 7	7.1	7.1	38.5	38.4	1.6	5	1.6	5
Type 8	4.8	7.9	48.8	55.4	1.9	8	2.2	12
Type 9	9.2	3.3	55.8	45.8	2.3	10	1.8	6
Type 10	7.9	4.3	42.6	40.6	1.7	6	1.7	7
Type 11	6.5	2.9	46.9	34.7	1.9	12	1.5	7
Type 12	6.7	1.6	51.7	26.8	2.1	12	1.4	8

Figure 3.4a. Cumulative probability distributions of the 12 synoptic types.

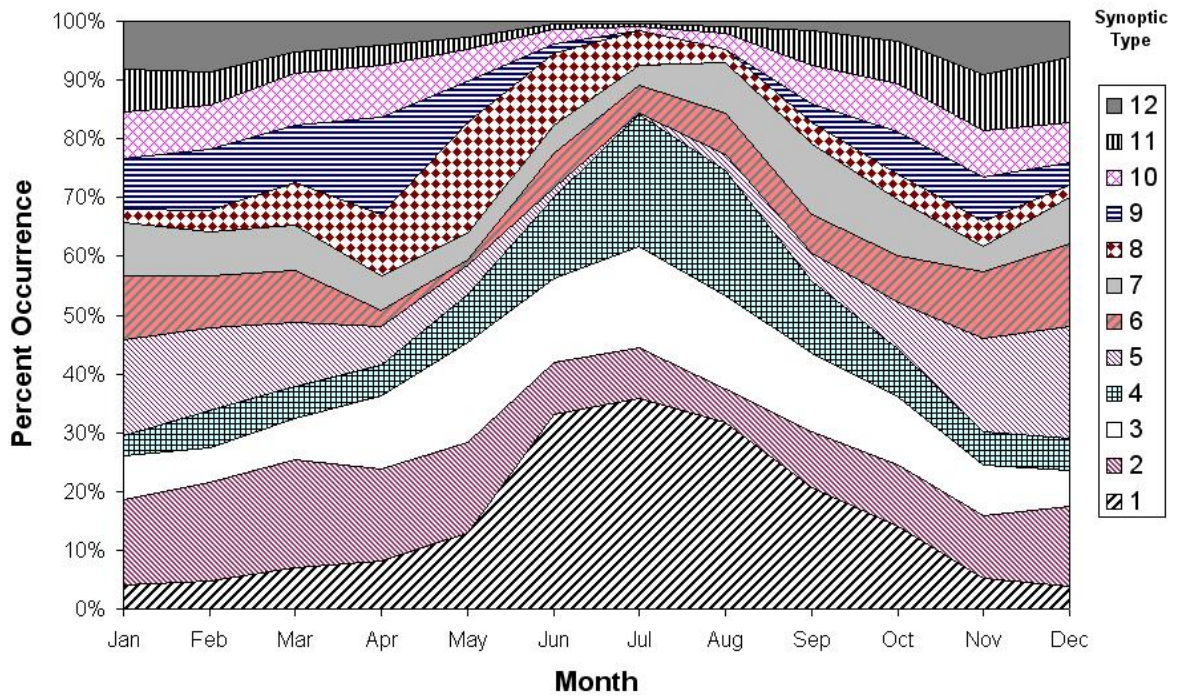
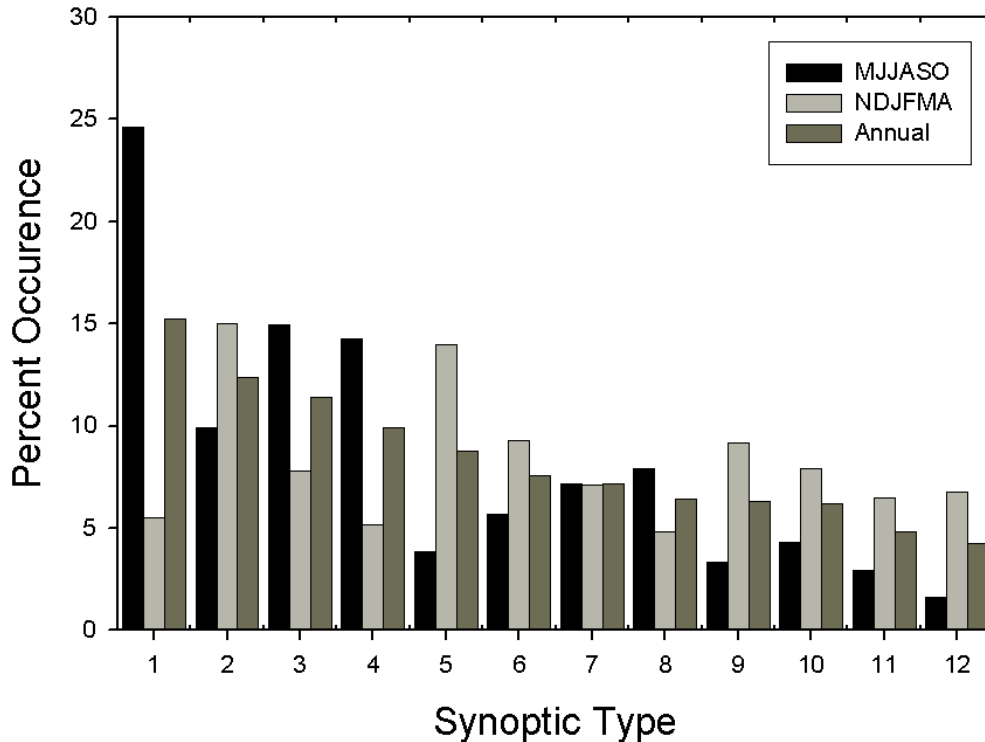


Figure 3.4b. Synoptic type percent occurrences for within MJJASO, NDJFMA, and the annual cycle.



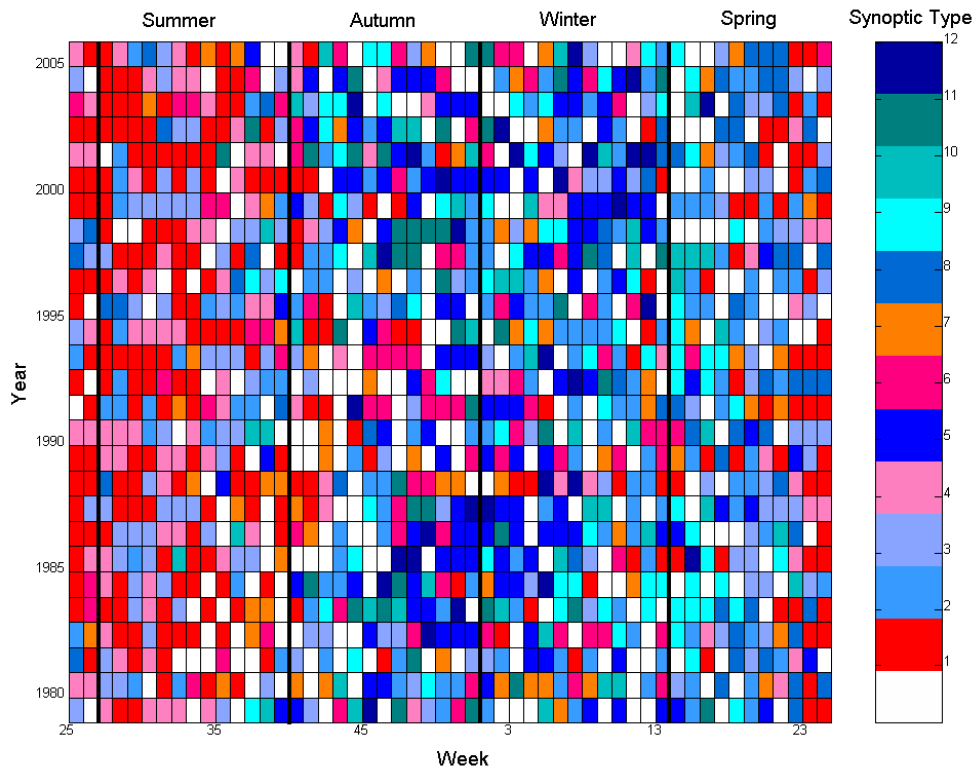
Type 1 mainly represents summer cyclones, with the highest frequencies occurring during MJJASO (Table 3.2). Type 6 represents cyclones with a greater mean frequency during NDJFMA. Type 7 is a strong cyclonic type with comparable frequencies for both seasons. Type 2 is anticyclonic type that occurs frequently throughout the year, tending towards higher (lower) frequencies in the winter (summer) season. Types 5, 10, 11 and 12 (anticyclonic types) occur most frequently during the cold season months. Types 3 and 4 (anticyclonic types) occur throughout the year, with a tendency towards higher mean frequencies during MJJASO than during NDJFMA (Table 3.2). Type 8 (anticyclonic) occurs most frequently from March to July, while type 9

(anticyclonic) occurs more frequently during the NDJFMA season. The results from this investigation suggest that the convergence of cyclones in the Canada Basin in summer noted in Sorteberg and Walsh (2008) may be characterized by cyclonic synoptic type 1, whereas cyclones that originated along the Alaska coastline may be associated with wintertime cyclonic types 6 and 7. Values for the mean duration of cyclone types (Table 3.1) are also consistent with residence times associated with cyclone types entering the Arctic presented in *Sorteberg and Walsh* [2008].

The seasonal persistence and duration of a particular synoptic type is related to its average seasonal frequency, and thus may vary between seasons. Subtracting the persistence values for the NDJFMA from the MJJASO values reveals notable seasonal differences within several synoptic types, where negative (positive) values indicate the type is more persistent in NDJFMA (MJJASO). Type 1 (+20.5%), type 3 (+14.1%), type 4 (+19.2%) and type 8 (+6.6%) are more persistent during MJJASO than during NDJFMA. Type 2 (-5.8%), type 5 (-14.9%), type 6 (-12.7%), type 9 (-10.0%), type 11 (-12.3%), and type 12 (-24.9%) are more persistent during NDJFMA than during MJJASO. Types 7 and 10 show little variability in seasonal persistence. Comparison of NDJFMA and MJJASO duration statistics reveals that extended durations of types 1, 3, 4, 8, have occurred during the summer months, with maximum durations of 17, 11, 10 and 12 days respectively. This suggests that higher frequencies of one or more of these types may be at least partly related to reversals of the BG.

Weekly synoptic type classifications were created from week 25 of 1979 to week 24 of 2006 (Figure 3.5). A number of weeks have no dominant synoptic type, and are therefore denoted as 'unclassifiable.'

Figure 3.5. Dominant weekly synoptic types from 1979 to 2006 show weekly types from week 25 to week 24 of the following year. Cyclonic (anticyclonic) types are shown in warm (cool) colors. Weeks with no dominant synoptic type are white.



The week-by-year synoptic patterns for the study period show a general seasonal pattern where types 1, 3, 4 and 8 dominate during the summer season, and types 2, 5, 6, 7, 10, 11 and 12 dominate during the cold season. The occurrence of Arctic cyclone types 1, 6 and 7 during the summer portray the incursion of cyclones into the SBSR. Type 1 is the dominant summer cyclone type, occurring nearly three times as frequently as types 6 and 7 combined (Figure 3.4b). The frequency of type 7 is somewhat higher in August and September, and thus characterizes some variability in cyclones during the latter half of summer. The occasional dominance of high pressure during the summer is represented by types 3 and 4, which both represent high-pressure systems that are centered over different locations. Type 4 also shows a mean centre of low pressure

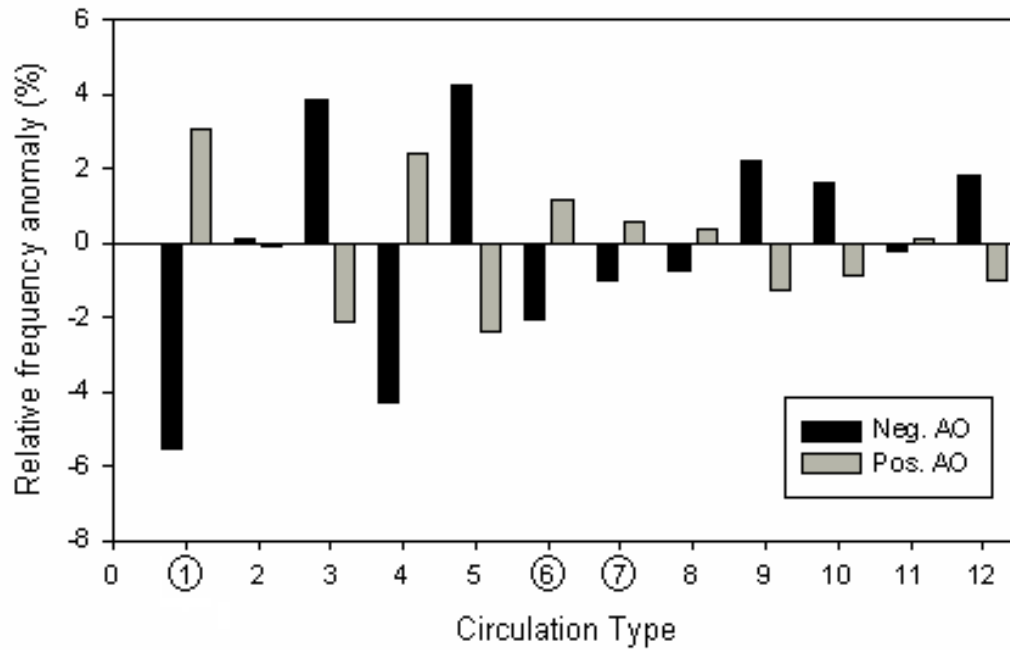
centered to the east of the Kamchatka Peninsula, which likely represents an area of summer cyclogenesis.

The interlaced dominance of types 1, 3, 4, and 8 starts around week 24, and can persist for up to 20 weeks, this represents the synoptic circulation pattern observed over the SBSR when sea ice concentrations are in decline, and increasingly larger areas of open water are present. The combination of pack ice to the north, a marginal ice zone, and areas of open water characteristic of the SBSR may significantly influence baroclinicity during this period and increase the duration and persistence of cyclonic types. A strong summer cyclonic circulation (type 1) can persist for up to several weeks (Figure 3.5). During the winter, high ice concentrations and a wide sea ice extent help reinforce a cold, stable airmass characteristic of anticyclonic circulation types (types 2, 5, 10 – 12). Winter Arctic cyclones (types 6 and 7) are less frequent and shorter in duration than summer storms, but are notable features in the winter synoptic climatology of the SBSR. Noteworthy also is the feature where Type 1 appears to dominate the summer synoptic circulation pattern more during the latter part of the 20th century and most notably during the early part of the 21st century. In order to understand the mechanisms responsible for decadal-scale variability in synoptic types, connections between large-scale atmospheric circulation patterns characterized by the AO and regional-scale circulation patterns characterized by synoptic types, are examined in the next section.

3.3.3 Synoptic types and the AO

The AO index is known to be negative for all years from 1979 – 1988, and positive for all years from 1989 – 1995. The AO has been neutral since 1995 [Comiso, 2006]. Here the chi-square test shows that interannual variability in the frequencies of the synoptic types is significantly linked to the AO at the 95% level ($p < 0.05$), with the exception of type 2 and 11 (Figure 3.6). Type 1, a prominent summer Arctic cyclone type, is strongly linked to the AO. An increase (decrease) in frequencies of type 1 corresponds to the positive (negative) phases of the AO. An increase in type 1 may be also be partially attributable to decreasing summer sea ice concentrations and increasing sea ice mobility; however, linking changes in synoptic type frequencies to changes in sea ice concentration is beyond the scope of this section. The other cyclonic types 6 and 7 also exhibit increased (decreased) relative frequencies when positive (negative) AO conditions dominate. Types 6 and 7 are predominant during the summer and early fall when positive AO conditions prevail. Types 4 and 8 also exhibit increased (decreased) relative frequencies when positive (negative) AO conditions are present. Anticyclonic types 3, 5, 9, 10, and 12 reveal increased (decreased) relative frequencies during negative (positive) AO conditions, just the opposite of the cyclonic types. Noteworthy from this investigation is the existence of a statistical relationship between cyclonic synoptic types and the AO for the SBSR, which reflects the characterization of the positive (negative) AO phase as a period of relatively low (high) Arctic SLP, captured by cyclonic (anticyclonic) synoptic types.

Figure 3.6. Residuals of the Chi-square test of annual synoptic type frequencies in relation to the AO with Arctic cyclone types identified by circles.

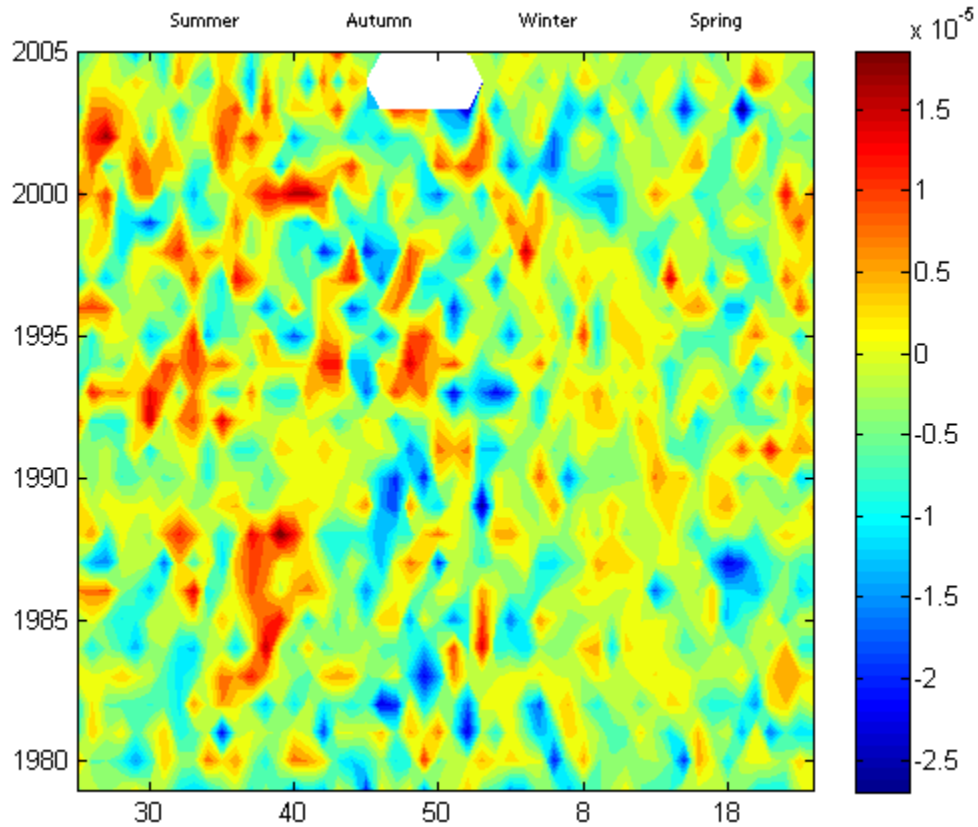


Further work is required to investigate how closely the synoptic types are influenced by the AO and whether we could use the AO index as a means of predicting the probability of certain synoptic types, and the response of the sea ice, as a function of season.

3.3.4 Synoptic Types and BG Reversals

The weekly synoptic types provide a means to link daily synoptic type frequency and persistence to the sea ice spatially averaged weekly vorticity values following *Lukovich and Barber* [2006]. Investigation of mean ice relative vorticity as a function of week and year (Figure 3.7) highlights reversals in the BG associated with transitions from anticyclonic to cyclonic activity [*Lukovich and Barber*, 2006]. (The white block between autumn and winter for 2003 – 2005 indicates an absence of data in Figure 3.7.) Note the predominantly anticyclonic activity throughout the annual cycle, and cyclonic activity during summer and early autumn noted in previous studies (*McLaren et al.*, 1987; *Serreze et al.*, 1989, *LeDrew et. al.*, 1991, *Lukovich and Barber*, 2006). During the 1980s, dominant reversals occurred during summer (weeks 30 to 40), while during the decade of the 90s and into 2000s, reversals occurred over a longer period (weeks 30 to 50), characteristic of the shift from the low-index to the high-index phase in the AO from the 1980s to the 1990s. Following 2000, significant variability in ice relative vorticity is observed throughout the annual cycle, with a return to predominantly anticyclonic activity during winter months. We speculate that this may reflect decreasing sea ice concentrations, and the trend towards the replacement of multi-year ice with first-year ice. Our speculation is that with less ice, and thinner ice, the gyre is becoming more active with detectable reversals occurring throughout a longer period of the annual cycle.

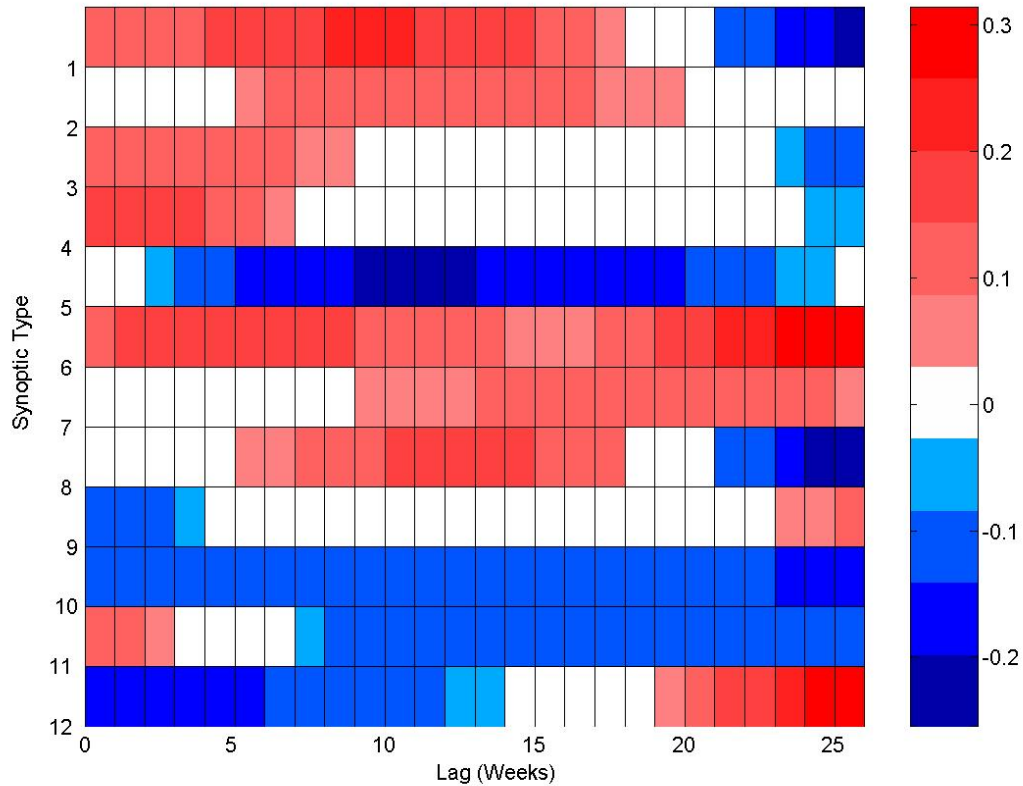
Figure 3.7. BG sea ice average weekly vorticity. Cyclonic (Anticyclonic) sea ice motion is indicated in shades of red (blue). Data missing in 2004, weeks 46 - 52: (After Lukovich and Barber, 2006).



A visual comparison between the weekly synoptic circulation patterns and the weekly sea ice spatially averaged vorticity values in the SBSR demonstrates a relationship between the increased summer frequencies of type 1, and more frequent periods of positive vorticity within the SBSR. Periods of cyclonic activity (positive vorticity) in the BG occur during and following the summer cyclonic atmospheric regime, and conversely, anti-cyclonic activity (negative vorticity) occurs throughout the rest of the season, corresponding to the persistence of anticyclonic atmospheric synoptic types such as types 2 and 5.

A lag correlation analysis was used to examine connections between synoptic type frequencies and spatially-averaged BG sea ice vorticity that have been smoothed with two, four, six, eight, ten and twelve-week running means. Lag correlations for one-week running means were not calculated due to insufficient daily synoptic type frequencies at that timescale. Lag correlations for two and four-week running means yielded noisy non-significant correlations, and were dropped. Stronger correlations emerge as the synoptic type frequency counts increase in the larger running-average intervals. The larger time intervals also smooth the lag correlation curves and improve the interpretability of the analysis. Significant correlations appear at a six-week running mean interval, and lag correlations for eight, ten, and twelve-week running means reveal a pattern of strengthening significant correlations. We present and interpret the twelve-week running-average interval (Figure 3.8) as this interval provides an optimal estimate of lagged correlations between synoptic types and ice relative vorticity.

Figure 3.8. Lag correlations between twelve-week running mean synoptic type frequencies and spatially-averaged BG sea ice vorticity data that are significant at the 95% level ($p < 0.05$).



The lag correlations for the twelve-week running-average periods show several interesting positive and negative correlations for all types at various time lags, significant at the 95% level ($p < 0.05$) (Figure 3.8). Positive correlations between frequencies associated with cyclonic synoptic types 1, 6, and 7 and ice relative vorticity for time lags ranging from 0 – 18, 0 – 24, and 9 – 26 weeks, respectively (Figure 8), illustrate correspondence between cyclonic activity in sea ice and atmospheric phenomena. Negative correlations between frequencies associated with anticyclonic synoptic types 5, 9, 10, 11 and 12 for lags of 2 – 25, 0 – 4, 0 – 26, 7 – 26, and 0 – 14 weeks, respectively, highlights that an increase in frequency in anticyclonic events results in a decline in ice relative vorticity. Similarity in correlations between Types 1 and 3 and ice relative

vorticity despite significant differences in circulation patterns for the former may be an artifact of seasonality – the similarity in correlation patterns disappears for data smoothed over shorter (less than twelve week) timescales. Anticyclonic synoptic types 2, 3, 4, and 8 positively correlate weakly with ice relative vorticity for time lags of 6 – 18, 0 – 7, 0 – 9, and 6 – 20 weeks. This indicates that anticyclonic synoptic types with a displaced Beaufort High or weakened flow over the SBSR will limit the ability of the type to influence ice vorticity.

The apparent contradiction between sea ice relative vorticity and anticyclonic synoptic types may be attributed to regional influence from coastlines in addition to local MSLP patterns, in keeping with previous studies showing negative correlations between ice and atmospheric relative vorticity to 500mb [*Lukovich and Barber, 2006*], which showed sea ice response to wind stress over the Arctic basin, with regional influence from coastlines and local relative vorticity or, in this instance, local MSLP patterns. The persistence of types 2 and 3 throughout the annual cycle may also result in overlap with residual positive vorticity generated by other cyclone types during summer. Positive (negative) correlations between frequencies of cyclonic types 1 and 6 (anticyclonic types 9, 10, and 12) and ice vorticity at zero time lag also suggest contributions from both cyclonic and anticyclonic synoptic types to reversals in the BG. Moreover, correspondence between types 1 and 6 and ice vorticity at zero time lag indicate contributions from cyclones originating both in the Atlantic and Pacific regions.

3.3.5 Within-type Variability of BG Vorticity

Our analysis thus far has focused on the relationship between the frequencies and durations of the synoptic types to BG sea ice vorticity; however, an examination of within-type variability of BG vorticity is also prudent. A synoptic type may generate positive or negative vorticity in the BG, and may exhibit a proclivity towards positive values of Δ vorticity during a particular vorticity regime. The K-S test is employed to compare Δ vorticity distributions within each synoptic type between the positive and negative vorticity regimes. The analysis is conducted for all synoptic types within both of the NDJFMA and MJJASO seasons (table 3.3).

Table 3.3. Kolmogorov D and P-values from a Kolmogorov-Smirnov test for seasonal variability in Δ vorticity distributions between positive and negative BG vorticity regimes for all types. Boldface is significant at the 95% level.

Synoptic Type	MJJASO		NDJFMA	
	<i>D</i>	<i>p</i>	<i>D</i>	<i>p</i>
Type 1	0.491	<0.001	0.503	<0.001
Type 2	0.438	<0.001	0.487	<0.001
Type 3	0.449	<0.001	0.560	<0.001
Type 4	0.465	<0.001	0.563	<0.001
Type 5	0.450	<0.001	0.407	<0.001
Type 6	0.429	<0.001	0.467	<0.001
Type 7	0.428	<0.001	0.550	<0.001
Type 8	0.417	<0.001	0.405	<0.001
Type 9	0.589	<0.001	0.534	<0.001
Type 10	0.370	<0.001	0.479	<0.001
Type 11	0.564	<0.001	0.528	<0.001
Type 12	0.374	0.007	0.511	<0.001

The K-S null hypothesis is that within each synoptic type, there is no difference in Δ vorticity distributions between the positive and negative circulation regimes. The K-S statistic D results in larger values representing dissimilarity in the distribution of the two datasets being compared. The calculated value of D is significant at the 95% level ($p < 0.05$) for every synoptic type during both the NDJFMA and MJJASO seasons, and we therefore reject the null hypothesis. These results show that for any given synoptic type, Δ vorticity varies depending on the circulation regime of the BG. Therefore the circulation regime of the BG is a source of within-type variability in atmospheric forcing of the BG.

Another source of within-type variability is seasonal, and is likely due to two factors. First, within-type variability in BG vorticity is greatest during the MJJASO season (although D values appear similar for MJJASO and NDJFMA in types 9 and 11) when ice concentrations and sea ice extent are in decline, and the mobility of the pack ice is greatest. Second, variability in atmospheric circulation may also play a role. A particular synoptic type may exhibit a greater degree of variability in atmospheric circulation patterns and strength, hence having a highly variable influence on BG vorticity. The dimensionless cluster homogeneity values from the k-means analysis show that every synoptic type contains a degree of variability in circulation pattern and strength. This coupled with increasing areas of open water, and increasingly mobile sea ice during the MJJASO season suggests increased sensitivity in BG vorticity to within-type atmospheric circulation variability during MJJASO than during NDJFMA when sea ice extent is growing.

Within-type variability may also arise from coupling between the sea ice cover and the lower troposphere. For example, a strong temperature gradient arising from the interaction of large areas of open water and the pack ice can increase wind speeds considerably and enhance the circulation strength of a given synoptic type. This would be most common in the late summer and autumn when the cold airmass is developing over the pack ice, but areas of open water remain.

3.4 Conclusions

A synoptic climatology is developed for the SBSR that resulted in twelve different synoptic circulation types (Figure 3.3). The occurrence, spatial pattern, frequency, persistence and duration of these types is used to assess the synoptic surface pressure pattern of the SBSR from 1979 – 2006 (Tables 3.1 and 3.2). The Beaufort High is depicted by synoptic types 2, 3, 5, 8, 9, 10 and 12 characteristic of anticyclonic atmospheric circulation patterns. Cyclonic circulation patterns are characterized by types 1, 6, and 7.

In consideration of our second research question, synoptic weather patterns (Figure 3.5) vary seasonally. In particular, types 1, 3, 4 and 8 dominate during MJJASO, and types 2, 5, 6, 9, 10, 11 and 12 dominate during NDJFMA. MJJASO is characterized by persistent episodes of cyclone type 1.

Significant large-scale circulation variability arising from the AO is found to be associated with the mean annual frequencies of all synoptic types, with the exception of type 2 and 11. Types 1, 4, 6, 7, and 8 exhibit increased (decreased) relative frequencies when positive (negative) AO conditions prevail. Types 3, 5, 9, 10, and 12 show increased (decreased) relative frequencies during negative AO conditions. The increase (decrease) in the frequencies of summer cyclone types (1 and 6) during positive (negative) AO conditions is identified as a significant large-scale interannual climatic control on BG circulation.

A comparison of weekly spatially averaged sea ice vorticity (Figure 3.7) data to derived weekly synoptic circulation types suggests that summer reversals are linked to multiple and/or persistent occurrences of Arctic cyclonic synoptic types (1, 6 and 7). Lag

correlation analysis between twelve-week running mean spatially-averaged sea ice vorticity and synoptic type frequencies reveals significant positive correlations between cyclonic synoptic types 1, 6, and 7 for time lags of 0 – 18, 0 – 24, and 9 – 26 weeks, respectively (Figure 3.8).

The synoptic types appear to contain strong seasonally-driven within-type variability in how they force BG sea ice vorticity. This likely arises from varying sea ice conditions (extent and concentration) between MJJASO and NDJFMA, or seasonal variability in atmospheric circulation strength. We expect current trends in the areal extent and thickness of Arctic sea ice to continue to decline (IPCC, 2007). This will result in a more mobile sea ice regime in the southern Beaufort Sea, and likely increase variability in the response of the BG to seasonal atmospheric circulation conditions. The sea ice gyre vorticity will likely increase in magnitude and reversals will most likely increase concomitantly.

This section has shed light on the relationship between synoptic SLP patterns and their relationship to the motion of sea ice in the BG. Some logical extensions of this work are to examine whether the statistical relationships observed here (between SLP and ice motion) are also found in high resolution coupled ocean-sea ice-atmosphere models and to determine whether these can be used to explain rapid annual reduction in sea ice extent. Another avenue is to examine in situ effects of these synoptic types on the surface energy balance of the marginal ice zones, through processes of divergence and convergence, of the local ice field. We would also like to see how well the relationship between synoptic types and the AO can be exploited to predict probabilities of atmospheric circulation types and related sea ice motion.

3.5 References

- Barry, R.G., Maslanik, J. (1989), Arctic sea ice characteristics and associated atmosphere – ice interactions in summer inferred from SMMR data and drifting buoys: 1979 – 1984.. *Geojournal*, 18 (1), 35 – 44.
- Barry, R.G. and Parry, A.H. (2001), Synoptic Climatology and its applications *in*: Barry, R.G., Carleton, A.M., *Synoptic and Dynamic Climatology*, ©2001, Routledge, London.
- Brümmer, B., Müller, G., Hoerber, H. (2003), A Fram Strait cyclone: properties and impact on ice drift as measured by aircraft and buoys. *J. Geophys. Res* 108, No. D7, 4217, doi: 10.1029/2002JD002638, 2003.
- Comiso, J.C., 2006, Abrupt decline in the Arctic winter sea ice cover. *Geophys. Res. Lett.*, L18054, doi:10.1029/2006GL027341.
- Fowler, C. 2003, updated 2007. Polar pathfinder daily 25 km EASE-grid sea ice motion vectors, <http://nsidc.org/data/nsidc-0116.html>. Boulder, Colorado USA. Natl. Snow and Ice Data Cent.
- Kalnay, E., Kanamitsu, M., Kistler, R., Collins, W., Deaven, D., Gandin, L., Iredell, M., Saha, S., White, G., Woollen, J., Zhu, Y., Chelliah, M., Ebisuzaki, W., Higgins, W., Janowiak, J., Mo, K. C., Ropelewski, C., Wang, J., Leetmaa, A., Reynolds, R., Jenne, R., Joseph, D. (1996), The NCEP/NCAR 40-year reanalysis project. *Bull. Amer. Meteor. Soc.*, 77, 431 – 437
- Keegan, T.J. (1958), Arctic synoptic activity in winter. *J. Meteor.* 15, 513 – 521.
- Kwok, R., (2006), Exchange of sea ice between the Arctic Ocean and the Canadian Arctic Archipelago, *Geophys. Res. Lett.*, 33, L16501, doi:10.1029/2006GL027094.
- LeDrew, E.L., Johnson, D., Maslanik, J.A. (1991), An examination of atmospheric mechanisms that may be responsible for the annual reversal of the Beaufort Sea ice field. *Int. J. of Clim.* 11, 841 – 859.
- Lukovich, J.V., Barber, D.G. (2006), Atmospheric controls on sea ice motion in the southern Beaufort Sea. *J. Geophys. Res.* 111, D18103, doi:10.1029/2005/JD006408.
- McCabe, G.J., Clark, M.P., Serreze, M.C. (2001), Trends in northern hemisphere surface cyclone frequency and intensity. *J. Clim.* 14, 2763 – 2768.
- McLaren, A.S., Serreze, M.C., Barry R.G. (1987). Seasonal variations of sea ice motion in the Canada basin and their implications, *Geophys. Res. Lett.*, 14, 1123-1126.

- Proshutinsky, A.Y., Bourke, R.H., McLaughlin, F.A. (2002), The role of the BG in Arctic climate variability: Seasonal to decadal climate scales. *Geophys. Res. Lett.*, 29 (23), 2100, doi:10.1029/2002GL015847.
- Serreze, M.C., Barry, R.G. (1988), Synoptic activity in the Arctic basin. 1979-85, *J. Clim.* 1, 1276 – 1295.
- Serreze, M.C., Barry, R.G., McLaren, A.S. (1989), Sea Ice Concentrations in the Canada basin, *J. Geophys. Res.* 94(C8), 10,955 – 10970
- Serreze, M.C., Box, J.E., Barry, R.G., Walsh, J.E., (1993), Characteristics of Arctic synoptic activity, 1952 – 1989. *Meteorol. Atmos. Phys.*, 51, 147 – 164.
- Serreze, M.C., (1995), Climatological Aspects of Cyclone Development and Decay in the Arctic. *Atmos. Ocean.* 33, (1), 1 – 23.
- Serreze, M.C., Walsh, J.E., Chapin III, F.S., Osterkamp, T., Dyurgerov, M., Romanovsky, V., Oechel, W.C., Morison, J., Zhang, T., Barry, R.G. (2000), Observational evidence of recent change in the northern high-latitude environment. *Climatic Change* 46, 159 – 207.
- Sorteberg, A., and J.E. Walsh, 2008, Seasonal cyclone variability at 70N and its impact on moisture transport in the Arctic, *Tellus*, 60A, 570 – 586.
- Stroeve, J., M. M. Holland, W. Meier, T. Scambos, and M. Serreze, (2007), Arctic sea ice decline: Faster than forecast, *Geophys. Res. Lett.*, 34, L09501, doi: 10.1029/2007GL029703.
- Thompson, D.W.J., and Wallace, J.M. (1998), The Arctic oscillation signature in wintertime geopotential height and temperature fields, *Geophys. Res. Lett.*, 25, 1297-1300.
- Thompson, D.W.J., and Wallace, J.M. (2000), Annular modes in the extratropical circulation, part I: Month-to-month variability, *J. Clim.*, 13, 1000-1016
- Yu, Y., Maykut, G.A., Rothrock, D.A. (2004), Changes in the thickness distribution of Arctic sea ice between 1958-1970 and 1993-1997, *J. Geophysical Res.* 109, C08004, doi: 10.1029/2003JC001982.
- Zhang, J., D. Rothrock and M. Steele, (2000), Recent changes in the Arctic Sea Ice: The interplay between ice dynamics and thermodynamics, *J. Clim.*, 13, 3099-3114.
- Zhang, X., J. E. Walsh, J. Zhang, U. S. Bhatt, and M. Ikeda, (2004), Climatology and interannual variability of Arctic cyclone activity, 1948-2002. *J. Climate*, 17, 2300-2317.

CHAPTER FOUR: SYNOPTIC ATMOSPHERIC CIRCULATION CHANGES AND SEA ICE LEAD FORMATION IN THE SOUTHERN BEAUFORT SEA

Asplin, M.G., Candlish, L., Else, B.G.T., Galley, R.J., Raddatz, R.L., Papakyriakou, T.N., Barber, D.G., 2013. Cyclone forced lead formation and ocean-sea ice-atmosphere coupling within a flaw lead region *Jour. Geophys. Res. (In Review)*

4.1 Introduction

Climate change is affecting Arctic sea ice thickness and volume [Rothrock *et al.*, 1999; Kwok *et al.*, 2009; Laxon *et al.*, 2013]. The passive microwave satellite record (spanning from 1979 – 2010) shows that the summer minimum sea ice extent in the Arctic is declining at an average rate of $81,310 \text{ km}^2 \cdot \text{year}^{-1}$ [Stroeve *et al.*, 2011a]. These phenomena are attributed to increasing regional air temperatures and increased summer ocean mixed-layer temperatures [IPCC 2007; Perovich *et al.*, 2008] coupled with wind forcing of sea ice [Ogi *et al.*, 2010, Ogi and Wallace, 2012], and considerable loss of multi-year ice in the Pacific sector of the Arctic [Kwok and Cunningham, 2010; Maslanik *et al.*, 2011]. The increasingly mobile and thinner Arctic sea ice cover is becoming more susceptible to wind forcing [Rampal *et al.*, 2009], which may drive large lead formation events, and subsequent releases of heat to the atmosphere during winter as a result of the leads refreezing. As the melt season lengthens [Markus *et al.*, 2009], the impacts of open water, thin ice, and sensible heat flux on the atmospheric boundary layer (ABL) above the Arctic sea ice become increasingly important to regional temperature anomalies [Overland, 2009], and cyclone intensities [Simmonds and Keay, 2009].

Numerous studies indicate that increased storm intensity and wind forcing in the Beaufort Sea may also impact the Beaufort Gyre (BG), which is an important ocean circulation feature that affects variability of the climate in the Arctic [McLaren *et al.*, 1987; Serreze *et al.*, 1989; LeDrew *et al.*, 1991; Proshuntinsky *et al.*, 1997; Asplin *et al.*,

2009; *Overland*, 2009; *Barber et al.*, 2010]. The circulation of the BG is driven by synoptic-scale atmospheric circulation and generally follows an anticyclonic pattern that promotes sea ice convergence and increased ice concentrations [*Proshutinsky et al.*, 2002]. Cyclone wind forcing can slow or even reverse the rotational circulation of the BG to a cyclonic pattern [*McLaren et al.*, 1987; *LeDrew et al.*, 1991; *Lukovich and Barber*, 2006]. The BG is particularly vulnerable to this effect if sea ice is mobile, which itself depends on several factors including the sea ice extent and sea ice thickness, in addition to the magnitude of the BG's vorticity [*Barry and Maslanik*, 1989; *Lukovich and Barber*, 2006]. Sea ice mobility [*Rampal et al.*, 2009; *Spreen et al.*, 2011; *Galley et al.*, 2013] and BG reversals also increase with decreased sea ice cover during the summer season, and remain high during the autumn, when new ice is rapidly forming and easily deforms into ridges and rubble ice due to wind forcing from storms [*Rampal et al.*, 2009].

Recently, an increase in the intensity of Arctic storms has been observed [*Stroeve et al.*, 2011a], due in part to changes in heat flux to the atmosphere [*Simmonds and Keay*, 2009; *Higgins and Cassano*, 2009], and in part to a strengthened North Atlantic storm track [*Stroeve et al.*, 2011b]. Although they are not likely a primary cause of sea ice decline [*Screen et al.*, 2011], more intense cyclones act to increase wind forced divergence of sea ice and the generation of dynamically formed features such as leads and polynyas [*Barry and Maslanik*, 1989; *Brümmer et al.*, 2003; *Dierer et al.*, 2005]. Recent evidence shows that this increase is impacting large-scale Arctic pack ice dynamics, as evidenced by the large fracturing events occurring in the Beaufort Sea in January through March of 2013 (*NSIDC*, 2013).

Energy loss from leads and/or polynyas can be as much as two orders of magnitude greater than that for snow-covered sea ice [Maykut, 1978; Cavalieri and Martin, 1994; Agnew et al., 1999; Raddatz et al., 2011; Raddatz et al., 2012], which can create modifications of the winter ABL up to heights of 2000 m [Maykut, 1978; Glendenning, 1995; Overland et al., 2000; Rinke et al., 2006]. This can have a significant influence on winter ABL climate, since the net radiation at snow-covered surfaces is negative [Uttal, et al., 2002; Persson et al., 2002]. Even leads occupying less than 5% of total surface area can substantially impact regional heat flux [Lupkes et al., 2008; Raddatz et al., 2011].

Modification of the ABL by leads or polynyas is characterized by the development of a thermal internal boundary layer (T-IBL) [*i.e.* Raddatz et al., 2012]; a feature that often develops downwind of a discontinuity in temperature and/or saturation absolute humidity of the earth's surface [Garratt, 1990]. The characteristics of both the upstream and downstream surfaces and the approaching atmospheric flow influence sensible heat flux and thus the nature of the T-IBL. Raddatz et al. [2012] explored the link between sea-ice cover in the Amundsen Gulf and the ABL, surmising that an unconsolidated pack ice cover with a persistent lead network, cold sea-surface water following break-up, and the temperature of the approaching flow were the critical factors controlling the presence and type of T-IBL. Heat and moisture fluxes from leads are also affected by wind direction [Crane, 1978; Andreas, 1985; Inoue and Hori, 2011]. Inoue and Hori [2011] noted a 1.5 K decrease in the near-surface ocean temperature after the passage of a cold front, which suggests a large transfer of heat to the cold dry air mass, and corresponds, with the similar findings of Andreas [1985].

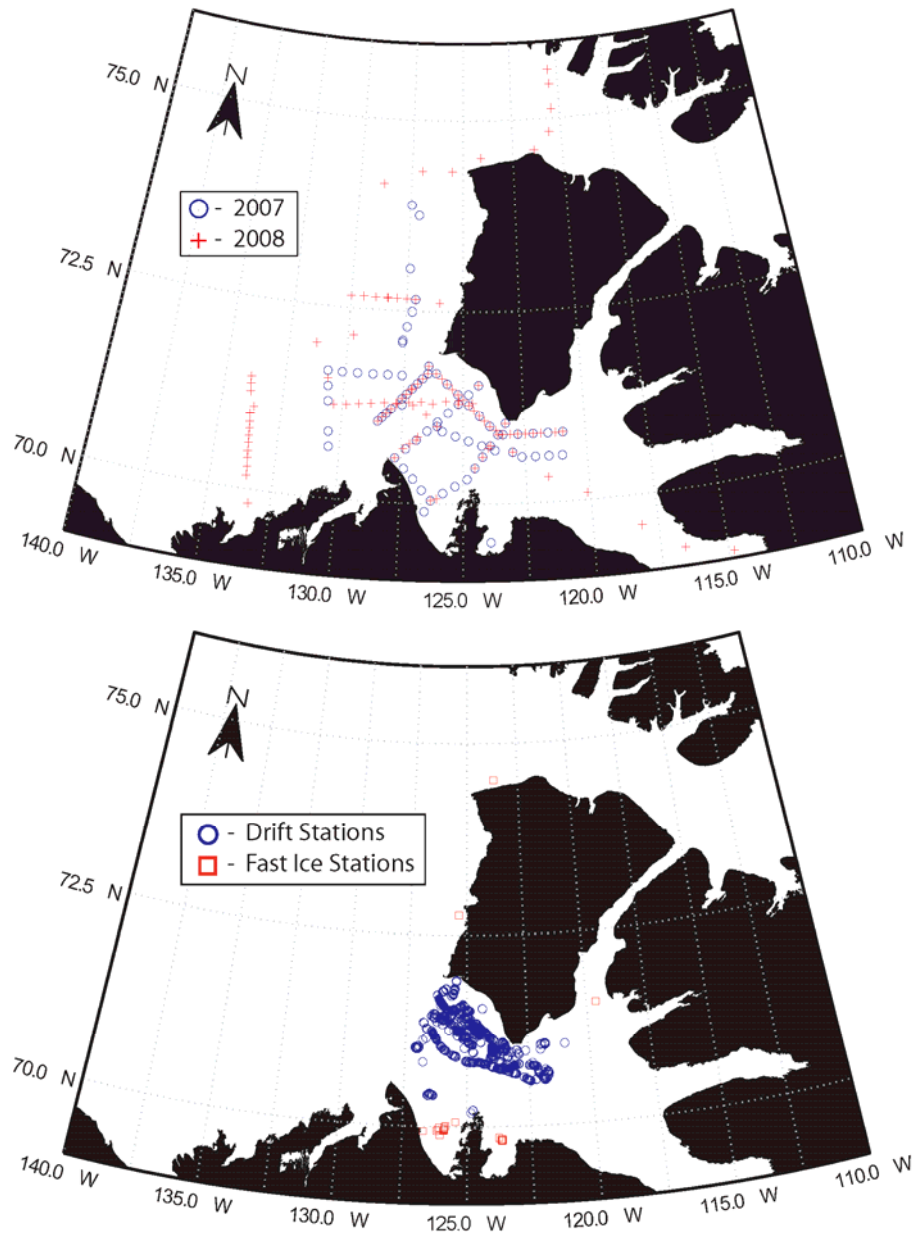
We investigate the relationship between the declining sea ice cover, synoptic-scale atmospheric circulation patterns, cyclone wind forcing of sea ice leads and subsequent surface heat fluxes to the ABL in the southern Beaufort Sea. Three interrelated research questions are addressed:

- 1) How does the timing, concentration and types of sea ice observed in the study region during the study period (2007 – 2008) compare to 1979 – 2006 sea ice climatology?
- 2) Is the declining Arctic sea ice cover leading to annual and/or seasonal changes in synoptic circulation patterns in the southern Beaufort Sea?
- 3) How does the interaction between declining sea ice cover and changing synoptic circulation patterns impact winter sea ice lead formation and sensible heat fluxes to the ABL?

4.2 Data and Methods

This study was conducted as part of the International Polar Year (2007 – 2008) Circumpolar Flaw Lead (CFL) System Study using the CCGS *Amundsen* as a platform physical and automated data collection throughout the project (Figure 4.1). *Barber et al.* [2010] provide further details on the CFL project.

Figure 4.1. Top: Distributed open-water sample sites sampled in the autumn of 2007 and the summer of 2008. Bottom: Drift stations and fast ice stations sampled in the winter and spring of 2007 – 2008.



4.2.1 Regional Synoptic Climatology

Daily gridded mean sea-level pressure data (MSLP) from 1979 – 2011 (inclusive) were retrieved from archives maintained by the NOAA-CIRES Climate Diagnostics Centre, which originated from the National Center for Environmental Prediction (NCEP) Reanalysis I Project [Kalnay *et al.*, 1996]. The spatial resolution of these data is a 2.5° x 2.5° (latitude and longitude) grid, encompassing the Beaufort and Chukchi Sea regions bounded by 55°N to 85°N, 120°W to 175°W. These boundaries were selected to ensure that the Aleutian low and synoptic scale meteorological features originating over Eurasia, and the North Pacific were encapsulated, as these may influence circulation of the BG [Asplin *et al.*, 2009].

Synoptic-scale atmospheric circulation patterns, hereafter termed ‘synoptic types’, were classified from daily MSLP data, thereby expanding the synoptic catalogue of Asplin *et al.*, [2009] to cover 1979 – 2011, including the CFL study (Figure 4.2). Daily synoptic classifications for the CFL study are shown in Figure 4.3. The synoptic types were derived using Synoptic Typer 2.2, an application developed by the Australian Bureau of Meteorology [Dahni and Ebert, 1998]. Synoptic Typer 2.2 applies a commonly used pattern recognition scheme comprising principal components analysis and a subsequent k-means cluster analysis. For full details on the synoptic classification process used in this paper, see Asplin *et al.*, [2009]. Changes in annual and seasonal synoptic type frequencies attributed to declining sea ice extent were assessed using chi-squared frequency analysis by comparing mean synoptic type frequencies during 1999 – 2011 where declining summer Arctic sea ice extents are observed to be accelerating to those from 1979 – 1998. Some spatial variability in atmospheric circulation is lost in the

synoptic classifications, as the MSLP composites presented for each synoptic type are averages of SLP on all days assigned within each synoptic type [Yarnal, 1993] and synoptic type transition cannot be assessed at sub-day intervals.

Figure 4.2. Mean sea level pressure (mb) composites for the 12 synoptic types for the analysis period 1979 – 2008. Prevailing circulation and time of year most prevalent (Yr = all-year, Sp = spring, Su = summer, A = autumn, W = winter) are described in parenthesis. Modified following Asplin et al., [2009].

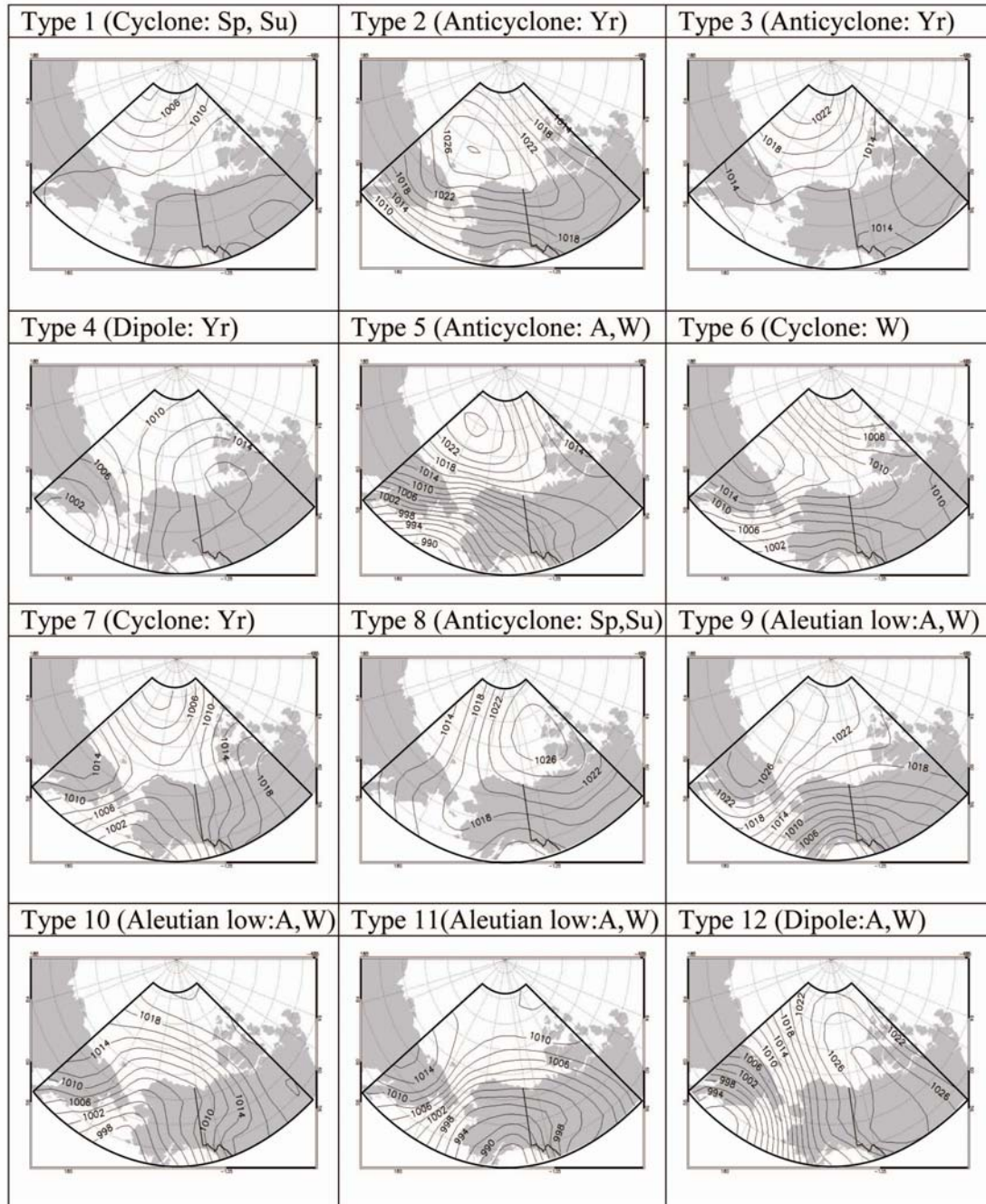
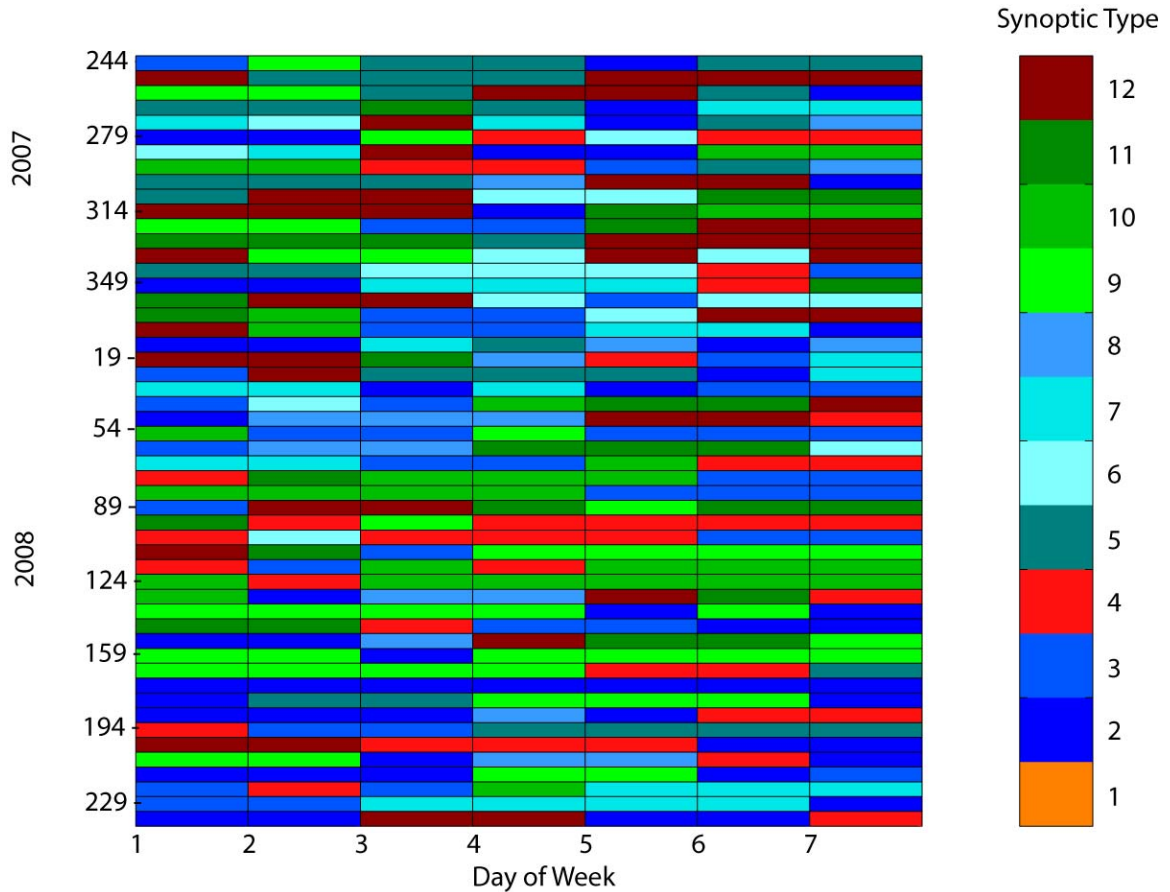


Figure 4.3. Daily synoptic type classifications for 01 September 2007 – 31 August 2008 presented weekly by day-of-year. Synoptic types are color-coded by the prevailing synoptic-scale circulation over the study region: green: easterly, blue: northerly, orange: southerly, cyan, westerly.



4.2.2 Regional Sea Ice Data

Weekly digital ice charts for the western Arctic were obtained from the Canadian Ice Service (CIS) digital archive and converted to a 2 x 2 km grid to characterize sea ice stage of development and coverage within the study area. Ice charts are prepared by expert interpretation of satellite imagery following CIS classification protocol [Fequet, 2002], and are suitable for time series studies (e.g. Tivy *et al.*, [2011]). For each digital ice chart, the fraction (in tenths of sea ice coverage) of total, old, first-year (a superset of thick first-year (> 120 cm), medium first-year (70 – 120 cm), and thin first-year (30 – 70

cm)), young (10 – 30 cm) and new ice (< 10 cm) in each pixel was used to obtain the areal coverage (in km²) of each ice type in each pixel. Coverage by type in each pixel (n = 159685) was summed and divided by the total study area (638740 km²) yielding the fractional coverage of the study area (Figure 4.1) by sea ice type for each weekly chart [e.g. Galley *et al.*, 2008; Tivy *et al.*, 2011]. AVHRR imagery was acquired from the NOAA/ AVHRR satellite via the receiving station at the Meteorological Service of Canada's Prairie and Arctic Storm Prediction Centre.

4.2.3 Ship-based Meteorology

A Radiometrics MP-3000A™ passive microwave profiling radiometer (MWRP) was installed on the CCGS *Amundsen* for the duration of the CFL study, providing high temporal resolution (~1 · minute⁻¹) atmospheric profiles for temperature (K), and absolute humidity (10⁻³ kg m⁻³) to an altitude of 10 km. The MWRP observes radiances from the zenith direction in eight channels at frequencies between 22 – 30 GHz (water band) for water vapor profiling, and fourteen channels between 51 – 59 GHz (oxygen band) for temperature profiling. The water vapor profiling channels were calibrated hourly with tipping curves [Gulder and Spankuch, 2001], while an external liquid nitrogen blackbody target is used to periodically calibrate the temperature channels. All 22 channels perform a relative calibration every 5 minutes by viewing an internal black body target. The profiles are processed in real-time providing a continuous time series profile of the lower troposphere. The instrument also includes sensors to monitor atmospheric pressure, ambient temperature, surface relative humidity, and an infrared radiometer (9.6 - 11.5 μm) to measure cloud-base altitude [Radiometrics, 2007]. Additional details on of the

radiometric profiling of temperature and water vapor are available elsewhere [Solheim *et al.*, 1998; Gulder and Spankuch, 2001; Ware *et al.*, 2003, and Gafford *et al.*, 2008].

The MWRP was positioned behind *Amundsen's* bridge about 18 m above sea level. The instrument was operated continuously from 26 November 2007 to 04 August 2008. The MWRP yielded volumetric temperature and humidity values with a resolution of 50 meter intervals from 0 to 0.5 km, 100 meter intervals for 0.5 to 2 km, and 250 meters for 2 to 10 km in the vertical. The values are derived from passive microwave brightness temperatures using supplier's neural network retrieval and radiative transfer model. The neural network was trained by historical radiosonde data from the closest upper-air station in Inuvik, N.W.T., Canada (68.30°N; 133.47°W). Data from a concurrent radiosonde program on the *Amundsen* during CFL were used to assess the validity of temperature and water vapor profiles obtained from the MWRP. Air temperatures are accurately portrayed by the MWRP from the surface to about 1500 – 2000 m. Water vapor values were more difficult to validate as values approach zero with increasing height, but generally agreed with values measured by radiosondes [Candlish *et al.*, 2012].

Sea level pressure, air temperature, relative humidity, and wind speed and direction were collected with an automated weather station, the AXYS Automated Voluntary Observation System (AVOS), located on the roof of the ship's wheelhouse. The AVOS obtained atmospheric pressure data using a Vaisala PTB210 sensor (0.01 mb resolution, accuracy of 0.15 mb). Wind speed and direction were collected using an RM Young 05103 anemometer (directional accuracy of 0.3°, magnitude accuracy within +/- 0.3 ms⁻¹). Air temperature and relative humidity were measured with a Rotronics MP

101A temperature and relative humidity sensor (resolution of 0.1°C, accuracy of +/- 0.3°C).

In situ observations of sea ice concentration and meteorological conditions were employed to explain observed coupling. For this paper, seasons are defined as autumn: October to December (OND), winter: January to March (JFM), spring: April to June, (AMJ) and summer: July to September (JAS). Temperature and water vapor profiles were averaged to create hourly and daily profiles of atmospheric temperature and water vapor for the entire MWRP data record. Daily profiles were grouped by season and overlain on the synoptic catalogue to identify wind-driven warm and cold advection events. Hourly profiles of temperature and water vapor were used to investigate case studies of temperature and water vapor advection and to identify surface-based coupling between open leads and the atmosphere.

Upward sensible heat flux was calculated from hourly MWRP temperature profiles following *Raddatz et al.*, [2013]. The Eulerian finite difference form of the heat continuity or thermodynamic energy equation gives the rate of change of the mean temperature, $(\Delta T_m(z)/\Delta t)$ of a layer (Δz) of the atmosphere due to the depletion (flux divergence, $\Delta Q(z)_{Flux}$) or accumulation (flux convergence, $-\Delta Q(z)_{Flux}$) of heat, plus the internal heating/cooling rate due to the phase change of water ($\Delta Q(z)_{Latent}$) within the sub-layer [*Oke* 1987; *Stull* 2000; *Arya* 2001].

$$\Delta Q(z)_{Flux} + \Delta Q(z)_{Latent} = \{\rho_a c_p \Delta z [T_m(z)_{i+1} - T_m(z)_i] / \Delta t\} \quad (4.1)$$

$$\text{where } \Delta Q(z)_{Flux} = \Delta Q(z)_R + \Delta Q(z)_{Wm} + \Delta Q(z)_{Wt} \quad (4.2)$$

The subscripts (*i*) and (*i+1*) indicate mean sub-layer temperatures separated by time, Δt , and ρ_a is the density of air and c_p is the specific heat for air at a constant pressure.

As our interest was upward sensible heat flux from leads, only hours with heat flux convergence in the near surface layers of the ABL were considered. Equation 4.2 equates the heat flux convergence, $\Delta Q(z)_{Flux}$, for a layer of the ABL to the sum of, $\Delta Q(z)_R$, radiation heat flux convergence, $\Delta Q(z)_{Wm}$, heat influx due to the horizontal and vertical components of the mean wind – the former is advection and the latter is subsidence, and, $\Delta Q(z)_{Wt}$, heat influx due to turbulent exchange of sensible heat at the surface and entrainment at the top of the ABL.

Sensible heat flux calculations were restricted to hours when warming of the temperature profile could be attributed to sensible heat flux from the surface, thus removing all heat flux convergence terms except $\Delta Q(z)_{Wt}$ at the atmosphere – surface interface. Restricting our calculations further to clear-sky cases allows us to ignore $\Delta Q(z)_{Latent}$ [Raddatz et al., 2013]. For the hours that fit these criteria, sensible heat flux (SHF) at the surface was obtained by integrating the simplified form of equation. 4.1 from the surface, $z = 0$ to $z = h$, the level where the heat flux convergence dropped to ≤ 0 or began to increase with height [Arya, 2001]. In finite difference form the sensible heat flux at the surface is:

$$SHF = \sum_0^h \{ \rho_a c_p \Delta z [T_m(z)_{i+1} - T_m(z)_i] / \Delta t \} \quad (4.3)$$

4.3 Results and Discussion

4.3.1 Synoptic Climatology and Declining Sea Ice Extent

We first investigate the linkage between 1999 – 2011 atmospheric circulation patterns and declining sea ice extents using the twelve synoptic types (Figure 4.2) representing the full synoptic climatology for the southern Beaufort Sea described in *Asplin et al.*, [2009]. The synoptic climatology of *Asplin et al.*, [2009] is extended to cover the period 1979 – 2011 and is divided into the periods 1979 – 1998 and 1999 – 2011 corresponding to periods when summer sea ice extent is relatively stable, and in rapid decline respectively. Mean annual percent frequencies, persistence, and durations of each synoptic type for 1979 – 1998 and 1999 – 2011 are summarized in Table 4.1. A chi-square frequency test revealed only the annual mean frequency of type 8 changes significantly (+1.9%) at the 90% level ($p = 0.051$). Statistically insignificant increases in annual frequency are detected for type 11 (+1.2%), and type 1 (+0.8%). Synoptic types showing notable decreases were type 2 (-1.0%), type 6 (-1.2%) and type 7 (-1.2%). The changes in the annual frequencies of types 2 and 8, representing anticyclonic circulation, appeared to show a net strengthening of the Beaufort high. Statistically insignificant decreases in the frequencies of type 6 and 7 coupled with an increase in the frequency of type 1 suggest no change in annual cyclone frequencies.

There are notable differences in the mean annual persistence and duration of several synoptic types during 1999 – 2011 compared to 1979 - 1998. Type 8 increased significantly ($p < 0.05$) in persistence by 8.3% suggesting greater longevity for the Beaufort high, however types 2 and 5, which also represent the Beaufort high, changed significantly ($p < 0.1$) in persistence by -3.6% and -4.9% respectively, and suggest a

weakening of the Beaufort high during winter. The mean duration of type 8 decreased by 0.4 days suggesting that type 8 occurred more frequently, but not for longer durations. The persistence of type 6 changed significantly ($p < 0.1$) by -8.3%, however a mean duration increase of 0.3 days indicates fewer but longer-lived winter storms, or a shifted storm track. Type 11 increased significantly ($p < 0.1$) in persistence by 4.9%, which could lead to more frequent durations of easterly wind forcing on sea ice.

*Table 4.1. Synoptic type climatology for 1979 – 1998 and for 1999 – 2011. Significant associations at the 90% and 95% levels are indicated by * ($p < 0.1$) or + ($p < 0.05$).*

Synoptic Type	Frequency (% occurrence of type)			Persistence (% of time same type follows)			Mean Duration (days)	
	Annual			Annual			Annual	
	1979 to 1998	1999 to 2011	(1999 - 2011) - (1979 - 1998)	1979 - 1998	1999 - 2011	(1999 - 2011) - (1979 - 1998)	1979 - 1998	1999 - 2011
Type 1	14.9	15.7	0.8	55.1	57.5	2.4	2.4	2.2
Type 2	12.6	11.6	-1.0	49.5	45.9	-3.6*	1.8	2.0
Type 3	11.6	11.2	-0.3	50.5	50.0	-0.5	2.0	2.0
Type 4	9.9	9.4	-0.6	46.8	49.4	2.6	2.0	1.9
Type 5	8.3	8.1	-0.2	52.9	48.0	-4.9*	1.9	2.1
Type 6	7.9	6.7	-1.2	49.2	40.9	-8.3+	1.7	2.0
Type 7	7.5	6.3	-1.2	38.9	37.5	-1.4	1.6	1.6
Type 8	6.2	8.1	1.9*	50.5	58.8	8.3+	2.4	2.0
Type 9	6.3	6.8	0.5	53.6	50.0	-3.6*	2.0	2.2
Type 10	6.2	6.2	0.0	41.7	41.9	0.2	1.7	1.7
Type 11	4.5	5.7	1.2	40.7	45.6	4.9*	1.8	1.7
Type 12	4.1	4.2	0.1	47.6	45.1	-2.5	1.8	1.9

Changes in the seasonal percent frequencies were considerably more pronounced (Table 4.2). Chi-squared frequency analysis revealed that several seasonal synoptic type frequencies were found to vary significantly at the 95% confidence level ($p < 0.05$). The increased frequency (+4.3%) of Type 1 during JAS indicates an increase in summer cyclone activity. Type 6 decreased ($p < 0.1$) by -2.9% in JFM and -2.0% in OND, which indicates a decrease in cold season cyclone activity. Type 8 increased significantly ($p < 0.05$) by 5.2% AMJ and represents a stronger spring Beaufort high from 1999 – 2011. Significant ($p < 0.05$) increases in frequencies of types 9 and 11 during OND indicate an increase in easterly wind forcing during 1999 – 2011.

Table 4.2. Seasonal percent synoptic type frequencies. 1979 – 1998, 1999 – 2011, and (1999-2011) – (1979 – 1998). Significant associations at the 90% and 95% levels are indicated by * ($p < 0.1$) or + ($p < 0.05$).

Synoptic Type	Seasonal Frequency (%) occurrence)				Seasonal Frequency (%) occurrence)				Seasonal Frequency Anomaly (%)			
	Seasonal				Seasonal				Seasonal			
	1979 – 1998				1999 – 2011				(1999 – 2011)-(1979 – 1998)			
	JFM	AMJ	JAS	OND	JFM	AMJ	JAS	OND	JFM	AMJ	JAS	OND
Type 1	5.9	17.2	27.7	8.5	5.2	18.0	31.9	7.4	-0.7	0.8	4.3+	-1.1
Type 2	17.2	12.9	8.2	12.1	16.1	12.8	7.0	10.5	-1.2	-0.1	-1.2	-1.6
Type 3	6.3	14.6	16.1	9.1	7.9	15.3	14.3	7.4	1.6	0.7	-1.8	-1.8
Type 4	5.2	9.3	18.8	6.4	5.0	7.5	17.6	7.3	-0.2	-1.8+	-1.2	0.9
Type 5	12.2	4.9	2.7	13.6	13.2	3.1	2.8	13.5	0.9	-1.8	0.1	-0.2
Type 6	10.7	3.2	6.1	11.6	7.8	3.8	5.9	9.5	-2.9+	0.6	-0.2	-2.0*
Type 7	8.7	4.9	8.6	7.8	8.0	4.5	6.1	6.8	-0.7	-0.5	-2.5*	-1.0
Type 8	3.9	13.2	4.1	3.8	4.5	18.3	5.6	3.9	0.6	5.2+	1.5	0.1
Type 9	9.6	9.3	1.5	4.9	10.4	6.8	0.9	9.0	0.9	-2.5*	-0.6	4.1+
Type 10	7.9	6.2	3.2	7.6	8.9	5.4	2.8	7.9	0.9	-0.7	-0.4	0.3
Type 11	5.2	2.0	2.3	8.5	6.3	1.9	3.4	11.1	1.2	-0.2	1.1	2.6+
Type 12	7.3	2.3	0.8	6.2	6.8	2.5	1.8	5.8	-0.5	0.3	0.9	-0.4

4.3.2 ABL Profiles for 2007 - 2008

SLP, air temperature time series at the surface and 1500 m, and MWRP temperature profiles (0 – 10 km altitude) are presented for the CFL study 26 November 2007 to 04 August 2008 in Figure 4.4. Lower troposphere (0 – 2 km) air temperature and water vapor density profiles are also presented for JFM and AMJ (Figure 4.5). The SLP record provides a clear summary of the passage of cyclones and anticyclones relative to the position of the *CCGS Amundsen* within Amundsen Gulf (Figure 4.4). Periods of warm and cold air advection associated with the variable synoptic conditions were identified as pulses of warm and cold air in the MWRP temperature record, and correspond with respective decreases and increases in atmospheric pressure. The seasonal shift from winter to warmer spring temperatures was evident with temperatures at 1500 m altitude climbing above freezing (273 K) around the first week of May (DOY 150), and coincides with the beginning of the breakup of the Amundsen Gulf sea ice cover (Figure 4.5).

Figure 4.4. Top) Daily mean sea level pressure from 22 November (J326) to 04 August 2008 (J217), Middle) Daily mean air temperature at surface (~18m) and 1500m from the microwave profiling radiometer, Bottom) 0 – 10 km daily mean atmospheric temperature profile from the microwave profiling radiometer.

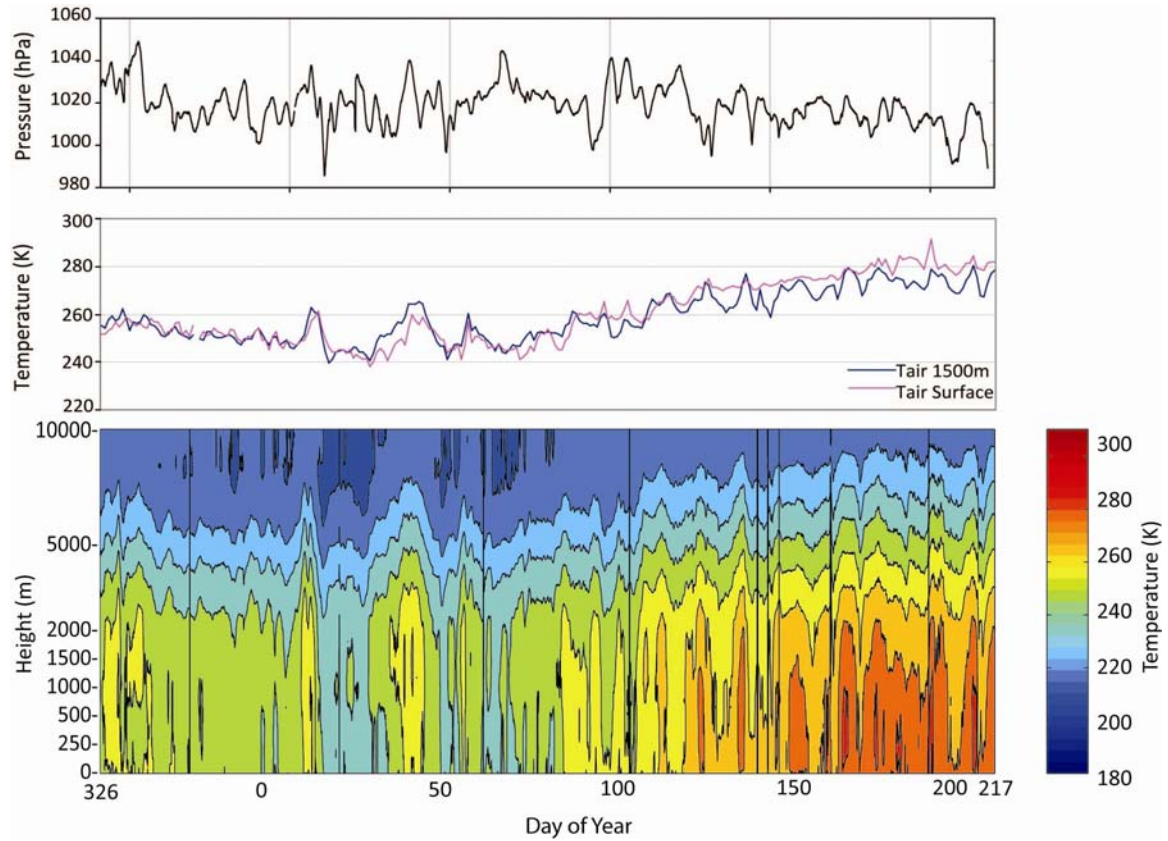
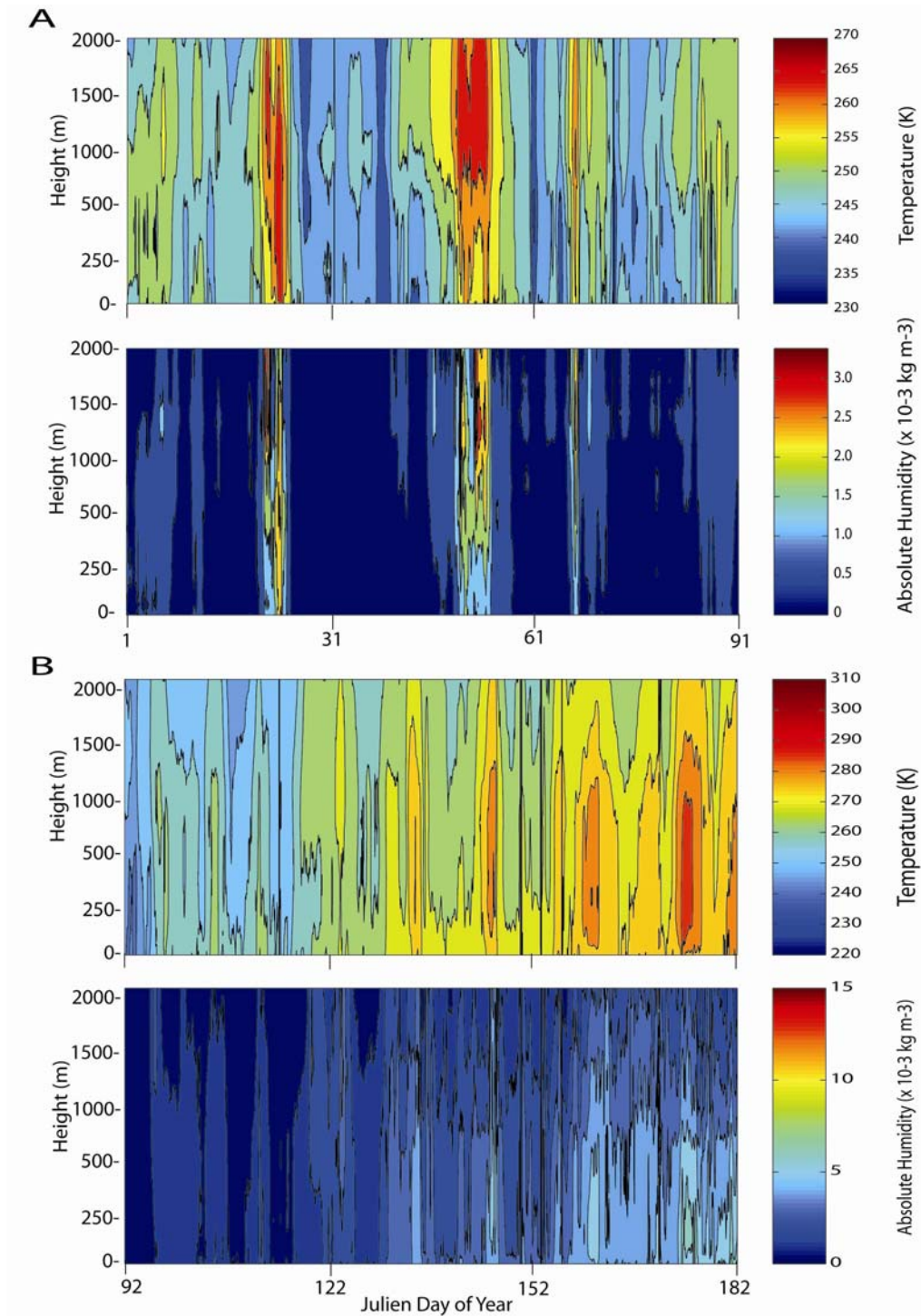


Figure 4.5. 0 – 2000 m microwave profiling radiometer temperature profile (top) and absolute humidity profile (bottom) for JFM (A) and AMJ (B).



Temperature inversions occur where air temperature at 1500 m exceeds the air temperature observed at the surface, and are typically accompanied by moisture aloft. A large moist, warm-air advection event occurred from 11 – 12 February 2008 (DOY 42 – 43), with temperatures at 1500 m approaching 260 K (Figure 4.4). The pulse of warm-air was followed immediately by cold-air advection and a concurrent drop in air temperatures at 1500 m to 240 K. Temperatures at 1500 m and at the surface are strongly controlled at the synoptic scale as a result of warm and cold air advection, however surface temperatures are also strongly influenced by heat fluxes at the underlying surface. Heat fluxes from open sea ice leads likely influenced the near-surface ABL, thereby affecting the surface air temperature throughout the study period [e.g. *Raddatz et al.*, 2012].

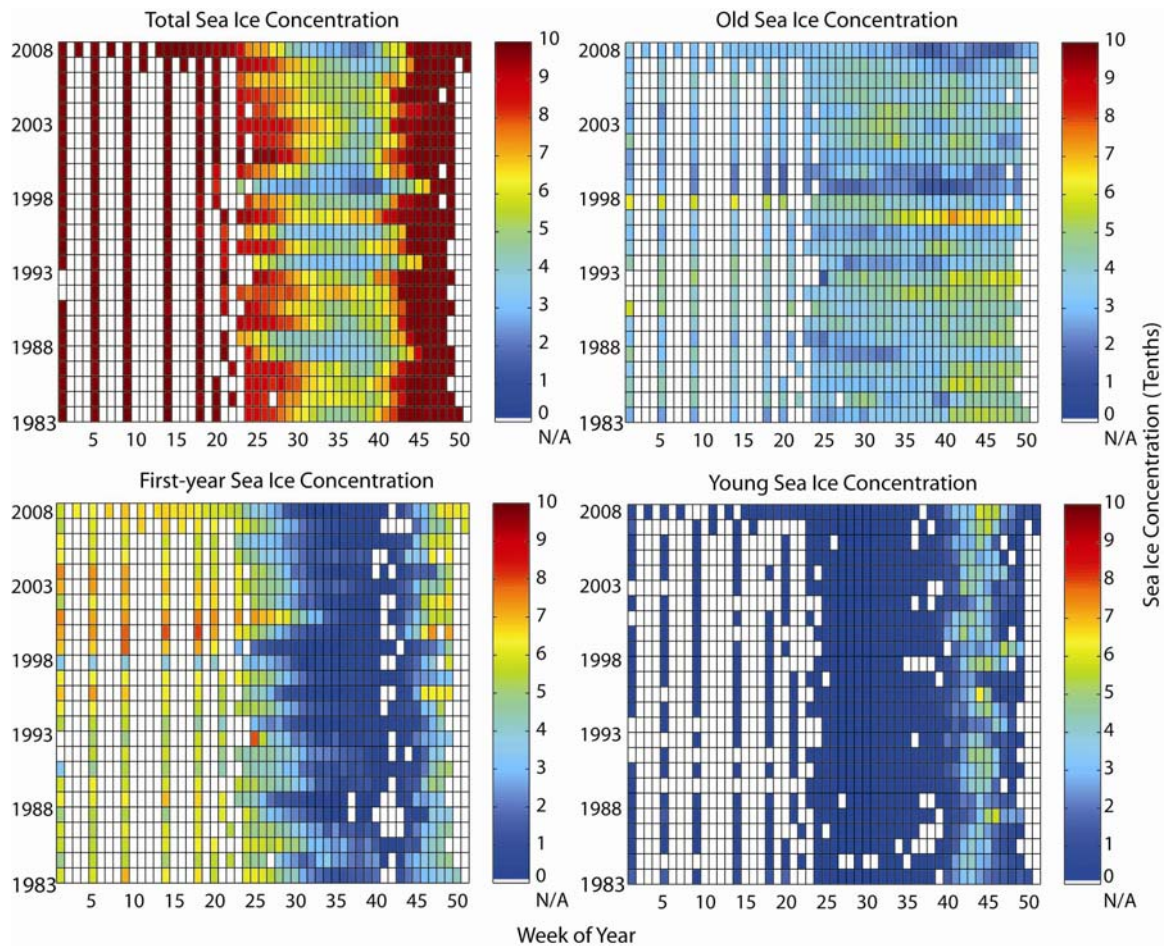
4.3.3 Sea Ice in the southern Beaufort Sea

The percent cover of sea ice age classes are summarized over the period 1983 – 2008 (Figure 4.6) for the southern Beaufort Sea study region (coincident with Figure 4.1) to provide climatological context for the present study, and to highlight trends leading up to the IPY-CFL overwintering period. Old ice is present ($>1/10^{\text{th}}$ coverage) in the study region during autumn in all years with the exceptions of 1998 and 2000 and 2007. Old ice typically rotates clockwise southward with the wind-driven BG during autumn, circulating old ice southward along the coastline of the Canadian Arctic Archipelago. The spring break-up of ice in the study region is driven by dynamic processes such as wind forcing, and strain forcing from clockwise circulation of the BG [*Galley et al.*, 2008]. The open water season (ice concentrations $<3/10$) in the study region usually

occurs between the middle of June and the end of October. The total concentration in the study region depends on the proportion of landfast sea ice in Amundsen Gulf; one out of four years, the entire Amundsen Gulf sea ice cover remains mobile throughout the winter [Galley *et al.*, 2008], as was observed during winter 2007 – 2008 [Barber *et al.*, 2010].

The progression of the freeze-up season in winter 2007-2008 is of particular interest as it followed the dramatic reduction in summer sea ice extent observed during September 2007. Freeze-up was delayed by approximately a month in Amundsen Gulf relative to the regional sea ice climatology [Galley *et al.*, 2008]. At the beginning of September 2007 (week 36), sea ice in the study area consisted mainly of old ice, with small amounts of young sea ice types which rapidly thickened into thin first-year ice, covering 9+/10^{ths} of the region throughout much of the study period (Figure 4.6). Small concentrations of young ice types occurred throughout the winter indicating the presence of leads.

Figure 4.6. 1983 – 2008 areal average week-year sea ice concentration (in tenths) for total sea ice (top left), old sea ice (top right), first-year sea ice (bottom left), and young sea ice types (bottom right).



A substantial reduction in summer old sea ice occurred in 2007 and 2008 in the region corresponding with the minimum hemispheric sea ice extents in those years. Large areas of open water in the Arctic during summer that, barring any import of old sea ice, would refreeze and produce large extents of first-year and younger ice cover types during the autumn season. Notable quantities of young sea ice cover were observed to persist late into 2007 and into early 2008 in the study region. This indicates an overall younger and thinner Arctic ice cover within the study region for the period, which is more susceptible to wind forcing [Spren et al., 2011].

In Figure 4.7 a breakdown of monthly areal quantities of young ice types in the study region for 2007 – 2008 is provided. New and young sea ice types began to form around the third week of September, and signalled the start of freeze-up in the southern Beaufort Sea (Figure 4.7). The southern Beaufort Sea became predominantly ice-covered by the end of October (week 44); however areas of open water persisted within the Amundsen Gulf. The sea ice had thickened into medium (70 – 120 cm) first-year sea ice by mid-December (week 50), and into thick first-year (> 120 cm) sea ice by January 2008 (week 1 - 4) which dominated the region until late April (week 13 - 17). Wind-forcing on the sea ice formed new and young sea ice leads throughout the autumn and winter, documented with *in situ* observations in November 2007 (week 44 - 48) and February 2008 (week 4 - 8) (Figure 4.8). Sea ice in the Amundsen Gulf remained mobile throughout the winter and began to break up in the first week of May (week 18), declining to only 2/10^{ths} coverage of first-year ice by the second week of August 2008 (week 34) (Figure 4.6).

Figure 4.7. Flaw lead areas in Amundsen Gulf during 2007 - 2008 and component areas of young ice types. Total flaw lead area is the cumulative areas of component young ice types including thin first-year (FYtn, 30 – 70 cm), young (Yng, 10 – 30 cm), and new ice (New, < 10 cm).

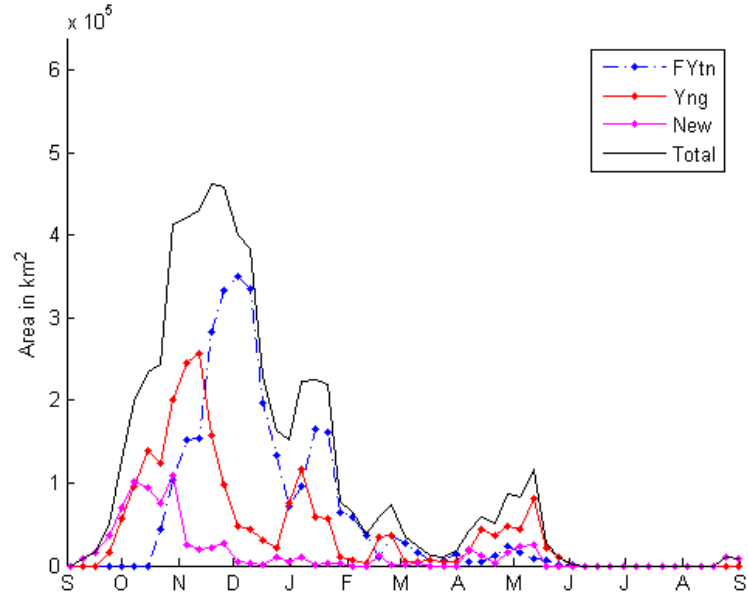


Figure 4.8. Top: photo taken near Nelson Head, Banks Island, N.W.T. Canada on 19 November 2007 showing young and new ice that persisted in this region into early December 2007 due to strong easterly winds associated with synoptic types 10 and 11. Bottom: rapidly refreezing winter lead observed 14 February 2008.



4.3.4 Cyclone Wind Forcing and Lead Formation in 2007-08

Section 3.1 shows that seasonal atmospheric circulation patterns may be shifting, at least in part, as a result of declining summer sea ice extent. Alternating frequencies of synoptic types that force sea ice motion in opposite directions through changes in surface wind forcing cause increased inertial strain within the sea ice cover [Asplin *et al.*, 2009], promoting lead formation. Attribution of lead formation due to wind forcing from cyclones is assessed in the context of declining sea ice cover, changing frequencies of synoptic types, and their combined influence on sea ice motion in the BG.

New ice formation was initially detected in early September in the northernmost areas of the study region, and rapidly spread to all regions by early October 2007. New ice area increased rapidly in October and grew to a peak area of $1.0 \times 10^5 \text{ km}^2$ before declining rapidly in November to $0.3 \times 10^5 \text{ km}^2$ and halted in December. Young ice area peaked in November with an area of $2.4 \times 10^5 \text{ km}^2$ as new ice thickened thermodynamically. Despite the seasonal progression of new ice to young ice, new ice cover was steady at $0.2 - 0.3 \times 10^5 \text{ km}^2$ throughout November, and is attributable to leads forming from frequent and persistent episodes of strong easterly wind forcing arising from high frequencies of synoptic types 9 and 11 during the period (Figure 4.3). Persistent easterly wind forcing drove sea ice in Amundsen Gulf westward, opening new leads for ice production [Barber *et al.*, 2010; Else *et al.*, 2013]. This dynamic wind forcing process persisted throughout November, allowing new leads to open in the young and thin first-year sea ice even as it continued to grow thicker. Strong easterly wind forcing abated in early December 2007, reducing the dynamic forcing responsible for the occurrence of thinner than expected ice types.

Areal extents of thin first-year, young and new ice cover provide a good proxy for wind-driven flaw lead activity during winter and spring when (near) complete sea ice cover is expected. The winter areal maximum coverage of young ice types occurred in early December as the total area of new, young and thin first-year sea ice peaked at $4.6 \times 10^5 \text{ km}^2$ in late November, and then rapidly declined to an area of $1.5 \times 10^5 \text{ km}^2$ in December as thin first-year graduated to medium first-year sea ice almost completely covering the region in sea ice. A local maximum in total flaw lead area occurred in January ($2.2 \times 10^5 \text{ km}^2$) attributed to pulses of new and young ice formation in the Amundsen Gulf associated with episodes of strong easterly wind forcing on the sea ice cover arising from a combination of synoptic types 9 – 11 (Figure 4.3). New ice production stopped for a brief period in March and April 2008 attributed to a strong Beaufort high (types 2, 5 and 8) preventing the passage of storms over the study region (Figure 4.3). This represents a period of *in situ* thermodynamic sea ice growth during which the sea ice extent reached its seasonal maximum. A second local maximum area of total flaw lead area of $1.1 \times 10^5 \text{ km}^2$ was observed in mid-May 2008, corresponding with easterly wind forcing of the BG from synoptic types 9 and 10, and dynamic removal of sea ice from Amundsen Gulf, typical at this time of year [Galley *et al.*, 2008].

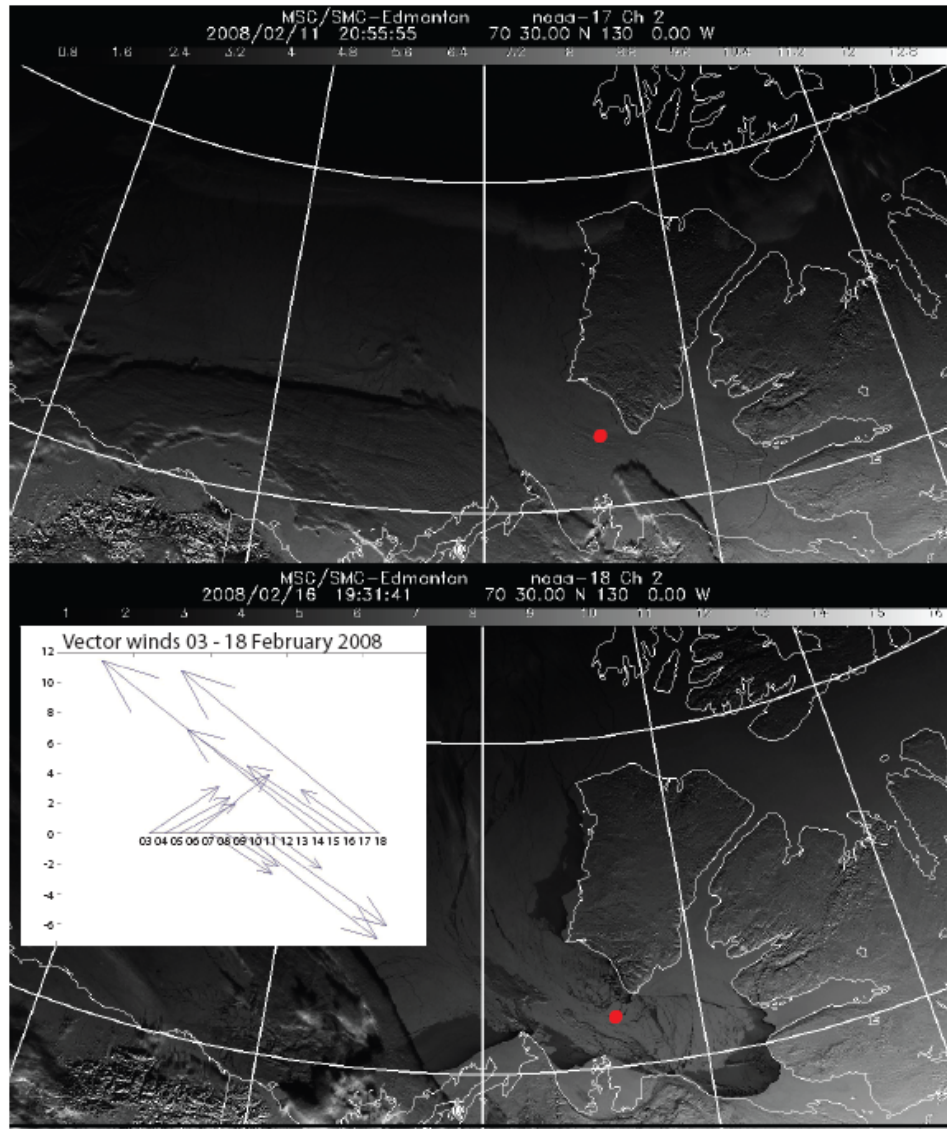
New ice formation continued in the Amundsen Gulf until the end of May 2008 after which air temperature no longer supported the production of new ice (Figure 4.4). A high frequency of type 8 (anticyclone) during spring (Figure 4.3) reinforced anticyclonic vorticity within the BG, and advected sea ice westward, away from the Cape Bathurst region. This follows the findings of Barber *et al.*, [2010] that describe

abnormally high BG vorticity and sea ice mobility during the winter and spring of 2007 – 2008.

4.3.5 Lead Formation Case Study: 03 – 18 February 2008.

An open lead or polynya in Arctic sea ice during winter represents a step-like change in surface air temperature and humidity and creates a T-IBL. We present a case study of cyclone-forced sea ice lead formation observed 03 - 18 February 2008 (DOY 34 – 49) captured by AVHRR infrared satellite images (Figure 4.9). The image for 16 February 2008 20:55:55 UTC (DOY 42) showed consolidated first-year sea ice in Amundsen Gulf. A prominent lead (dark linear feature) was visible along the coast in southeast Amundsen Gulf. The image for 18 February 2008 (DOY 49) showed considerable lead formation, particularly east of Banks Island, north of Tuktoyaktuk, and in the southeast sector of the Amundsen Gulf.

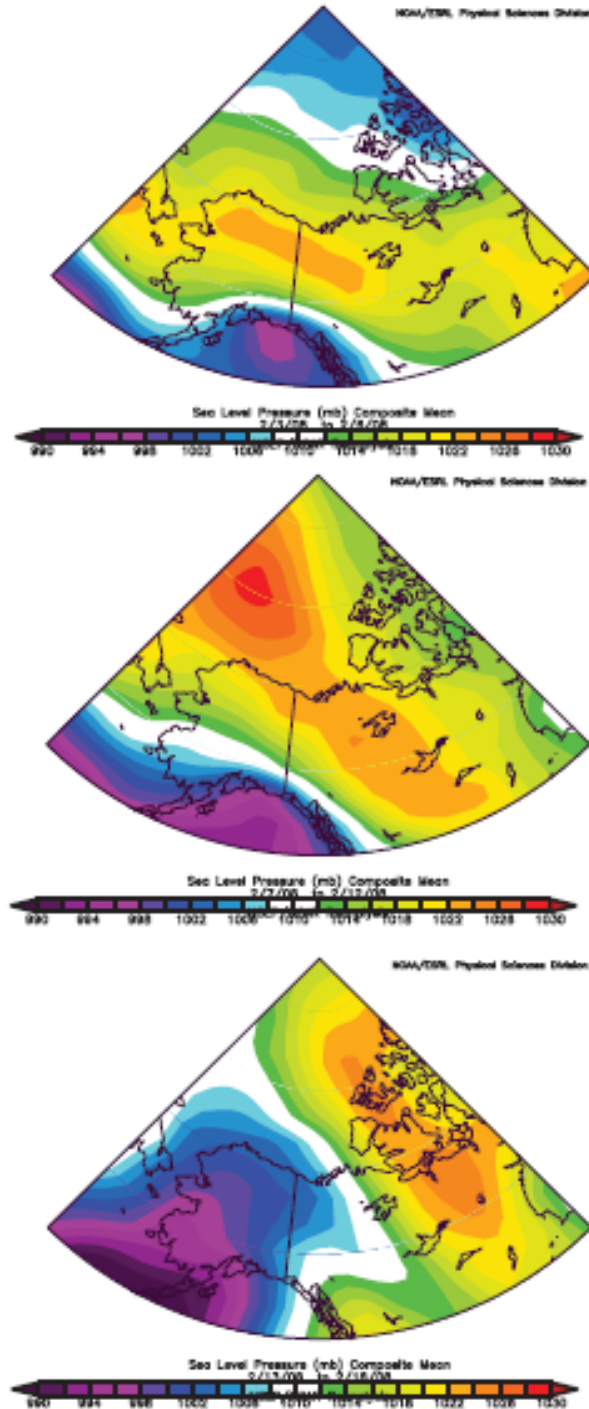
Figure 4.9. Top: Advanced Very High Resolution Radiometer (AVHRR) image for 11 February 2008 20:55:55 UTC showing consolidated sea ice in Amundsen Gulf, and a lead forming southeast of the ship's position (denoted in red). Bottom: AVHRR image for 16 February 2008 19:31:41 UTC showing 85% of Amundsen Gulf sea ice cover as fractured, containing numerous sea ice leads. Vector winds for 03 – 18 February 2008 show wind forcing during this period. AVHRR imagery acquired from the NOAA/AVHRR satellite via the receiving station at the Meteorological Service of Canada's Prairie and Arctic Storm Prediction Centre.



It is likely that the lead visible on 11 February 2008 (DOY 42) image (Figure 4.9) had been formed by wind forcing from the passage of cyclones that impacted the region from 01 – 06 February 2008 (DOY 32 - 37), identified by the occurrence of type 6 from

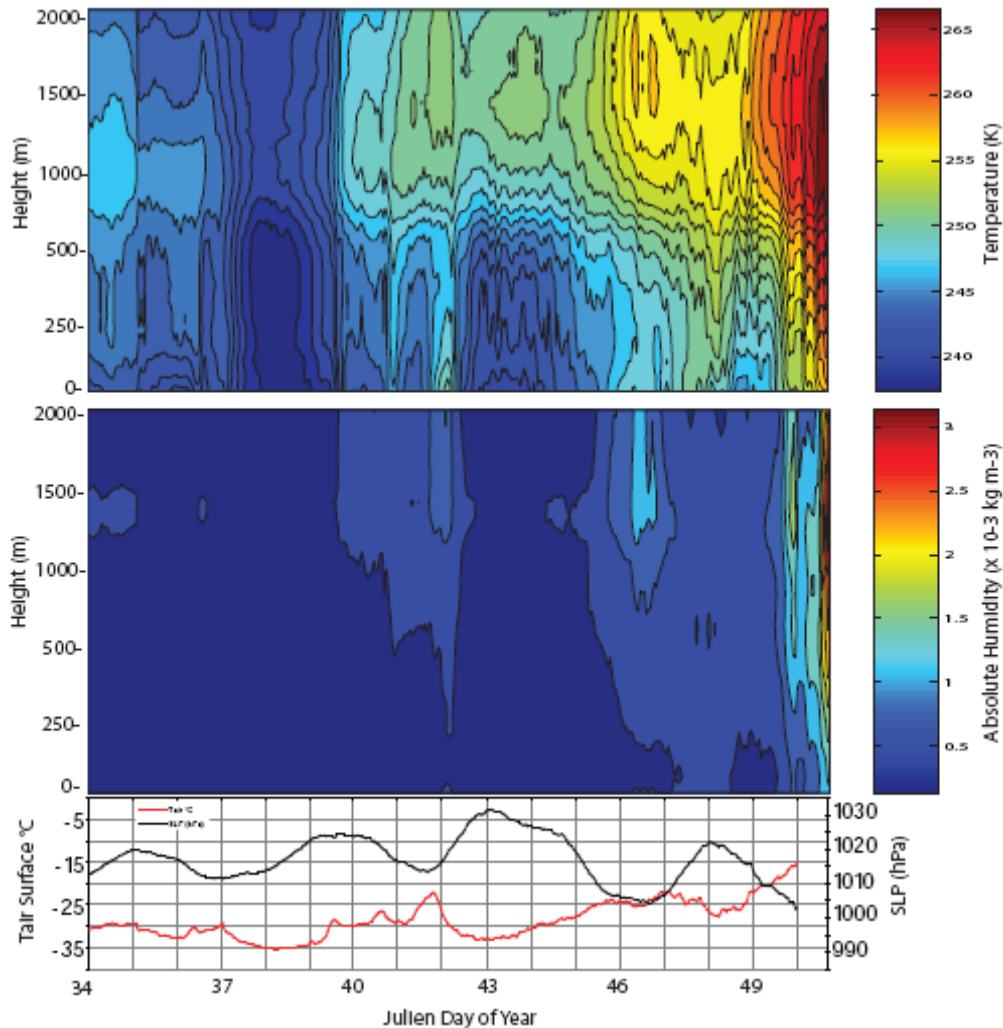
01 – 03 and 05 February 2008, and type 1 on 04 and 06 February 2008 (Figure 4.9). Surface *in situ* wind data (Figure 4.9) indicate southwesterly winds reaching speeds of 8 – 9 m·s⁻¹ by 06 February 2008 (DOY 37) associated with a cyclone (types 1 and 6), then backing to northwesterly winds associated with the building ridge of high pressure from 07 – 11 February 2008 (DOY 38 – 42), characterized by type 2 on 07 – 09 and 11 February 2008, and type 5 on 10 February 2008. Winds then increased to 10 – 12 m·s⁻¹ by 11 - 12 February 2008 (DOY 43 – 43), characterized by the transition from type 2 (anticyclone) to type 9 (Aleutian low). Winds became calm on 13 February 2008 (DOY 44) (type 9 transitioning to type 10), and then became strong (12 – 18 m·s⁻¹) synoptic-scale southeasterly winds persisted from 14 – 18 February 2008 (DOY 45 – 49) (Figure 4.9). These winds are characteristic of types 10 – 11 (Aleutian low), occurring on 14 and 15 February 2008 respectively, transitioning to the passage of another cyclone comprised of type 1 on 16 February 2008 and type 7 from 17 - 18 February 2008 (Figure 4.10). The variation in strength and direction of wind, arising from the transition between synoptic types, likely introduced significant strain within the sea ice cover in Amundsen Gulf, thereby promoting the widespread development of leads (evident as a pulse of new and young sea ice in Figure 4.9) observed on 14 February 2008 (DOY 45), and documented with *in situ* photography (Figure 4.8).

Figure 4.10. Mean sea level pressure composites for 03 – 07 February 2008 (top), 08 – 12 February 2008 (middle), and 13 – 18 February 2008 (bottom) (Images provided by the NOAA/ESRL Physical Sciences Division, Boulder Colorado from their Web site at <http://www.cdc.noaa.gov/>).



The impacts of heat and vapor fluxes from the sea ice leads arising from this event on the ABL are shown for temperature and water vapor profiles for 0 – 2000 m and surface temperatures for 03 – 18 February 2008 (DOY 34 – 49) (Figure 4.11). The presence of a T-IBL was identified on 11 February 2008 (DOY 42) where surface and near-surface (0 – 500 m) air temperatures exhibit periods of warming attributable to sensible heat fluxes from leads, overlaid with cold air above (Figure 4.11). Surface and near-surface ABL temperatures also appear noisy from 15 – 18 (DOY 46 - 49) February 2008, and describe a weakly stable T-IBL due to upward heat fluxes from the surface, despite warm-air advection aloft. During this period, the *CCGS Amundsen* was navigating through open leads. Profiles collected during this period were subject to a highly variable surrounding sea ice surface, ranging from large open-water leads, to 9+/10 sea ice concentrations.

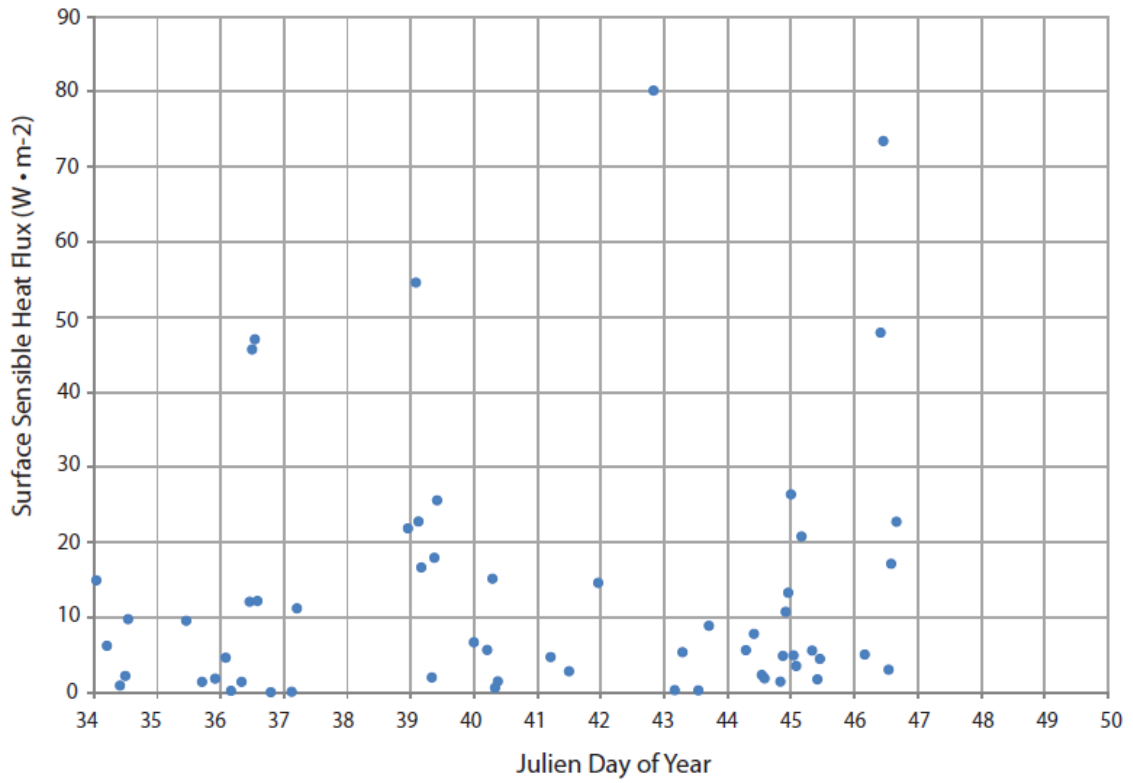
Figure 4.11. Microwave profiling radiometer temperature (top) and water vapor (middle) profiles for 0 – 2000m, and SLP and surface air temperature (bottom) for 03 – 18 February 2008 (DOY 34 – 49). A thermal internal boundary layer (T-IBL) is present from 08 – 12 February 2008 (DOY 39 – 42) and from 15 – 16 February (DOY 46 – 47), and is identified as periods of near-surface atmospheric warming caused by sensible heat fluxes to the atmosphere. Warm air advection reaching the surface on 17 February (DOY 48) removes the contrast between the area-average surface temperature and the air temperature, thereby eliminating sensible heat fluxes to the atmosphere and preventing the formation of a T-IBL.



Values of total sensible heat flux from the surface were calculated for clear-sky cases (figure 4.12). Sensible heat flux typically ranged between 0 – 50 W · m² throughout the event, with a maximum value of 80.14 W · m² on 13 February 2008 (DOY 48), which corresponds to period of maximum regional ice growth, immediately following the lead

formation event. The impact of surface sensible heat fluxes on the near-surface ABL is particularly noticeable between 08 – 12 February 2008 (DOY 39 – 42), evidenced by erratic surface and near-surface ABL temperatures, despite near-surface cold-air advection (Figure 4.11) associated with northwesterly winds during the same period (Figure 4.9). This reflects the influence of mesoscale area-average heat fluxes from large leads developing a T-IBL upstream from the ship location [e.g. *Raddatz et al., 2012*]. Warm air advection penetrating down to the surface is evident from 15 – 18 February 2008 (DOY 46 - 49) (Figure 4.11). The ABL profile for 18 February 2008 (DOY 49) stands-out as a T-IBL was not present (Figure 4.11). The absence of a T-IBL on 18 February 2008 was attributed to the warm air advection that increased the air temperature significantly, eliminating both the contrast between the area-average surface temperature and the air temperature and the sensible heat flux from the surface, allowing the radiative boundary layer (surface-based inversion) to remain [*Raddatz et al., 2012*]. This follows the analysis of *Burk and Thomsson [1995]*, where the passage of a strong frontal inversion was shown to limit the vertical influence of heat fluxes from the surface on the ABL.

Figure 4.12. Clear-sky upward surface sensible heat fluxes calculated for 03 – 18 February 2008 (DOY 34 – 49).



4.4 Conclusions

Three interrelated research questions have been addressed. Sea ice concentration in the study region for autumn 2007 was below normal, particularly due to the near absence of old ice. Complete freeze-up of the study region occurred in the last week of November, about one month later than normal [Galley *et al.*, 2008]. Sea ice concentrations in the study region followed expected seasonal trends through the winter. In spring, an early dynamically-driven break-up of the Amundsen Gulf began the 2008 melt season, decreasing sea ice concentrations in the study region in early June.

High rates of new and young ice production in November, January and May were identified through analysis of the total areal coverage of young ice type classes. Total flaw lead areal maximums of $4.6 \times 10^5 \cdot \text{km}^2$ in November 2007, $2.2 \times 10^5 \cdot \text{km}^2$ in January 2008, and $1.1 \times 10^5 \cdot \text{km}^2$ in mid-May 2008. These values, combined with observations of abnormally high BG vorticity [Barber *et al.*, 2010] indicate a high rate of flaw lead activity throughout the 2007 – 2008 study period.

An updated synoptic climatology [Asplin *et al.*, 2009] was employed to investigate the impacts of declining sea ice extent on atmospheric circulation patterns by contrasting mean synoptic type frequencies, persistence, and durations for 1979 – 1998, and 1999 – 2011, the latter of which represents years of rapidly declining Arctic sea ice cover. Most notably, Type 8 (anticyclone) increased significantly ($p < 0.05$) in annual persistence by 8.3%, suggesting greater longevity for the Beaufort high. Type 11 (Aleutian low) increased significantly ($p < 0.05$) in annual persistence by 4.9%, which represents increased easterly wind forcing on sea ice throughout the year.

Chi-squared frequency analysis investigated changes in synoptic type frequencies between 1979 – 1998 and 1999 – 2011, and revealed that 5 (7) of 12 seasonal synoptic type frequencies were found to vary significantly at the 95% (90%) confidence level ($p < 0.05$) for at least one season. Type 1 significantly ($p < 0.05$) increased in frequency by 4.3% during JAS, indicating an increase in summer cyclone activity while type 6, winter cyclone types, decreased significantly ($p < 0.05$). Types 9 and 11 increased significantly ($p < 0.05$) during OND by 4.1% and 2.6% respectively, and thus represent an increase in autumn easterly wind forcing over the southern Beaufort Sea in 1999 – 2011. Type 8 increased significantly ($p < 0.05$) by 5.2% in AMJ, representing a significantly stronger spring Beaufort high from 1999 – 2011.

Our third objective interlinks objectives one and two to investigate sea ice lead formation, and subsequent heat fluxes to the ABL. The high rate of flaw lead activity during autumn 2007 may be attributable to a relative increase in the frequency and duration of strong easterly wind forcing arising from significant increases in the frequencies of synoptic types 9 and 11 (+4.1% and +2.6% respectively) during OND in 1999 - 2011. Pulses of young ice formation in January and May 2008 were observed in conjunction with large-scale easterly wind-forcing of the regional sea ice cover associated with types 9 - 11. Furthermore, an enhanced spring and summer Beaufort high is indicated by a significant increase in the AMJ (+5.2%) frequency of type 8 (anticyclone) during 1999 – 2011.

A case study of the thermodynamic response of the ABL to a large cyclone-forced winter lead formation event was investigated. A case study was examined for 03 – 18 February 2008 and revealed a large lead formation event in Amundsen Gulf. The

synoptic weather pattern of the period was dynamic, characterized by a closed winter cyclone (type 6), followed by an anticyclone (types 2 and 5), then strong synoptic-scale easterlies over the southern Beaufort Sea (type 10). Calculated values of total sensible heat flux from the surface during the event ranged between 0 – 50 $\text{W}\cdot\text{m}^2$, with a maximum value of 80.14 $\text{W}\cdot\text{m}^2$ on 13 February 2008 (DOY 43), which corresponds with rapid new ice formation concurrent with the opening of the lead. MWRP temperature profiles and sensible heat flux data show that these leads contributed to variability in observed surface and near-surface temperatures before becoming decoupled due to the passage of a warm front.

Wind-induced fractures in sea ice [Barry and Maslanik, 1989], ranging from ephemeral leads to persistent polynyas may become more common due to changing seasonal synoptic circulation patterns in conjunction with a thinning [Laxon *et al.*, 2013] and increasingly mobile Arctic sea ice cover [Rampal *et al.*, 2009]. Furthermore, there is the potential for a positive feedback loop of lead formation, heat flux to the atmosphere, increased cyclone intensity, thus increased wind forcing of sea ice. Recent observations of a highly dynamic ice cover in the Beaufort Sea in the winter months (JFM) of 2013 (NSIDC, 2013) underscore the importance of these meteorological processes coupling the ocean-sea ice-atmosphere interface in a changing Arctic climate.

The net impact of this process on total sea ice extent and volume is presently unclear, and is an important topic for future research. Some possible extensions of this work are therefore to examine whether the relationships observed here (between sea level pressure classifications and lead formation) can be expressed in high resolution coupled ocean-ice-atmosphere models, to improve modeling of coupled dynamic sea ice

processes, and local weather forecasts. Further understanding of how the ABL can become decoupled from synoptic weather systems is important to understand the impacts of autumn and winter sea ice leads on regional cyclogenesis, and subsequent wind forcing of sea ice and near surface oceanic circulation (a topic of further study).

4.5 References

- Agnew, T.A., H. Le, and M. Shokr (1999), Characteristics of large winter leads over the Arctic basin from 85.5 GHz DMSP SSM/I and NOAA AVHRR imagery. *Can J. Remote Sens.* 25(1), 12 – 20.
- Andreas, E.L. (1985), Heat and moisture advection over Antarctic sea ice, *Mon. Wea. Rev.*, 113, 736 – 746.
- Arya, S.P. (2001). *Introduction to Micrometeorology* (2nd ed.) Academic Press, San Diego, CA, 420 pp.
- Asplin, M.G., J.V. Lukovich, and D.G. Barber (2009), Atmospheric forcing of the Beaufort Sea ice gyre: Part I: Surface pressure climatology and sea ice motion, *J. Geophys. Res.* doi: 10.1029/2008JC005127.
- Barber, D. G., M. Asplin, Y. Gratton, J. Lukovich, R. Galley, R.L. Raddatz, and D. Leitch (2010), The International Polar Year (IPY) Circumpolar Flaw Lead (CFL) System Study: introduction and physical system, *Atmos.- Ocean*, 48(4), 225-243, doi:3137/OC317.2010.
- Barry, R.G., and J. Maslanik (1989), Arctic sea ice characteristics and associated atmosphere – ice interactions in summer inferred from SMMR data and drifting buoys: 1979 – 1984, *Geojournal*, 18 (1), 35 – 44.
- Brümmer, B., G. Müller, G. and Hoerber, H. (2003), A Fram Strait cyclone: properties and impact on ice drift as measured by aircraft and buoys. *J. Geophys. Res.* 108, No. D7, 4217, doi: 10.1029/2002JD002638.
- Burk, S. D., and W.T. Thompson (1995), Passage of a shallow front across a Beaufort Sea polynya, *J. Geophys. Res.*, 100(C3), 4461–4472.
- Candlish, L., R.L., Raddatz, M.G. Asplin, and D.G. Barber (2012), Atmospheric temperature and absolute humidity profiles over the Beaufort Sea and Amundsen Gulf from a microwave radiometer. *J. Atmos. Ocean. Technol.* **29**, 1182-1201, doi: <http://dx.doi.org/10.1175/JTECT-D-10-05050.1>
- Cavalieri, D.J., and S. Martin (1994), The contribution of Alaskan, Siberian, and Canadian coastal polynyas to the cold halocline layer of the Arctic Ocean, *J. Geophys. Res.* 99(C9), 18343 – 18362.
- Dierer, S., K.H. Schlünzen, G. Birnbaum, B. Brümmer, and G. Müller, 2005, Atmosphere-sea ice interactions during a cyclone passage investigated by using model simulations and measurements. *Monthly Weather Review* 133: 3678 – 3692.

- Else, B. G. T., T. N. Papakyriakou, M.G. Asplin, D.G. Barber, R.J. Galley, L.A. Miller, and A. Mucci, (2013), Annual Cycle of Air-Sea CO₂ Exchange in an Arctic Polynya Region, *Global Biogeochem. Cy.*, DOI: 10.1002/gbc.20016 (*in press*).
- Fequet, D. (Ed.) (2002), MANICE: Manual of Standard Procedures for Observing and Reporting Ice Conditions, 9th ed., Can. Ice Serv., Environ. Can., Ottawa.
- Gafford, C., J. Nash, E. Walker, T. J. Hewison, J. Jones, and E. G. Norton EG (2008), High time resolution boundary layer description using combined remote sensing instruments, *Ann. Geophys.*, 26, 2597-2612.
- Galley, R.J., E. Key, D.G. Barber, B.J. Hwang, and J.K. Ehn, (2008), Spatial and temporal variability of sea ice in the southern Beaufort Sea and Amundsen Gulf: 1980 – 2004, *J. Geophys. Res.*, 113, C05S95, doi: 10.1029/2007JC004553.
- Galley, R.J., B.G.T. Else, S.J. Prinsenberg, and D.G. Barber (2013), Sea ice concentration, extent, age, motion and thickness in regions of proposed offshore oil and gas development near the Mackenzie Delta, Canadian Beaufort Sea. *Arctic*, 66(1).
- Garratt, J.R. (1990), The Internal Boundary Layer – A Review, *Boundary-Layer Meteorol.* 50, 171 – 203.
- Glendening, (1995), Horizontally integrated atmospheric heat flux from an Arctic lead, *J. Geophys. Res.* 100 (C3), 4613 – 4620.
- Gulder, J., and D Spankuch (2001), Remote sensing of the thermodynamic state of the atmospheric boundary layer by ground-based microwave radiometry, *J. Atmos. and Oceanic Tech.*, 19, 925 – 933.
- Higgins, M.E., and J.J. Cassano (2009), Impacts of reduced sea ice on winter Arctic atmospheric circulation, precipitation, and temperature, *J. Geophys. Res.*, 114, D16107, doi:10.1029/2009JD011884.
- Inoue, J., and M. E. Hori (2011), Arctic cyclogenesis at the marginal ice zone: A contributory mechanism for the temperature amplification?, *Geophys. Res. Lett.*, 38, L12502, doi:10.1029/2011GL047696.
- Intergovernmental Panel on Climate Change (2007), Climate Change 2007: The Physical Science Basis: Contribution of Working Group I to the Fourth Assessment Report of the Intergovernmental Panel on Climate Change, edited by S. Solomon et al., Cambridge Univ. Press, New York.
- Kalnay, E., M. Kanamitsu, R. Kistler, W. Collins, D. Deaven, L. Gandin, M. Iredell, S. Saha, G. White, J. Woollen, Y. Zhu, M. Chelliah, W. Ebisuzaki, W. Higgins, J. Janowiak, K. C. Mo, C. Ropelewski, J. Wang, A. Leetmaa, R. Reynolds, R. Jenne, and D. Joseph,

- 1996: The NMC/NCAR 40-Year Reanalysis Project. *Bull. Amer. Meteor. Soc.*, 77, 437-471.
- Kwok, R., G. F. Cunningham, M. Wensnahan, I. Rigor, H.J. Zwally, and D. Yi (2009), Thinning and volume loss of the Arctic Ocean sea ice cover: 2003 – 2008, *J. Geophys. Res.*, 114, C07005, doi:10.1029/2009JC005312.
- Kwok, R., and G.F. Cunningham (2010), Contribution of melt in the Beaufort Sea to the decline in Arctic multiyear sea ice coverage: 1993–2009, *Geophys. Res. Lett.*, 37, L20501, doi: 10.1029/2010GL044678.
- Laxon S. W., K. A. Giles, A. L. Ridout, D. J. Wingham, R. Willatt, R. Cullen, R. Kwok, A. Schweiger, J. Zhang, C. Haas, S. Hendricks, R. Krishfield, N. Kurtz, S. Farrell and M. Davidson (2013), CryoSat-2 estimates of Arctic sea ice thickness and volume, *Geophys Res Lett.*, 40, doi:10.1002/grl.50193.
- LeDrew, E.L., D. Johnson, J.A. Maslanik, (1991), An examination of atmospheric mechanisms that may be responsible for the annual reversal of the Beaufort Sea ice field. *Int. J. of Clim.* 11, 841 – 859.
- Lukovich, J.V., and D.G. Barber, (2006), Atmospheric controls on sea ice motion in the southern Beaufort Sea. *J. Geophys. Res.* 111, D18103, doi:10.1029/2005/JD006408.
- Lüpkes, C., T. Vihma, G. Birnbaum, and U. Wacker (2008), Influence of leads in sea ice on the temperature of the atmospheric boundary layer during polar night, *Geophys. Res. Lett.*, 35: L03805.
- Markus, T., Stroeve, J.C., Miller, J. (2009), Recent changes in Arctic sea ice melt onset, freeze-up and melt season length, *J. Geophys. Res.* 114, C12024, doi: 10.1029/2009/JC005436.
- Maslanik, J., J. Stroeve, C. Fowler, and W. Emery (2011), Distribution and trends in Arctic sea ice age through spring 2011, *Geophys. Res. Lett.*, 38, L13502, doi:10.1029/2011GL047735.
- Maykut, G.A. (1978), Energy exchange over young sea ice in the Central Arctic. *J. Geophys. Res.* 83 (C7), 3646 – 3658.
- McLaren, A.S., M.C. Serreze, and R.G. Barry (1987). Seasonal variations of sea ice motion in the Canada basin and their implications, *Geophys. Res. Lett.*, 114, 1123-1126.
- NSIDC 2013, <http://nsidc.org/arcticseaicenews/2013/03/a-fractured-maximum/>
- Ogi, M., Yamazaki, K. Wallace, J. (2010), Influence of winter and summer surface wind anomalies on summer Arctic sea ice extent, *Geophys. Res Lett.*, 37, L07701, doi: 10.1029/2009GL042356.

Ogi, M., and J. M. Wallace (2012), The role of summer surface wind anomalies in the summer Arctic sea ice extent in 2010 and 2011, *Geophys. Res. Lett.*, 39, L09704, doi:10.1029/2012GL051330.

Oke, T.R. (1987). *Boundary Layer Climates* (2nd ed.) Methuen, London, 435 pp.

Overland, J.E., S.L. McNutt, J. Groves, S. Salo, E.L. Andreas, and P.O.G. Persson, (2000), Regional sensible and radiative heat flux estimates for the winter Arctic during the Surface Heat Budget of the Arctic Ocean (SHEBA) experiment, *J. Geophys. Res.* 105: C6, 14,093 – 14,102.

Overland, J.E. (2009): Meteorology of the Beaufort Sea. *J. Geophys. Res.*, 114, C00A07, doi: 10.1029/2008JC004861.

Perovich, D.K., J.A. Richter – Menge, K.F. Jones, and B. Light (2008), Sunlight, water, and ice: Extreme Arctic sea ice melt during the summer of (2007), *Geophys. Res. Lett.* 35, L11501, doi: 10.1029/2008GL034007.

Persson, P.O.G., C.W. Fairall, E.L. Andreas, P.S. Guest, and D.K. Perovich (2002), Measurements near the atmospheric surface flux group tower at SHEBA: Near-surface conditions and surface energy budget, *J. Geophys. Res.*, 107 (C10), doi:10.1029/2000JC000705.

Proshutinsky, A. Y., R.H. Bourke, and F.A. McLaughlin (2002), The role of the BG in Arctic climate variability: Seasonal to decadal climate scales. *Geophys. Res. Lett.*, 29 (23), 2100, doi: 10.1029/2002GL015847.

Raddatz, R.L, M.G. Asplin, L. Candlish, and D.G. Barber (2011), General characteristics of the atmospheric boundary layer in a flaw lead polynya region for winter and spring, *Boundary Layer Meteorol.*, doi: 10.1007/s10546-010-9557-1.

Raddatz, R.L., R.J. Galley, and D.G. Barber (2012) Linking the atmospheric boundary layer to the Amundsen Gulf sea-ice cover: a mesoscale to synoptic-scale perspective from winter to summer 2008, *Boundary Layer Meteorol.*, 142, 123 – 148.

Raddatz, R.L., R.J. Galley, L.M. Candlish, M.G. Asplin, and D.G. Barber, (2013), Integral profile estimates of sensible heat flux from an unconsolidated sea-ice surface, *Atmos.- Ocean*, 51(2), 145 – 152, doi: 10.1080/07055900.2012.759900.

Rampal, P. J., Weiss, and D. Marsan (2009), Positive trend in the mean speed and deformation rate of Arctic sea ice, 1979 – 2007, *J. Geophys. Res.*, 114, C05013, doi:10.1029/2008JC005066.

- Rinke, A., Maslowski, W., Dethloff, K., Clement, J. (2006), Influence of sea ice on the atmosphere: A study with an Arctic atmospheric regional climate model. *J. Geophys. Res.* 111, D16103, doi: 10.1029/2005JD006957.
- Rothrock, D.A., Yu, Y., and G.A. Maykut (1999), Thinning of the Arctic sea-ice cover. *Geophys. Res. Lett.*, 26(23), 3469 – 3472.
- Screen J.A., I. Simmonds, and K. Keay (2011). Dramatic inter-annual changes of perennial Arctic sea ice linked to abnormal summer storm activity, *J. Geophys. Res.*, 116, D15105, doi:10.1029/JD015847.
- Serreze, M.C., R.G. Barry, and A.S. McLaren (1989), Sea Ice Concentrations in the Canada basin, *J. Geophys. Res.* 94(C8), 10,955 – 10970.
- Simmonds, I., and K. Keay (2009), extraordinary September Arctic sea ice reductions and their relationships with storm behavior over 1979 – 2008, *Geophys. Res. Lett.*, 36, L19715, doi:10.1029/2009GL039810.
- Solheim, F., J. R. Godwin, E. R. Westwater, Y. Han, S. J. Keihm, K. March, and R. Ware (1998), Radiometric profiling of temperature, water vapor, and cloud liquid water using various inversion methods, *Radio Science*, 33, 393 - 404.
- Spreen, G., R. Kwok, and D. Menemenlis (2011), Trends in Arctic sea ice drift and role of wind forcing: 1992–2009, *Geophys. Res. Lett.*, 38, L19501, doi:10.1029/2011GL048970.
- Stroeve, J.C., M.C. Serreze, M.M. Holland, J.E. Kay, J. Maslanik, and A.P. Barrett (2011a), The Arctic's rapidly shrinking sea ice cover: a research synthesis, *Clim. Ch.* doi:10.1007/s10584-011-0101-1.
- Stroeve, J.C., M.C. Serreze, A. Barrett, and D. Kindig (2011b) Attribution of recent changes in autumn cyclone associated precipitation in the Arctic. *Tellus A* 63(4): 653 – 663, doi:10.1111/j.1600-0870.2011.00515.x.
- Stull, R. (2000). *Meteorology for Scientists and Engineers* (2nd Ed.) Brooks/Cole Thomson Learning, 502 pp.
- Tivy, A., S. E. L. Howell, B. Alt, S. McCourt, R. Chagnon, G. Crocker, T. Carrieres, and J. J. Yackel (2011), Trends and variability in summer sea ice cover in the Canadian Arctic based on the Canadian Ice Service Digital Archive, 1960–2008 and 1968–2008, *J. Geophys. Res.*, 116, C03007, doi: 10.1029/2009JC005855.
- Uttal, T., J. A. Curry, M. G. McPhee, D. K. Perovich, R. E. Moritz, J. A. Maslanik, P. S. Guest, H. L. Stern, J. A. Moore, M. R. Turenne, A. Heiberg, M. C. Serreze, D. P. Wylie, O. G. Persson, C. A. Paulson, C. Halle, J. H. Morrison, P. A. Wheeler, A. Makshtas, H.

Ware, R., R. Carpender, J. Guldner, J. Liljegren, T. Nehr Korn, F. Solhelm, and F. Vandenberghe (2003), A multichannel profiler of temperature, humidity, and cloud liquid. *Radio Science*, 38, 44.1- 44.13.

Yarnal, B. (1993) *Synoptic Climatology in Environmental Analysis: A Primer*. Belhaven Press, London.

CHAPTER FIVE: FRACTURE OF SUMMER PERENNIAL SEA ICE BY OCEAN SWELL AS A RESULT OF ARCTIC STORMS.

Asplin, M.G., Galley, R.J., Barber, D.G., Prinsenberg, S., 2012. Fracture of summer perennial sea ice by ocean swell as a result of Arctic storms, *J. Geophys. Res. Oceans*. doi:10.1029/2011JC007221.

5.1 Introduction

Dramatic reductions in sea ice thickness [Rothrock *et al.*, 1999; Hilmer and Lemke, 2000], age of ice [Maslanik *et al.*, 2007; Nghiem *et al.*, 2007; Maslanik *et al.*, 2011], volume [Kwok *et al.*, 2009], and an increasing melt season length [Markus *et al.*, 2009] have been observed in the northern hemisphere. The passive microwave record from 1979 – 2010 shows a decline in summer minimum Arctic sea ice extent at a rate of approximately $81,310 \text{ km}^2 \text{ year}^{-1}$ (12.4% decade⁻¹) [Stroeve *et al.*, 2011a]. A trend in multi-year (MY) ice loss by *in situ* melting in the Southern Beaufort Sea has been identified [Kwok and Cunningham, 2010] and the oldest types (5 years and older) of sea ice have all but disappeared comprising only $3.04 \times 10^5 \text{ km}^2$ (10%) of remaining MY Arctic sea ice in 2010 [Maslanik *et al.*, 2011]. These phenomena are attributed to increasing regional air temperatures and increased summer ocean mixed layer temperatures [IPCC 2007; Stroeve *et al.*, 2011a] coupled with wind forcing of sea ice [Ogi *et al.*, 2010], persistence of the Beaufort Sea high during summer, increased ocean heat fluxes [Shimada *et al.*, 2006; Woodgate *et al.*, 2006; Steele *et al.*, 2008], and increased surface solar heating [Perovich *et al.*, 2008]. Due to the decline of sea ice extent, large open-water anomalies have been observed in the Chukchi, Siberian, Laptev, and Beaufort seas in 2007 – 2010, as well as large areas of heavily decayed first-year (FY) and MY sea ice [Barber *et al.*, 2009].

The observed rapid reduction of summer sea ice extent and decreasing regional albedos highlight the importance of ocean heat fluxes. Two important ocean heat processes to consider are increasing rates of advective ocean heat transfer from lower latitudes, and increases in solar heating of the ocean surface. An increase of total heat flux into the Arctic through the Bering Strait identified by *Woodgate et al.* [2006] between 2001 and 2004 is capable of melting 640,000 km² of 1-m-thick ice, which matches the reduction in sea ice extent in September (~700,000 km²) for the same period. *Steele et al.* [2008] identifies an average increase in the upper ocean heat content of the summertime southern Chukchi and western Beaufort Seas of about 50 MJ · m⁻² decade⁻¹ during 1965 – 1995 (150 MJ m⁻² over 30 years). *Perovich et al.* [2008] investigated solar heating 1979 – 2005 in the northern Chukchi Sea and identified an average increase of 200 MJ · m⁻².

The declining extent of Arctic sea ice is statistically linked to increasing latent heat fluxes to the atmosphere [*Simmonds and Keay, 2009; Stroeve et al., 2011b*]. Increased latent heat fluxes are purported to be linked to a concurrent increase in Arctic cyclone intensity [*Simmonds and Keay, 2009; Higgins and Cassano, 2009*]; however, a recent study by *Stroeve et al., [2011b]* indicates that this linkage is not yet clear. Storms that form over Eastern Siberia during the summer and autumn can migrate into the Chukchi and Beaufort Seas [*Serreze and Barry, 1988; Zhang et al., 2004*]. Cyclones that become coupled to the cold polar vortex aloft may persist for several weeks [e.g. *LeDrew et al., 1991*], and cyclone winds can even reverse the rotational circulation of the Beaufort Sea Ice Gyre [*McLaren et al., 1987*], which can lead to divergence in the pack ice [*Proshutinsky et al., 2002*]. This process leads to fracturing within the pack ice,

thereby affecting regional albedos and thermodynamic sea ice processes [Serreze *et al.*, 2003; Stroeve *et al.*, 2005]. Changes in summer precipitation from Arctic cyclones may also be contributing to summer sea ice decline. Summer Arctic precipitation occurring as rain (snow) has increased (decreased) by 40% over the period 1989 – 2009, thereby resulting in less snow-covered summer sea ice and decreased regional albedos [Screen and Simmonds, 2011].

The interaction of strong winds from persistent, intense Arctic summer cyclones with increased fetch distances introduces the potential for swells to originate within the Arctic basin. Waves propagating through sea ice are attenuated by friction, scattering interactions between leads and pressure ridges [Wadhams, 1973], and their amplitudes are attenuated exponentially with an exponent of 3 [Squire *et al.*, 2009]. However, wave trains containing long waves are fast-moving and can propagate far into the pack ice. Analysis of ocean wave train evolution and propagation in a 1670 km-long profile of irregular Arctic sea ice obtained from a submarine transect shows that ocean waves with a period of 22 seconds can propagate through the ice cover, and waves with period of 17 and 13 seconds penetrate 350 km and 80 km respectively [Squire *et al.*, 2009]. Long wave propagation has previously been documented deep in the Arctic pack ice [Hunkins, 1962; Liu and Mollo-Christensen, 1988], and corresponds with measurements showing low-amplitude (sub-mm) oscillations in ice floes and ice islands at wave periods of 15 – 60 seconds [Wadhams and Doble, 2009].

Long waves propagating through Antarctic sea ice have been observed to cause flexural swell and fracture within the sea ice cover [Wadhams *et al.*, 1988]. This process has been observed to fracture Antarctic sea ice into smaller, mobile floes that are more

susceptible to lateral melting and dynamic forcing [Toyota *et al.*, 2006; Steer *et al.*, 2008]. The minimum size of a resultant ice floe depends on the ice thickness of the parent floe, where minimum floe diameters after breakup of 14, 24, and 33 m are identified for 1, 2 and 3 m parent ice floe thicknesses respectively [Mellor, 1986]. Flexural swell is most effective at causing fracture within large, contiguous ice floes, and may not affect smaller floes at all [Rothrock and Thorndike, 1984]. Fracturing of sea ice depends highly on the ice floe physical properties, where ice temperature, salinity, and strength are interrelated [Frankenstein and Garner, 1967; Timco and O'Brien, 1994; Timco and Johnston, 2002].

In this section, we present *in situ* observations of large swell propagation into MY Arctic sea ice, and (what we believe to be) first-ever observations of simultaneous fracturing of thick, MY sea ice floes in the southern Beaufort Sea. We determine the origins of the swell, and discuss the physical implications of flexural failure on MY Arctic sea ice dynamic and thermodynamic processes. Because of the recent increase in the open water in summer, this swell induced fracturing may now be a significant feedback mechanism, increasing sea ice decay in the Arctic Ocean.

5.2 Data and Methods

In situ observations of the atmosphere-sea ice-ocean system in the southeastern Beaufort Sea were made from the Canadian Coast Guard Research Icebreaker (CCGS) *Amundsen*. The case study presented here is extracted from the joint ArcticNet/IPY–GeoTraces project, which took place between 27 August and 12 September 2009. The objectives of the ice program during this period were to investigate the geophysical characteristics of the summer ice and to study how sea ice responds to thermodynamic and dynamic forcing. Canadian Ice Service (CIS) digital ice charts were employed for real-time ship and science operations planning during the cruise. CIS digital ice charts are based on expert manual interpretation of Radarsat-1 data (the primary data source since 1996), NOAA-AVHRR and Envisat ASAR data and *in situ* aerial and marine surveys. They include total sea ice concentration and partial concentrations by development stage.

Sea ice thickness surveys were made using a helicopter-mounted electromagnetic induction (EMI) system. This system is well established [*e.g. Prinsenberg and Holladay, 1993*] and consists of the electromagnet, a laser profiler, a nadir-facing video system and navigation, control and archive systems. The near-circular footprint of the helicopter EMI system is about 2.5 times the altitude at which it is flown (~4 – 6 m). The nadir-looking digital camera acquired video of the sea surface from 130 m of altitude. The video width is at a 1 to 1 ratio with altitude. We use this ratio to manually estimate ice floe diameters on video images prior to and after the flexural fracture event. The distribution of ice floe diameters is then fitted to a power-law curve to create two sea ice floe-size cumulative number distributions which can subsequently be used to calculate the change in sea ice floe perimeter.

The distribution of ice floe sizes typically follows a cumulative number distribution that behaves like a power-law relationship (equation 5.1) that can vary from year to year and by region [Rothrock and Thorndike, 1984]:

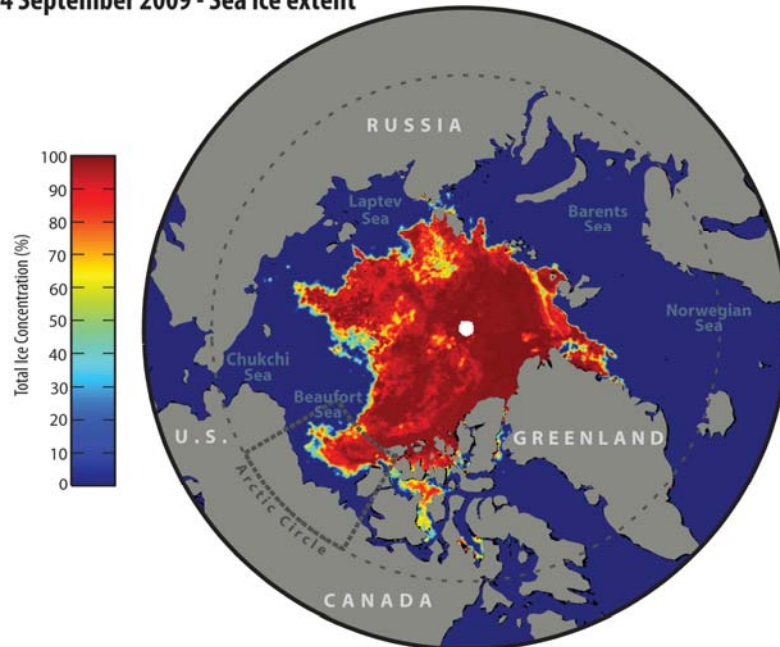
$$N(d)_i \propto ad_i^k \quad (5.1)$$

where $N(d)$ is the cumulative number distribution for floe size regime i , k is the scaling exponent, and a is a constant. Recent studies identify distinct floe size regimes with their own distinct power law distributions [Toyota *et al.*, 2006; Steer *et al.*, 2008]. Toyota *et al.*, [2006] identify two distinct ice floe size distributions: 0 – 40 m diameter, and > 40 m. Steer *et al.*, [2008] describes floe size distributions during the Ice Station Polarstern program (ISPOL), and three distinct distributions are identified for ice floe size: 2 – 20 m, 20 – 50 m, and > 50 m. Each distribution follows a power law distribution with its own unique exponent k .

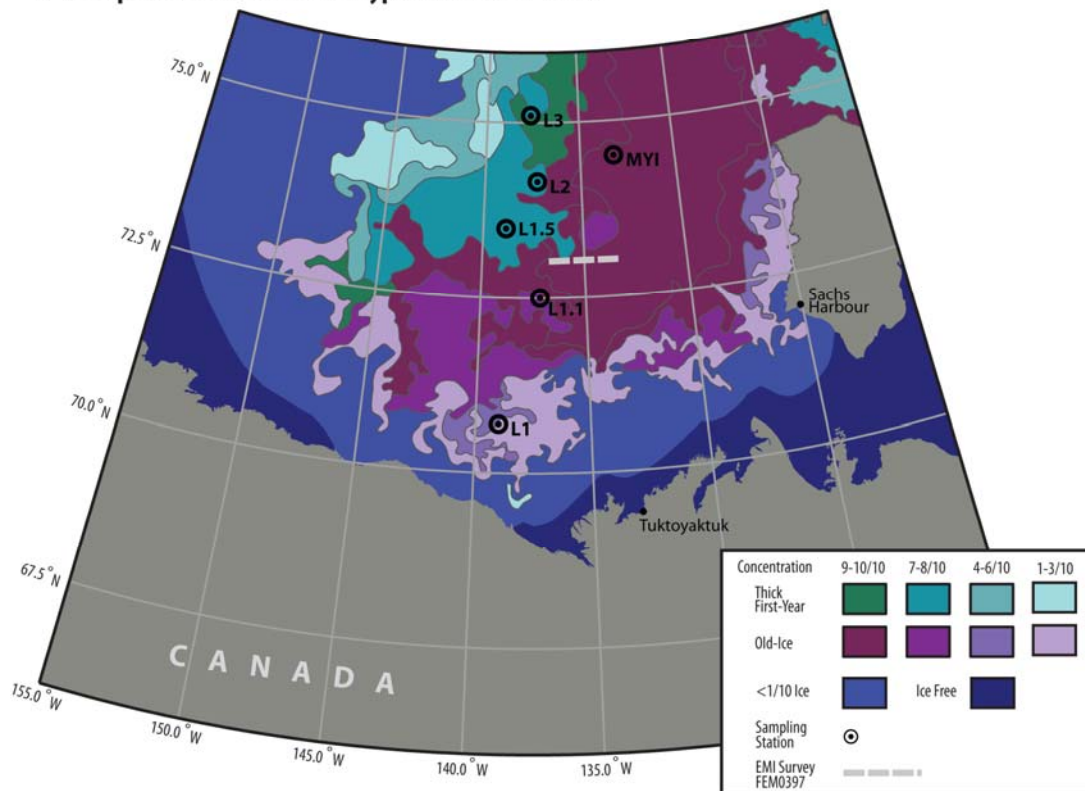
MY ice was physically sampled at station L1 on 31 August 2009 (Figure 5.1), and heavily-decayed first-year (FY) ice at station L2 on 04 September 2009 (Figure 5.1) using a Kovacs Mark II coring system. Sea ice temperature profiles were measured immediately after extracting the ice core by placing a temperature probe in holes drilled at 10 cm intervals beginning at 5 cm from the sea ice surface. Sea ice salinity was measured by cutting a second core into 10 cm sections, placing them in sealed buckets and melting them. Salinity of the melt was calculated from conductivity and temperature using a HACH SENSION5 portable conductivity meter. Sea ice thickness was measured *in situ* with a measuring tape. A conductivity-temperature-depth (CTD) profile of the near-surface ocean column was made from the ship's zodiac using an Idronaut Ocean Seven model 304 CTD.

Figure 5.1. a, National Snow and Ice Data centre (NSIDC) sea ice aerial extent, b, Canadian Ice Service ice chart for 07 September 2009 showing sea ice concentration and stage of development. Ship-based sampling sites and EMI survey FEM09397, flown on 09 September 2009, are shown.

a 04 September 2009 - Sea ice extent



b 07 September 2009 - Sea ice type and concentration



Meteorological data including sea level pressure, air temperature, relative humidity, and vector winds were collected with an AXYS Automated Voluntary Observation System (AVOS), located on the roof of the ship's wheelhouse. Cloud heights were measured using a Vaisala CT25K ceilometer, mounted directly behind the wheelhouse on the port side of the ship. Cloud fractional cover was assessed manually every three hours, and later compared with imagery from an all-sky camera system, consisting of a Nikon D-90 camera with an upward-looking fisheye lens. Downwelling long wave ($L\downarrow$) and shortwave radiation ($K\downarrow$) were collected using an Eppley PIP pyrgeometer and a PSP pyranometer mounted on top of the wheelhouse. A Radiometrics TP/WVP 3000A microwave radiometer profiler (MWRP) measured atmospheric temperature and absolute humidity to a height of 10 km. Temperature and humidity values were derived from microwave brightness temperatures using the manufacturer's neutral network retrievals trained with rawinsonde measurements, and a radiative transfer model [Solheim *et al.*, 1998].

Daily and six-hourly gridded atmospheric data were retrieved from archives maintained by the NOAA-CIRES Climate Diagnostics Centre (CDC), which originate from the National Center for Environmental Prediction (NCEP) Reanalysis I Project [Kalnay *et al.*, 1996]. The spatial resolution of these data is a $2.5^\circ \times 2.5^\circ$ (latitude and longitude) grid. Daily composites of mean sea level pressure (MSLP) and mean vector winds are created for 01 – 06 September 2009 to show the development and movement of the cyclone, and resulting surface winds. It should be noted that the accuracy of NCEP Reanalysis I project MSLP and daily scalar wind data is poor, and must be accounted for when interpreting analysis results. Bromwich and Wang (2005) compared Arctic

rawinsonde wind measurements obtained as part of the CEAREX project with NCEP reanalysis I data, and show that average magnitudes of u and v component winds are understated by NCEP reanalysis I. Correlation coefficients between observed and NCEP reanalysis I data for u and v of ($r = 0.24$ and $r = 0.63$ respectively) show that v component winds are better represented than u component winds; however, it is clear that there is considerable error in both fields.

We were able to directly measure heave, pitch and roll on the *Amundsen* during the swell propagation event while at the MYI and L3 stations (Figure 5.1), using an Applanix POSMv 320 v4 3-D motion sensor, with a sampling frequency of 100 Hz. It should be noted that ship heave depends on ship-hull characteristics and does not provide a direct measure of wave properties; however given the long wavelengths of the observed swells, we were able to obtain reasonable averaged estimates of wave amplitude and period. We then used our estimates of wave amplitude and period to calculate wavelength and wave phase velocity. In deep water, wavelength and period are related by equation 5.2:

$$\lambda = \frac{gt^2}{2\pi} \quad (5.2)$$

Where λ is wavelength (m), t is wave period (sec), and g is gravitational acceleration (9.81m s^{-2}) [Bearman, 1999]. Wave trains travel at half the average speed of the actual waves within the train, and therefore the energy associated with these waves travels at the speed of the wave train. Deep water wave phase velocity c ($\text{m} \cdot \text{s}^{-1}$) follows as equation 5.3:

$$c = \frac{\lambda}{2t} \quad (5.3)$$

Based on the wave phase velocity and direction of the longest wavelength wave groups, we were able to estimate an origin time and location of the swell.

Sea ice flexural strength can be related to the brine volume or total porosity of the ice where increasingly porous ice will have a corresponding decline in ice strength [Timco and O'Brien, 1994]. The flexural strength of sea ice in MPa (σ_f) can be described by:

$$\sigma_f = 1.76e^{-5.88} \sqrt{\nu_b} \quad (5.4)$$

where ν_b is expressed as a brine volume fraction. The brine volume of sea ice can be related to ice temperature (T_i) and ice salinity (S_i) [Frankenstein and Garner, 1967].

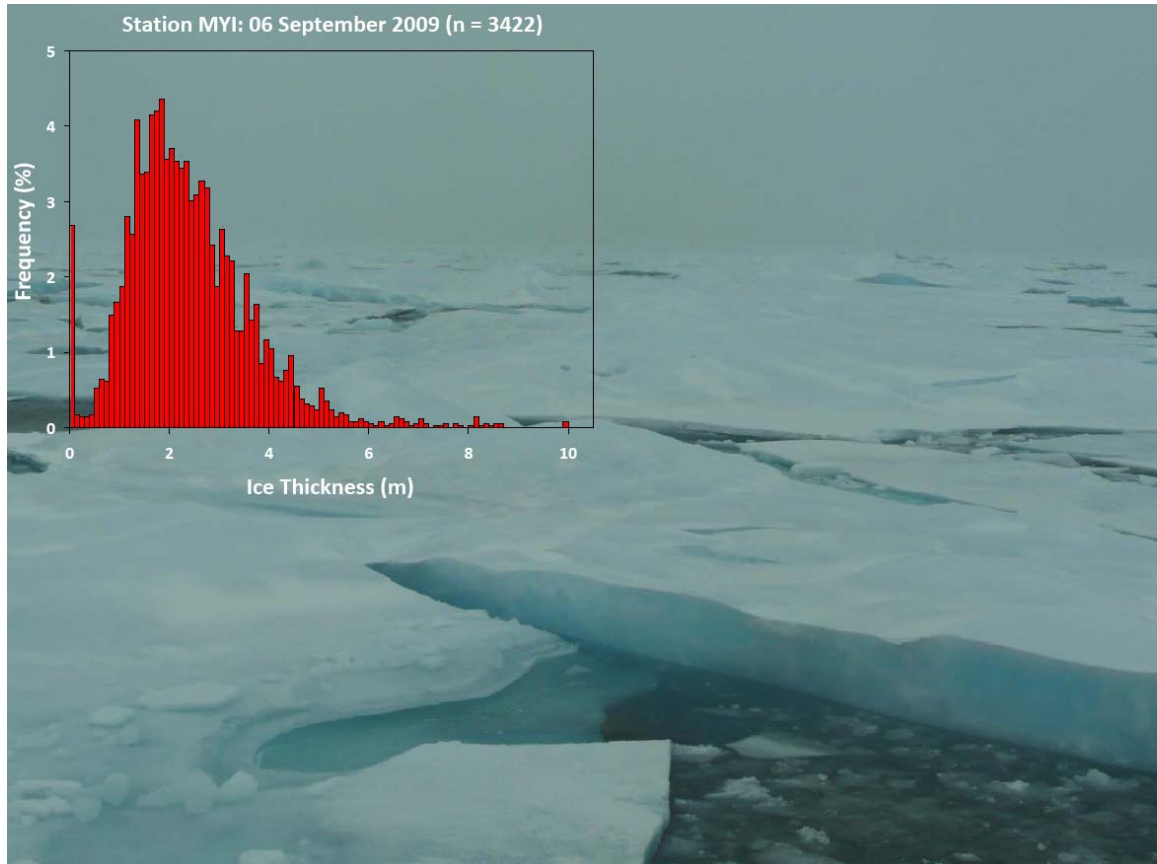
$$\nu_b = S_i \left[\frac{49.185}{T_i} + 0.532 \right] \text{ for } -0.5^\circ\text{C} \geq T_i \geq -22.9^\circ\text{C} \quad (5.5)$$

5.3 Results

On 04 September 2009; we expected the CCGS *Amundsen* to enter summer MY sea ice cover at about 71.333°N, 139.00°W where we had planned to follow a south-to-north transect penetrating as far north into the pack ice as conditions would allow (Figure. 5.1). The CIS chart for 07 September 2009 indicated 7 to 9 tenths old and MY sea ice cover, increasing to 9+ tenths cover as we progressed northward along our sampling line; however, we only encountered heavily decayed FY ice interspersed with fragments of MY ice along this route. This sea ice cover encompassed a large area in lieu of expected MY sea ice, and has been described in detail in *Barber et al.*, [2009].

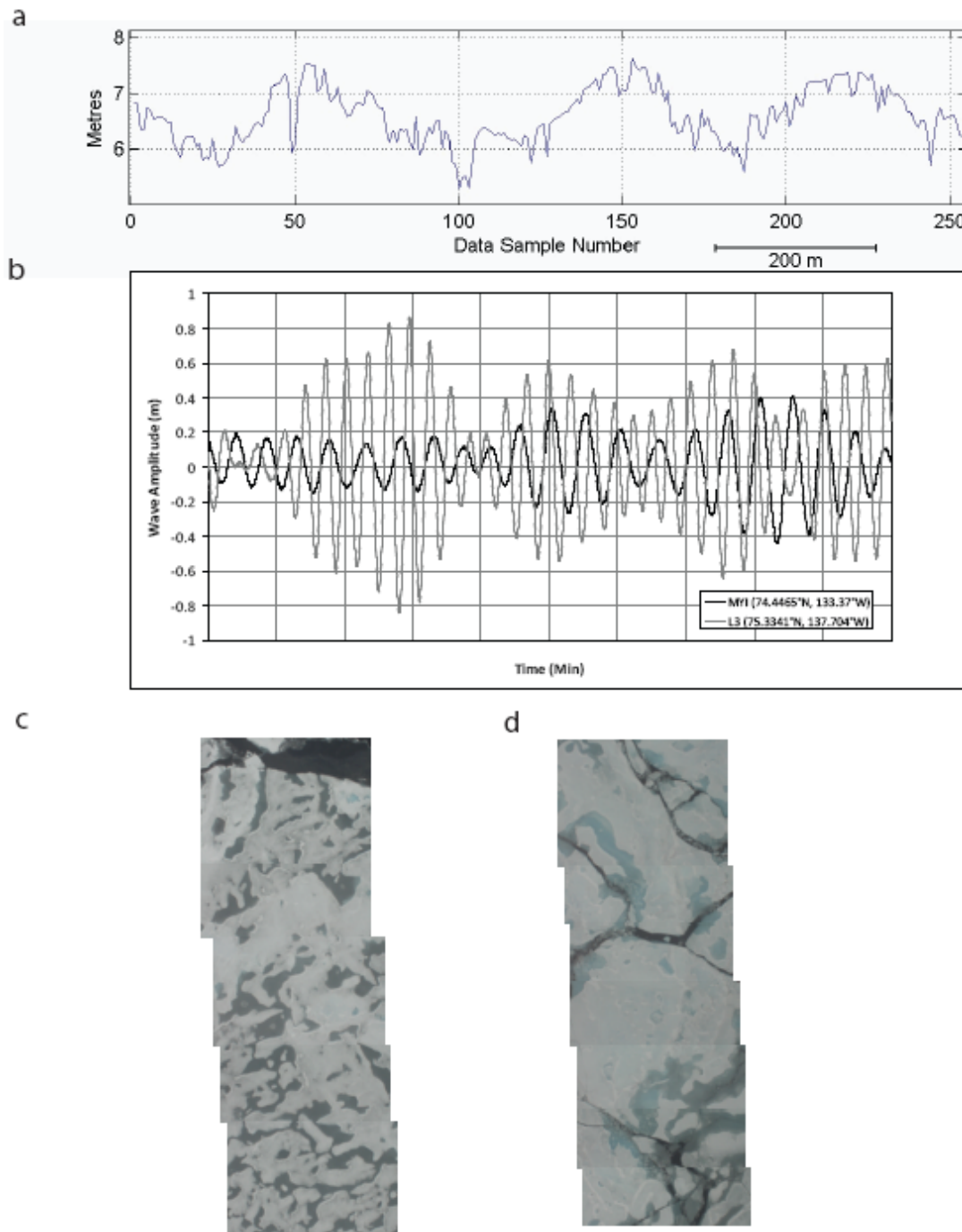
The lack of MY sea ice required us to alter our cruise plan. On 06 September, the CCGS *Amundsen* headed eastward towards the Queen Elizabeth Islands, a region with a high likelihood of large, thick MY ice floes. We progressed through the heavily decayed ice region into a transitional region containing a mix of decayed old and FY sea ice floes, and finally into thick late summer MY pack ice. Using the onboard helicopter to survey the area, we identified a vast MY floe (~10 km diameter), to which we intended to moor the ship, and conduct our typical science operations. The ice in this area was much thicker than the heavily-decayed FY ice that we had encountered the previous day to the west. Our helicopter EMI system recorded overall thicknesses of sea ice around station MYI (e.g., mean = 2.0m, max = 10m) (Figure. 5.2).

Figure 5.2. Summary of 06 September 2009 afternoon helicopter EMI survey (FEM09381) flown over multi-year ice floes at station MYI. The image shows a thick (~5 m) second-year ice floe after flexural fracture as observed from the wheelhouse of the ship. The histogram shows a distribution of ice thicknesses with a mean of 2.0 m.



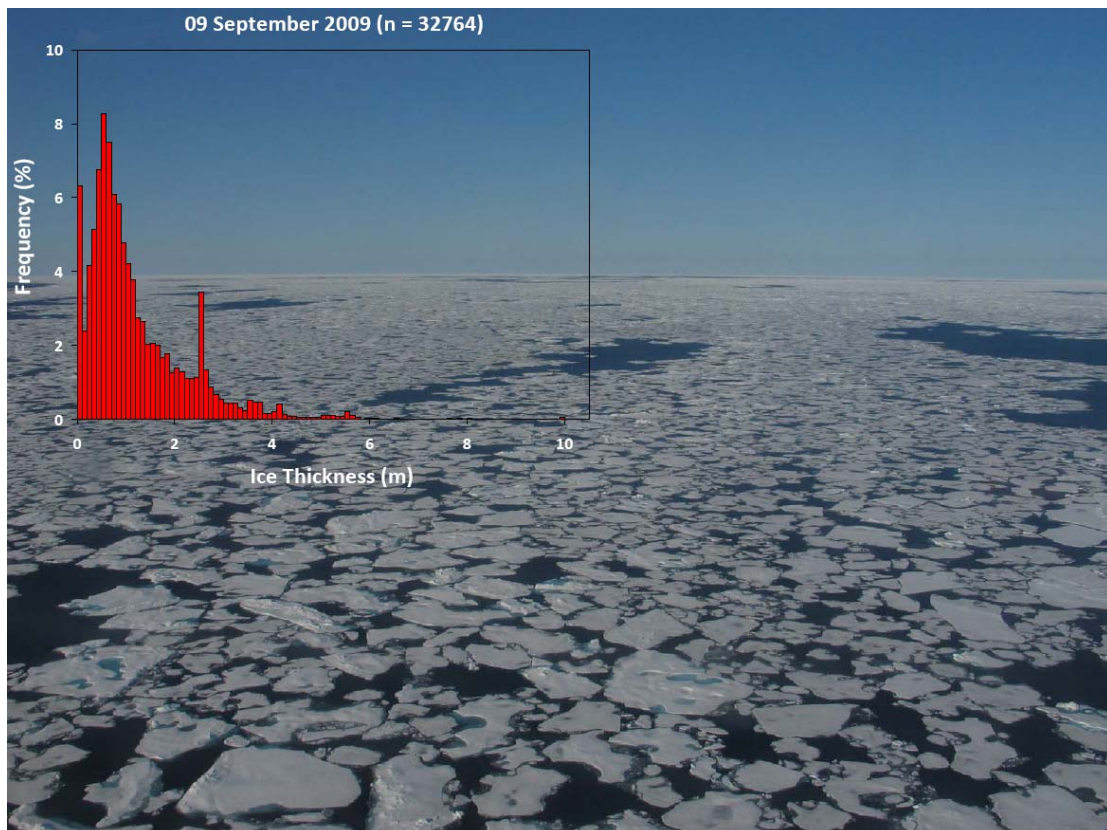
As ice teams initially prepared to deploy to the ice, we noticed the appearance of a swell from the ship's helicopter deck. Laser data collected during the helicopter EMI survey at station MYI indicated a swell period of 13.5 sec, and a wavelength ranging from 200 – 300 m (Figure 5.3). Laser data were collected while the helicopter hovered over a large MY ice floe. These data were augmented with three-dimensional dynamic ship positioning data, which revealed approximate ship heave amplitude of 0.4 m, also with a period of 13.5 sec. The swell caused the vast MY ice floe nearest the *Amundsen* to ride up one side of the swell and fracture as it crested the wave peak, creating smaller ice floes of width approximately one half of the wavelength of the swell. In a matter of minutes from the initial onset of swell propagation, all large MY ice floes in the region were fractured in this manner, yielding a new distribution of smaller MY ice floes ranging from 100 – 150 m in diameter. A helicopter-borne video system recorded this event in still photographs along its flight track which were later combined to create a series of photo mosaics (Figure 5.3). Photos of the fractured MY ice floes were also taken from the ship wheelhouse (Figure 5.2).

Figure 5.3. a, Laser altimeter data from the EMI system at 13:30LST. b, Example of 100 Hz ship heave while at station MYI (06 September 2009, 18:00 to 18:05 UTC) and at station L3 (07 September 2009, 13:40 to 13:45 UTC). c, 17:02 UTC from 06 September 2009 at station MYI, video width = 140. No cracks in old, 2m thick ice floe are visible. d, 19:00 UTC 06 September 2009. Thick ice (2m thick in level ice sections) at station MYI now has cracks aligned perpendicular to swell direction running from NW to SE. Crack spacing is approximately the width of the video (110 m).



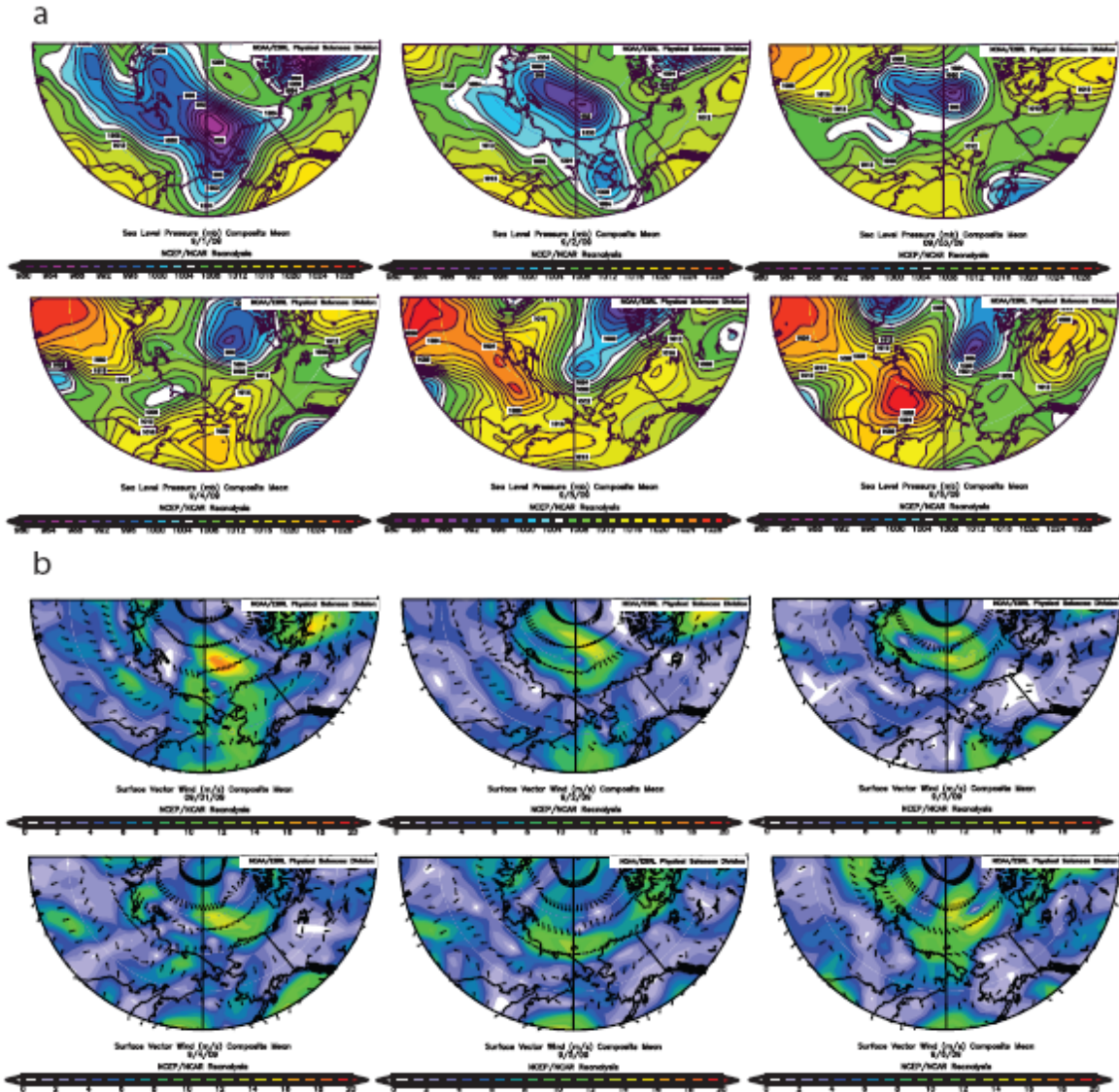
Upon completion of the helicopter-borne EMI and video surveys, the region of heaving MY sea ice cover was deemed unsafe to work on, and the *Amundsen* sailed west to continue regular science operations in areas of lower sea ice concentration (Station L3, 75.3341°N, 137.704°W). On 07 September 2009, we observed swells of shorter period (~9 sec) and amplitude of ~0.8 m. On 09 September 2009, we conducted a longitudinal helicopter EMI survey at 72.5°N (Figure 5.4), and determined the limit of the swell penetration into the pack ice at 72.526°N 134.51°W, a penetration of 350 km. Furthermore, the rotted FY ice margin was heavily fractured, with small floe sizes ranging from 20 – 50 m in diameter (Figure 5.4).

Figure 5.4. Summary of 09 September 2009 afternoon long-line (FEM09397) helicopter EMI survey flown over fractured first and second-year ice floes from 72.52°N 136.75°W to 72.52°N 133.40°W. Image shows rounded first-year ice floes ranging in diameter from 20 – 50 m as observed from the helicopter survey. The histogram describes the ice thickness distribution with a bi-modal distribution with peaks at 0.8 m and 2.5 m.



MSLP for the period 01 – 06 September 2009 revealed the development of two large low-pressure systems (cyclones) over the Siberian coastline on 01 and 04 September 2009, with minimum central pressures of 990 mb and 986 mb respectively (Figure 5.5). Both cyclones were coupled to the polar vortex and steered towards the northeast, tracking over the Chukchi and Beaufort Seas. Mean daily surface winds were calculated for 01 – 06 September 2009 (Figure 5.5). Of particular interest are the winds from the 04 September cyclone, which deepened rapidly on 04 – 05 September 2009 along the Siberian coast. This storm produced strong west and west-southwest winds averaging 12 – 14 $\text{m} \cdot \text{s}^{-1}$ from 04 – 05 September 2009. Spot wind analysis for 12Z 05 September 2009 (not shown) indicates wind speeds may have been gusting to 20 $\text{m} \cdot \text{s}^{-1}$.

Figure 5.5. a, Daily MSLP composites for 01 – 06 September 2009. b, Daily mean vector wind (m/s) composites for 01 – 06 September 2009. (Images provided by the NOAA/ESRL Physical Sciences Division, Boulder Colorado from their Web site at <http://www.cdc.noaa.gov/>).

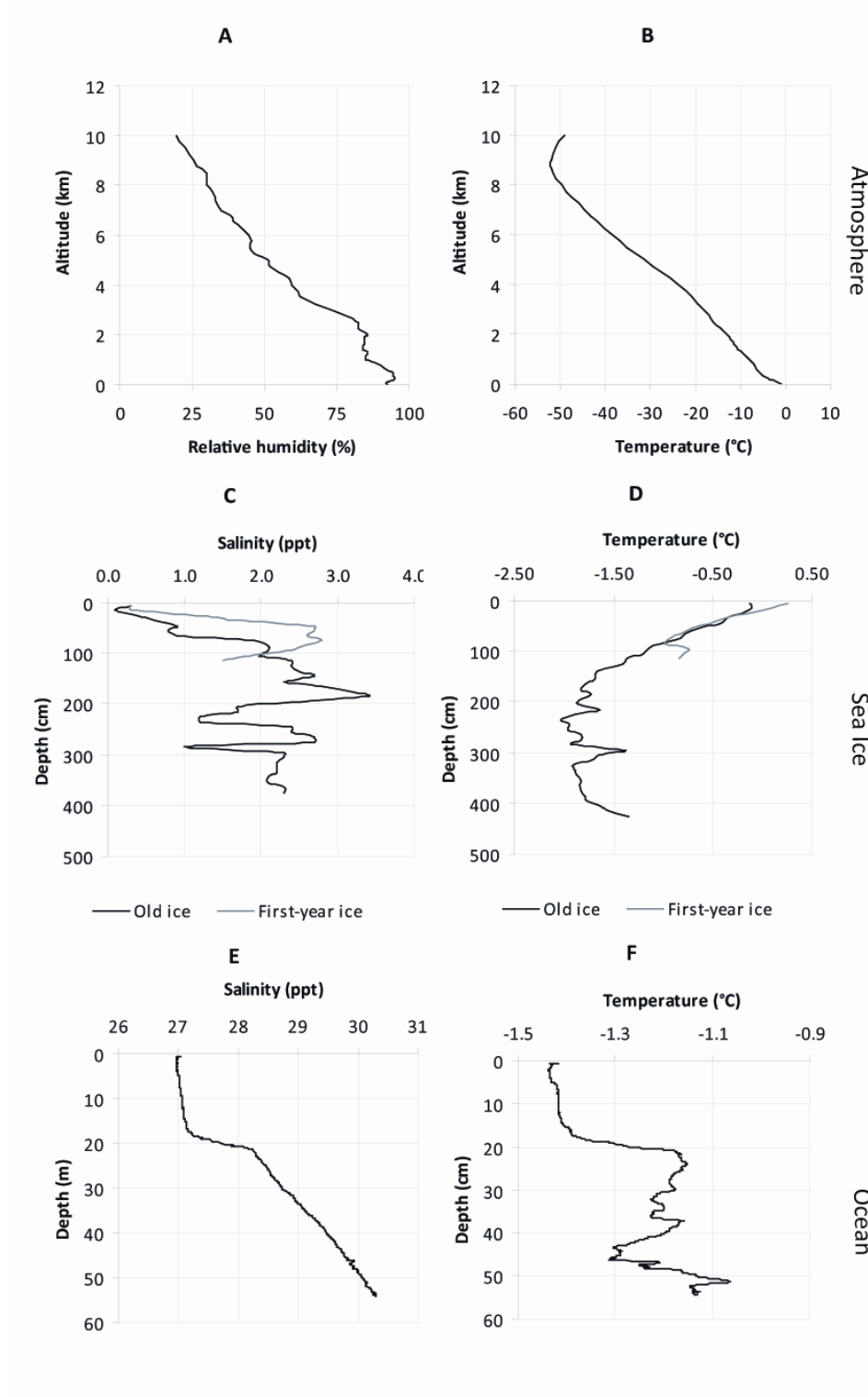


Westerly winds from the two cyclones interacted with the large wind-fetch associated with the ice free Chukchi and Siberian Seas, and forced the development of swells. Using our predetermined periods of 13.5 s and 8.5 s, and wavelengths of 285 m and 150 m, we calculated wave phase velocities of $11 \text{ m} \cdot \text{s}^{-1}$ and $6.81 \text{ m} \cdot \text{s}^{-1}$ respectively. We estimated that the centre of the storm was 970 km from station MYI,

thereby yielding a travel time for wave groups of 24.5 and 39.5 hours respectively. This indicates that the swell development was driven by winds from the 04 September 2009 cyclone, with the waves groups containing the longest wavelengths traveling the fastest.

The strength of sea ice played a key role in permitting the penetration of the swell into the pack ice, and to its flexural fracture. Sea ice strength was assessed by examining temperature and salinity profiles from physical ice core samples (Figure 5.6). By applying equations 5.4 and 5.5, we calculated the average flexural strength to be 64.3 kPa for the FY ice at station L2 and 40.9 kPa for the MY ice at station MYI. These values reflect weak and brittle sea ice and are in agreement with typical late-summer values which can range from 30 – 60 kPa [Timco and Johnson, 2002]. The weak sea ice conditions were attributed to well-drained ice profiles and nearly isothermal temperature profiles. Temperature values from both ice core samples show nearly isothermal temperature profiles. In addition, MWRP temperature values for the atmosphere near the surface were $\sim 0^{\circ}\text{C}$, indicating that the sea ice and atmosphere were nearly in thermal equilibrium. The CTD ocean profile shows clear stratification near the surface where cold, fresh melt water (salinity of 27, and temperature of -1.4°C) lies above a mixed layer (salinity > 28 , and temperature of $-1.25^{\circ}\text{C} - 1.0^{\circ}\text{C}$).

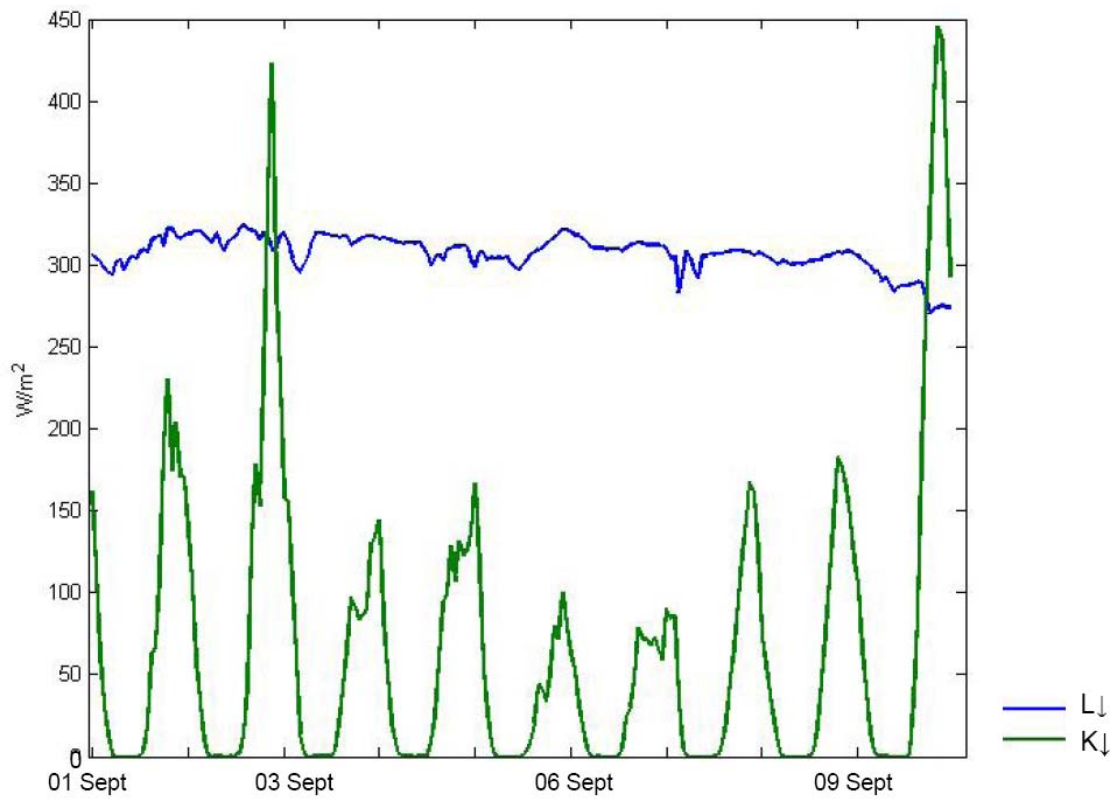
Figure 5.6. a, Atmospheric relative humidity and b, temperature profiles for 06 September 2009. c, Ice salinity d, and temperature profiles for old ice and heavily decayed first-year ice taken at stations MYI and L2 respectively. e, 0 – 50m ocean salinity and f, temperature profiles taken at station L2.



After the ~ 10 km MY ice floe underwent the observed flexural failure event, a helicopter-borne aerial assessment of the regional ice cover revealed a distribution of ice floe diameters ranging from 100 – 150 m. Ice floes in the FY ice were reduced from ~1km in size to 20 – 50m. These small floes are difficult to break mechanically and therefore distributions of small ice floes are governed primarily by thermodynamics [Mellor, 1986]. Sea ice concentration in the ‘rotten’ FY ice zone [Barber *et al.* 2009] was observed at eight-tenths coverage on 07 September 2010, a decrease of one-tenth from prior to the event.

In situ observations of cloud cover, K_{\downarrow} and L_{\downarrow} were used to characterize the surface radiation budget for 06 September 2009 (Figure. 5.7). Two distinct cloud layers were detected throughout the day at an average height of 550m and 3000m respectively. Cloud-fraction cover initially was 75% and became 100% at 06:00 UTC. K_{\downarrow} initially was $167.5 \text{ W}\cdot\text{m}^{-2}$ (hourly-average for 00:00 – 01:00 UTC), $0 \text{ W}\cdot\text{m}^{-2}$ from 05:45 – 12:20 UTC and then reached an hourly-average intensity of $79.9 \text{ W}\cdot\text{m}^{-2}$ by 23:00 UTC. The daily-average value of L_{\downarrow} at the surface was $307.4 \text{ W}\cdot\text{m}^{-2}$.

Figure 5.7. Incoming shortwave ($K\downarrow$) and longwave ($L\downarrow$) radiation time series measured from the CCGS Amundsen from 01 – 09 September 2009.



5.4 Discussion

The long wave swells responsible for the flexural failure in the MY sea ice are due to two key environmental factors. First, the increased wind fetch across the open water in the East Siberian and Chukchi Seas permits migratory Arctic cyclones to generate large waves and swells within the Arctic Ocean. Second, the heavily decayed ice margin did little to attenuate the large swells, and allowed them to penetrate 350 km into the pack ice in the Southern Beaufort Sea. The available wind-fetch distance (coastline-to-ice edge) was on the order of 1800 km. Strong west-southwest winds associated with the slow-tracking 04 September cyclone persisted over the predominantly ice-free Chukchi and Siberian Seas for at least 36 hours. Winds from this cyclone appear to have built upon pre-existing sea state conditions generated by strong winds from the 01 September cyclone, thus a lesser duration of strong winds was required to build a fully-developed sea state. The travel time for the long wave packets observed at station MYI from their place of origin is estimated at 24.5 hours, thereby indicating that the 04 September storm was the source of the long waves.

Fracturing of sea ice due to wind stress, or wave stress depends greatly on sea ice strength. The physical strength of a sea ice floe depends on its internal temperature [Timco and O'Brien, 1994; Tison *et al.*, 2008], with decreasing compressive strength with increasing temperature of the ice. Ice floe properties and ice floe distributions in a given region are dependant on the mechanical and physical properties of the surrounding sea ice [Tison *et al.*, 2008]. It is apparent that deteriorated ice strength attributed to summer warming [Eicken *et al.*, 1995] played a critical role in the flexural failure of the MY ice

floes at station MYI. Furthermore, the heavily decayed ice edge margin [Barber *et al.*, 2009] represents a very weak ice cover that did little to attenuate the incoming swell.

To better estimate the post-flexural failure potential rates of lateral melt, we followed the analysis conducted by Toyota *et al.*, [2006] to investigate the influence that an increasing distribution of smaller floe sizes has on lateral melting within the fractured MY pack ice in our study region. The technique involves estimating total ice floe perimeter before and after the occurrence of flexural failure, using ice floe size distributions from prior-to and following the penetration of the long wave swell. Floe diameters were set to range from 150 – 1500 m and 40 – 150 m before and after the event respectively. Ice floe size distributions were derived following and prior to the flexural failure event with power law exponents of $k_1 = 1.35$ and $k_2 = 1.93$ respectively. Our values of k are comparable with earlier studies. Rothrock and Thorndike, [1984] estimated values of k for ice floes greater than 100 m of $1.7 < k < 2.5$, and $k = 1.11$ for ice floe distributions < 40 m. Our value of $k_1 = 1.93$ for ice floe sizes of > 150 m is comparable to that found by Rothrock and Thorndike [1984]. Our value of $k_2 = 1.35$ for ice floe sizes of 40 – 150 m is reasonable, given that the value of k increases with mean floe size.

Following Toyota *et al.*, [2006], the integration was evaluated against a fixed sea ice concentration ($A = 0.8$) in equation 5.6:

$$A = \int_{d_1}^{d_2} n_a(x)s(x)dx + \int_{d_2}^{d_3} n_b(x)s(x)dx \tag{5.6}$$

Evaluating the integral gives equation 5.7:

$$A = -\frac{\pi\beta k}{4(k-2)}(d_2^{-k_1+2} - d_1^{-k_1+2}) - \frac{\pi\beta k}{4(k-2)}(d_3^{-k_2+2} - d_2^{-k_2+2}) \quad (5.7)$$

where $d_1 = 40$ m, $d_2 = 150$ m, $d_3 = 1500$ m are floe diameters (the upper and lower sizes before and after the event), $n_a(x)dx$ are the number of floes whose diameters are x to $x+dx$ per unit area, $s(x)$ is area of a floe ($\pi d^2/4$), and β is a coefficient for the power law distribution. Assuming approximately rounded floes, this exercise estimates that total ice floe perimeter immediately following flexural failure was approximately 4.5 times greater than before. The actual increase in floe perimeter is likely less as we assume round ice floes, when in fact many of the floes are elliptical or rectangular.

It is expected that flexural failure of MY sea ice, and a corresponding decrease in mean floe diameter size would affect thermodynamic forcing upon sea ice mass balance. Reductions in mean ice floe diameter results in an approximately 4.5 times increase in ice floe perimeter exposed to the ocean, thereby increasing lateral melting via ocean heat flux. The concurrent reduction of sea ice concentration will decrease the regional albedo, resulting in increased entrainment of $L\downarrow$ and $K\downarrow$ to the ocean surface, also enhancing rates of lateral melt. Lateral melting becomes dominant for floes less than several hundred meters in diameter [Steele, 1992], and floes < 40 m in diameter are highly susceptible to lateral melting [Toyota *et al.*, 2006]. Steer *et al.*, [2008] attributed a significant increase in the number of small floes (< 100 m) over a 23-day period in the western Weddell Sea during the ISPOL program to wave-forced divergence in the pack ice, followed by lateral melt. Lateral melting in these areas is likely enhanced due to efficient radiation entrainment in surrounding waters, and a marked increase in initial total ice floe perimeter [Toyota *et al.*, 2006; Steer *et al.*, 2008]. It is also expected that smaller mean floe sizes combined with increased ocean heat fluxes via increased solar

surface heating [e.g. *Perovich et al.*, 2008], and ocean heat advection [e.g. *Woodgate et al.*, 2006], may also enhance the efficiency of bottom-melting. Small ice floes are also more susceptible to dynamic forcing from the wind and ocean currents in the area. They may become easily entrained into the Beaufort Gyre, and moved towards the Chukchi Sea, and Bering Strait where they would be exposed to enhanced ocean heat fluxes from Pacific water intrusions through the Bering Strait [*Shimada et al.*, 2006; *Woodgate et al.*, 2006; *Perovich et al.*, 2008], and would also be vulnerable to wave-induced melt as described by *Wadhams et al.*, [1979].

This process may also have several dynamical implications for the autumn freeze-up period. Small MY ice floes that survive the summer may actually promote ice growth and ice thickness redistribution through rafting and ridging of young FY ice types. Conglomerate ice floes containing young FY ice and small MY ice floes are likely to be initially more susceptible to breakup during freeze-up season which may enhance sea ice mobility and increased ice ridging during the early stages of the freeze-up season. As freeze-up progresses, this process may actually increase ice pack stability where ice thicknesses have increased due to ridging and dynamic ice growth. The impacts of this process on freeze-up processes therefore warrant investigation as this may represent a positive feedback on ice growth.

If this event is analogous to the ongoing wind-wave forcing described by *Steer et al.*, [2008], we expect the distribution of ice floes to shift rapidly towards small diameter ice floes. Although the event occurred close to the 12 September 2009 minimum summer Arctic sea ice extent, measured values of K_{\downarrow} and L_{\downarrow} radiation suggest that sufficient net radiative energy was available at this particular latitude to drive melting for a period

following our departure. 80% of the net thermal energy that enters the ocean through leads goes toward melting ice, while the rest warms the ocean [*Steele*, 1992]. The decrease in mean surface albedo following fracture would allow the ocean surface to absorb a greater amount of incoming radiation, which then would drive lateral melting in the ice floes. Furthermore, ocean heat fluxes would also continue to drive bottom melting.

5.5 Conclusions

The mechanical sea ice decay process described in this section is presented as the result of a combination of several dynamical environmental factors: 1) Reduced summer sea ice extent results in a large area of open water providing a long wind fetch distance, 2) Two large cyclones, originating from a zone of cyclogenesis in Eastern Siberia, tracking over a large area of open water. 3) An overall decline in mean Arctic ice thickness, 4) a heavily-decayed ('rotten') FY ice cover flanking the MY pack ice in the Southern Beaufort Sea with a calculated average flexural strength of 64.3 kPa. 5) Warm, nearly isothermal and low-strength MY ice coverage with a calculated average flexural strength of 40.9 kPa. These factors are driven by climate change, and are representative of a shift in the Arctic sea ice regime, from one characterized by a predominately MY ice cover, towards a new regime comprised of seasonal FY sea ice. The most striking result of this event is the large spatial extent over which fractured sea ice cover was observed, and represents a nearly instantaneous reduction in regional mean ice floe size, thereby affecting regional albedo values and surface energy budgets. The resulting smaller floes are highly susceptible to lateral melting and decay, especially when transported dynamically to the south and west in the Beaufort sea ice gyre where they are subject to increased solar radiation, to increased bottom melt from Pacific warm water intrusions, or advection of warmer surface mixed layer waters from open water areas, under the remnant pack ice.

This event represents a new mechanical forcing mechanism upon sea ice cover in the Arctic Basin. Of note, this represents a positive feedback process that may accelerate the loss of sea ice cover, particularly during the summer months. We are convinced that

events of this nature will continue to occur in future years, especially when large wind fetch distances emerge early in the melt season, and are bound to have implications for coastal erosion, transportation, and industrial activities in the Arctic Basin. Continued monitoring of the Arctic Basin is essential to better understanding new forms of ocean-sea ice-atmosphere interactions and coupling as they emerge in the coming seasonal Arctic sea ice regime. This process will have implications for modeling future sea ice dynamics and thermodynamics, and needs to be included in regional and large scale climate models to enhance processes of sea ice decay, formation and motion.

5.6 References

- Barber, D.G., Galley, R., Asplin, M.G., De Abreu, R., Warner, K.A., Pućko, M., Gupta, M., Prinsenberg, S., and Julien, S., (2009), Perennial pack ice in the southern Beaufort Sea was not as it appeared in the summer of 2009, *Geophys. Res. Lett.*, 36, 24, doi:10.1029/2009GL041434.
- Bearman, G. (1999) *Waves, tides and shallow-water processes*, 2nd edition, Butterworth-Heinemann, Oxford, ISBN 0-7506-4281-5, 12 – 47.
- Bromwich, D.H., and Wang, S-H., (2005), Evaluation of the NCEP-NCAR and ECMWF 15- and 40-yr reanalyses using rawinsonde data from two independent Arctic field experiments, *Mon. Weather. Rev.*, 133, 3562 – 3578.
- Dierer, S., Schlünzen, K.H., Birnbaum, G., Brümmer, B., and Müller, G. (2005), Atmosphere-sea ice interactions during a cyclone passage investigated by using model simulations and measurements, *Mon. Weather. Rev.*, 133, 3678 – 3692.
- Frankenstien, G.E. and Garner, R. (1967), Equations for determining the brine volume of sea ice from 0.5 – 22.9 C. *J. Glaciol.* 6, 943 – 944.
- Kalnay, E., Kanamitsu, M., Kistler, R., Collins, W., Deaven, D., Gandin, L., Iredell, M., Saha, S., White, G., Woollen, J., Zhu, Y., Chelliah, M., Ebisuzaki, W., Higgins, W., Janowiak, J., Mo, K. C., Ropelewski, C., Wang, J., Leetmaa, A., Reynolds, R., Jenne, R., Joseph, D. (1996), The NCEP/NCAR 40-year reanalysis project. *Bull. Amer. Meteor. Soc.*, 77, 431 – 437.
- Kay, J.E., and Gettelman, A., (2009), Cloud influence on and response to seasonal Arctic sea ice loss, *J. Geophys. Res.*, 114, D18204, doi: 10.1029/2009JD011773.
- Kwok, R., G. F. Cunningham, M. Wensnahan, I. Rigor, H.J. Zwally, and D, Yi (2009), Thinning and volume loss of the Arctic Ocean sea ice cover: 2003 – 2008, *J. Geophys. Res.*, 114, C07005, doi: 10.1029/2009JC005312.
- Kwok, R., and Cunningham, G.F., (2010), Contribution of melt in the Beaufort Sea to the decline in Arctic multiyear sea ice coverage: 1993–2009, *Geophys. Res. Lett.*, 37, L20501, doi: 10.1029/2010GL044678.
- Higgins, M.E., and Cassano, J.J. (2009), Impacts of reduced sea ice on winter Arctic atmospheric circulation, precipitation, and temperature, *J. Geophys. Res.*, 114, D16107, doi: 10.1029/2009JD011884.
- Hilmer, M., and Lemke, P., (2000), On the decrease of Arctic sea ice volume, *Geophys. Res. Lett.*, 27(2), 3751 – 3754.

Hunkins, K. (1962), Waves on the Arctic Ocean, *J. Geophys. Res.*, 67, 2477– 2489.

Intergovernmental Panel on Climate Change (2007), *Climate Change 2007: The Physical Science Basis: Contribution of Working Group I to the Fourth Assessment Report of the Intergovernmental Panel on Climate Change*, edited by S. Solomon *et al.*, Cambridge Univ. Press, New York.

Liu, A. K., and Mollo-Christensen, E., (1988), Wave propagation in a solid ice pack, *J. Phys. Oceanogr.*, 18, 1702–1712.

Markus, T., Stroeve, J.C., and Miller, J. (2009), Recent changes in Arctic sea ice melt onset, freeze-up and melt season length, *J. Geophys. Res.*, 114, C12024, doi: 10.1029/2009/JC005436.

Maslanik, J.A., Fowler, C., Stroeve, J., Drobot, S., Zwally, J., Yi, D., Emery, W., (2007), A younger, thinner Arctic ice cover: Increased potential for rapid extensive sea ice loss, *Geophys Res. Lett.*, 34, L24501, doi: 10.1029/2007GL032043.

Maslanik, J., Stroeve, J. Fowler, C. and Emery, W. (2011), Distribution and trends in Arctic sea ice age through spring 2011, *Geophys. Res. Lett.*, 38, L13502, doi: 10.1029/2011GL047735.

McLaren, A.S., Serreze, M.C. and Barry, R.G. (1987), Seasonal variations of sea ice motion in the Canada Basin and their implications. *Geophys. Res. Lett.*, 14, 1123 – 1126.

Mellor, M., (1986), Mechanical behaviour of sea ice, in Untersteiner, N (ed.), *The geophysics of Sea ice*, Plenum, New York, 165 – 281.

Nghiem, S. V., Rigor, I. G., Perovich, D. K. Clemente-Colon, P., Weatherly, J. W. and Neumann, G. (2007), Rapid reduction of Arctic perennial sea ice, *Geophys. Res. Lett.*, 34, L19504, doi: 10.1029/2007GL031138.

Ogi, M., Yamazaki, K. and Wallace, J. (2010), Influence of winter and summer surface wind anomalies on summer Arctic sea ice extent, *Geophys. Res. Lett.*, 37, L07701, doi: 10.1029/2009GL042356

Perovich, D.K., Richter-Menge, J.A., Jones, K.F., and Light, B. (2008), Sunlight, water, and ice: Extreme Arctic sea ice melt during the summer of (2007), *Geophys. Res. Lett.*, 35, L11501, doi: 10.1029/2008GL034007.

Prinsenber, S.J. and Holladay, J.S. (1993), Using an air-borne electromagnetic ice-thickness sensor to validate remotely sensed marginal ice zone properties. In: *Proceedings of the 12th International Conference on Port and Ocean Engineering under Arctic Conditions*, August 17 – 20, Hamburg (FRG). Vol. 2: pp. 936 – 948.

- Proshutinsky, A.Y., Bourke, R.H., and McLaughlin, F.A. (2002), The role of the BG in Arctic climate variability: Seasonal to decadal climate scales. *Geophys. Res. Lett.*, 29 (23), 2100, doi: 10.1029/2002GL015847.
- Rothrock, D.A. and Thorndike, A.S. (1984), Measuring the sea ice floe distribution, *J. Geophys. Res.* 89 (C4), 6477 – 6486.
- Rothrock, D.A., Yu, Y., and Maykut, G.A. (1999), Thinning of the Arctic sea-ice cover. *Geophys. Res. Lett.*, 26(23), 3469 – 3472.
- Screen, J. and Simmonds, I. (2011), Declining summer snowfall in the Arctic: causes, impacts and feedbacks, *Clim. Dyn.* DOI: 10.1007/s00382-011-1105-2.
- Serreze, M.C., and Barry, R.G. (1988), Synoptic activity in the Arctic Basin. 1979-85, *J. Clim.*, 1, 1276 – 1295.
- Shimada, K., T. Kamoshida, M. Itoh, S. Nishino, E. Carmack, F. McLaughlin, S. Zimmermann and A. Proshutinsky (2006): Pacific Ocean inflow: Influence on catastrophic reduction of sea ice cover in the Arctic Ocean. *Geophys. Res. Lett.*, 33, L08605, doi: 10.1029/2005GL025624.
- Simmonds, I., and Keay, K. (2009), extraordinary September Arctic sea ice reductions and their relationships with storm behavior over 1979 – 2008, *Geophys. Res. Lett.*, 36, L19715, doi: 10.1029/2009GL039810.
- Solheim, F., J. R. Godwin, E. R. Westwater, Y. Han, S. J. Keihm, K. March, and R. Ware (1998), Radiometric profiling of temperature, water vapor, and cloud liquid water using various inversion methods, *Radio Science*, 33, 393 - 404.
- Squire, V.A., Vaughan, G.L., and Bennetts, L.G. (2009), Ocean surface wave evolution in the Arctic basin. *Geophys. Res. Lett.*, 36, L22502, doi: 10.1029/2009GL040676.
- Steele, M. (1992), Sea Ice Melting and Floe Geometry in a Simple Ice-Ocean Model, *J. Geophys. Res.*, 97(C11), 17,729–17,738, doi: 10.1029/92JC01755.
- Steele, M., Ermold, W., and Zhang, J. (2008), Arctic Ocean surface warming trends over the past 100 years, *Geophys. Res. Lett.*, 35, L02614, doi: 10.1029/2007GL031651.
- Steer, A., Worby, A., and Heil, P. (2008), Observed changes in sea-ice floe distribution during early summer in the Western Weddell Sea. *Deep-Sea Res. II* (2008), 933 – 942.
- Stroeve, J. C., Serreze, M.C., Fetterer, F. Arbetter, T. Meier, W. Maslanik, J. and Knowles, K. (2005), Tracking the Arctic's shrinking ice cover: Another extreme September minimum in 2004, *Geophys. Res. Lett.*, 32, L04501, doi: 10.1029/2004GL021810.

- Stroeve, J.C., Serreze, M.C., Holland, M.M., Kay, J.E., Maslanik, J., and Barrett, A.P. (2011a), The Arctic's rapidly shrinking sea ice cover: a research synthesis, *Clim. Ch.* doi: 10.1007/s10584-011-0101-1.
- Stroeve, J.C., Serreze, M.C., Barrett, A., and Kindig, D., (2011b) Attribution of recent changes in autumn cyclone associated precipitation in the Arctic, *Tellus A* 63(4): 653 – 663: DOI:10.1111/j.1600-0870.2011.00515.x.
- Timco, G.W. and O'Brien, S. (1994), Flexural strength equation for sea ice, *Cold Reg. Sci. Technol.*, 22(3): 285 – 298.
- Timco, G.W. and Johnston, M.E., (2002), Sea ice strength during the melt season. Ice in the environment: Proceedings of the 16thP LAHR International symposium on ice, Dunedin, New Zealand, 2 – 6 December.
- Tison, J.L., Worby, A.P., Delille, B., Brabant, F., Papadimitriou, S., Thomas, D., de Jong, J., Lannuzel, D., Haas, C., (2008), Temporal evolution of decaying summer first-year sea ice in the western Weddell Sea, Antarctica, *Deep-Sea Research II* (55), doi:10.1016/j.jdsr.2007.12.021).
- Toyota, T., Takatsuji, S., and Nakayama, M., (2006), Characteristics of sea ice floe size distribution in the seasonal ice zone, *Geophys. Res. Lett.*, 33, L02616, doi:10.1029/2005GL024556.
- Wadhams, P., (1973), Attenuation of Swell by Sea Ice, *J. Geophys. Res.*, 78 (18): 3552 – 3563.
- Wadhams, P., Gill, A. E. & Linden, P. F., (1979) Transects by submarine of the East Greenland Polar Front. *Deep-Sea Res.* 26A, 1311–1327.
- Wadhams, P., Squire, V.A., Goodman, D.J., Cowan, A.M., and Moore, S.C., (1988), The attenuation of ocean waves in the marginal ice zone, *J. Geophys. Res.*, 93, 6799– 6818.
- Wadhams, P., and Doble, M.J. (2009), Sea ice thickness measurement using episodic infragravity waves from distant storms, *Cold Reg. Sci. Technol.*, 56, 98 – 101.
- Woodgate, R. A., Aagaard, K. and Weingartner, T. J., (2006), Interannual changes in the Bering Strait fluxes of volume, heat and freshwater between 1991 and 2004, *Geophys. Res. Lett.*, 33, L15609, doi: 10.1029/2006GL026931.
- Zhang, X., Walsh, J. E., Zhang, J., Bhatt, U.S., and Ikeda, M., (2004), Climatology and interannual variability of Arctic cyclone activity, 1948-2002. *J. Clim.*, 17, 2300 – 2317.

CHAPTER SIX: IMPLICATIONS OF FRACTURED ARCTIC PERENNIAL ICE COVER ON THERMODYNAMIC AND DYNAMIC SEA ICE PROCESSES.

Asplin, M.G., Scharien, R., Else, B.G.T., Barber, D.G., Papakyriakou, T.N., Howell, S., Prinsenberg, S. (2013) Dynamic and thermodynamic implications of ocean swell fracturing of Arctic perennial sea ice, *Jour. Geophys. Res. (In Review)*.

6.1 Introduction

The Arctic sea ice cover continues to transition from a predominately perennial sea ice cover to one consisting primarily of seasonal sea ice cover. This change is evident from the continuing decline of summer minimum Arctic sea ice extents, observed within the passive microwave record (1979 – 2010) to be declining at a rate of approximately -81,310 km² per year (-12.4% per decade for September) [Stroeve *et al.*, 2011a]. The rate of decline increases to -91,600 km² per year if the 2011 and 2012 minimums are factored in, [NSIDC, 2012]. This change is occurring in concert with reductions in sea ice thickness [Rothrock *et al.*, 1999; Hilmer and Lemke, 2000], age and volume of ice [Maslanik *et al.*, 2007; Ngheim *et al.*, 2007; Kwok *et al.*, 2009; Maslanik *et al.*, 2011; Laxon *et al.*, 2013], and an increasing melt season length [Markus *et al.*, 2009]. Sea ice decline is generally attributed to increasing regional air temperatures [Overland, 2009], anomalous atmospheric forcing via the Arctic Dipole anomaly [Wu *et al.*, 2006; Wang *et al.*, 2009; Overland *et al.*, 2012] and increased summer ocean mixed-layer depth temperatures [IPCC 2007; Stroeve *et al.*, 2011a] coupled with wind forcing of sea ice [Ogi *et al.*, 2010, Ogi and Wallace, 2012], increased ocean heat fluxes [Shimada *et al.*, 2006; Woodgate *et al.*, 2006; Steele *et al.*, 2008], and increased surface solar heating and bottom melt [Perovich *et al.*, 2008].

The decline of the summer minimum Arctic sea ice extent has recently been highlighted by a new record minimum extent of 3.41×10^6 km², observed on 16

September 2012 [NSIDC, 2012; Parkinson and Comiso, 2013]. The rate of areal sea ice decline in 2012 was impressive as it represents the greatest single-year Arctic ice extent loss ($11.83 \times 10^6 \text{ km}^2$) in the satellite record. The 2012 summer Arctic sea ice extent surpassed the 18 September 2007 extent ($4.2 \times 10^6 \text{ km}^2$) on 26 August 2012, with approximately a month of potential melt season remaining for further ice loss. Furthermore, the 2012 record minimum was influenced by an extreme summer cyclone (966 hPa on 06 August, 2012, 13th deepest on record for the Arctic Ocean) termed the ‘Great Arctic Cyclone of 2012’ [Simmonds and Rudeva, 2012], although the new record minimum would have occurred regardless of the cyclone [Parkinson and Comiso, 2013; Zhang *et al.*, 2013].

The six lowest summer minimum Arctic ice extents in the satellite record have all occurred during the last six years (2007 – 2012) [NSIDC, 2012]. During these years, the Arctic Ocean was characterized by large open water anomalies spanning the Chukchi, Siberian, Laptev and Beaufort Seas, large expanses of heavily decayed first-year (FY) and multi-year (MY) sea ice [Barber *et al.*, 2009], declining ice volumes [Laxon *et al.*, 2013], and declining age of sea ice cover, with only $3.04 \times 10^6 \text{ km}^2$ (10%) of remaining MY sea ice in 2010 being five years or older [Maslanik *et al.*, 2011]. Large regions of open water and thinner, younger, and weaker sea ice represent a change in surface cover which affects the following: 1) increased fetch for generation of waves and large swells and their impact on the remaining ice cover [Squire *et al.*, 2009; Asplin *et al.*, 2012], 2) decreased regional surface albedo and the ice-albedo feedback mechanism [Curry *et al.*, 1995; Perovich *et al.*, 2002], 3) increased radiative heating of the ocean surface layer [Perovich *et al.*, 2008] 4) transfer of sensible and latent heat between the ocean,

atmosphere, and remaining ice cover and 5) cyclone wind-driven upwelling, mixing of the surface mixed layer and impacts on the remaining ice cover [*Wettlaufer, 1991; Perovich and Elder, 2002; Rainville and Woodgate, 2009*].

Increased fetch during the summer in the Arctic Ocean is resulting in an increase in wave energy, which can impact the sea ice cover [*Asplin et al., 2012*]. Waves propagating through sea ice are attenuated exponentially (exponent of 3) [*Squire et al., 2009*] by scattering interactions between leads and pressure ridges and friction [*Wadhams, 1973*]. Long waves can propagate deep into Arctic pack ice [*Squire et al., 2009*], causing flexural swell and fracture of large contiguous ice floes into smaller floes [*Rothrock and Thorndike, 1984; Wadhams et al., 1988; Toyota et al., 2006; Steer et al., 2008*]. The incidence of fracture depends highly on the interrelated parent ice floe physical properties of ice temperature, salinity, strength [*Frankenstein and Garner, 1967; Timco and O'Brien, 1994; Timco and Johnston, 2002*], as well as the original parent floe size [*Rothrock and Thorndike, 1984*]. The resulting ice floe size depends on the thickness of the original ice floe, where minimum floe diameters after breakup of 14, 24, and 33 m are identified for 1, 2 and 3 m parent ice floe thicknesses respectively [*Mellor, 1986*]. This process is commonly observed in Antarctica [*Wadhams et al., 1988*]; however may become more common within the Arctic Basin with emerging seasonal fetch.

A case of Arctic long wave generation and flexural failure of MY ice floes was observed within the Beaufort Sea in September 2009 [*Asplin et al., 2012*]. On 06 September, the CCGS *Amundsen* was west of the Canadian Arctic Archipelago in an area containing large thick MY ice floes flanked by heavily-decayed first-year sea ice to the south and west [*Barber et al., 2009*]. Long waves (period = 13.5 s), originating from

winds from cyclones passing over large fetch to the west, began to propagate into the region, causing flexural swell and failure within the large MY ice floes. A helicopter-borne aerial survey of sea ice cover underway at the time revealed a distribution of MY ice floe diameters ranging from 100 – 150 m. Furthermore, the rotted FY ice margin was heavily fractured, with floe diameters ranging from 20 – 50 m in diameter. Smaller, mobile floes are more susceptible to lateral melting by radiative forcing [Ebert *et al.*, 1995; Toyota *et al.*, 2006;], and wind forcing [Steer *et al.*, 2008], and therefore flexural fracture of sea ice may be a positive feedback in the broader ice-albedo feedback mechanism described by Curry *et al.*, [1995].

The process described in Asplin *et al.*, [2012] represents a net reduction in the regional albedo of the affected area, following typical seasonal evolution of surface albedos [e.g. Perovich *et al.*, 2002]. The interaction of shortwave radiation with sea ice depends on the albedo (α) (reflectivity) of the sea ice surface [Ebert and Curry, 1993]. The albedo of Arctic surfaces varies by surface type and by season. There are five distinct phases of seasonal evolution over MY sea ice, which include dry snow ($\alpha = 0.8 - 0.9$), melting snow ($\alpha = 0.8 - 0.7$), pond formation ($\alpha = 0.7 - 0.5$), pond evolution ($\alpha = 0.5 - 0.4$) and fall freeze-up ($\alpha = 0.4 - 0.8$) [Perovich *et al.*, 2002]. In summer, regional surface albedo tends to decrease and become more variable as the ice cover becomes heterogeneous with meltponds and interspersed open water. Perovich *et al.*, [2002] describes summer albedo values of 0.07 for open water, 0.2 for dark melt ponds, 0.4 for light melt ponds, and 0.6 – 0.7 for summer MY ice (melting surface). Albedo values for MY ice are typically higher than those for FY sea ice under the same conditions in the

summer as MY ice tends to form a surface scattering layer due to melting and drainage of the MY surface [*Perovich et al.*, 2002].

Open water fraction also depends on sea ice dynamics as ice motion can drive divergence in the ice cover, thereby lowering regional albedos. Sea ice motion within the Arctic has been increasing in recent years [*Lukovich et al.*, 2011; *Rampal et al.*, 2009; *Kwok et al.*, 2013; *Galley et al.*, 2013]. Over 90% of the area of the Arctic ocean exhibited an increase in ice motion from 2001 – 2009, with drift speeds increasing by +23.6% / decade and +17.7% / decade in winter and summer respectively [*Kwok et al.*, 2013]. This corresponds with a significant increase in inertial motion within the Arctic pack ice observed from 1979 – 2008 throughout all seasons, with the greatest increase observed during summer [*Gimbert et al.*, 2012b]. These changes are attributed to declining thick, MY ice coverage [*Kwok et al.*, 2013], and also represent a mechanical weakening of the Arctic sea ice cover [*Gimbert et al.*, 2012a]. Such mechanical weakening will have strong consequences in terms of ice drifting speeds, deformation rates [*Rampal et al.*, 2009], sea ice export through Fram Strait [*Kwok et al.*, 2013], and therefore on sea ice mass balance [*Rampal et al.*, 2011]. It is also possible that strengthening of inertial motion may simply be a result from a thinner ice cover (reduction of areal ice mass), and could also be the result of a modification of vertical penetration of turbulent momentum within the ocean boundary layer [*Gimbert et al.*, 2012b].

Large areas of open water, and heavily fractured sea ice cover may introduce new opportunities for wind-driven mixing of the ocean surface-mixed layer [*e.g. Wettlaufer*, 1991; *Perovich and Elder*, 2002; *Rainville and Woodgate*, 2009], and may enhance wind-

driven coastal upwellings [e.g. *Pickart et al.*, 2009]. This could augment existing trends in the upper-ocean heat content of the Arctic Ocean. *Steele et al.* [2008] identified an average increase in the upper ocean heat content of the summertime southern Chukchi and western Beaufort Seas of about $50 \text{ MJ m}^{-2} \text{ decade}^{-1}$ during 1965 – 1995 ($150 \text{ MJ} \cdot \text{m}^{-2}$ over 30 years). *Perovich et al.* [2008] investigated solar heating 1979 – 2005 in the northern Chukchi Sea and identified an average increase of $200 \text{ MJ} \cdot \text{m}^{-2}$ of insolation. Large-scale upwelling events may entrain heat fluxes from depth (below 50 m), which are observed to be increasing in total magnitude [*Woodgate et al.* 2006]. More recently, *Zhang et al.*, [2013] analyzed the impact of the August 2012 ‘Great Arctic Cyclone’ on rates of sea ice decay. A comparison with a sensitivity simulation suggests that cyclone-enhanced bottom melt strongly reduced ice extent for about two weeks, with a reduced effect afterwards. The net impact of the cyclone on the 2012 minimum sea ice extent was estimated to be $\sim 0.15 \times 10^6 \text{ km}^2$ (4.4% of the total summer melt for 2012), thus, even without the storm, 2012 would have still produced a record minimum summer sea ice extent [*Zhang et al.*, 2013].

The Arctic sea ice cover is increasingly becoming ‘preconditioned’ for sea ice loss due to abnormal seasonal cyclone distributions [*Screen et al.*, 2011] and increasing areas of seasonally open water which are susceptible to wind and solar radiative forcing. Long wave generation within the Arctic Ocean could lead to recurrent reductions in mean MY ice floe size, which in concert with wind and solar forcing would likely affect dynamic and thermodynamic decay processes in MY sea ice [*Asplin et al.*, 2012]. Wind forcing may transport the highly mobile fractured MY floes south, and exacerbate the trend in MY ice loss by *in situ* melting in the Southern Beaufort Sea as identified by

Kwok and Cunningham, [2010]. This section therefore investigates the implications of the flexural fracture positive feedback process presented by *Asplin et al.*, [2012] and addresses the following interrelated objectives:

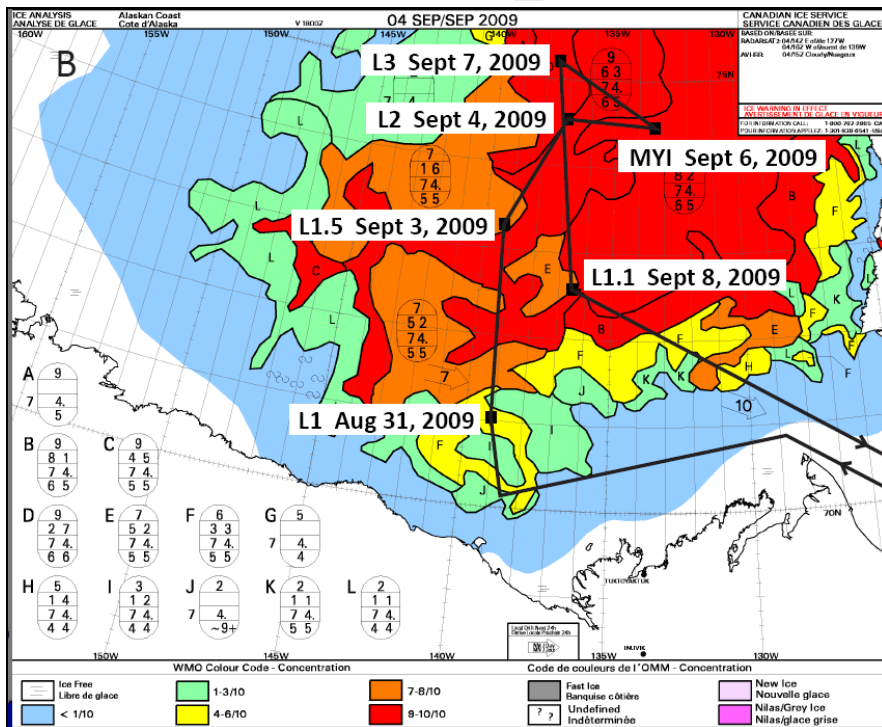
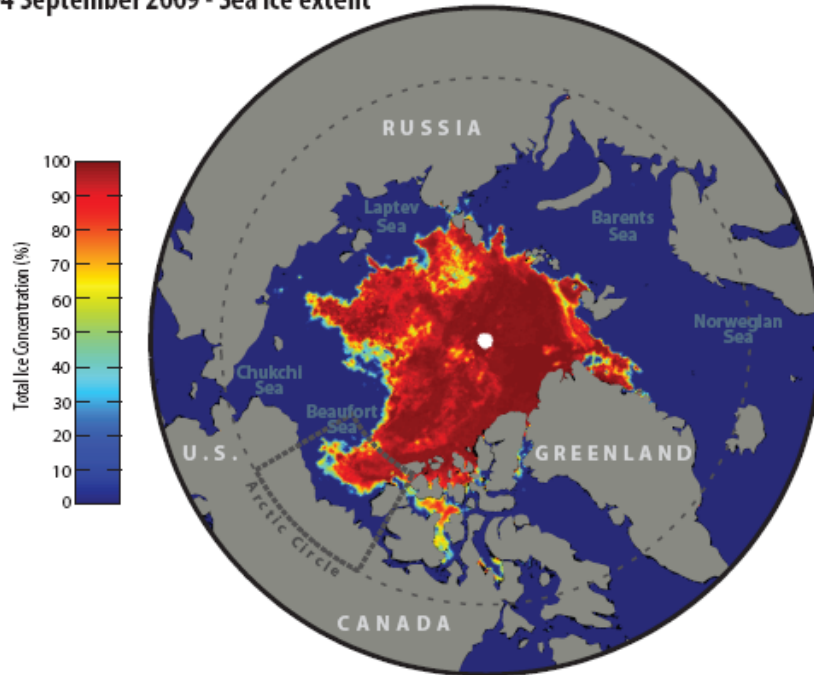
- 1) What were the physical characteristics of the sea ice cover after the storm swell fracturing in September 2009?
- 2) What impact does fracture have on rates of thermodynamic decay?
- 3) What are the implications of this process occurring in concert with cyclone-forced mixing and upwelling of ocean heat fluxes?
- 4) What are the implications of this process on sea ice dynamic processes?

6.2 Data and Methods

In situ observations of the atmosphere-sea ice-ocean system in the southern Beaufort Sea were made from the Canadian Research Icebreaker CCGS *Amundsen* during the joint ArcticNet/IPY-GeoTraces and Imperial Oil Industrial Partnership cruise, which took place between 17 July and 15 October 2009 (Figure 6.1). Canadian Ice Service (CIS) digital ice charts were used for real-time science planning and ship operations during the cruise. CIS digital ice charts (e.g. Figure 6.1) are based on expert manual interpretation of Radarsat-1 data (the primary data source since 1996), NOAA-AVHRR and Envisat ASAR data and *in situ* aerial and marine surveys [Fequet, 2002]. They include total sea ice concentration, partial concentrations by development stage, and ice floe size information.

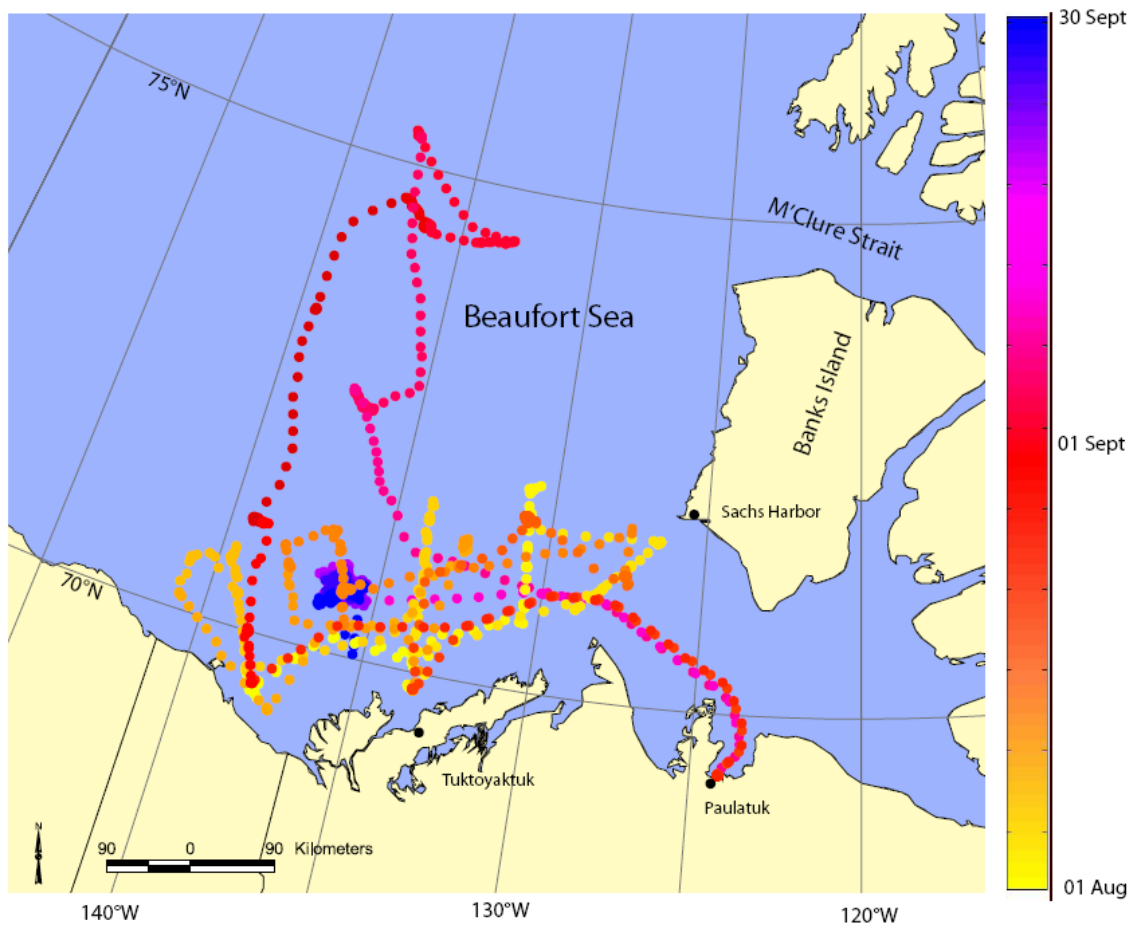
Figure 6.1. Top: National Snow and Ice Data centre (NSIDC) sea ice aerial extent with study area boundary, Bottom: Canadian Ice Service ice chart for 04 September 2009 showing sea ice concentration and stage of development. Ship-based sampling sites and cruise plan are shown.

04 September 2009 - Sea ice extent



This section focuses on the period between 01 August – 30 September 2009 (Figure 6.2). Meteorological data including sea level pressure, air temperature, relative humidity, and vector winds were collected with an AXYS Automated Voluntary Observation System (AVOS), located on the roof of the ship's wheelhouse. Cloud heights were measured using a Vaisala CT25K ceilometer, mounted directly behind the wheelhouse on the port side of the ship, and positioned to ensure a clear view of the sky. The ceilometer has a vertical resolution of 15 m (lowest possible cloud base is 15 m above the ship's deck) to approximately 7.6 km. Cloud fractional cover was assessed manually every three hours, and later compared with imagery from an all-sky camera system, consisting of a Nikon D-90 camera with an upward-looking fisheye lens. Manual meteorological observations were collected at 3-hour intervals, including cloud fractional cover, visibility, and sea ice concentration. The nominal horizon for visual observations is typically about 25 km; however fog often limited visibility and the area to which these data apply.

Figure 6.2. Southern Beaufort Sea study region. CCGS Amundsen Cruise average hourly positions are shown for 01 August – 30 September 2009.



Downwelling shortwave ($K\downarrow$) and longwave ($L\downarrow$) radiation were measured on the *Amundsen* at an interval of ~ 1 minute using a pyranometer ($0.285\text{-}2.8\ \mu\text{m}$, Eppley PSP[®]), and by a pyrgeometer ($4\ \text{to}\ 50\ \mu\text{m}$, Eppley PIR[®]) in “non-battery” mode respectively. The view of the pyranometer and the pyrgeometer varied somewhat with the pitch and roll of the ship. Both instruments were mounted >20 m above sea level. In the worst conditions (storm state with open water) the ship could roll up to $\approx 10^\circ$, however, storm conditions were episodic and relatively short lived. As the pyrgeometer responds weakly to radiation at large zenith angles (cosine response), [Minnett, 1999], potential errors in $L\downarrow$ measurement caused by radiation emitted from the ocean surface

were assumed to be negligibly small. The L_{\downarrow} radiation measurements were corrected to compensate for the sensor's temperature (blackbody correction) and for bias from solar heating of the dome [*Philipona et al.*, 1995]. The correction factors were $k_1 = 0$, $k_2 = 1$, and $k_3 = 4$ [*Marty et al.*, 2003]. For the pyranometer, at sun elevations much larger than the maximum ship pitch and roll amplitude, the effect of non-cosine response evidences itself as the effects of time averaging over pitch and roll [*Katsaros and Devault*, 1986; *MacWhorter and Weller*, 1991]. Shading is much more severe than the deviation from cosine response of the sensor surface as it rolls away from the sun.

Ocean mixed-layer temperatures were measured by a thermocouple installed in the *Amundsen's* ocean water intake system at a depth of ~ 5 m. A linear correction was applied to account for the warming of the water once inside the hull. The median water inflow was about $2.3 \text{ l} \cdot \text{min}^{-1}$. Ice occasionally restricted the intake, reducing the water flow and accuracy of the water temperature measurements. Thus, water temperature data were discarded when the water flow was $< 1 \cdot \text{min}^{-1}$. An ocean-surface mixed layer with approximately uniform temperature and salinity was assumed as one is typically present [*e.g. Sirevaag et al.* 2011].

Sea ice thickness surveys were made using a helicopter-mounted electromagnetic induction (EMI) system. This system is well established [*e.g. Prinsenberg and Holladay*, 1993] and consists of the electromagnet, a laser profiler, a nadir-facing video system and navigation, control and archive systems. The near-circular footprint of the helicopter EMI system is about 2.5 times the altitude at which it is flown ($\sim 4 - 6$ m). The nadir-looking digital camera acquired video of the sea surface from 130 m of altitude. The video width is at a 1 to 1 ratio with altitude. We use existing sea ice floe-size cumulative number

distributions [Rothrock and Thorndike, 1984] following Asplin *et al.*, [2012]. These distributions were derived from a power-law curve (equation 6.1) to create two sea ice floe-size cumulative number distributions

$$N(d)_i \propto ad_i^k \quad (6.1)$$

where $N(d)$ is the cumulative number distribution for floe size regime i , k is the scaling exponent, and a is a constant.

To investigate drift and divergence / convergence of ice floes we deployed Oceanetics Model 703 ice drifter beacons during the study which transmitted their location every two hours. These beacons were deployed by ship along the cruise path, as well as in triangular configurations during helicopter surveys. Beacons were deployed in an 8" diameter auger hole drilled 12" deep into the ice, and then packed with snow. Unfortunately several beacons failed during September and October 2009 due to heavily-decayed ice conditions and storms. Three beacons were identified with sufficient life spans for discussion of ice motion following the flexural failure event. These beacons (6-digit id) were deployed at the following locations and times: 282070 (72° 33.77', 136° 41.88'; 08 September 2009), 284060 (72°N 59.61' 135°W 38.92'; 08 September 2009), and 520590 (74°N 26.266', 133°W 23.141'; 06 September 2009, station MYI). Data is classified by month to qualify ice divergence and motion in the southern Beaufort Sea from time of deployment into the freeze-up season.

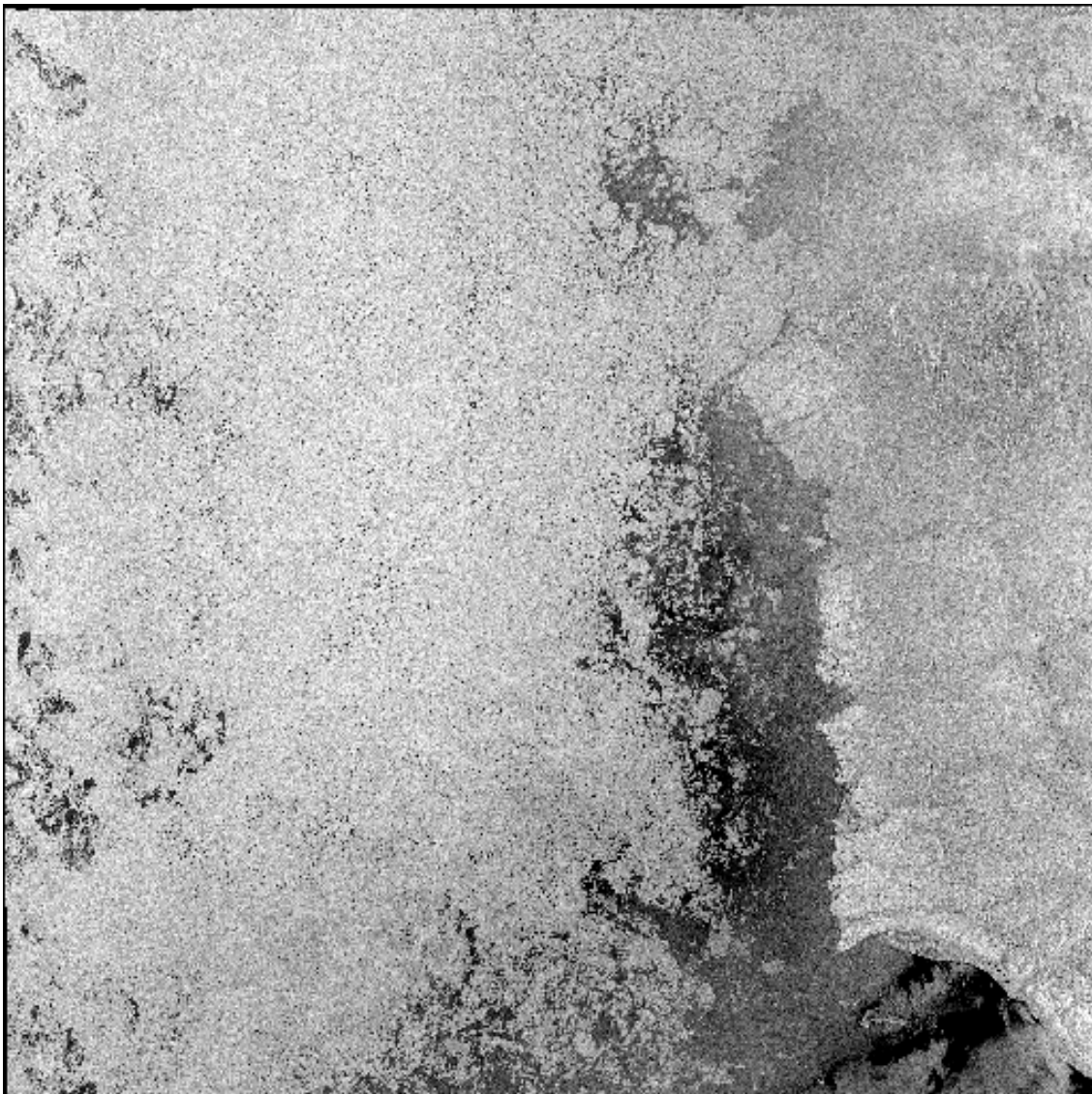
Two Radarsat-2 ScanSAR Wide scenes covering the study area were obtained for the purpose of evaluating the distribution of ice floes and relative fractions of ice and

open water in the study region. Radarsat-2 is polar-orbiting C-band synthetic aperture radar which, in ScanSAR mode, provides backscatter information in two horizontal (H) and vertical (V) transmit-receive polarization combinations, in this case HH and HV. As open water generally does not depolarize incident radiation, the HV backscatter is low compared to sea ice and relatively unaffected by wind-wave roughness. The combined use of HH and HV thus allows for a robust separation of ice and open water [*Scheuchl et al.*, 2004]. The first scene (Figure 6.3) on 06 September at 15:25:31 UTC, captured the ice conditions immediately prior to the storm induced ice fracture event, and the second scene (Figure 6.4) on 09 September at 15:38:12 UTC captured conditions three days later.

Figure 6.3. Radarsat-2 image for 1513 UTC 03 September 2009, three days prior to the 06 September 2009 flexural failure event.



Figure 6.4. Radarsat-2 image for 1538 UTC 06 September 2009, immediately following the 06 September 2009 flexural failure event.



Each scene was calibrated to HH and HV radar backscatter coefficient σ° values in decibel (dB) format, georeferenced to a common projection on the basis of location information embedded in the product headers (60 m pixel spacing), and spatially subset into a 25 by 25 km area of interest centered on 74°26.27N and 133°23.14W (figure 6.5). The area was chosen because it comprised the thickest ice and largest floes directly

observed during the MY ice fracture event. A supervised minimum distance classifier was applied on the basis of user selected training areas to convert each scene into a binary map composed of ice and open water. The classification procedure yielded accuracies greater than 99%, though an overestimation of the ice class in each scene is expected due to the tendency for mixed pixels to be classed as ice.

Nilsson et al. [2001] show that a radiation budget for a mosaic open water/sea ice surface can be written as follows:

$$R_n = [\alpha R_{n-ice}] + [(1-\alpha)R_{n-water}] \quad (6.2)$$

Where:

$$R_{n-water} = [K\downarrow - (\gamma_{water} K\downarrow,)] + [L\downarrow - \varepsilon_w \sigma T_{water}^4] \quad (6.3)$$

$$R_{n-ice} = [K\downarrow - (\gamma_{ice} K\downarrow,)] + [L\downarrow - \varepsilon_i \sigma T_{ice}^4] \quad (6.4)$$

The net radiation, R_n , is the sum of the net radiation for the fractional surface areas for open water and for sea ice. γ_{water} and γ_{ice} are, respectively, the albedo of the open water, and of the remaining ice floes whose surfaces may include melt ponds. The albedo times $K\downarrow$, gives the out-going shortwave radiation ($K\uparrow$). The Stefan-Boltzman relationship was used to calculate the out-going longwave radiation ($L\uparrow$); σ is the Stephan-Boltzman constant, T_{water} is the surface temperature, ε_w the emissivity of the open water, T_{ice} is the surface temperature, and ε_i the emissivity of the ice floes.

We first determine the average fractional coverage of each surface type, and partition varying albedo values accordingly through analysis of the Radarsat-2 imagery and helicopter video data. Surface types and albedos used are snow-covered ice ($\alpha = 0.8$), light meltponds ($\alpha = 0.5$), dark meltponds ($\alpha = 0.2$), and open water ($\alpha = 0.07$) [*Perovich et al.*, 2002]. The change in open water albedo with respect to sea state and the incident

angle of the global radiation was ignored. For fractional-area of the surface with sea ice, an area-average albedo was used for the ensemble of snow, ice and melt ponds that comprised the ice floes [Perovich *et al.*, 2002]. Melt ponds, which markedly alter the albedo of the sea ice, often constitute a large fraction of the surface area of ice floes [Nilsson *et al.*, 2001]. To account for the temporal state of the ice surface including the expansion and freeze-over of melt ponds, the ice floes were assigned a seasonally-evolving albedo that varied with the air temperature, and corresponds with the melt pond evolution period described by Perovich *et al.* [2002]. The albedo of the ice floes was set to decrease linearly from 0.5 to 0.4 during the study period. Fractional coverage of all surface types is adjusted according to conditions observed prior to and following the fracture event. We then use hourly averaged values of K_{\downarrow} to determine the total hourly solar energy input ($\text{MJ} \cdot \text{m}^{-2}$) into all surfaces for 01 August – 30 September 2009.

The net longwave radiation budget (L^*) is estimated using hourly-averaged *in situ* L_{\downarrow} measurements and by calculating L_{\uparrow} with the Stefan-Boltzman relationship (the last term in equations 6.3 and 6.4) and *in situ* ocean-mixed layer temperatures. The temperatures of the ocean surface and ocean-mixed layer as measured at ~ 5 m depth were assumed to be the same [Sirevaag *et al.* 2011]. When the air temperature was above freezing, promoting presence of melt pond, the surface temperature of the ice floes was set to 0°C , the melting point of fresh water. When the air temperature was at or below 0°C , promoting the freezing-over of melt ponds, the temperature of the surface of the ice floes was set to the air temperature [Raddatz *et al.*, 2012a]. The emissivity of the components of the surface, water and sea ice, were both set to 0.99 [Persson *et al.*, 2002].

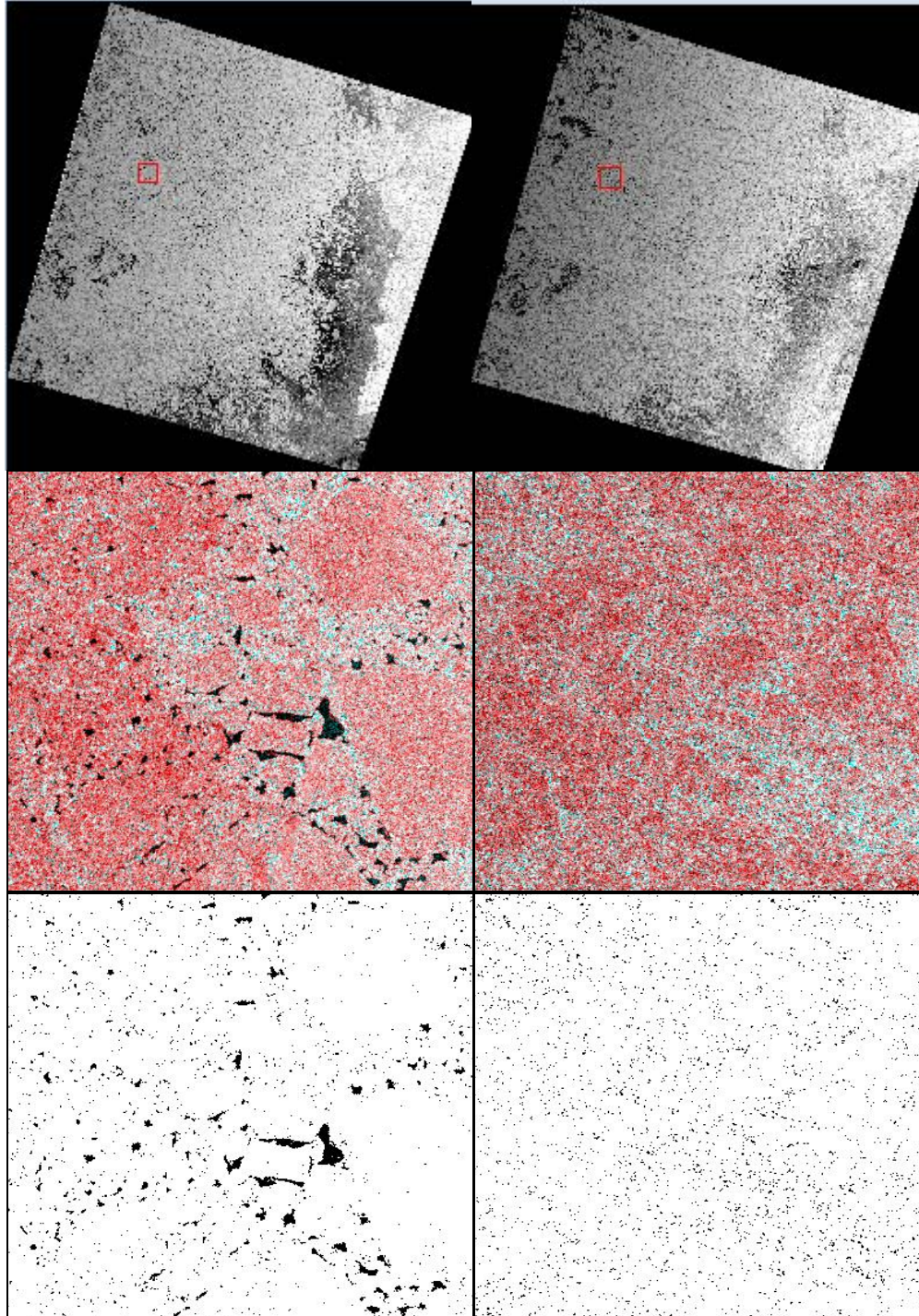
L^* is partitioned by surface fractional coverage, and the net hourly values of longwave energy into open water area is then calculated.

We derived estimates of radiative energy that goes to lateral melting prior to and following a sea ice flexural fracture event. First, an assessment of net radiation (Q^*) was conducted for the study period. Hourly cumulative values of Q^* ($K^* + L^*$) were calculated for all surfaces and then summed over the entire two-month period. We focused on the energy input into sea ice open water area. Following [Steele, 1992], 80% of this energy goes into lateral melting while the rest warms the ocean. The flexural fracture event was described as an instantaneous reduction in regional surface albedo by *Asplin et al.*, [2012]. To better understand the impacts of the timing of flexural fracture events on lateral melting, we estimated the cumulative contribution of radiative energy to lateral melting for flexural failure events if they had occurred on 01 August, 15 August, 01 September, and compared to 06 September (observed), and a case where ‘no fracture’ event occurs. We therefore must adjust the partitioning of surface types, and corresponding albedo values, in correspondence with the timing of each fracture case, using the observed surface albedos prior to and following the 06 September 2009 flexural fracture event.

6.3 Results

An analysis of Radarsat-2 ScanSAR imagery was conducted to better assess the regional extent of the 06 September 2009 flexural fracture event [Asplin *et al.*, 2012], and determine open-water percent coverage prior to and following the flexural fracture event (Figure 6.5). The 25 by 25km image subset, which includes station MYI, yielded an open-water fractional coverage of 3.7% before the fracture event, and decreasing to 2.7% following the event. A regional analysis shows that the total open water area increases by about 8% at larger spatial scales due to compression of the ice pack, as well as a northward retreat of the ice edge. An area of approximately 40,000 km² was identified as having been influenced by flexural swell and flexural failure on 06 September 2009.

Figure 6.5. ROI: 25 by 25km square centred on 74°N 26.266' 133°W 23.141' full scene prior to the flexural fracture event 03 September 2009 1525 UTC (top left), and following the flexural fracture event 06 September 2009 1538UTC (top right). ROI Subset RGB: $r = hh$; $g = hv$; $b = hv$. Before (middle left) and after (middle right) flexural failure event. Open water classification: (class: 0 = open water; 1 = ice). Open water 3.7% before (bottom left), and 2.7% after (bottom right) flexural failure event.



The helicopter-borne video system recorded still photographs along its flight track which were later combined to create a series of photo mosaics. An example of the photo mosaics is presented in Figure 6.6, and represents a real-time observation of the ice surface at station MYI prior to and immediately following the flexural swell event. Open water areas are limited to small patches interspersed around the large MY ice floes and comprise ~2% of the photo area. Sea ice concentration in the heavily-decayed first-year ice region was estimated at 80% on 09 September 2009, a reduction of ~10% from observations prior to the storm.

Figure 6.6. Left: 17:02 UTC from 06 September 2009 at station MYI, video width = 140. No cracks in old, 2m thick ice floe are visible. Right: 19:00 UTC 06 September 2009.

Thick ice (2m thick in level ice sections) at station MYI now has cracks aligned perpendicular to swell direction running from NW to SE. Fractured ice floes have a diameter approximately the width of the video (110m). Surface is characterized by old and new meltponds ranging from 10 – 30% coverage. Open water coverage between floes is <5%, but total floe perimeter exposed to ocean has increased by a factor of 4.

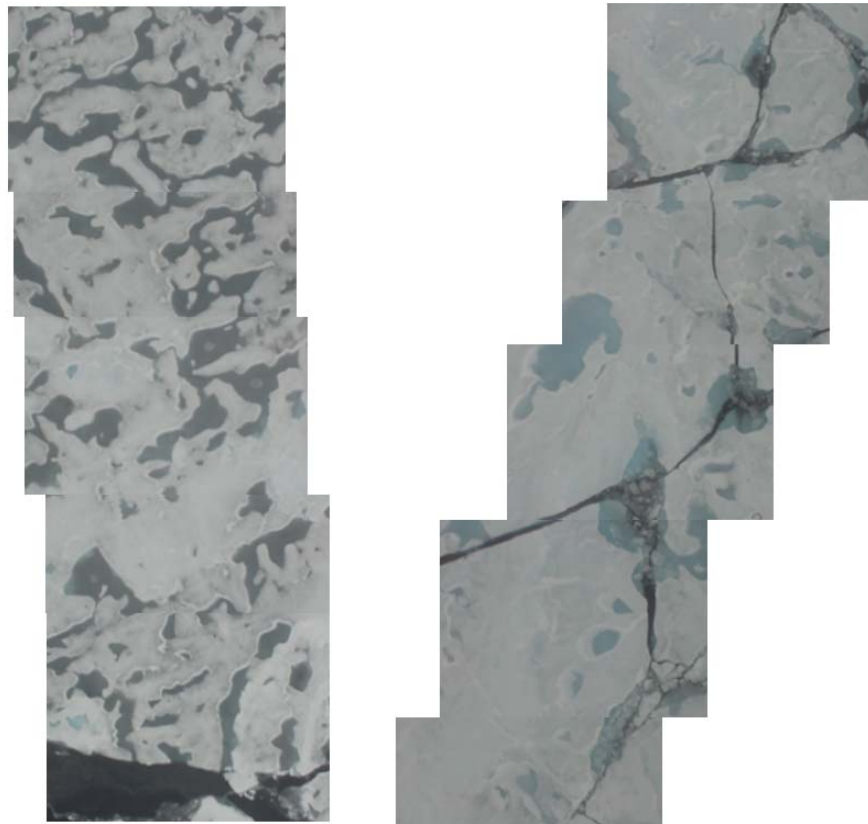


Figure 6.7. Image taken during 09 September 2009 afternoon long-line (FEM09397) helicopter EMI survey flown over fractured first and second-year ice floes 20 – 50m in diameter from 72.52°N 136.75°W to 72.52°N 133.40°W. Fractured ice floes have diverged to 80% sea ice coverage and yield a heterogenous surface in conjunction with meltponds.



Radiation values and cloud cover properties specific to the timing of the flexural failure event are discussed in *Asplin et al.*, [2012]. We used this same dataset to characterize K^* and L^* for August and September of 2009 to generate estimates of radiative energy. *In situ* observations of cloud cover, K_{\downarrow} and L_{\downarrow} were used to characterize the surface radiation budget for 01 August – 30 September 2009. Hourly-average values, corresponding to averaged ship position (Figure 6.2) were calculated for K_{\downarrow} (Figure 6.8) and L_{\downarrow} (Figure 6.9). Values of K_{\downarrow} ranged from 0 (night time) to $550 \text{ W} \cdot \text{m}^{-2}$, with maximum values decreasing steadily from 01 August – 30 September. Hourly

averaged values of $L\downarrow$ ranged from 225 – 375 $W \cdot m^{-2}$, with the greatest values associated with periods of thick cloud cover.

Figure 6.8. Hourly average values of in situ $K\downarrow$ for 01 August to 30 September 2009.

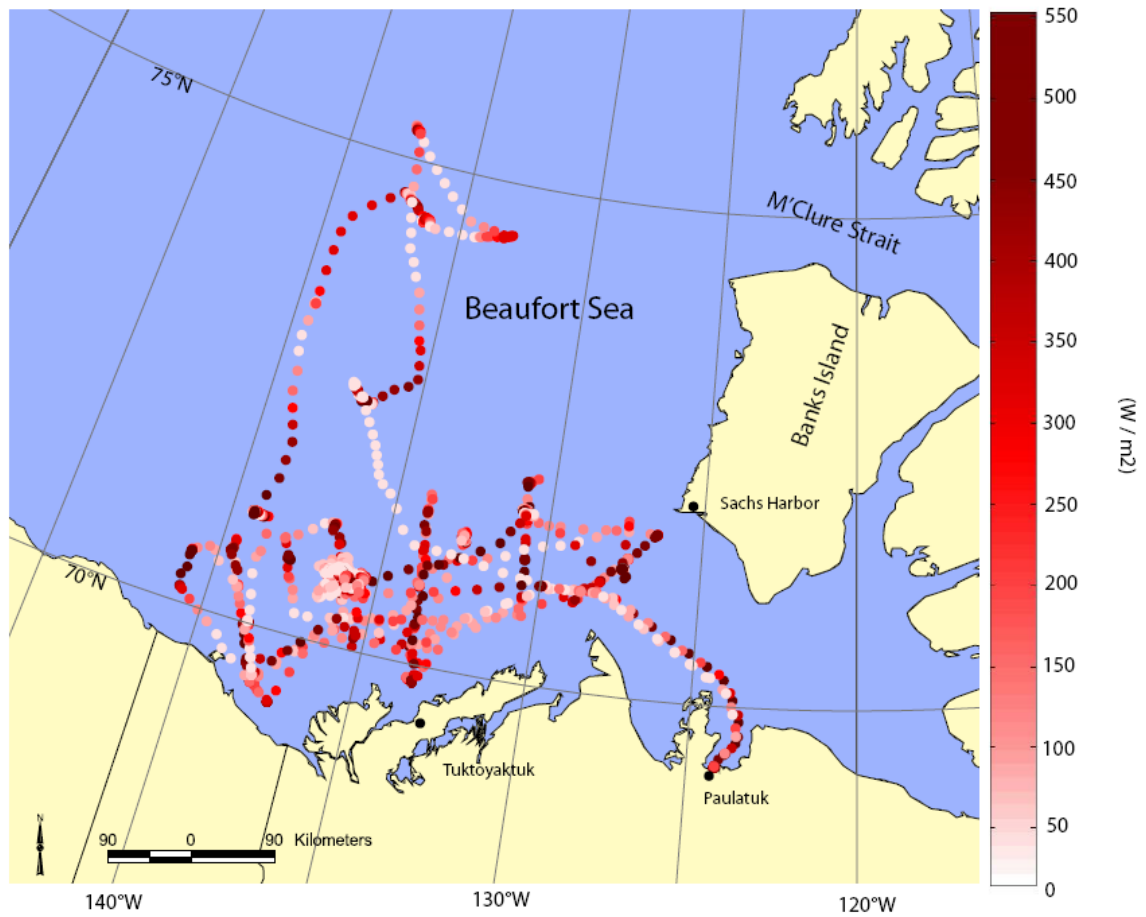
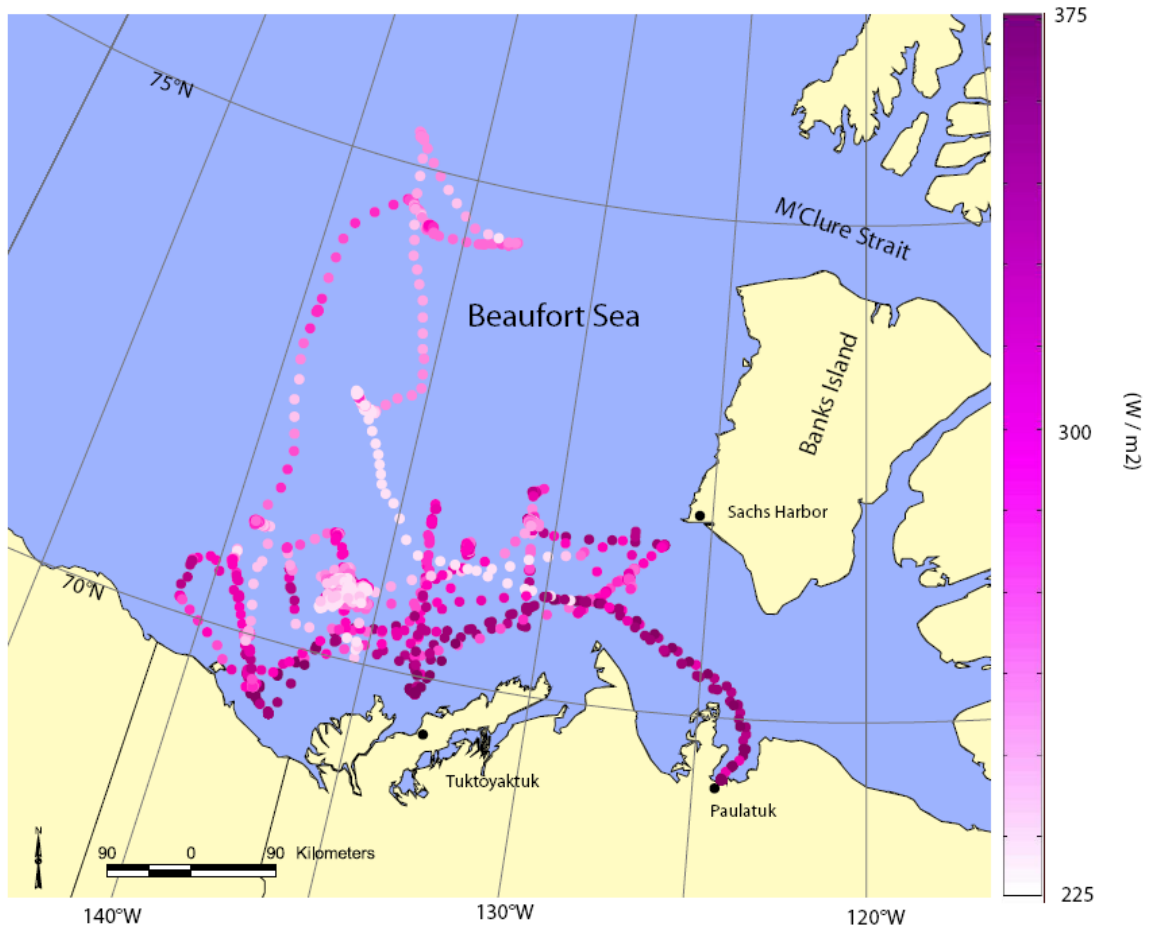


Figure 6.9. Hourly average values of in situ L_{\downarrow} for 01 August to 30 September 2009.



To classify surface albedo, we divided the surface into four surface types: Young melt ponds (light blue), dark melt ponds (black and deep), snow-covered sea ice, and open water. Mean regional albedo was found to decrease from $\alpha = 0.66$ to 0.585 following the fracture event. The fractional coverage of each surface type and corresponding surface albedos prior to and following flexural failure and hourly averaged values of K_{\downarrow} and L_{\downarrow} were used to estimate the net radiative energy that goes to sea ice leads, and consequently to lateral melting (Figure 6.10). The estimation was conducted for the sea ice surface in a pre-fracture and post-fracture state. The pre-fracture (post-fracture) state consists of a sea ice surface comprised of 70% (60%) coverage by sea ice, 15% (15%) coverage by young melt ponds, 10% (5%) coverage by dark melt ponds, and

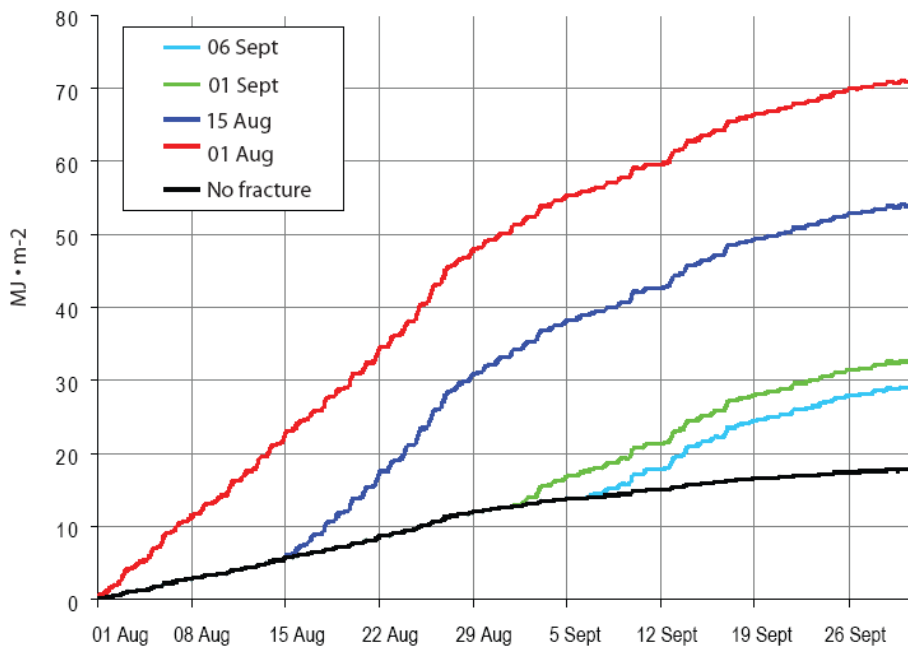
5% (20%) coverage by sea ice leads. A reduction in dark melt pond area was assumed as these areas represent the weakest part of the parent sea ice floes, and are thus most likely to be aligned with new sea ice leads arising from fracture.

To better understand the influence of a fractured ice surface on entrainment of K_{\downarrow} and L_{\downarrow} into the ocean mixed-layer throughout the study period, we calculated cumulative running totals of net all-wave radiative energy to lateral melting for five cases: 1) No fracture, 2) The flexural fracture event occurring as observed on 06 September 2009, and 3 cases if the flexural fracture event had occurred earlier in the season: 3) 01 September, 4) 15 August, and 5) 01 August 2009 (Figure 6.10). Total cumulative all-wave radiative energy for 01 August – 30 September 2009 was estimated in units of $\text{MJ} \cdot \text{m}^{-2}$ (Table 1). The total cumulative radiation estimated to go into lateral melting of ice floes was approximately $29.36 \text{ MJ} \cdot \text{m}^{-2}$ for the period 01 August – 30 September 2009 with the flexural fracture event occurring on 06 September 2009. A ‘no fracture’ case estimated $17.82 \text{ MJ} \cdot \text{m}^{-2}$ available for lateral melting in the same period, and we can thus determine that the 06 September 2009 flexural fracture event resulted in $\sim 11.54 \text{ MJ} \cdot \text{m}^{-2}$ cumulative radiation entrainment into the ocean mixed-layer which goes to lateral melting. Similar comparisons were made for flexural fracture occurring earlier in the year (Table 6.1).

Table 6.1. Cumulative radiative energy to lateral melting in sea ice leads versus timing of the flexural failure event.

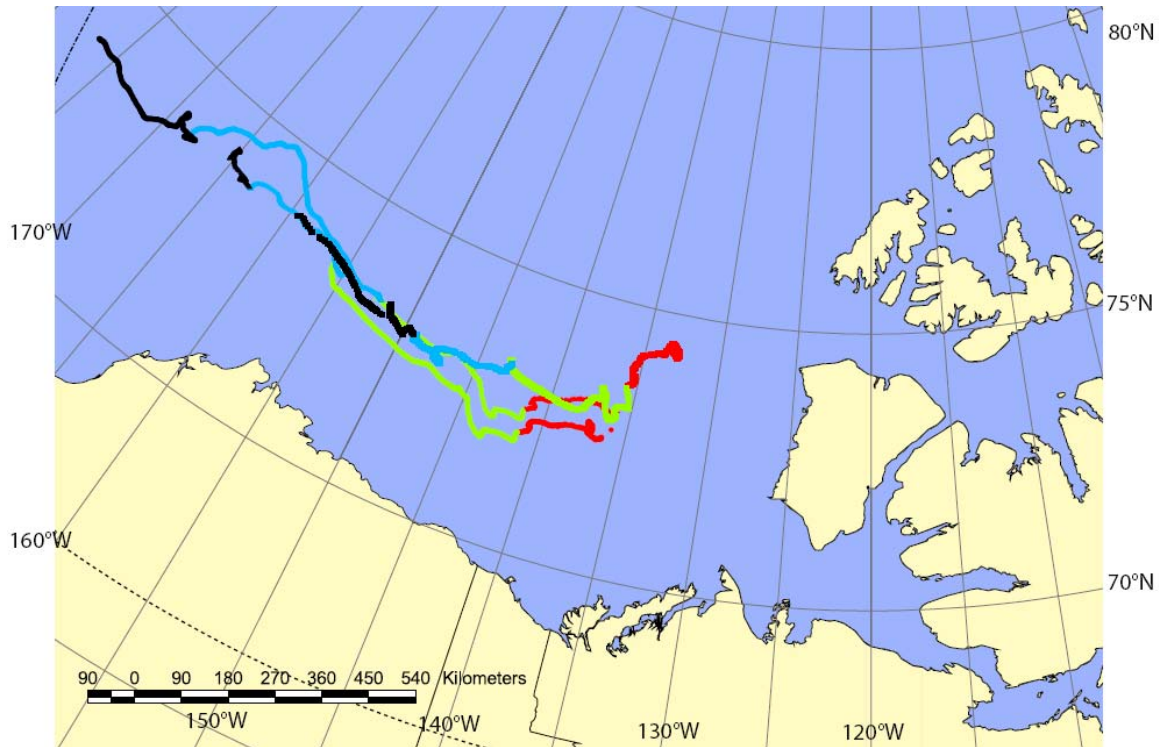
	Timing of flexural fracture				
	No Fracture	06 Sept	01 Sept	15 Aug	01 Aug
$\text{MJ} \cdot \text{m}^{-2}$	17.82	29.36	32.91	54.25	71.29
$\Delta \text{MJ} \cdot \text{m}^{-2}$	-	+11.54	+15.09	+36.44	+53.47

Figure 6.10. Estimated cumulative radiative energy ($L^* + K^*$) going into lateral melting via sea ice leads versus timing of a regional swell-driven flexural fracture event.



The key parameter in determining the cumulative radiation is the fractional coverage of open water. This value varies greatly throughout the Arctic, and furthermore dynamically evolves with ice motion and divergence. We investigated basic divergence by looking at monthly profiles of ice beacon drift trajectories from three beacons deployed in September 2009 (Figure 6.11). The ice beacon trajectories show rapid transport westward of the two ice beacons deployed on first-year ice fragments (284060 and 282070). The beacon deployed at station MYI (520590) moved predominantly to the southwest. The three beacons appear to show typical Beaufort gyre rotational movement; however speed and directional shear is noted between the FY and MY ice zones, therefore indicating a diverging ice surface. Ice motion for October – December 2009 shows divergence of the three ice beacons along an east-west axis, spread over nearly 1200 km by December 2009.

Figure 6.11. Drifting ice beacon data from beacons deployed on 08 September (282070, 284060), 520590 (06 September 2009; deployed during flexural failure event at station MYI). Data is classified by month (red = September, green = October, blue = November, Black = December) and shows considerable divergence of the beacons over time.



6.4 Discussion

The results from analysis of two Radarsat-2 ScanSAR wide scenes (Figure 6.5) provide further information about the sea ice surface prior to and following the 06 September 2009 flexural fracture event as described by *Asplin et al.*, [2012]. The distribution of ice floes and relative fractions of ice and open water in the study region revealed that an area of $\sim 40,000 \text{ km}^2$ containing large thick, MY ice floes was impacted by the long wave swells. A 25 by 25 km image subset, including station MYI, shows that open-water fractional cover actually decreased from 3.7% before the fracture event to 2.7% following the event (Figure 6.5). This may be partially due to soft, weak, summer ice conditions [*Eicken et al.*, 1995], and broken-up floes initially being prone to convergence in the region. The geometry of the ice floes following flexural fracture is rectangular (Figure 6.6), which may favor the ice cover remaining consolidated until oceanic currents or atmospheric forcing induces divergence of the large, thick fractured MY ice floes. In contrast, the much smaller (20 – 50 m diameter) ice floes in the heavily-decayed FY ice zone (Figure 6.7) were observed to have diverged to sea ice concentrations of $\sim 80\%$ (20% open water), a reduction of $\sim 10\%$ ice concentration. The area containing the fractured FY ice floes was surveyed three days following the fracture event, and some divergence of the ice surface likely occurred.

It is expected that flexural failure of MY sea ice and a corresponding decrease in mean floe diameter size will affect thermodynamic forcing upon sea ice mass balance. Reductions in mean ice floe diameter at site MYI on 06 September 2009 resulted in approximately a 4.5 times increase in ice floe perimeter exposed to the ocean [*Asplin et al.*, 2012], thereby increasing the surface area of sea ice exposed directly to ocean heat

fluxes by ~ 4.5 as well. The effect is expected to be more pronounced for MY sea ice cover due to greater ice draft with large keels, and larger mean thicknesses. Mean ice thickness at station MYI was measured to be 2.0 m, with a maximum thickness of 10 m. This contrasts a mean thickness of 0.8 m in the heavily-decayed FY ice, and thus a greater amount of underwater sea ice surface area emerges within a fractured MY ice surface than a fractured FY ice surface. This will have ramifications for sea ice thermodynamic processes in both MY and FY ice cover as lateral melting becomes dominant for floes less than several hundred meters in diameter [Steele, 1992], and floes < 40 m in diameter are difficult to further break mechanically and are governed by thermodynamic melting laterally [Toyota *et al.*, 2006] and underneath [Mellor, 1986].

Although the flexural fracture event described by Asplin *et al.*, [2012] occurred close to the 18 September 2009 minimum summer Arctic sea ice extent, measured *in situ* values of K_{\downarrow} and L_{\downarrow} radiation suggest that sufficient all-wave radiation was available at this particular latitude to drive enhanced lateral melting for at least 2 – 3 weeks following the event. The concurrent reduction of sea ice concentration will decrease the regional albedo, resulting in increased entrainment of L_{\downarrow} and K_{\downarrow} to the ocean surface, also enhancing rates of lateral melt. Our analysis of the sea ice surface prior to and following the 06 September 2009 fracture event allow us to parameterize regional surface albedo prior to and following the event. Furthermore, we are able to apply the same changes in regional surface albedo to hypothetical fracture events occurring earlier in the 2009 Arctic melt season (Figure 6.10). The total cumulative radiative energy estimated to go into lateral melting of ice floes changes considerably with the timing of the fracture events (table 1) and is mainly due to higher values of K_{\downarrow} earlier in the season [Figure

6.8]. A fracture event occurring on 01 August 2009 would have resulted in $71.29 \text{ MJ} \cdot \text{m}^{-2}$ of cumulative radiative energy to lateral melting over the period 01 – August – 30 September 2009. This represents an increase of $53.47 \text{ MJ} \cdot \text{m}^{-2}$ cumulative radiative energy for lateral melt, 300% more than $17.82 \text{ MJ} \cdot \text{m}^{-2}$ for the ‘no fracture’ case.

In addition to lateral melting, a fractured sea ice surface may introduce new opportunities for storm-driven upwelling [e.g. *Pickart et al.*, 2009] and mixing of the ocean surface mixed layer [e.g. *Wettklaufer*, 1991; *Perovich and Elder*, 2002; *Rainville and Woodgate*, 2009]. It is apparent that the Arctic sea ice cover is becoming increasingly vulnerable to anomalous spring and early-summer atmospheric forcing, such as extreme storms [e.g. *Simmonds and Rudeva*, 2012], anomalous wind forcing due to the Arctic dipole anomaly [*Wu et al.*, 2006; *Wang et al.*, 2009], and anomalous high pressure blocking over Greenland since 2007 [*Overland et al.*, 2012]. Long wave swells responsible for the *in situ* observation of flexural failure in the MY sea ice cover as described by *Asplin et al.*, [2012] are due to typical summer Arctic cyclones interacting with increased fetch across open water anomalies, and a heavily decayed ice margin. Although this event was observed late in the melt season (the 2009 sea ice minimum extent was observed on 18 September 2009), it is highly likely that the potential for similar events occurring earlier in the melt season will increase with the observed lengthening of the Arctic melt season [*Markus et al.*, 2009], and as mean sea ice thickness [*Maslanik et al.*, 2011] and volume continue to decline [*Laxon et al.*, 2013].

The influence of large abnormal cyclones on wave generation, wind forcing, and oceanic upwelling is of great interest and concern to thermodynamic and dynamic studies of sea ice. *Simmonds and Rudeva* [2012] present an excellent case of an otherwise normal

Siberian summer cyclone migrating over the Arctic Ocean, and encountering favorable upper-level dynamics and surface baroclinity, intensifying rapidly, and subsequently impacting the sea ice and ocean water column. The storm reached a central minimum pressure of 966 hPa on 06 August 2012, and then became coupled with favorable upper-level dynamic atmospheric forcing within the polar vortex and persisted in the Basin until it finally succumbed to cyclolysis over the Canadian Arctic Archipelago on 14 August 2012. The central pressure of this storm was the lowest of all Arctic August storms on record (1979 – 2012), and rated as the 13th most extreme storm in the Arctic basin on record. Baroclinity is a key factor attributed to the rapid decrease in central pressure when the storm migrated over the East Siberian Sea, and is typically strong along ice edges [*Screen et al., 2011*].

The significant reduction in areal sea ice coverage with concurrent observed reductions in sea ice thickness and volume [*Laxon et al., 2013*], left the summer ice cover in 2012 more vulnerable to this storm than it would have been in earlier decades [*Parkinson and Comiso, 2013*]. There is little evidence to suggest that the large negative anomalies of sea ice extent had any substantial impact on the cyclone, following the findings of *Stroeve et al., [2011b]*. In contrast, there is considerable evidence that wind and wave forcing from the storm greatly impacted the ice distribution through wave forcing, bottom melt, and possible oceanic upwelling [*Simmonds and Rudeva, 2012; Zhang et al., 2013*]. The cyclone occurred when Arctic sea ice was thin and the simulated Arctic ice volume had already declined ~40% from the 2007 – 2011 mean [*Laxon et al., 2013*]. The thin sea ice pack and the presence of ocean heat in the near surface temperature maximum layer created conditions that made the ice particularly vulnerable

to storms. During the storm, ice volume decreased about twice as fast as usual, owing largely to a quadrupling in bottom melt caused by increased upward ocean heat transport [Zhang *et al.*, 2013]. This increased ocean heat flux was due to enhanced mixing in the oceanic boundary layer, driven by strong winds and rapid ice movement.

A comparison with a sensitivity simulation driven by reduced wind speeds during the cyclone indicates that cyclone-enhanced bottom melt strongly reduces ice extent for about two weeks, with a reduced effect afterwards [Zhang *et al.*, 2013]. As stated previously, the net impact of this cyclone the 2012 minimum sea ice extent is estimated to only be $0.15 \times 10^6 \text{ km}^2$ (4.4%). Thus without the storm, 2012 would still have produced a record minimum [Zhang *et al.*, 2013]. Future changes in the frequency or timing of this process during the melt season, could exacerbate high rates of bottom melt observed recently in the southern Beaufort Sea [e.g. Perovich *et al.*, 2008], thereby contributing to further thermodynamic decay of Arctic sea ice cover.

Distributions of smaller ice floes tend to be more mobile and susceptible to wind forcing [Steer *et al.*, 2008]. Ice motion data available for our study period shows rapid westward ice motion and divergence at the monthly time scale, with the three beacons eventually spread along a 1200km west – east axis. This likely shows that fractured sea ice cover as a result of swells from Arctic storms is contributing to increasing variability in ice motion observed in recent years in the Arctic [Rampal *et al.*, 2009; Gimbert *et al.*, 2012a; Rampal *et al.*, 2011], with the greatest increases observed during summer [Gimbert *et al.*, 2012b]. Fracture of MY sea ice would correspond with the mechanical weakening of the Arctic sea ice cover, which is attributed to increased sea ice mobility [Gimbert *et al.*, 2012a]. This may result in ice floes being transported to areas where

conditions may be more favorable for melting, corresponding with *Rampal et al.*, [2011]. Furthermore, these conditions may have several implications for ice drifting speeds, deformation rates, export [*Rampal et al.*, 2009] during the autumn freeze-up period. Small MY ice floes that survive the summer may actually promote ice growth and ice thickness redistribution through rafting and ridging of young FY ice types. Conglomerate ice floes containing young FY ice and small MY ice floes are likely to be initially more susceptible to breakup during freeze-up season which may enhance sea ice mobility and increased ice ridging during the early stages of the freeze-up season. As freeze-up progresses, this process may act as a negative feedback by increasing ice volumes and thicknesses locally via ridging and deformation.

6.5 Conclusions

The implications of the mechanical sea ice decay process described in *Asplin et al.*, [2012] on dynamic and thermodynamic processes in Arctic sea ice have been investigated here as follows:

- 1) What were the physical characteristics of the sea ice cover after the storm swell fracturing in September 2009?
- 2) What impact does fracture have on rates of thermodynamic decay?
- 3) What were the implications of this process occurring in concert with cyclone-forced mixing and upwelling of ocean heat fluxes?
- 4) What were the implications of this process on sea ice dynamic processes?

The effects of the 06 September 2009 flexural fracture event on the sea ice cover are summarized as follows: 1) The area affected is estimated at 40,000 km², 2) Open water fractional coverage in the MY ice cover decreased from 3.7% to 2.7%, likely due to ice floe geometry or weak ice conditions favorable to ice convergence. 3) Heavily fractured FY ice cover had diverged to 80% sea ice cover by 09 September 2009, representing a 10% increase in sea ice open water area. 4). A shift in mean regional albedo from $\alpha = 0.66$ to 0.585 is detected following the fracture event, and reflects the increased presence of open water in the marginal ice zone, as well as drained shallow meltponds.

Understanding the implications of earlier occurrences of widespread fracture of Arctic sea ice is of key importance as large anomalous areas of open water are becoming commonplace in the changing Arctic Ocean. Furthermore, waves with longer periods than those observed by *Asplin et al.*, [2012] could penetrate further into the pack ice

[*Squire et al.*, 2009], thereby causing more widespread fracturing of the sea ice cover and reduction of mean regional albedo. The decrease in mean surface albedo following fracture allows the ocean surface to absorb a greater amount of incoming radiation, 80% of which goes to lateral melting [*Steele*, 1992]. We find that the decrease in mean surface albedo associated with the 06 September 2009 flexural fracture event resulted in $\sim 11.54 \text{ MJ} \cdot \text{m}^{-2}$ of additional cumulative radiative energy entrainment into the ocean mixed-layer than would have occurred had the fracture not taken place. The impact of this event occurring earlier in the season was also investigated. Radiative energy that goes to lateral melting was found to be enhanced by up to $53.47 \text{ MJ} \cdot \text{m}^{-2}$ in the case where the flexural fracture event occurred on 01 August 2009. Anomalous cyclone activity may further exacerbate rates of thermodynamic sea ice decay through increased mixing of the ocean mixed layer [*e.g. Zhang et al.*, 2013], and possibly through episodic deep water upwelling events.

Small ice floes are more susceptible to dynamic forcing from the wind and ocean currents in the southern Beaufort Sea. They may become easily entrained into the Beaufort Gyre, and moved towards the Chukchi Sea, and Bering Strait where they would be exposed to enhanced ocean heat fluxes from Pacific water intrusions through the Bering Strait [*Shimada et al.*, 2006; *Woodgate et al.*, 2006; *Perovich et al.*, 2008], and would also be vulnerable to wave-induced melt as described by *Wadhams et al.*, [1979]. Furthermore, a fragmented MY ice cover may serve to dynamically grow local sea ice volumes and thicknesses by inducing ridging during the freeze-up season.

We conclude that the physical forcing mechanism presented by *Asplin et al.*, [2012] may be a positive feedback process on Arctic sea ice decline, emerging as a direct

result of climate change. Furthermore, the initiation of this process earlier in the melt season coupled with anomalous cyclone activity may have devastating effects on the summer Arctic sea ice cover. We are convinced that this process is a feature of the newly emerging Arctic sea ice system, which is comprised predominantly of seasonal sea ice. Distributions of smaller, increasingly mobile MY and thick FY floes will be of great concern to transportation and industrial development within the Arctic Basin, and will require improved techniques for real-time monitoring and detection by remote sensing. Continued monitoring of the Arctic Basin is essential to developing better understanding new forms of ocean-sea ice-atmosphere interactions and coupling as they emerge as a result of Arctic climate change. This coupled process between the ocean, sea ice and atmosphere will have implications for modeling future sea ice dynamic and thermodynamic processes, and needs to be included in regional and large scale climate models to enhance processes of sea ice decay, formation and motion.

6.6 References

- Asplin, M. G., R. Galley, D. G. Barber, and S. Prinsenberg (2012), Fracture of summer perennial sea ice by ocean swell as a result of Arctic storms, *J. Geophys. Res.* 117, C06025, doi:10.1029/2011JC007221.
- Barber, D.G., R. Galley, M.G. Asplin, R. De Abreu, K.A. Warner, M. Pućko, M., Gupta, S. Prinsenberg, and Julien, S. (2009), Perennial pack ice in the southern Beaufort Sea was not as it appeared in the summer of 2009, *Geophys. Res. Lett.*, 36, 24, doi:10.1029/2009GL041434.
- Curry, J.A., J.L. Schramm, and E.E. Ebert (1995), Sea ice-albedo feedback mechanism. *J. Clim.*, 8:240-247.
- Ebert, E.E., and J.A. Curry (1993), An intermediate one-dimensional thermodynamic sea ice model for investigating ice-atmosphere interactions., *J. Geophys. Res.*, 98(C6):10085 – 10109.
- Ebert, E.E., J.L. Schramm., and J.A. Curry (1995), Disposition of solar radiation in sea ice and the upper ocean, *J. Geophys. Res.* 100, C8, 15965 – 15975.
- Fequet, D. (Ed.) (2002), MANICE: Manual of Standard Procedures for Observing and Reporting Ice Conditions, 9th ed., Can. Ice Serv., Environ. Can., Ottawa.
- Frankenstein, G.E. and R. Garner (1967), Equations for determining the brine volume of sea ice from 0.5 – 22.9 C. *J. Glaciol.* 6, 943 – 944.
- Galley, R.J., B.G.T. Else, S.J. Prinsenberg, and D.G. Barber (2013), Sea ice concentration, extent, age, motion and thickness in regions of proposed offshore oil and gas development near the Mackenzie Delta, Canadian Beaufort Sea. *Arctic*, 66(1).
- Gimbert, F., N.C. Jourdain, D. Marsan, J. Weiss, and B. Barnier (2012a), Recent mechanical weakening of the Arctic sea ice cover as revealed by larger sea ice inertial oscillations, *J. Geophys. Res.*, 117, C00J12, doi:10.1029/2011JC007633, 2012.
- Gimbert, F., D. Marsan, J. Weiss, N.C. Jourdain, and B. Barnier (2012b), Sea ice inertial oscillations in the Arctic Basin, *The Cryosphere*, 6, 1187-1201. 117, C00J12, doi:10.1029/2011JC007633, 2012.
- Katsaros, K.B., and J.E. Devault, (1986), On irradiance measurement errors at sea due to tilt of pyranometers. *J. of Atmos. Oceanic Tech.* 3, 740 – 745.
- Kwok, R., G. F. Cunningham, M. Wensnahan, I. Rigor, H.J. Zwally, and D. Yi (2009), Thinning and volume loss of the Arctic Ocean sea ice cover: 2003 – 2008, *J. Geophys. Res.*, 114, C07005, doi: 10.1029/2009JC005312.

Kwok, R., and G. F. Cunningham (2010), Contribution of melt in the Beaufort Sea to the decline in Arctic multiyear sea ice coverage: 1993–2009, *Geophys. Res. Lett.*, 37, L20501, doi: 10.1029/2010GL044678.

Hilmer, M., and P. Lemke (2000), On the decrease of Arctic sea ice volume, *Geophys. Res. Lett.*, 27(2), 3751 – 3754.

Intergovernmental Panel on Climate Change (2007), *Climate Change 2007: The Physical Science Basis: Contribution of Working Group I to the Fourth Assessment Report of the Intergovernmental Panel on Climate Change*, edited by S. Solomon *et al.*, Cambridge Univ. Press, New York.

Laxon S. W., K. A. Giles, A. L. Ridout, D. J. Wingham, R. Willatt, R. Cullen, R. Kwok, A. Schweiger, J. Zhang, C. Haas, S. Hendricks, R. Krishfield, N. Kurtz, S. Farrell and M. Davidson (2013), CryoSat-2 estimates of Arctic sea ice thickness and volume, *Geophys Res Lett.*, 40, doi:10.1002/grl.50193.

Lukovich, J. V., D. G. Babb, and D. G. Barber (2011), On the scaling laws derived from ice beacon trajectories in the southern Beaufort Sea during the International Polar Year - Circumpolar Flaw Lead study, 2007–2008, *J. Geophys. Res.*, 116, C00G07, doi:10.1029/2011JC007049.

MacWhorter, M.A., and R.A. Weller (1991), Error in measurement of incoming short-wave radiation made from ships and buoys. *J. of Atmos. Oceanic Tech.* 8, 108 – 117.

Markus, T., J.C Stroeve, and J. Miller (2009), Recent changes in Arctic sea ice melt onset, freeze-up and melt season length, *J. Geophys. Res.*, 114, C12024, doi: 10.1029/2009/JC005436.

Marty, C., R. Philipona, J. Delamere, E.G. Dutton, J. Michalsky, K. Stamnes, R. Stordvold, T. Stoffel, S.A. Clough, and E.J. Mlawer (2003), Downward Longwave irradiance uncertainty under Arctic atmospheres: measurements and modeling. *J. Geophys. Res.*, 108, D12, 4358, doi:10.1029/2002JD002937.

Maslanik, J.A., C. Fowler, J. Stroeve, S. Drobot, J. Zwally, D. Yi, and W. Emery (2007), A younger, thinner Arctic ice cover: Increased potential for rapid extensive sea ice loss, *Geophys Res. Lett.*, 34, L24501, doi: 10.1029/2007GL032043.

Maslanik, J., J.C. Stroeve, Fowler, and W. Emery (2011), Distribution and trends in Arctic sea ice age through spring 2011, *Geophys. Res. Lett.*, 38, L13502, doi: 10.1029/2011GL047735.

Mellor, M., (1986), Mechanical behaviour of sea ice, in Untersteiner, N (ed.), *The geophysics of Sea ice*, Plenum, New York, 165 – 281.

Minnett, P.J. (1999), The influence of solar zenith angle and cloud type on cloud radiative forcing at the surface in the Arctic. *J. Clim.*, 12, 147- 158.

Ngheim, S. V., I.G. Rigor, D.K. Perovich, P. Clemente-Colon, J.W. Weatherly, and G. Neumann (2007), Rapid reduction of Arctic perennial sea ice, *Geophys. Res. Lett.*, 34, L19504, doi: 10.1029/2007GL031138.

Nilsson, E.D., U. Rannik, and M. Hakansson (2001), Surface energy budget over the central Arctic Ocean during late summer and early freeze-up. *J. Geophys. Res.*, 106, 32,187-32,205.

Ogi, M., K. Yamazaki, and J. Wallace (2010), Influence of winter and summer surface wind anomalies on summer Arctic sea ice extent, *Geophys. Res. Lett.*, 37, L07701, doi: 10.1029/2009GL042356.

Ogi, M., and J. M. Wallace (2012), The role of summer surface wind anomalies in the summer Arctic sea ice extent in 2010 and 2011, *Geophys. Res. Lett.*, 39, L09704, doi:10.1029/2012GL051330.

Overland, J.E. (2009): Meteorology of the Beaufort Sea. *J. Geophys. Res.*, 114, C00A07, doi: 10.1029/2008JC004861.

Overland, J.E., J.A. Francis, E. Hanna, and M. Wang (2012), The recent shift in early summer Arctic atmospheric circulation, *Geophys. Res. Lett.*, 39, L19804. doi:10.29/2012GL053268.

Parkinson, C. L., and J. C. Comiso (2013), On the 2012 record low Arctic sea ice cover: Combined impact of preconditioning and an August storm, *Geophys. Res. Lett.*, 40, doi:10.1002/grl.50349.

Perovich, D.K., and B. Elder (2002), Estimates of ocean heat flux at SHEBA, *Geophys. Res. Lett.*, 29(9), doi:10.1029/2001GL014171.

Perovich, D.K., T.C. Grenfell, B. Light, and P.V. Hobbs (2002), Season evolution of the albedo of multiyear Arctic sea ice. *J. Geophys. Res.* 107(C10), doi:10.1029/2000JC000438.

Perovich, D.K., J.A. Richter-Menge, K.F. Jones, and B. Light (2008), Sunlight, water, and ice: Extreme Arctic sea ice melt during the summer of (2007), *Geophys. Res. Lett.*, 35, L11501, doi: 10.1029/2008GL034007.

Persson, P.O.G., C.W. Fairall, E.L. Andreas, P.S. Guest, and D.K. Perovich (2002), Measurements near the atmospheric surface flux group tower at SHEBA: Near-surface conditions and surface energy budget, *J. Geophys. Res.*, 107 (C10), doi:10.1029/2000JC000705.

Philipona, R., C. Betz, and C. Frohlich (1995), Characterization of pyrgeometer and the accuracy of atmospheric longwave radiation measurements. *Appl.*

Opt., 34(9), 1598– 1605.

Pickart, R. S., G. W. K. Moore, D.J. Torres, P.S. Fratantoni, R.A. Goldsmith, and J. Yang (2009), Upwelling on the continental slope of the Alaskan Beaufort Sea: Storms, ice, and oceanographic response, *J. Geophys. Res.*, 114, C00A13, doi:10.1029/2008JC005009.

Prinsenber, S.J. and J.S. Holladay (1993), Using an air-borne electromagnetic ice-thickness sensor to validate remotely sensed marginal ice zone properties. *In: Proceedings of the 12th International Conference on Port and Ocean Engineering under Arctic Conditions*, August 17 – 20, Hamburg (FRG). Vol. 2: pp. 936 – 948.

Raddatz, R.L., R.J. Galley, L.M. Candlish, M.G. Asplin, and D.G. Barber (2012), Water vapour over the western maritime Arctic: surface inversions, intrusions and total column. *Int. J. Climatol.*, doi:10.1002/joc.3524.

Rainville, L., and R.A. Woodgate (2009). Observations of internal wave generation in the seasonally ice free Arctic. *Geophys. Res. Lett.*, 36, L23604, doi:10.1029/2009GL041291.

Rampal, P., J. Weiss, and D. Marsan (2009), Positive trend in the mean speed and deformation rate of Arctic sea ice, 1979–2007, *J. Geophys. Res.*, 114, C05013, doi:10.1029/2008JC005066.

Rampal, P., J. Weiss, C. Dubois, and J.M. Campin (2011), IPCC climate models do not capture Arctic sea ice drift acceleration: consequences in terms of projected sea ice thinning and decline, *J. Geophys. Res.*, 116, C00D07, doi:10.1029/2011JC007110, 2011.

Rothrock, D.A. and A.S. Thorndike (1984), Measuring the sea ice floe distribution, *J. Geophys. Res.* 89 (C4), 6477 – 6486.

Rothrock, D.A., Y. Yu, and G.A. Maykut (1999), Thinning of the Arctic sea-ice cover. *Geophys. Res. Lett.*, 26(23), 3469 – 3472.

Scheuchl, B., D. Flett, C. Caves, and I. Cumming (2004), Potential of RADARSAT-2 for operational sea ice monitoring, *Can. J. Remote Sensing*, 30(3), 448-461.

Screen, J., I. Simmonds, and K. Keay (2011), Dramatic interannual changes of perennial Arctic sea ice linked to abnormal summer storm activity, *J. Geophys. Res.* 116, D15105, doi: 10.1029/2011JD015847.

Shimada, K., T. Kamoshida, M. Itoh, S. Nishino, E. Carmack, F. McLaughlin, S. Zimmermann and A. Proshutinsky (2006): Pacific Ocean inflow: Influence on catastrophic reduction of sea ice cover in the Arctic Ocean. *Geophys. Res. Lett.*, 33, L08605, doi: 10.1029/2005GL025624.

- Simmonds, I., and I. Rudeva (2012), The great Arctic cyclone of August 2012, *Geophys. Res. Lett.*, 39, L23709, doi:10.1029/2012GL054259.
- Sirevaag, A., S. de la Rosa, I. Fer, M. Nicolaus, M. Tjernstrom, and M.G. McPhee (2011), Mixing, heat fluxes and heat content evolution of the Arctic Ocean mixed layer. *Ocean Sci. Discuss.*, 8, 247–289. doi:10.5194/osd-8-247-2011.
- Squire, V.A., G.L. Vaughan, and I.G. Bennetts (2009), Ocean surface wave evolution in the Arctic basin. *Geophys. Res. Lett.*, 36, L22502, doi: 10.1029/2009GL040676.
- Steele, M. (1992), Sea Ice Melting and Floe Geometry in a Simple Ice-Ocean Model, *J. Geophys. Res.*, 97(C11), 17,729–17,738, doi: 10.1029/92JC01755.
- Steele, M., W. Ermold, and J. Zhang (2008), Arctic Ocean surface warming trends over the past 100 years, *Geophys. Res. Lett.*, 35, L02614, doi: 10.1029/2007GL031651.
- Steer, A., A. Worby, and P. Heil (2008), Observed changes in sea-ice floe distribution during early summer in the Western Weddell Sea. *Deep-Sea Res. II* (2008), 933 – 942.
- Stroeve, J.C., M.C. Serreze, M.M. Holland, J.E. Kay, J. Maslanik, J., and A.P. Barrett (2011a), The Arctic's rapidly shrinking sea ice cover: a research synthesis, *Clim. Ch.* doi: 10.1007/s10584-011-0101-1.
- Stroeve, J.C., M.C. Serreze, A. Barrett, and D. Kindig (2011b) Attribution of recent changes in autumn cyclone associated precipitation in the Arctic, *Tellus A* 63(4): 653 – 663: DOI:10.1111/j.1600-0870.2011.00515.x.
- Timco, G.W. and S. O'Brien (1994), Flexural strength equation for sea ice, *Cold Reg. Sci. Technol.*, 22(3): 285 – 298.
- Timco, G.W. and M.E. Johnston (2002), Sea ice strength during the melt season. Ice in the environment: Proceedings of the 16PthP LAHR International symposium on ice, Dunedin, New Zealand, 2 – 6 December.
- Toyota, T., S. Takatsuji, and M. Nakayama (2006), Characteristics of sea ice floe size distribution in the seasonal ice zone, *Geophys. Res. Lett.*, 33, L02616, doi:10.1029/2005GL024556.
- Wadhams, P., (1973), Attenuation of Swell by Sea Ice, *J. Geophys. Res.*, 78 (18): 3552 – 3563.
- Wadhams, P., A.E. Gill, and P.F. Linden (1979), Transects by submarine of the East Greenland Polar Front. *Deep-Sea Res.* 26A, 1311–1327.
- Wadhams, P., V.A. Squire, D.J. Goodman, A.M. Cowan, and S.C. Moore (1988), The attenuation of ocean waves in the marginal ice zone, *J. Geophys. Res.*, 93, 6799– 6818.

Wettlaufer, J.S. (1991). Heat flux at the ice-ocean surface. *J. Geophys. Res.*, 96(C4):7215 – 7236.

Woodgate, R. A., K. Aagaard, and T.J. Weingartner (2006), Interannual changes in the Bering Strait fluxes of volume, heat and freshwater between 1991 and 2004, *Geophys. Res. Lett.*, 33, L15609, doi: 10.1029/2006GL026931.

Wang, J., J. Zhang, E. Watanabe, M. Ikeda, K. Mizobata, J.E. Walsh, X. Bai, and B. Wu, 2009: Is the Dipole Anomaly a major driver to record lows in Arctic summer sea ice extent? *Geophys. Res Lett.*, 36, L05706, doi:10.1029/2008GL036706.

Wu, B., J. Wang, and J.E. Walsh, 2006: Dipole Anomaly in the Winter Arctic Atmosphere and Its Association with Sea Ice Motion. *J. Clim.*, 19, 210-225, doi:10.1175/JCLI3619.1.

Zhang, J., R. Lindsay, A. Schweiger, and M. Steele (2013), The impact of an intense summer cyclone on 2012 Arctic sea ice retreat, *Geophys. Res. Lett.*, doi: 10.1002/grl.50190.

CHAPTER SEVEN: CONCLUSIONS AND RECOMMENDATIONS

7.1 Summary of contributions

Chapter one provides an introduction to this thesis and the rationale for performing the work contained herein.

Chapter two provides a review of the pertinent literature that encompasses Arctic sea ice, Arctic cyclones, and trends in Arctic climate with an emphasis on the interaction of Arctic cyclones with thermodynamic and dynamic processes in snow-covered sea ice at different spatial and temporal scales, and their importance in the changing Arctic climate system.

Chapter three details a synoptic climatology (1979 – 2006) created using Principal Components Analysis and k-means clustering for the southern Beaufort Sea. The twelve categories (synoptic types) characterize cyclonic and anticyclone sea level pressure patterns that make up the synoptic climatology of the study region. The seasonal frequency, persistence and duration statistics are calculated for each of the twelve synoptic types, and are used to investigate sea level pressure atmospheric forcing on sea ice vorticity in the Beaufort Gyre.

Chapter four extends the synoptic climatology presented in section 3 to characterize sea level atmospheric circulation patterns for the period 1979 – 2011, which includes the five most recent years of record low summer minimum sea ice extents. This period also covers the 2007 – 2008 International Polar Year (IPY) Circumpolar Flaw Lead System Study (CFL), and the 2009 ArcticNet / IPY-GEOTRACES / Imperial Oil Industrial Partnership field programs, which are the main field campaigns for field data

used in this thesis. Changes in atmospheric circulation are assessed for recent years of rapidly declining Arctic sea ice extent (1999 – 2011) versus climatology (1979 – 1998).

Chapter five presents first-ever *in situ* observations of a new physical forcing mechanism between Arctic cyclones, the ocean, multi-year sea ice, and large fetch in the southern Beaufort Sea that has emerged recently as a result of sea ice decline and climate change. The process illustrates a coupled forcing between declining summer sea ice extent, and winds from Siberian cyclones that can migrate over the Arctic Ocean. The interaction of strong winds with the fetch generated long waves, which were observed to penetrate deep (~350km) into multi-year ice, causing flexural swell and fracture within the ice cover. This process contributes to the ice-albedo feedback mechanism, has implications for rates of thermodynamic ice decay, ice mobility, and freeze-up, and is important for consideration in future Arctic sea ice models.

Chapter six further investigates the implications of the process described in chapter five on rates of lateral melting, sea ice dynamics, and discusses the role of this process in conjunction with cyclone-induced upwelling. This section specifically focuses on investigating the timing of future flexural fracture events as occurrence earlier in the season would decrease regional albedo earlier in the melt season, thereby creating conditions favorable for increased entrainment of solar radiation. Results show that earlier occurrences of flexural fracture could permit considerably more radiative energy to be entrained in the ocean for lateral melting.

7.2 Conclusions

The research presented in this thesis investigates cyclone-forcing of dynamic and thermodynamic processes in Arctic sea ice and across the ocean-sea ice-atmosphere interface at different spatial and temporal scales throughout the annual cycle. Furthermore, these processes are studied in the context of a changing Arctic climate system, characterized by declining sea ice thickness, volume, and extent with the greatest declines of the latter being observed in summer and early autumn.

Chapter three investigates the role of summer Arctic cyclones and associated surface winds on the changing nature of reversals of the Beaufort Gyre. A catalogue of daily synoptic weather types is generated for the Beaufort Sea Region covering the period 1979 to 2006 using NCEP/NCAR reanalysis mean sea level pressure data, principle components and k-means cluster analyses. Mean synoptic type frequency, persistence and duration values are calculated for each synoptic type and contrasted between summer and winter. Daily synoptic types are linked to changes in sea ice vorticity by using correlation analysis on lagged sea ice vorticity data. Lag-correlations are found between synoptic types and sea ice vorticity smoothed over a 12-week running mean, and show that cyclonic types, which promote southerly or easterly atmospheric circulation over the southern Beaufort Sea, commonly precede summer reversals.

Chapter four investigates the synoptic atmospheric forcing of winter sea ice leads and how rates of wind-forced lead formation responded to the extreme summer sea ice minimum of 2007, and how the atmosphere subsequently responded to heat fluxes from open water areas within the marginal ice zone (MIZ). The synoptic climatology for the southern Beaufort Sea presented in chapter three was extended to cover the period 1979 –

2011 and was employed to compare synoptic type frequencies between when Arctic sea ice cover was observed to be rapidly declining in extent and thickness (1999 – 2011) to climatology. Significant ($p < 0.05$) seasonal synoptic type frequency anomalies were revealed, indicating a stronger Beaufort high, increased easterly wind forcing in autumn and winter, and greater seasonal variability in synoptic circulation patterns during 1999 – 2011. Sea ice concentrations in the study region followed expected seasonal trends through the winter, but were below normal in the autumn and summer periods. High rates of young ice production in November and December in Amundsen Gulf were linked to synoptic types that promoted large-scale easterly wind forcing over the region. Investigation of the atmospheric boundary layer following a large lead formation event (03 – 18 February 2008) forced by strong easterly winds revealed a thermodynamically-coupled response between sea ice lead formation and near-surface temperatures. Calculated sensible heat fluxes revealed an event maximum of $80.14 \text{ W}\cdot\text{m}^2$ on 13 February 2008.

Chapter five presents first-ever observations of a new physical forcing mechanism between Arctic cyclones, the ocean and Arctic multi-year sea ice that has emerged recently as a result of sea ice decline and climate change in the southern Beaufort Sea. Large expanses of open water in the Siberian, Laptev, Chukchi, and Beaufort Seas result from declining summer sea ice cover, and consequently introduce long fetch distances within the Arctic Basin. Strong winds from migratory cyclones coupled with increasing fetch distances generate large waves that can propagate into the pack ice and break it up. On 06 September 2009, we observed the intrusion of large swells into the multi-year pack ice approximately 250 km from the ice edge. These large swells induced nearly

instantaneous widespread fracturing of the multi-year pack ice, reducing the large, and (> 1 km diameter) parent ice floes to small (100 – 150 m diameter) floes. This process increased the total ice floe perimeter exposed to the open ocean, allowing for more efficient distribution of energy from ocean heat fluxes, and incoming radiation into the floes, thereby enhancing lateral melting. This process of storm-driven mechanical sea ice decay is therefore presented as a potentially powerful positive feedback process that will accelerate the loss of Arctic sea ice.

Chapter six further investigates the thermodynamic and dynamic implications of ocean swell-driven flexural fracturing within perennial pack ice as presented in chapter five. Analysis of Radarsat-2 imagery shows that the 06 September 2009 flexural fracture event affected an area of $\sim 40,000 \text{ km}^2$. Open water fractional area in the multi-year ice cover initially decreased from 3.7% to 2.7%, but later increased to $\sim 20\%$ with wind-forced divergence of the ice pack. Energy available for lateral melting was assessed by estimating the change in energy entrainment from longwave and shortwave radiation in the mixed-layer of the ocean following flexural fracture of the ice cover. $11.54 \text{ MJ} \cdot \text{m}^{-2}$ of additional energy for lateral melting of ice floes was identified as a result of the 06 September 2009 fracture event. Model estimates show that hypothetical earlier occurrences of similar fracture events could provide up to three times the additional energy for lateral melt, thereby accelerating the rate of summer sea ice decline. Furthermore, large areas of fetch combined with a fractured ice cover may increase the likelihood of storm-driven upwelling of ocean heat to the surface, enhancing bottom melt in the ice cover.

It is evident from the research presented in this dissertation that cyclone forcing of Arctic sea ice is both linked and becoming enhanced with sea ice decline. Changing frequency and persistence of synoptic-scale atmospheric circulation combined with declining sea ice extent is driving more frequent reversals of the Beaufort Gyre (Chapter 3), which leads to widespread sea ice divergence within the Arctic Ocean. Increased frequencies of easterly wind forcing in autumn and winter over the southern Beaufort Sea are linked to declining sea ice extent in the synoptic climatology of the southern Beaufort Sea. An increase in easterly wind forcing, coupled with declining multi-year ice cover, and an increasingly mobile ice pack may be increasing rates of sea ice MIZ open water formation and young ice production in the Beaufort Sea, and subsequently impacting the near-surface atmospheric boundary layer (Chapter 4). Furthermore, these processes may be preconditioning the sea ice cover for continued decline of summer sea ice extent. Large anomalous expanses of fetch in the Arctic Ocean are being forced by winds from Arctic cyclones, leading to the generation of large swells which can penetrate deep into the multi-year ice pack, and cause flexural fracture in thick multi-year ice cover (Chapter 5). This process, combined with sea ice divergence driven by wind or ocean forcing increases open water fractional coverage, thereby reducing regional mean albedo. This results in increased entrainment of radiative energy into the ocean that can enhance lateral melting of ice floes (Chapter 6). It is expected that this process may occur earlier in the melt season in coming years, thereby exacerbating recent declines in summer sea ice extent, and multi-year sea ice cover. This process is linked to the research described in chapter 3 as reversals of the Beaufort Gyre can drive sea ice divergence, thereby reducing regional albedo, and may also enhance the processes discussed in chapter 4

through continued decay of the multi-year sea ice cover, thereby leading to an increase in sea ice mobility during the autumn and winter.

7.3 Future Work

First and foremost, the implications of the coupled ocean-sea ice-cyclone process described in chapter 5 require further investigation via field and modeling studies. As the Arctic sea ice cover progresses towards a seasonally ice-free state, the remaining multi-year ice is likely to be subsequent to long wave forcing from storms, and will be at considerable risk for fracture. This will have ongoing implications for modeling sea ice dynamic and thermodynamic processes. This will also have implications for detection of extreme ice features and ice hazards as defined by industrial interests in the Arctic. In the case of offshore oil development, understanding the conditions that lead to the formation of extreme ice features are critical in developing techniques to be able to detect and track them using remote sensing techniques as required by ice management by this industry.

With respect to atmospheric forcing of sea ice, reversals of the Beaufort Gyre and open water formation, the work completed in chapters three and four should be enhanced by repeating the study for the entire Arctic basin including recent years of declining seasonal sea ice thickness, as well as total sea ice volume. In particular, the role of cyclones and atmospheric forcing of the Beaufort Gyre resulting in large-scale mid-winter fracture events needs more attention. This is in light of the widespread winter fracturing event driven by strong easterly wind forcing observed in winter 2013.

In general, future work should focus on cyclone interactions with an Arctic Ocean that is becoming a marginal ice zone in its entirety. Decreasing seasonal ice extents have been linked to changes in atmospheric circulation both at the mesoscale and hemispheric scale and it is prudent to continue to continue building an understanding of how Arctic cyclones influence the increasingly ice free summer Arctic, as well as the evolution of an

increasing areal first-year sea ice extent each year. Furthermore, the role of large cyclones driving large-scale oceanic upwelling needs further observation and study. It is my hope that the new scientific infrastructure developments in Canada designed to support Arctic research will enable the future research proposed here a reality.

The recently observed acceleration of the decline of Arctic sea ice extents, and increasing mobility of the pack ice are strong evidence that stress the importance for improving the parameterization of sea ice dynamics in general circulation models. Another important direction for general circulation model development is to better forecast the future intensities, frequencies and storm tracks of Arctic cyclones. The rapidly decreasing summer Arctic sea ice cover will lead to greater expanses of open water persisting late into the winter season. This represents an increase in areas that are subject to ocean-atmosphere coupling of heat and vapor fluxes, and may impact future cyclogenesis rates, precipitation formation, and wind patterns.

APPENDIX A: CONTRIBUTIONS OF COLLABORATING AUTHORS

Chapter 3

I formulated the key objectives, collected the data and conducted the central analysis of this section. Jennifer Lukovich provided the vorticity data, and both David Barber and Jennifer Lukovich provided valuable discussion and revision advice for the manuscript.

Chapter 4

I formulated the key objectives, collected the data and conducted the central analysis of this section. Lauren Candlish and I co-collected the microwave profiler and radiosonde data in the field. Ryan Galley provided me with a gridded sea ice dataset. Tim Papakyriakou provided me with heat flux data, processed by Brent Else, and along with Rick Raddatz, all three provided me with valuable feedback on my manuscript. David Barber provided comments on the manuscript at various stages of preparation.

Chapter 5

I formulated the key objectives, collected the data and conducted the central analysis of this section. Simon Prinsenbergh operated the helicopter-based electromagnetic induction system and provided the ice thickness survey dataset and video imagery. Brent Else and Ryan Galley provided invaluable advice for revising the manuscript. David Barber provided comments on the manuscript at various stages of preparation.

Chapter 6

I formulated the key objectives, collected the data and conducted the central analysis of this section. Randall Scharien helped me with fractional ice / open water analysis on SAR imagery, obtained via Stephen Howell at Environment Canada. Tim Papakyriakou and Brent Else provided me with radiation data, and commentary on its use. Simon Prinsenbergh operated the helicopter-based electromagnetic induction system and provided the ice thickness survey dataset and video imagery. David Barber provided comments on the manuscript.

APPENDIX B: ADDITIONAL CONTRIBUTIONS TO THE PEER-REVIEWED LITERATURE

In addition to the four peer-reviewed journals that compose this thesis, I have co-authored 19 journal articles, three technical documents, and two book chapters during the course of my Ph.D. work. This work is related to my thesis but is considered more a contribution to the collaborative research at CEOS arising directly from my collaboration in multidisciplinary field programs in the Arctic.

1. Babb, D., **M.G. Asplin**, R.J. Galley, R. Scharien, J.V. Lukovich and D.G. Barber, (2013), Multiyear sea ice export through Bering Strait during winter 2011/12. *J. Geophys. Res. (In Review)*.
2. Raddatz, R.L., Galley, R.J., T. Papakyriakou, **M.G. Asplin**, L.M. Candlish, B. Else, and D.G. Barber (2013), All-sky Surface Radiation & Clear-Sky Surface Energy Budgets: summer to freeze-up in the western maritime Arctic, *Int. J. of Climatol. (In review)*.
3. Else, B.G.T., T.N. Papakyriakou, **M.G. Asplin**, David G. Barber, Ryan J. Galley, Lisa A. Miller, Al Mucci (2013), Annual and Interannual Variability of Air-Sea CO₂ Exchange in an Arctic Polynya Region, which has been submitted for possible publication in Global Biogeochemical Cycles, *Global. Biogeochem. Cycles, Manuscript #2012GB004425. In press*.
4. Candlish L.M., R.L. Raddatz, **M.G. Asplin**, D.G. and D.G. Barber (2013), A Validation of CloudSat and CALIPSO's Temperature, Humidity, Cloud Detection and Cloud Base Height over the Arctic Marine Cryosphere. *Atmosphere-Ocean (In press)*.
5. Raddatz R.L., **M.G. Asplin**, T. Papakyriakou, L.M. Candlish, R.J. Galley, B. Else, B. and D.G. Barber (2013), All Sky Downwelling Longwave Radiation and Atmospheric-Column Water Vapour and Temperature over the Western Maritime Arctic. *Atmos.-Ocean*, 51(2), 145-152, doi.org/10.1080/07055900.2012.760441
6. Raddatz, R.L., R.J. Galley, L.M. Candlish, **M.G. Asplin**, D.G. Barber (2013), Integral profile estimates of latent heat flux under clear skies at an unconsolidated sea-ice surface, *Atmos.-Ocean*, 1–10. doi.org/10.1080/07055900.2013.785383.
7. Raddatz, R.L., R. Galley, L. Candlish, **M.G. Asplin**, and Barber, D.G. (2013) Integral profile estimates of sensible heat flux from an unconsolidated sea-ice surface, *Atmos.-Ocean*, 5 (2), 135-144. doi.org/10.1080/07055900.2012.759900.

8. Raddatz, R., R. Galley, L. Candlish, **M.G. Asplin**, and Barber, D.G. (2013) Water vapor over the western maritime Arctic: surface inversions, intrusions and total column. *Int. J. Climatol.*, 33, 1436-1443. doi:10.1002/joc.3524.
9. **Asplin, M.G.**, and R. Scharien (Eds.)(2012) ArcticNet 2011 Expedition of the CCGS Amundsen: Data Report, *CEOS-TEC-2012-01-25*.
10. Barber, D.G., **M.G. Asplin**, J. Lukovich, R. Galley, R. Scharien, D. Isleifson, L. Candlish, R. Raddatz, S. Prinsenberg, J. Iacozza, M. Gupta, and C.J. Mundy, Section 3.2: Ocean-Sea Ice-Atmosphere Interactions *in: Barber, D.G., Tjaden, T., Barber, L., Leitch, D., and Chan, W. (Eds.)(2012), On the edge: From knowledge to action during the fourth International Polar Year Circumpolar Flaw Lead System Study (2007-2008)*. ©2012 University of Manitoba, ISBN 978-0-9813265-1-1.
11. **Asplin, M.G.**, J. Michaud, and J.E. Friddell, Chapter 5: The IPY-CFL Data Legacy *in: Barber, D.G., Tjaden, T., Barber, L., Leitch, D., and Chan, W. (Eds.) (2012), On the edge: From knowledge to action during the fourth International Polar Year Circumpolar Flaw Lead System Study (2007-2008)*. ©2012 University of Manitoba, ISBN 978-0-9813265-1-1.
12. **Asplin M.** and R. Galley, (Eds.)(2011), CCGS Amundsen 2010 Field Program, ArcticNet / BP Partnership Met/Ocean Data Report, *CEOS-TEC-2011-01-31*.
13. Barber, D. G., **M. G. Asplin**, T. Papakyriakou, L. Miller, B.G.T. Else, J. Iacozza, C.J. Mundy, M. Gosselin, N.C. Asselin, S. Ferguson, J.V. Lukovich, G.A. Stern, A. Gaden, M. Pucko, N.-X. Geilfus, and F. Wang (2012), Consequences of change and variability in sea ice on the marine ecosystem and biogeochemical processes during the 2007-2008 Canadian international polar year program, *Clim. Ch.*, 115, 135 – 159, doi:10.1007/s10584-012-0482-9.
14. Barber, D. G., **M. G. Asplin**, R. L. Raddatz, L.M. Candlish, S. Nickels, R. Scharien, S. Meakin, K.P. Hochheim, J. Lukovich, R.J. Galley, and S. J. Prinsenberg (2012), Causes of change and variability in sea ice during the 2007 – 2008 Canadian international polar year program, *Clim. Ch.*, 115, 115 -133, doi:10.1007/s10584-012-0477-6.
15. Candlish, L.M., R.L. Raddatz, **M.G. Asplin**, and D.G. Barber (2012), Atmospheric Temperature and Absolute Humidity Profiles over the Beaufort Sea and Amundsen Gulf from a Microwave Radiometer. *Journal of Atmospheric and Oceanic Technology*, doi: 10.1175/JTECH-D-10-05050.1.
16. Nghiem, S.V., I.G. Rigor, A. Richter, J.P. Burrows, P.B. Shepson, J.W. Bottenheim, D.G. Barber, A. Steffen, J.R. Latonas, F. Wang, G.A. Stern, P. Clemente-Colon, S. Martin, D.K. Hail, L. Kaleschike, P.J. Tackett, G. Nuemann, G, and **M.G. Asplin** (2012), Field and satellite observations of the formation a

distribution of Arctic atmospheric bromine above a rejuvenated sea ice cover, *J. Geophys. Res.*, doi: 10.1029/2011JD016268.

17. Scharien, R.K., J.J. Yackel, D.G. Barber, **M. Asplin**, M. Gupta, and D. Isleifson (2012) Geophysical and morphological controls on in situ C band polarimetric scattering from melt pond covered Arctic first-year sea ice, *J. Geophys. Res.* 117, C9, doi: 10.1029/2011JC007353.
18. Seabrook, J., J. Whiteway, R.M. Staebler, J.W. Bottenheim, L. Komguem, L.H. Gray, D. Barber, and **M. Asplin** (2011) LIDAR measurements of Arctic Boundary Layer Ozone Depletion Events Over the Frozen Arctic Ocean, *J. Geophys. Res.* 116, D00S02, doi:10.1029/2011JD016335, 2011.
19. Tremblay, J.E., S. Belanger, D.G. Barber, **M. Asplin**, J. Martin, G. Darnis, L. Fortier, Y. Gratton, H. Link, P. Archambault, A. Sallon, C. Michel, W.G. Williams, B. Phillippe, and M. Gosselin (2011), Climate forcing multiplies biological productivity in the coastal Arctic Ocean, *Geophys. Res. Lett.* 38, L18604, doi:10.1029/2011GL048825, 2011.
20. Raddatz, R.L., **M.G. Asplin**, L. Candlish, and D.G. Barber (2011), General characteristics of the atmospheric boundary layer in a flaw lead polynya region for winter and spring, *Boundary Layer Meteorology*, 138:321 – 335, doi: 10.1007/s10546-010-9557-1.
21. Barber, D. G., **M. Asplin**, Y. Gratton, J. Lukovich, R. Galley, R.L. Raddatz, R.L., and D. Leitch (2010), The International Polar Year (IPY) Circumpolar Flaw Lead (CFL) System Study: introduction and physical system, *Atmos.- Ocean*, 48(4), 225-243, doi:10.1007/OC317.2010.
22. Barber, D.G., R. Galley, M.G. **Asplin**, R. De Abreu, K. Warner, M. Pucko, M. Gupta, S. Prinsenberg, and S. Julien, (2009). The summer perennial pack ice in the southern Beaufort Sea was not as it appeared in the summer of 2009, *Geophys. Res. Lett.* 36, L24501, doi:10.1029/2009GL041434.
23. **Asplin M.** and L. Candlish, (Eds.)(2009), CCGS Amundsen 2009 Field Program: ArcticNet / IOL Partnership Met/Ocean Data Report, 2009, (Eds.) *CEOS-TEC-2009-12-05*.
24. Lukovich, J.V., **M.G. Asplin**, and D.G. Barber, D.G. (2008), Atmospheric forcing of the Beaufort Sea ice gyre: Part II: Stratospheric-surface coupling, *Jour. Geophys. Res.* (2008JC004849).